Jordan Journal of
PHYSICS
An International Peer-Reviewed Research Journal

Volume 15, No. 2, June 2022, Dhū al-Qa'dah 1443 H

Jordan Journal of Physics (*JJP*): An International Peer-Reviewed Research Journal funded by the Scientific Research and Innovation Support Fund, Jordan, and published quarterly by the Deanship of Research and Graduate Studies, Yarmouk University, Irbid, Jordan.

EDITOR-IN-CHIEF: **Mahdi Salem Lataifeh**
Department of Physics, Yarmouk University, Irbid, Jordan.
mahdi.q@yu.edu.jo

EDITORIAL BOARD:	**ASSOCIATE EDITORIAL BOARD**
Prof. Nabil Y. Ayoub *Department of Basic Sciences, School of Basic Sciences and Humanities, German Jordanian University, Jordan.* *nabil.ayoub@gju.edu.jo* **Prof. Marwan S. Mousa** *Department of Physics, Mu'tah University, Al-Karak, Jordan.* *mmousa@mutah.edu.jo* **Prof. Tareq F. Hussein** *Department of Physics, The University of Jordan, Amman, Jordan.* *t.hussein@ju.edu.jo* **Prof. Mohammad Al-Sugheir** *Department of Physics, The HashemiteUniversity, Zarqa, Jordan.* *msugh@hu.edu.jo* **Prof. M-Ali H. Al-Akhras (AL-Omari)** *Department of Physics, Jordan University of Science & Technology, Irbid, Jordan.* *alakmoh@just.edu.jo* **Prof. Ibrahim A. Bsoul** *Department of Physics, Al al-Bayt University, Mafraq, Jordan.* *Ibrahimbsoul@yahoo.com*	**Prof. Mark Hagmann** *Desert Electronics Research Corporation, 762 Lacey Way, North Salt Lake 84064, Utah, U. S. A.* *MHagmann@NewPathResearch.Com.* **Dr. Richard G. Forbes** *Dept. of Electrical and Electronic Engineering, University of Surrey, Advanced Technology Institute and Guildford, Surrey GU2 7XH, UK.* *r.forbes@surrey.ac.uk* **Prof. Roy Chantrell** *Physics Department, The University of York, York, YO10 5DD, UK.* *roy.chantrell@york.ac.uk* **Prof. Susamu Taketomi** *2-35-8 Higashisakamoto, Kagoshima City, 892-0861, Japan.* *staketomi@hotmail.com*

Editorial Secretary: Majdi Al-Shannaq. **Languages Editor**: Haider Al-Momani

Manuscripts should be submitted to:

Prof. Mahdi Salem Lataifeh
Editor-in-Chief, Jordan Journal of Physics
Deanship of Research and Graduate Studies
Yarmouk University-Irbid-Jordan
Tel. 00 962 2 7211111 Ext. 2075
E-mail: *jjp@yu.edu.jo*
Website: *http://Journals.yu.edu.jo/jjp*

Jordan Journal of
PHYSICS
An International Peer-Reviewed Research Journal

Volume 15, No. 2, June 2022, Dhū al-Qa'dah 1443 H

INTERNATIONAL ADVISORY BOARD:

Prof. Dr. Humam B. Ghassib
Department of Physics, The University of Jordan, Amman 11942, Jordan.
humamg@ju.edu.jo

Prof. Dr. Sami H. Mahmood
Department of Physics, The University of Jordan, Amman 11942, Jordan.
s.mahmood@ju.edu.jo

Prof. Dr. Nihad A. Yusuf
Department of Physics, Yarmouk University, Irbid, Jordan.
nihadyusuf@yu.edu.jo

Prof. Dr. Hardev Singh Virk
#360, Sector 71, SAS Nagar (Mohali)-160071, India.
hardevsingh.virk@gmail.com

Dr. Mgr. Dinara Sobola
Department of Physics, Brno University of Technology, Brno, Czech Republic.
Dinara.Dallaeva@ceitec.vutbr.cz

Prof. Dr. Shawqi Al-Dallal
Department of Physics, Faculty of Science, University of Bahrain, Manamah, Kingdom of Bahrain.

Prof. Dr. Jozef Lipka
Department of Nuclear Physics and Technology, Slovak University of Technology, Bratislava, llkovicova 3, 812 19 Bratislava, Slovakia.
Lipka@elf.stuba.sk

Prof. Dr. Mohammad E. Achour
Laboratory of Telecommunications Systems and Decision Engineering (LASTID), Department of Physics, Faculty of Sciences, Ibn Tofail University, BP.133, Kenitra, Morocco (Morocco)
achour.me@univ-ibntofail.ac.ma

Prof. Dr. Ing. Alexandr Knápek
Group of e-beam lithograpy, Institute of Scientific Instruments of CAS, Královopolská 147, 612 64 Brno, Czech Republic.
knapek@isibrno.cz

The Hashemite Kingdom of Jordan

Yarmouk University

Jordan Journal of PHYSICS

An International Peer-Reviewed Research Journal

Funded by the Scientific Research and Innovation Support Fund

Volume 15, No. 2, June 2022, Dhū al-Qa‘dah 1443 H

Instructions to Authors

Instructions to authors concerning manuscript organization and format apply to hardcopy submission by mail, and also to electronic online submission via the Journal homepage website (http://jjp.yu.edu.jo).

Manuscript Submission

1- **E-mail to** : jjp@yu.edu.jo

2- **Online**: Follow the instructions at the journal homepage website.

Original *Research Articles*, *Communications* and *Technical Notes* are subject to critical review by minimum of two competent referees. Authors are encouraged to suggest names of competent reviewers. *Feature Articles* in active Physics research fields, in which the author's own contribution and its relationship to other work in the field constitute the main body of the article, appear as a result of an invitation from the Editorial Board, and will be so designated. The author of a *Feature Article* will be asked to provide a clear, concise and critical status report of the field as an introduction to the article. *Review Articles* on active and rapidly changing Physics research fields will also be published. Authors of *Review Articles* are encouraged to submit two-page proposals to the Editor-in-Chief for approval. Manuscripts submitted in *Arabic* should be accompanied by an Abstract and Keywords in English.

Organization of the Manuscript

Manuscripts should be typed double spaced on one side of A4 sheets (21.6 x 27.9 cm) with 3.71 cm margins, using Microsoft Word 2000 or a later version thereof. The author should adhere to the following order of presentation: Article Title, Author(s), Full Address and E-mail, Abstract, PACS and Keywords, Main Text, Acknowledgment. Only the first letters of words in the Title, Headings and Subheadings are capitalized. Headings should be in **bold** while subheadings in *italic* fonts.

Title Page: Includes the title of the article, authors' first names, middle initials and surnames and affiliations. The affiliation should comprise the department, institution (university or company), city, zip code and state and should be typed as a footnote to the author's name. The name and complete mailing address, telephone and fax numbers, and e-mail address of the author responsible for correspondence (designated with an asterisk) should also be included for official use. The title should be carefully, concisely and clearly constructed to highlight the emphasis and content of the manuscript, which is very important for information retrieval.

Abstract: A one paragraph abstract not exceeding 200 words is required, which should be arranged to highlight the purpose, methods used, results and major findings**.**

Keywords: A list of 4-6 keywords, which expresses the precise content of the manuscript for indexing purposes, should follow the abstract.

PACS: Authors should supply one or more relevant PACS-2006 classification codes, (available at http://www.aip.org/pacs/pacs06/pacs06-toc.html)

Introduction: Should present the purpose of the submitted work and its relationship to earlier work in the field, but it should not be an extensive review of the literature (e.g., should not exceed 1 ½ typed pages).

Experimental Methods: Should be sufficiently informative to allow competent reproduction of the experimental procedures presented; yet concise enough not to be repetitive of earlier published procedures.

Results: should present the results clearly and concisely.

Discussion: Should be concise and focus on the interpretation of the results.

Conclusion: Should be a brief account of the major findings of the study not exceeding one typed page.

Acknowledgments: Including those for grant and financial support if any, should be typed in one paragraph directly preceding the References.

References: References should be typed double spaced and numbered sequentially in the order in which they are cited in the text. References should be cited in the text by the appropriate Arabic numerals, enclosed in square brackets. Titles of journals are abbreviated according to list of scientific periodicals. The style and punctuation should conform to the following examples:

1. Journal Article:

a) Heisenberg, W., Z. Phys. 49 (1928) 619.
b) Bednorz, J. G. and Müller, K. A., Z. Phys. B64 (1986) 189
c) Bardeen, J., Cooper, L.N. and Schrieffer, J. R., Phys. Rev. 106 (1957) 162.
d) Asad, J. H., Hijjawi, R. S., Sakaji, A. and Khalifeh, J. M., Int. J. Theor. Phys. 44(4) (2005), 3977.

2. Books with Authors, but no Editors:

a) Kittel, C., "Introduction to Solid State Physics", 8th Ed. (John Wiley and Sons, New York, 2005), chapter 16.
b) Chikazumi, S., C. D. Graham, JR, "Physics of Ferromagnetism", 2nd Ed. (Oxford University Press, Oxford, 1997).

3. Books with Authors and Editors:

a) Allen, P. B. "Dynamical Properties of Solids", Ed. (1), G. K. Horton and A. A. Maradudin (North-Holland, Amsterdam, 1980), p137.
b) Chantrell, R. W. and O'Grady, K., "Magnetic Properities of Fine Particles" Eds. J. L. Dormann and D. Fiorani (North-Holland, Amsterdam, 1992), p103.

4. Technical Report:

Purcell, J. "The Superconducting Magnet System for the 12-Foot Bubble Chamber", report ANL/HEP6813, Argonne Natt. Lab., Argonne, III, (1968).

5. Patent:

Bigham, C. B., Schneider, H. R., US patent 3 925 676 (1975).

6. Thesis:

Mahmood, S. H., Ph.D. Thesis, Michigan State University, (1986), USA (Unpublished).

7. Conference or Symposium Proceedings:

Blandin, A. and Lederer, P. Proc. Intern. Conf. on Magnetism, Nottingham (1964), P.71.

8. Internet Source:

Should include authors' names (if any), title, internet website, URL, and date of access.

9. Prepublication online articles (already accepted for publication):

Should include authors' names (if any), title of digital database, database website, URL, and date of access.

For other types of referenced works, provide sufficient information to enable readers to access them.

Tables: Tables should be numbered with Arabic numerals and referred to by number in the Text (e.g., Table 1). Each table should be typed on a separate page with the legend above the table, while explanatory footnotes, which are indicated by superscript lowercase letters, should be typed below the table.

Illustrations: Figures, drawings, diagrams, charts and photographs are to be numbered in a consecutive series of Arabic numerals in the order in which they are cited in the text. Computer-generated illustrations and good-quality digital photographic prints are accepted. They should be black and white originals (not photocopies) provided on separate pages and identified with their corresponding numbers. Actual size graphics should be provided, which need no further manipulation, with lettering (Arial or Helvetica) not smaller than 8 points, lines no thinner than 0.5 point, and each of uniform density. All colors should be removed from graphics except for those graphics to be considered for publication in color. If graphics are to be submitted digitally, they should conform to the following minimum resolution requirements: 1200 dpi for black and white line art, 600 dpi for grayscale art, and 300 dpi for color art. All graphic files must be saved as TIFF images, and all illustrations must be submitted in the actual size at which they should appear in the journal. Note that good quality hardcopy original illustrations are required for both online and mail submissions of manuscripts.

Text Footnotes: The use of text footnotes is to be avoided. When their use is absolutely necessary, they should be typed at the bottom of the page to which they refer, and should be cited in the text by a superscript asterisk or multiples thereof. Place a line above the footnote, so that it is set off from the text.

Supplementary Material: Authors are encouraged to provide all supplementary materials that may facilitate the review process, including any detailed mathematical derivations that may not appear in whole in the manuscript.

Revised Manuscript and Computer Disks

Following the acceptance of a manuscript for publication and the incorporation of all required revisions, authors should submit an original and one more copy of the final disk containing the complete manuscript typed double spaced in Microsoft Word for Windows 2000 or a later version thereof. All graphic files must be saved as PDF, JPG, or TIFF images.

Allen, P.B., "…….", in: Horton, G.K., and Muradudin, A. A., (eds.), "Dynamical…….", (North……..), pp….

Reprints

Twenty (20) reprints free of charge are provided to the corresponding author. For orders of more reprints, a reprint order form and prices will be sent with the article proofs, which should be returned directly to the Editor for processing.

Copyright

Submission is an admission by the authors that the manuscript has neither been previously published nor is being considered for publication elsewhere. A statement transferring copyright from the authors to Yarmouk University is required before the manuscript can be accepted for publication. The necessary form for such transfer is supplied by the Editor-in-Chief. Reproduction of any part of the contents of a published work is forbidden without a written permission by the Editor-in-Chief.

Disclaimer

Opinions expressed in this Journal are those of the authors and neither necessarily reflects the opinions of the Editorial Board or the University, nor the policy of the Higher Scientific Research Committee or the Ministry of Higher Education and Scientific Research. The publisher shoulders no responsibility or liability whatsoever for the use or misuse of the information published by JJP.

Indexing

JJP is currently indexing in:

Scopus	ULRICHSWEB GLOBAL SERIALS DIRECTORY

Obituary for

Prof. Jamil M. Khalifeh (March 1, 1950 – March 10, 2021)

Amman, Jordan

A Loving Husband and a Father, Distinguished Physicist, and a Teacher

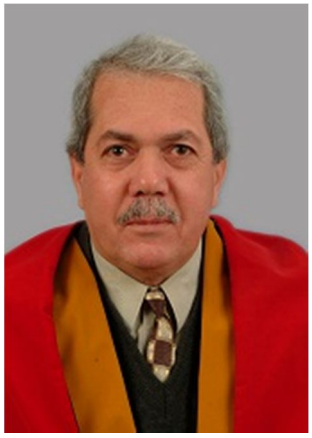

Professor Jamil Mahmoud Khalifeh passed on March 10 2021, in Amman Jordan. He was 71 years old. He is survived by his wife Maha Khalifeh, his daughters Nancy and Areej, and his sons Rami and Mahmoud.

Prof. Khalifeh was a very gentle and caring man with a level of infectious optimism and joy for life and science. Many who learned from Prof. Khalifeh described him as a generous and an inspirational mentor and a friend. His friends, colleagues and students enjoyed his good humor, his charm, and his enthusiasm. His family cherished his unconditional love, his caring, and his smile. Prof. Khalifeh was a unique of individual and will be missed by everyone who knew him.

Jamil Khalifeh was a professor of theoretical condensed matter physics at the University of Jordan. Prof. Khalifeh received his BSc in physics from the University of Jordan in 1972, and then completed his PhD on the electronic structure of transition metal-based alloys from Louis Pasteur University, France, in 1982. Such an analysis was important in its own right, as a precision test of the electronic properties of metals, but also served to further our understanding of semiconductors and insulators.

Upon establishing the PhD physics program at the University of Jordan two decades ago, Prof. Khalifeh was thrilled to build a research group and to have his former PhD students; the junior and senior faculty members then, continue to collaborate with his group, and more importantly to mediate their knowledge and skills to the new graduate students, so they can take part in research at the condensed matter frontier, and to

participate in analyses that will undoubtedly lead to future prestigious prizes. As a marvelous harvest, Prof. Khalifeh, being the group's leader, was able to explore many analyses covering wide scope of the realm of condensed matter (such as magnetic and electronic structures, defects in solid, Hydrogen in metals, surfaces and interfaces, overlayers, Heusler alloys, and catalysis) using innovative techniques and computational facilities. He also examined analytically the applications of lattice Green's function in mathematical physics. These calculations (over 170 peer-reviewed articles) were published in a highly selective tier of prestigious journals in physics. As a result, it was no wonder that Prof. Khalifeh had received many honors and recognitions, including Scopus recognition for his contribution to science in 2009, and the recognition of ISI web of knowledge for contribution to science in 2011.

Prof. Khalifeh enjoyed teaching and interacting with students. His lectures and presentations were notable for their clarity. He expressed himself clearly and calmly. As decisive evidence of his excellent classroom and communication abilities, he used to teach courses at all levels; from an introductory general physics course, intended for non-technical majors, all the way up to quite rigorous courses that appeal to graduate students. With such diverse audiences, he was able to elucidate the themes of the lectures properly, and give his students a great deal of guidance.

Prof. Khalifeh was in residence at numerous institutions for a considerable time as a visiting professor; including Louis Pasteur University (1991, 1992, 1993, 1994, 1995), Warwick University - England (1990, 1991), Alexander von Humboldt fellowship – Frankfurt University - Germany (1991), Martin Luther University - Germany (1994, 1995), and ICTP - Trieste - Italy (1983, 1985, 1987, 1990). He served as a member on the editorial board of the International Journal of Science and Technology (EIJST), Jordan Journal of Physics (JJP), and European International Journal of Engineering and Emerging Technologies (IJEET). Prof. Khalifeh chaired the physics department for two terms; (1989-1990) and (2007-2009). He was the chairman of the 7^{th} (2000) and 8^{th} (2016) international Petra school of physics that took place at the University of Jordan, and was a founding member and patriarch of the Jordanian association of physicists. Prof. Khalifeh was the editor of the Arabic version of the textbook "Physics, Principles and Applications" by D. Giancoli, and the editor of the Arabic version of the textbook "Conceptual Physical Science" by P.Hewitt, J. Suchocki and L. Hewitt.

Mohammad Hussein
Physics Department - University of Jordan
Amman, Jordan

Obituary for

Prof. Saed O. Dababneh (February 11, 1963 – August 22, 2021)
Amman, Jordan

Professor Saed Odeh Dababneh was born on the 11th of February 1963 and passed on the 22nd of August 2019 aged 56, lived alongside his wife, Shereen Dababneh, and two kids Haneen and Odeh.

Prof. Saed was described as an enthusiast for science and knowledge, but also a caring teacher, a role model, a loving father, and a loyal friend and colleague. Prof. Saed was one of a kind. Everyone who knew him would recognize his generosity and positive attitude towards life. His family cherishes every memory, every smile, and every lesson he taught. His kids describe him as the ideal father who never failed to make them proud. He will never be forgotten and will always be missed for his brilliance.

Born in Amman Jordan, Prof. Saed started his studies and graduated from the National Orthodox School, Amman. He then finished his B.Sc. in Physics from the University of Baghdad, College of Sciences, 1986, after that his M.Sc. in Physics from the University of Jordan, Faculty of Graduate Studies, 1990, and lastly his Ph.D. in Nuclear Physics from Heidelberg University and Karlsruhe Institute of Technology (KIT), Germany in 2002.

Prof. Saed Dababneh was the dean of scientific research and a professor at Al-Balqa Applied University, Salt, Jordan. He established, managed, and supervised the graduate program in nuclear physics at the University. He also worked as a visiting professor at the Institute for Applied Physics, Goethe University, Frankfurt am Main, Germany during the summer of 2015, 2016, and 2017, and as Vice Chairman of the Board of Directors at Jordan Nuclear Regulatory Commission (JNRC), Amman, Jordan, 2008-2012. He taught 17 courses as a professor some of which include: Nuclear Reactor Physics, Nuclear Physics, Experimental Techniques in Nuclear Physics, Computational Physics, Theoretical Nuclear Physics, Radiation Detection and Measurement, Advanced Mathematical Physics, Advanced Statistical Physics, Accelerator Physics, and other graduate and undergraduate courses.

Some of his positions, research, and other activities include; a technical visit to the CTBTO headquarters to discuss and launch technical cooperation related to the radionuclide component of the Verification Regime. The cooperation included benchmarking the results produced by CTBTO's VGSL with those produced by GEANT4 Monte Carlo simulations, in addition to scientific input for new/modified ideas on radioxenon (beta-gamma coincidence) measurements. To add on, he also managed the King Abdullah II Fund for Development (KAFD) supporting the specialized graduate program in Applied Nuclear Physics at Al Balqa Applied University, and paid research visits to the European Organization for Nuclear Research (CERN), Geneva, Switzerland, 2000–2004, and visited as a research scientist at the Institut für Kernphysik, Forschungszentrum Karlsruhe, Germany, and as a research associate to the Department of Physics, University of Notre Dame, and at the Joint Institute for Nuclear Astrophysics, USA. He also visited the scientific Institute of Nuclear Solid-State Physics (INFP), Forschungszentrum Karlsruhe, Germany, and was a part of the Interregional Training Course on Interfacing in Nuclear Experiments at The International Atomic Energy Agency, held in Antananarivo, Madagascar. He was also a Member of the SESAME users committee, Amman, Jordan, and a member of the Dissi Water Consultative Committee, Amman, Jordan, and many others.

Before his passing, he also started a laboratory for Radiation Measurements which is located at Al-Balqa Applied University, Salt, Jordan, which was named after him after his passing as the Saed Dabanneh Laboratory (SDL). The SDL Lab is one of the few research labs in Jordan that are specified in improving radiation measurement and different applications in nuclear security, environmental applications, food, and water-related safety, and others. In 2018, the BALQARAD Active Shielded Clover detector, the first of its kind in the Middle East, was acquired at the lab. This detector was funded by the Scientific Research Support under the project “Improvement and Adaptation of Ultra-Sensitive Coincidence Gamma-Ray Detection Array for Environmental, Energy, Security, Water- and Food-Safety Applications”.

Prof. Saed has also achieved both the Georg Forster Fellowship award for Advanced Researchers, the Alexander von Humboldt Foundation, and the Forschungszentrum Karlsruhe INFP award. He was a very active member of the Jordanian Club of Humboldt Fellows.

Lastly, Professor Saed was very enthusiastic about learning, he always believed in his students and guided many onto the roads of success. He was a gentle mentor with a lovable approach. Losing him caused much pain to many and even after his passing his name still remains remarkable and is respected.

Prof. Dr. Marwan S. Mousa
&
Haneen Saed Dababneh

Amman, Jordan

Jordan Journal of
PHYSICS
An International Peer-Reviewed Research Journal

Volume 15, No. 2, June 2022, Dhū al-Qa'dah 1443 H

Table of Contents:

Volume 15, Number 2, 2022. pp. 107-118

Jordan Journal of Physics

ARTICLE

Ab-initio and Monte Carlo Simulations of the New Half-Heusler Alloy NiCrGa

S. Idrissi[a], **H. Labrim**[b,c], **S. Ziti**[d] and **L. Bahmad**[a]

[a] *Laboratoire de la Matière Condensée et des Sciences Interdisciplinaires (LaMCScI), Mohammed V University of Rabat, Faculty of Sciences, B.P. 1014 Rabat, Morocco.*

[b] *USM/DERS/Centre National de l'Energie, des Sciences et des Techniques Nucléaires (CNESTEN), Rabat, Morocco.*

[c] *Advanced Systems Engineering Laboratory, National School of Applied Sciences, Ibn Tofail University, Kénitra, Morocco.*

[d] *Intelligence Artificial and Security of Systems, Mohammed V University of Rabat, Faculty of Sciences, B.P. 1014 Rabat, Morocco.*

Doi: **https://doi.org/10.47011/15.2.1**

Received on: 20/08/2020; *Accepted on: 6/12/2020*

Abstract: In this work, we are investigating the electronic and magnetic properties of the new NiCrGa half-Heusler alloy (HHA), by using the *ab-initio* and Monte Carlo simulations (MCSs). The *ab-initio* method is performed under the pseudo-potential method and the generalized gradient approximation GGA. The density of states (DOS) and the band structure calculations show that the alloy NiCrGa reveals a nearly half-metallic (HM) behavior. In particular, the Slater-Pauling (SP) rule has been confirmed when using the magnetic moments of the individual constituents of the NiCrGa compound. The Monte Carlo simulations (MCSs) are accomplished using the Metropolis algorithm. In order to determine the transition temperature, we are based on the behavior of the total magnetization and susceptibility of this material. We also presented and discussed the hysteresis loops of the half-Heusler compound, for fixed values of temperature, exchange coupling interactions and crystal field. It is found that when increasing the crystal field, the surface of the loops increases and *vice versa*.

Keywords: Half-Heusler alloy, NiCrGa, Slater pauling, DFT method, Monte Carlo study.

1. Introduction

The recent development of spintronics has attracted much attention by several researches [1-4]. The common character of materials used in the spintronic applications is the half-metallic ferromagnets behavior [5-10]. The first materials expected to be half-metallic ferromagnets were the half-Heusler alloys NiMnSb and PtMnSb. These alloys crystallize in cubic $C1_b$ structure [11–15]. In addition, the Heusler alloy NiMnSb has been described to exhibit a high Curie temperature [16]. It also possesses an integral magnetic moment of 4.00 μ_B per unit cell [17–21]. The Heusler alloys fall into three separate categories: half-Heusler, full Heusler and equiatomic quaternary Heusler with XYZ, X2YZ and XYMZ formulations, respectively, where X, Y and M are usually atoms of transition metals or alkali-earth metals and Z is a main group element.

Recently, a number of half-Heusler alloys have been studied, such as: NaZrM (M =P, As, Sb) [22], LiMnZ (Z=N, P, Si) [23], XYZ (X =Li, Na, K and Rb, Y=Mg, Ca, Sr and Ba, Z=B, Al and Ga) [24], MnPK [25] and LiZnM (M =P and As) [26]. On the other hand, the half-Heusler alloys have shown promising half-metallic behaviors. For example, the half-

Corresponding Author: S. Idrissi **Email**: samiraidrissi2013@gmail.com

Heusler alloy LiCrS shows a half-metallic property at its parameter of optimized lattice constant with the magnetic moment value of 5.00 μ_B [22, 27]. Moreover, Luo *et al*. [28] have performed the electronic and magnetic properties of the half-Heusler alloys: NiCrAl, NiCrGa and NiCrIn using the density functional theory (DFT). There are some other computational research studies on the other half-Heusler materials [29-31]. In addition, several Ni-based half-Heusler alloys have been investigated, such as: NiCrZ (Z = Si, Ge, Ga, Al, In and As) [32] and NiCrGa [33].

The purpose of this paper is to combine the *ab-initio* and Monte Carlo simulations to investigate the half-metallic behavior and the critical magnetic properties of the Ni-based half-Heusler alloy NiCrGa. We present our results in the framework of the *ab-initio* study, using the density functional theory (DFT) method under the Quantum Espresso package. On the other hand, we perform the Monte Carlo simulations under using Metropolis algorithm. Indeed, some of our recent works have been based on such simulations applying not only the DFT method, but also other numerical simulations [34, 35].

This work is organized as follows: In Section 2, we present and discuss the first principles and calculations. In Section 3, we illustrate the obtained results of *ab-initio* method including the density of states and band structures of the half-Heusler alloy NiCrGa. Also, the Slater Pauling rule is presented and discussed. In Section 3, we present the method and the computational procedures of the Monte Carlo simulations. Finally, we discuss the obtained results of the latter method in Section 4 and we give a summary in Section 5.

2. The *Ab-initio* Method for the NiCrGa Half-Heusler Alloy

2.1 Structural Properties

The first principles and calculations were performed using the Quantum Espresso (QE) package [36], combined with the Density Functional Theory (DFT), in order to investigate the electronic and magnetic properties of the half-Heusler alloy NiCrGa. For this purpose, we have applied the ultra-soft pseudo-potential approximation [37]. This method was used to calculate the interaction between the atom core and valence electrons in the studied alloy. Furthermore, the exchange and correction between electrons were calculated by the generalized gradient approximation (GGA) [38-39]. In the Brillouin zone integrations, we take 5x5x5 k-points. The plane-wave basis is set to a cut-off energy value of 25 Ry. The convergence energy is taken to be 10^{-6} eV/atom.

The NiCrGa half-Heusler alloy (HHA) crystallizes in the cubic structure belonging to the space-group F-43m (216), as can be seen in Fig.1. Our simulation has been performed choosing the experimental lattice parameter value a = b = c = 5.80 Å [33]. The NiCrGa alloy (XYZ) crystallizes in the $C1_b$ structure, with Ni (X), Cr (Y) and Ga (Z) atoms occupying the Wyckoff positions: 4c (1/4, 1/4, 1/4), 4b (1/2, 1/2, 1/2) and 4a (0, 0, 0), respectively. These positions are derived from Ref. [33]. On the other hand, the VESTA package [40] was used to illustrate the geometry of the studied alloy, see Fig.1.

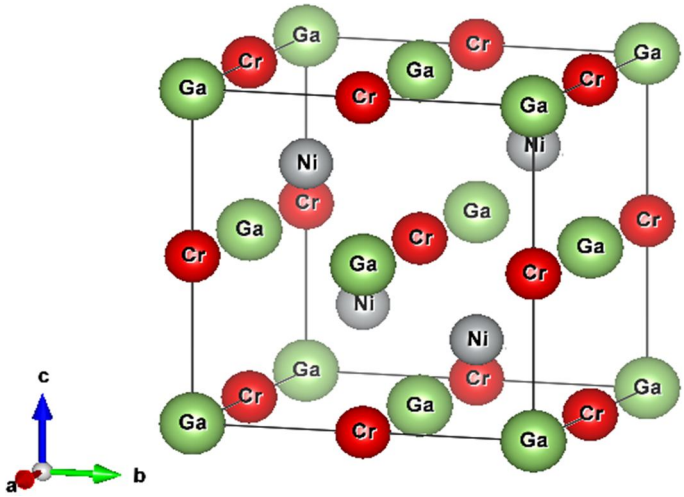

FIG. 1. The geometry of the half-Heusler alloy NiCrGa, using VESTA software [40].

2.2 Results of the *Ab-initio* Method

In order to investigate the total and the partial density of states (DOS) of the half-Heusler alloy NiCrGa, we report our results in Figs. 2(a) and 2(b), respectively. In fact, Fig. 2(a) represents the total density of states for spin-up and spin-down of the NiCrGa alloy. The non-symmetry between spin-up and spin-down states confirms the magnetic behavior of the studied material. Also, at Fermi level, there are states of spin-up, while there is almost an absence of spin-down states. Such behavior supports the nearly HF character of this compound. This finding is in good agreement with [32-33]. On the other hand, the partial density of states of the half-Heusler alloy NiCrGa for the individual elements: Ni, Cr and Ga is presented in Fig. 2(b). From this figure, it is found that the Cr and Ni elements are the most contributing to the total DOS of the NiCrGa compound, while, the Cr element is the only element contributing to the conduction band (CB). Moreover, the magnetic behavior of the half-Heusler alloy NiCrGa comes mainly from the transition metals: Ni and Cr.

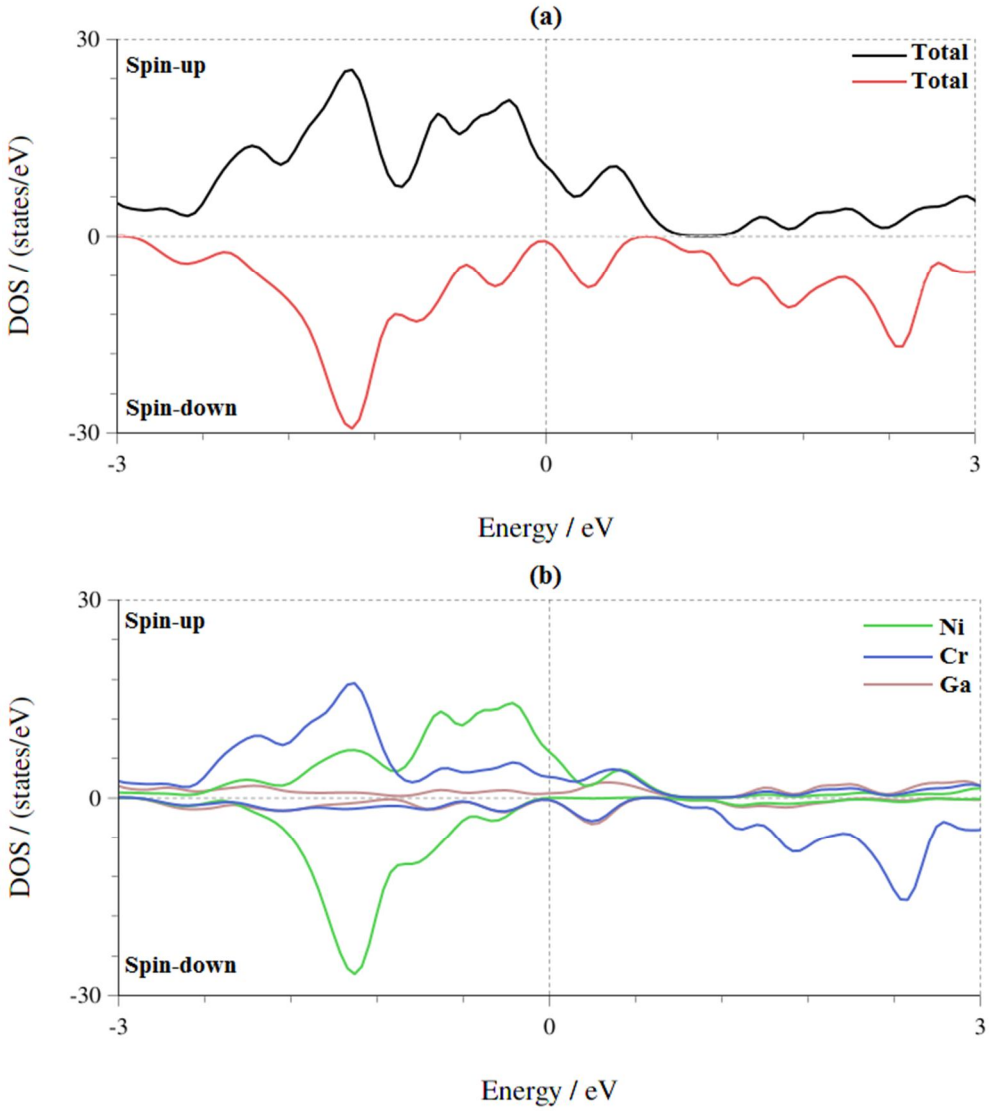

FIG. 2. Total (a) and partial (b) density of states of the half Heusler alloy NiCrGa.

To investigate the band structures of the half-Heusler alloy NiCrGa, we plot in Figs. 3(a) and 3(b) the obtained results for spin-up and spin-down states, respectively. From these figures, it is clear that at Fermi level, there are states of spin-up in Fig. 3(a), while there is almost an absence of spin-down states, see Fig. 3(b). In other words, the studied material gathers two behaviors: a metallic one in the spin-up channel and a near semi-conductor one in the spin-down channel. In this latter situation, the band gap value in the spin-down channel is almost equal to 0.4 eV.

When combining the results of density of states, see Figs. 2(a) and 2(b), and those of the band structures, see Figs. 3(a) and 3(b), we conclude that the NiCrGa alloy exhibits a nearly HM behavior.

Concerning the (SP) rule, it can be defined in this study following Refs. [41-43] that:

$$M_T = N_v\text{-}18 \quad (1)$$

M_T: Total spin magnetic moment.

N_v: Total number of valence electrons.

To explicit the valence electrons for the Heusler alloy NiCrGa unit cell, we use the electronic configurations for individual atoms: $4s^2 3d^8$ for Ni, $4s^1 3d^5$ for Cr and $4s^2 4p^1$ for Ga. Hence, the total number of valence electrons (N_v) of the Heusler alloy NiCrGa is close to 19. Using Eq. (1) of the Pauling Slater rule, we found that $M_T = 1.00\ \mu_B$. This result is confirmed in Table 1 for the total and the partial magnetic moments of the (HHA) NiCrGa. This table summarizes the total and partial magnetic moments of the (HHA) NiCrGa with the individual magnetic moment value of each element: m(Ni), m(Cr) and m(Ga).

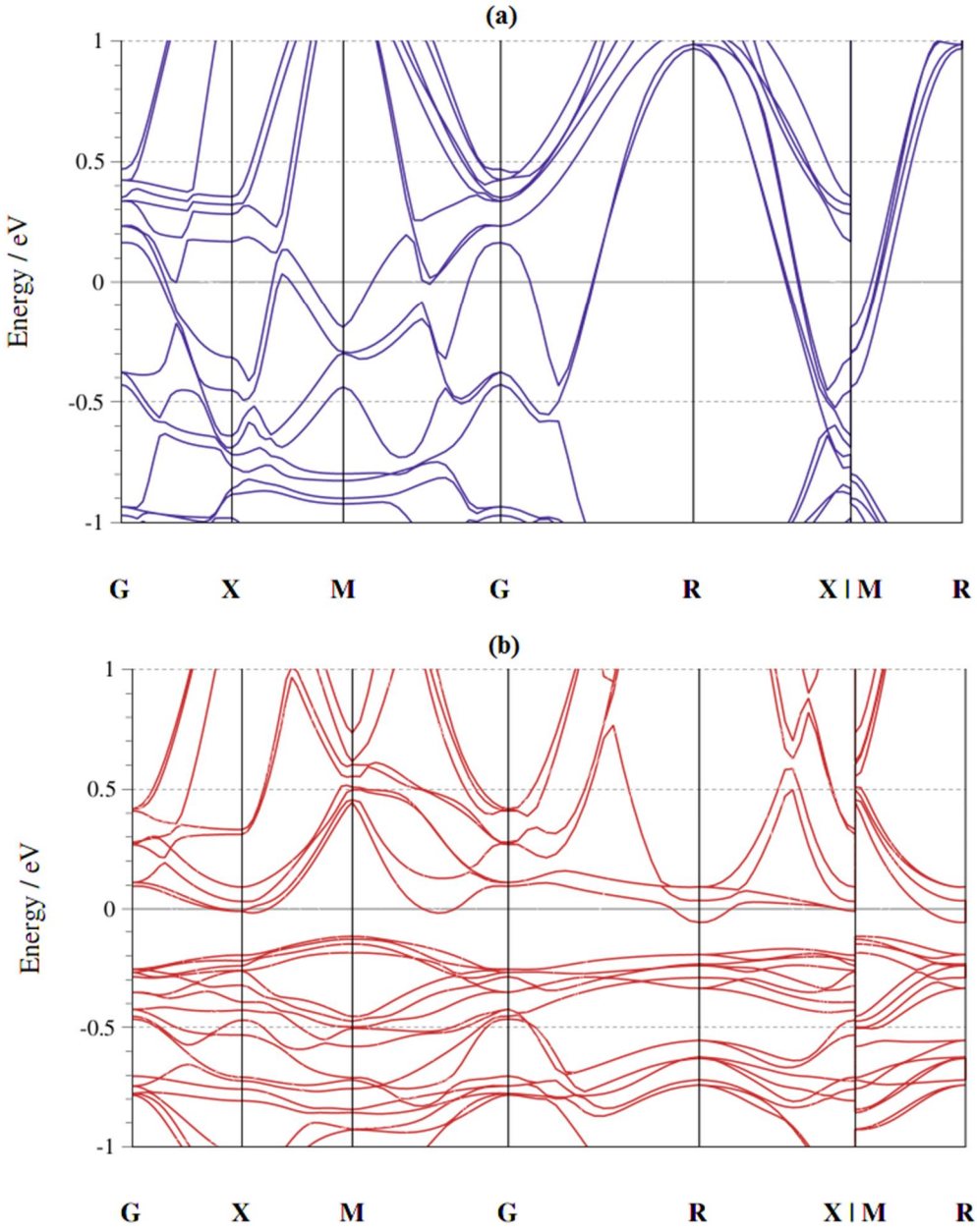

FIG. 3. Band structures of the half-Heusler alloy NiCrGa: (a) spin-up and (b) spin-down.

TABLE 1. Total and partial magnetic moments of the half-Heusler alloy NiCrGa with individual magnetic moment value of each element: m(Ni), m(Cr) and m(Ga).

Half-Heusler alloy	*m(Ni)* (μ_B)	*m(Cr)* (μ_B)	*m(Ga)* (μ_B)	M_{Total}(μ_B)	Slater Pauling rule M_T (μ_B)
NiCrGa	0.51	1.60	-0.44	1.67	1.00

3. Powder X-Ray Diffraction Patterns of the NiCrGa Heusler alloy

To simulate the powder X-Ray diffraction patterns (diffractograms) of the NiCrGa Heusler alloy in the $C1_b$ structure, we use the VESTA software package [40]. The powder X-Ray diffraction patterns (diffractograms) of the studied Heusler alloy are presented in Fig. 4. It is found that the theoretical XRD spectrum is similar to the experimental one shown in Ref. [33]. Indeed, a more intense peak is appearing at the (220) plane. Such behavior is a specific character of single crystals.

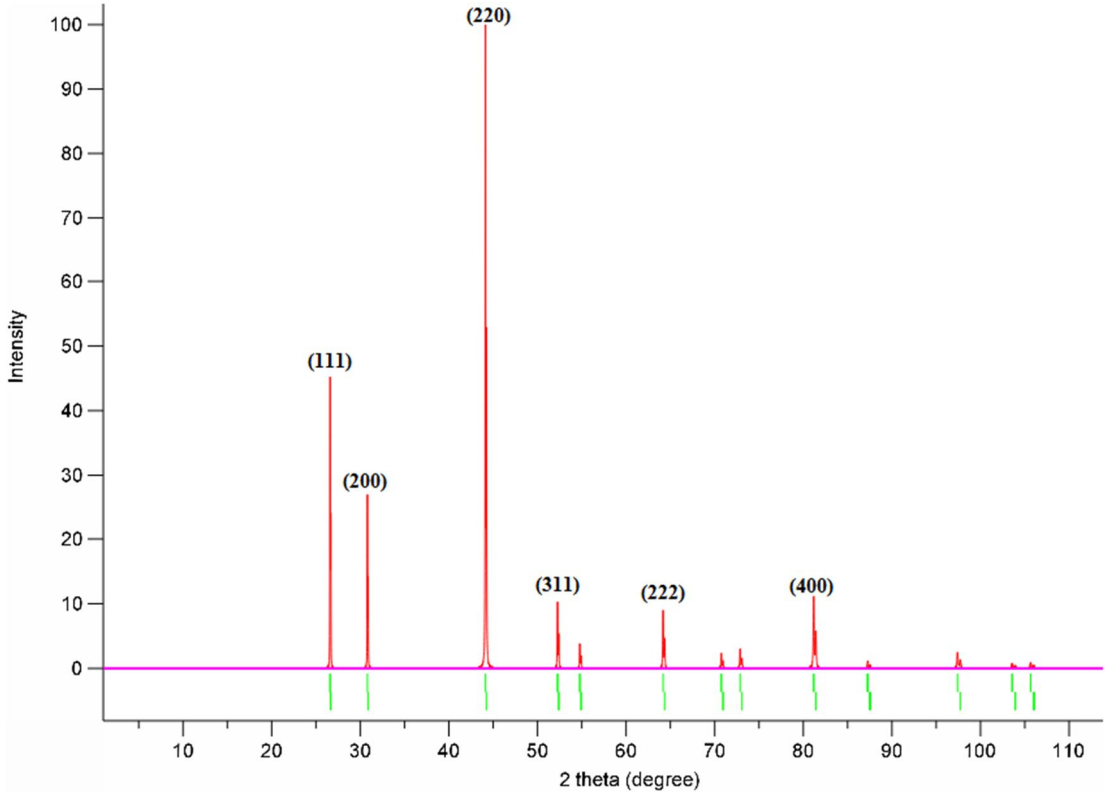

FIG. 4. Powder X-Ray diffraction patterns of Heusler alloy NiCrGa using the Vesta software.

4. Method of Monte Carlo Simulations

4.1 Methodology of Simulations

Since the studied compound contains the magnetic elements Ni and Cr as highlighted in Section 2 by the *ab-initio* method, we apply the MCS in order to deduce the critical magnetic behavior of the NiCrGa alloy. Hence, we propose the Hamiltonian of Eq. (2) to study the magnetic properties of the half-Heusler compound NiCrGa. The calculations are accomplished under the Metropolis algorithm. The periodic boundary conditions are imposed to the unit cell lattice. The results of the studied system are obtained for the specific super-cell size 5x5x5. For each spin configuration, we implement 10^5 Monte Carlo steps. For each MCS, all sites of the system are visited individually. A single-spin flip attempt is accepted or rejected according to the Boltzmann statistics.

The Hamiltonian modeling the half-Heusler alloy NiCrGa can be expressed as:

$$\left.\begin{aligned}\mathcal{H} = &-J_{Ni-Ni}\sum_{i,j} S_i S_j \; -J_{Cr-Cr}\sum_{k,l}\sigma_k\sigma_l \\ &-J_{Ni-Cr}\sum_{i,k} S_i\sigma_k \; - H\sum_i (S_i+\sigma_i) \\ &-\Delta_S\sum_i S_i^2 - \Delta_\sigma\sum_i \sigma_i^2\end{aligned}\right\} \quad (2)$$

where the magnetic spins S_i = 1 correspond to the Ni atoms, while σ_i=2 represents the Cr atoms.

The exchange coupling interactions are: $J_{Ni\text{-}Ni}$ between Ni atoms, $J_{Cr\text{-}Cr}$ between Cr atoms and $J_{Ni\text{-}Cr}$ between Ni- Cr atoms.

It is worth to note that the exchange coupling is the way in which two magnetic atoms (or ions) in a specific material interact with each other. When two magnetic atoms are situated very close together, their electrons can interact directly, in the same way as when forming a chemical bond.

For simplicity, we will limit this study to the unique crystal field: $\Delta = \Delta_S = \Delta_\sigma$, where Δ_S is the crystal field of the Ni ions and Δ_σ is the crystal field of the Cr ions.

The total energy per site is given by:

$$E_T = \frac{1}{N} < \mathcal{H} > \quad (3)$$

where N= N_σ + N_S, with N_σ and N_S being the numbers of σ- and S-atoms in the super cell unit, respectively.

The partial and total magnetizations are expressed as:

$$m_S = \frac{1}{N_S}\sum_i S_i \quad (4)$$

$$m_\sigma = \frac{1}{N_\sigma}\sum_i \sigma_i \quad (5)$$

$$m_T = \frac{N_\sigma m_\sigma + N_S m_S}{N_\sigma + N_S} \quad (6)$$

The partial and total susceptibilities are given by:

$$\chi_S = \frac{<M_S^2> - <M_S>^2}{K_B T} \quad (7)$$

$$\chi_\sigma = \frac{<M_\sigma^2> - <M_\sigma>^2}{K_B T} \quad (8)$$

$$\chi = \frac{<M_T^2> - <M_T>^2}{k_B T} \quad (9)$$

where $\beta = \frac{1}{k_B T}$ and k_B is the Boltzmann constant. T is the absolute temperature. In the following part, we will assume that k_B=1.

4.2 Results of Monte Carlo Simulations

The obtained results of the MCS concerning the thermal behavior of the partial and total magnetizations and susceptibilities of the HHA NiCrGa atoms are plotted in Figs. 5(a), 5(b) and 5(c) for H=1, Δ=1 and $J_{Ni\text{-}Ni}$= $J_{Cr\text{-}Cr}$=$J_{Ni\text{-}Cr}$= 1. In fact, Fig. 5(a) represents the magnetization and susceptibility of the individual Ni atoms. From this figure, it is clear that for very low temperature values, the magnetization undergoes the value m_S =1. Moreover, the peak of the susceptibility corresponds to the critical temperature value Tc ≈ 20 K. Concerning the individual magnetization and susceptibility of the Cr atoms, the obtained results are summarized in Fig. 5(b). This figure confirms the value m_σ = 2 for very low temperature. Also, the peak susceptibility is located at Tc≈20 K. The total magnetization and susceptibility of the (HHA) NiCrGa are presented in Fig. 5(c). From this figure, it is found that for low temperature values, the results of the ground state phase of the total magnetization show that m_T = (m_S+m_σ)/2 = 1.5.

Fig.5 (a)

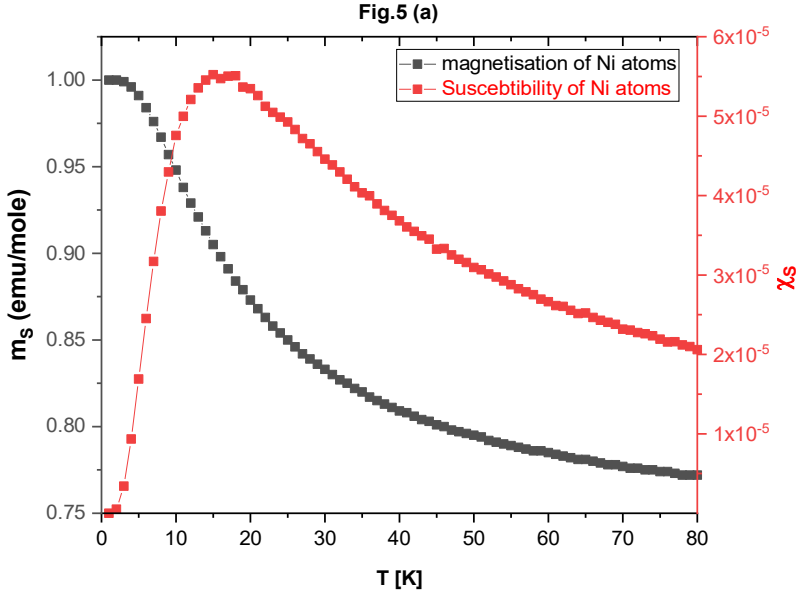

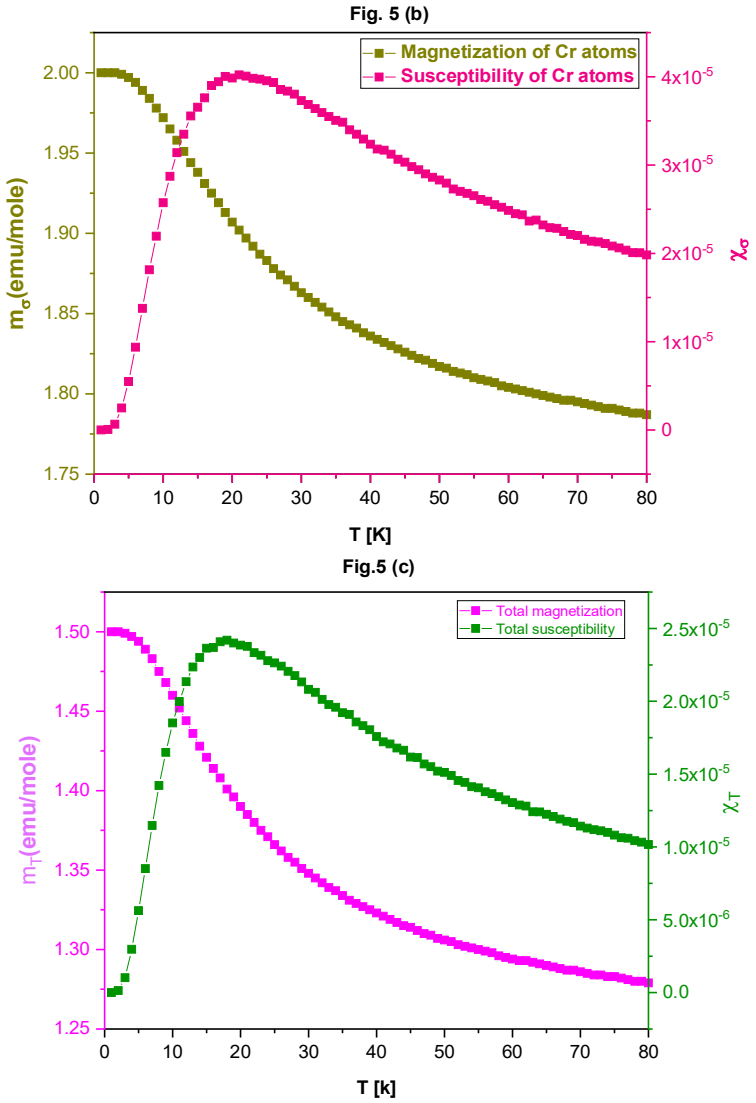

FIG. 5. The thermal behavior of the half-Heusler alloy NiCrGa for H = 1, Δ = 1 and $J_{Ni\text{-}Cr} = J_{Cr\text{-}Cr} = J_{Ni\text{-}Ni} = 1$: (a) the partial magnetization and susceptibility of Ni atoms, (b) the partial magnetization and susceptibility of Cr atoms and (c) the total magnetization and susceptibility.

In order to study the effect of different exchange coupling interactions $J_{Ni\text{-}Ni}$, $J_{Cr\text{-}Cr}$ and $J_{Ni\text{-}Cr}$ on the behavior of the total magnetizations of the (HHA) NiCrGa, we illustrate in Figs. 6(a), 6(b) and 6(c) the obtained results for H = 1, T = 20 K and different crystal field values. In fact, Fig. 6(a) corresponds to the effect of the exchange coupling interaction $J_{Ni\text{-}Ni}$ for fixed values of Jcr-cr = $J_{Ni\text{-}Cr}$ = 1. From this figure, it is seen that the effect of increasing exchange coupling interaction $J_{Ni\text{-}Ni}$ is to reach the saturation values of the total magnetizations. Indeed, this saturation is positive for positive values of the crystal field Δ = +5 and 0, while this saturation is negative for Δ = -5. Also, for negative values of the parameter $J_{Ni\text{-}Ni}$, the total magnetizations are not affected by the increasing this parameter. In Fig. 6(b), we provided the effect of varying the exchange coupling interaction parameter $J_{Cr\text{-}Cr}$ on the behavior of the total magnetizations. From this figure, it is clear that for negative values of the parameter $J_{Ni\text{-}Cr}$, the total magnetizations are not affected neither by the increasing effect of $J_{Ni\text{-}Cr}$, for its negative values, nor by the variations of the crystal field Δ, see Fig. 6(b). For positive values of the parameter $J_{Cr\text{-}Cr}$, the saturation of the total magnetizations is positive for positive values of the crystal field Δ = +5 and 0, whereas for Δ = -5, the saturation is negative. Contrary to Fig. 6(a), Fig. 6(c) shows a similar, but inverse, behavior in the sign of the total magnetization. The only difference is that for Δ = 0, the total magnetization undergoes a similar behavior to that one of the value Δ = -5. These figures show that the transitions of the magnetizations are of second-order type.

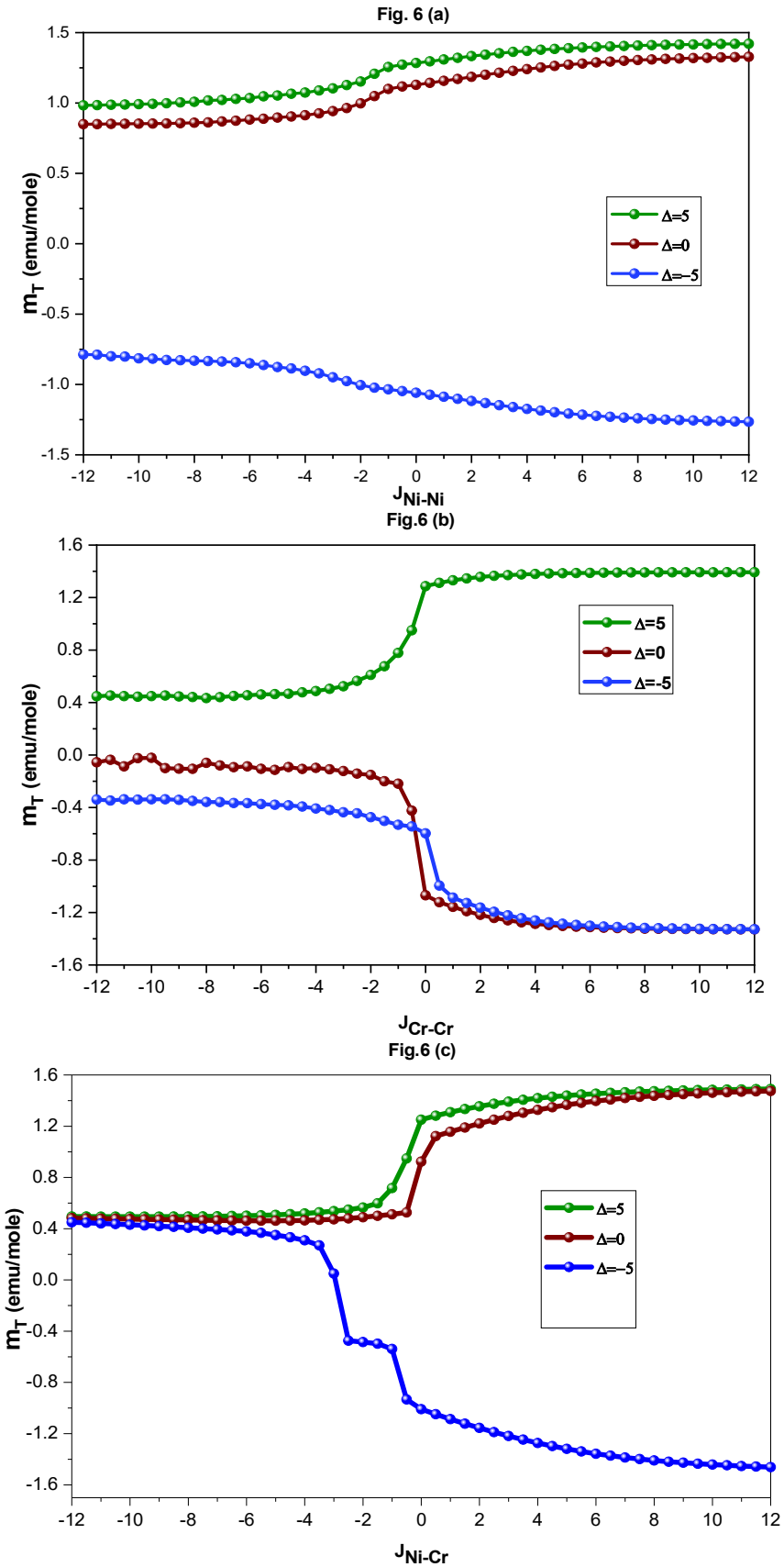

FIG. 6. The total magnetization of the half-Heusler alloy NiCrGa for H = 1, T = 20 K and selected values of the crystal field: Δ = -5, 0 and +5: (a) as a function of the exchange coupling interaction J_{Ni-Ni} for $J_{Cr-Cr} = J_{Ni-Cr} = 1$, (b) as a function of the exchange coupling interaction J_{Cr-Cr} for $J_{Ni-Ni} = J_{Ni-Cr} = 1$ and (c) as a function of the exchange coupling interaction J_{Ni-Cr} for $J_{Ni-Ni} = J_{Cr-Cr} = 1$.

To complete this study, we provide Figs. 7(a), 7(b) and 7(c) that show the hysteresis loops of the (HHA) NiCrGa, as a function of the external magnetic field H. In Fig. 7(a), we illustrate the obtained results for T = 15, Δ = 0 and selected different values of the exchange couplings. This figure shows that, when all exchange coupling interactions take the value +1, the surface of the hysteresis cycle is maximum. When fixing the value -1 of $J_{Cr\text{-}Cr}$, the surface of the cycle decreases and the steps corresponding to intermediate states are appearing. For $J_{Ni\text{-}Cr}$ = -1, the surface of the cycle decreases more and more. This surface tends towards the null value when imposing the value -1 for all exchange coupling interactions.

In order to show the effect of varying the temperature on the hysteresis cycles, we plot in Fig. 7(b) such behavior for Δ = 1, $J_{Ni\text{-}Ni}$ = $J_{Cr\text{-}Cr}$ = $J_{Ni\text{-}Cr}$ = 1 and selected different values of temperature T = 20 K, T = 55 K and T = 150 K. It is found that the surface of the hysteresis cycles decreases and consequently the corresponding coercive field, see Fig. 7(b). The effect of varying the crystal field on the hysteresis loops is summarized in Fig. 7(c) for T = 25 K, $J_{Ni\text{-}Ni}$ = $J_{Cr\text{-}Cr}$ = $J_{Ni\text{-}Cr}$ = 1 and selected values of the crystal field Δ = 0, Δ = 2 and Δ = 4. It is clear that when increasing the crystal field, the surface of the loops increases and *vice versa*. To confirm such results, we illustrate in Fig. 8 the coercive field dependency on the crystal field for T = 25 K and $J_{Ni\text{-}Ni}$ = $J_{Cr\text{-}Cr}$ = $J_{Ni\text{-}Cr}$ = 1. It is found that when increasing the crystal field, the corresponding coercive field increases to reach the value H_c = 3.75 at the crystal field value of Δ = 4.

Fig.7 (a)

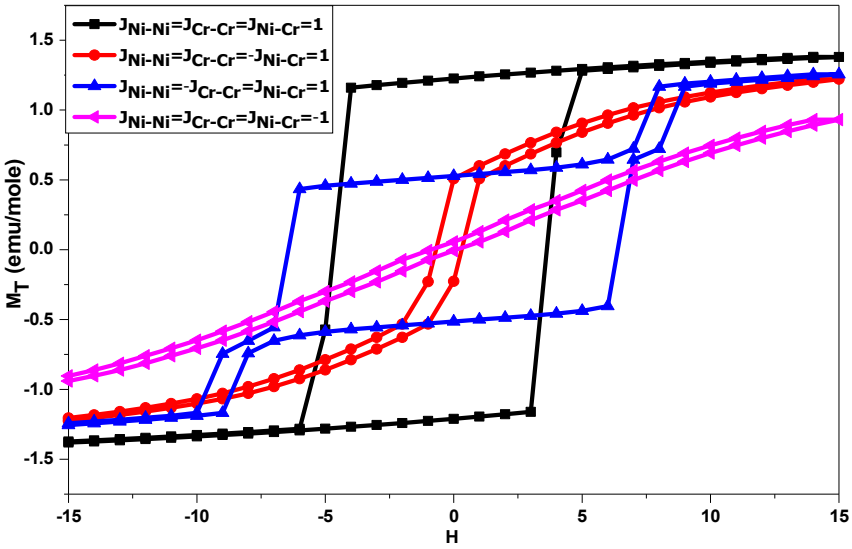

Fig. 7 (b)

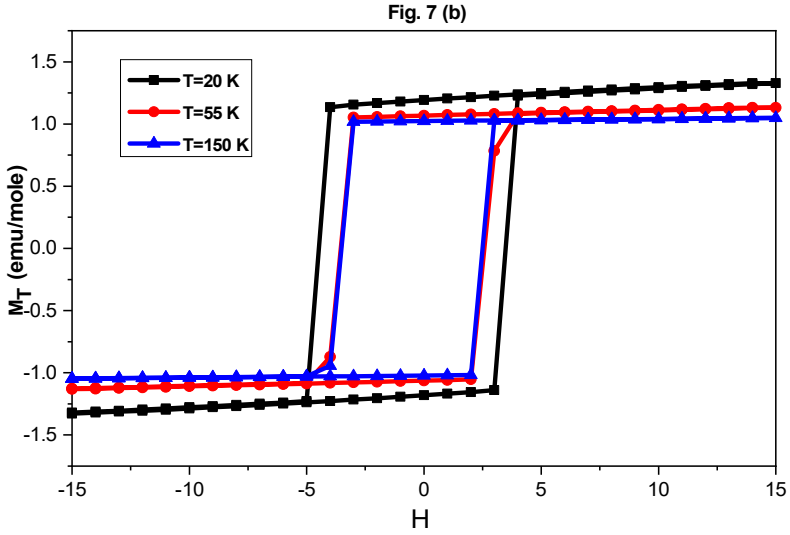

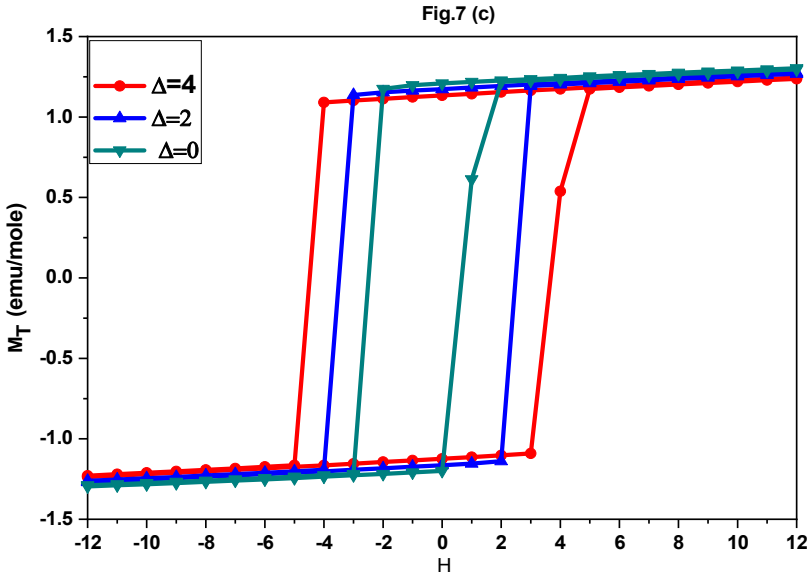

FIG. 7. Hysteresis loops of the half-Heusler alloy NiCrGa: (a) for T = 15 K, Δ = 0 and selected different values of the exchange coupling, (b) for Δ = 1, $J_{Ni-Ni} = J_{Cr-Cr} = J_{Ni-Cr} = 1$ and selected different values of temperature T = 20 K, T = 55 K and T = 150 K and (c) for T = 25 K, $J_{Ni-Ni} = J_{Cr-Cr} = J_{Ni-Cr} = 1$ and selected values of the crystal field Δ = 0, Δ = 2 and Δ = 4.

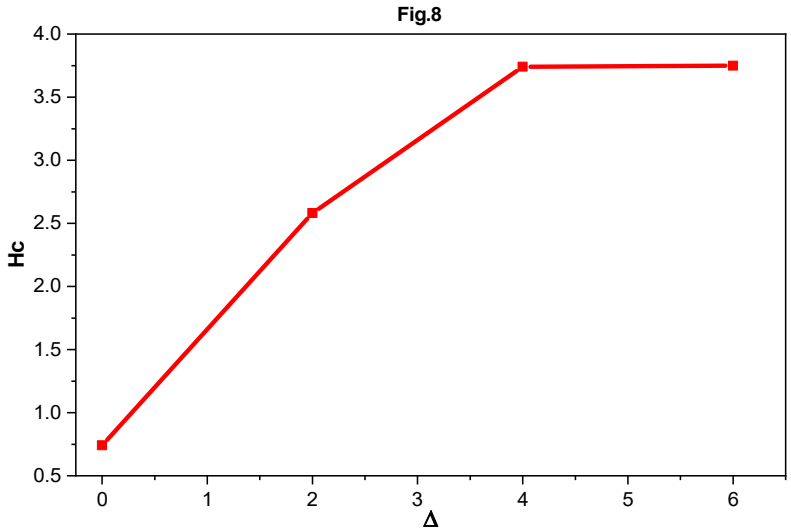

FIG. 8. Coercive field of Heusler alloy NiCrGa dependency on the crystal field for T = 25 K and $J_{Ni-Ni} = J_{Cr-Cr} = J_{Ni-Cr} = 1$.

5. Conclusion

In this paper, we have studied the electronic and magnetic properties as well as the critical behavior of the NiCrGa alloy using Monte Carlo simulations and DFT calculations.

The density of states (DOS) showed that this material exhibits a nearly half-metallic (HM) behavior. Moreover, the SP rule has been confirmed when using the magnetic moments of the individual constituents of the NiCrGa compound.

On other hand, the Monte Carlo method has been performed under the Metropolis algorithm to simulate the critical behavior of the half-Heusler NiCrGa alloy. Also, we have presented and discussed the magnetizations and susceptibilities as functions of temperature and other physical parameters.

To complete this study, we presented and illustrated the hysteresis loops of the (HHA) NiCrGa, for selected values of temperature, exchange coupling interactions and crystal field. It is found that when increasing the crystal field, the surface of the loops increases and *vice versa*. In particular, we have shown that when increasing the crystal field, the corresponding coercive field increases.

References

[1] Prinz, G.A., Phys. Today, 48 (1995) 58.

[2] Kobayashi, K.I., Kimura, T., Sawada, H., Terakura, K. and Tokura, K., Nature, 395 (1998) 677.

[3] Park, J.H., Vescovo, E., Kim, H.J., Kwon, C., Ramecsh, R. and Venkatesan, T., Nature, 392 (1998) 794.

[4] Hashemifar, S.J., Kratzer, P. and Scheffler, M., Phys. Rev. Lett., 94 (2005) 096402.

[5] Idrissi, S., Labrim, H., Ziti, S. and Bahmad, L., Journal of Superconductivity and Novel Magnetism, 33 (2020) 3087.

[6] Idrissi, S., Labrim, H. and Ziti, S., Appl. Phys. A, 126, (2020) 190.

[7] Idrissi, S., Labrim, H., Ziti, S. and Bahmad, L., Physics Letters A, 384 (24) (2020) 126453.

[8] Idrissi, S., Bahmad, L., Khalladi, R., El Housni, I., El Mekkaoui, N., Mtougui, S., Labrim, H. and Ziti, S., Chinese Journal of Physics, 60 (2019) 549.

[9] Zhang, L., Wang, X. and Cheng, Z., J. Alloys Compd., 718, (2017) 63.

[10] Gao, G.Y., Hu, L., Yao, K.L., Luo, B. and Liu, N., J. Alloys Compd., 551 (2013) 539.

[11] de Groot, R.A., Mueller, F.M., van Engen, P.G. and Buschow, K.H.J., Phys. Rev. Lett., 50 (1983) 2024.

[12] Kulatov, E. and Mazin, I.I., J. Phys.: Condens. Matter, 2 (1990) 343.

[13] Ebert, H. and Schutz, G., J. Appl. Phys., 69 (1991) 4627.

[14] Wang, X., Antropov, V.P. and Harmon, B.N., IEEE Trans. Magn., 30 (1994) 4458.

[15] Youn, S.J. and Min, B.I., Phys. Rev. B, 51 (1995) 10436.

[16] Otto, M.J., van Woerden, R.A.M., van der Valk, P.J., Wijngaard, J., van Bruggen, C.F. and Haas, C., J. Phys.: Condens. Matter, 1 (1989) 2341.

[17] Helmholdt, R.B., de Groot, R.A., Muller, F.M., van Engen, P.G. and Buschow, K.H.J., J. Magn. Magn. Mater., 43 (1984) 249.

[18] Kabani, R., Terada, M., Roshko, A. and Moodera, J.S., J. Appl. Phys., 67 (1990) 4898.

[19] Tanaka, C.T., Nowak, J. and Moodera, J.S., J. Appl. Phys., 81 (1997) 5515.

[20] Hordequin, C., Nozieres, J.P. and Pierre, J., J. Magn. Magn. Mater., 183 (1998) 225.

[21] Caballero, J.A., Park, Y.D., Childress, J.R., Bass, J., Chiang, W.-C., Reilly, A.C., Pratt, W.P. and PetroffFero, J.A., J. Vac. Sci. Technol. A, 16 (1998) 1801.

[22] Moradi, M., Taheri, N. and Rostami, M., Phys. Lett. A, 382 (41) (2018) 3004.

[23] Damewood, L., Busemeyer, B., Shaughnessy, M., Fong, C.Y., Yang, L.H. and Felser, C., Phys. Rev. B, 91 (2015) 064409.

[24] Umamaheswari, R., Yogeswari, M. and Kalpana, G., J. Magn. Magn. Mater., 350 (2014) 167.

[25] Dehghan, A. and Davatolhagh, S., J. Alloys Compd., 772 (2019) 132.

[26] Montag, B.W., Reichenberger, M.A., Arpin, K.R., Sunder, M., Nelson, K.A., Ugorowski, P.B. and McGregor, D.S., J. Cryst. Growth, 412 (15) (2015) 103.

[27] Zhang, R.L., Damewood, L., Fong, C.Y., Yang, L.H., Peng, R.W. and Felser, C., AIP Adv., 6 (2016) 115209.

[28] Luo, H., Zhu, Z., Liu, G., Xu, S., Wu, G., Liu, H., Qu, J. and Li, Y., Physica B: Condensed Matter, 403 (1) (2008) 200.

[29] Harmening, T., Eckert, H. and Pöttgen, R., Solid State Sci., 11 (2009) 900.

[30] Roy, A., Bennett, J.W., Rabe, K.M. and Vanderbilt, D., Phys. Rev. Lett., 109 (2012) 037602.

[31] Chadov, S., Qi, X., Kübler, J., Fecher, G.H., Felser, C. and Zhang, S.C., Nat. Matters, 9 (2010) 541.

[32] Amudhavalli, A., Rajeswarapalanichamy, R. and Iyakutti, K., Computational Materials Science, 148 (2018) 87.

[33] Baral, M., Chattopadhyay, M.K., Jangir, R., Chakrabarti, A. and Ganguli, T., Journal of Magnetism and Magnetic Materials, 475 (2019) 675.

[34] Idrissi, S., Ziti, S., Labrim, H. and Bahmad, L., Materials Science in Semiconductor Processing, 122 (2021) 105484.

[35] Idrissi, S., Ziti, S., Labrim, H. and Bahmad, L., Journal of Materials Engineering and Performance, 29 (11) (2020) 7361.

[36] Giannouzzi, P. *et al*., J. Phys.: Condens. Matter, 21 (2009) 395502.

[37] Vanderbilt, D., Phys. Rev. B, 41 (1990), 7892.

[38] Perdew, J.P., Burke, K. and Ernzerhof, M., Phys. Rev. Lett., 77 (1996) 3865.

[39] Perdew, J.P., Chevary, J.A., Vosko, S.H., Jackson, K.A., Pederson, M.R., Singh, D.J. and Fiolhais, C., Phys. Rev. B, 46 (1992) 6671.

[40] Momma, K. and Izumi, F., J. Appl. Crystallogr., 44 (2011) 1272.

[41] Özdoğan, K., Şaşıoğlu, E. and Galanakis, I., Journal of Applied Physics, 113 (19) (2013) 193903.

[42] Skaftouros, S., Ozdoğan, K., Şaşıoglu, E. and Galanakis, I., Phys. Rev. B., 87 (2013) 024420.

[43] Boumia, L., Dahmane, F., Doumi, B., Rai, D.P., Shakeel, A., Khandy, H., Khachai H. and Meradji, A.H., Chinese. J. Phys., 59 (2019) 281.

Volume 15, Number 2, 2022. pp. 119-124

Jordan Journal of Physics

ARTICLE

Estimating Fundamental Parameters of Celestial Objects Using Some Observational Parameters

Mandapati Bhavani Prasad, G. C. Vishnu Kumar and **Dilip A. Shah**

Hindustan Institute of Technology and Science, Chennai, India.

Doi: **https://doi.org/10.47011/15.2.2**

Received on: 02/10/2020; *Accepted on: 24/12/2020*

Abstract: Far away objects seem to appear smaller than the original size. There is confusion about the concept of the perceived size of objects based on distance. In this work, new mathematical formulae are given for the apparent size of objects in both isoscele view and scalene view in terms of absolute distance. The new formulae for the temperature of black bodies and the true diameter of luminous objects are obtained from the apparent size relations. The present study will highlight the diameter of luminous objects and the expression for the temperature of black bodies.

Keywords: Apparent size, Appearance, Isoscele view, Scalene view.

1. Introduction

The apparent size of an object changes with the distance and orientation of the object. The parallel lines seem to be converged at some point. Boring (1964) [1] gave only a theoretical explanation of the concept of converging parallel lines. A few years ago, many experiments were conducted on the perceived size of objects based on distance. Holway and Boring (1941) developed the concept of perceived size of objects based on perceived distance. According to them, the perceived size is a function of perceived distance. In many studies, there is evidence that the relationship between perceived size and distance is unclear [2]. The constancy in the apparent size of the object is commonly known as size constancy and is also based on the perceptual distance from the observer [1]. The application of Titius-Bode law [3] to study the exoplanetary systems results showed that it can be applied to predict the positions of exoplanets and to study their deviations. The Schwarzschild spacetime [4] is applied to determine the relation between the observed flux and the strength of gravitational field of a neutron star and the emission angle. Thouless (1931) concluded that the apparent size of the object agrees with the absolute size constancy with the angle subtended by the object. The accurate values of the apparent size of the objects couldn't be given and the useful applications were not developed from the relationships of perceived size. The concept of apparent size of the object with the absolute distance is not analyzed. So, in this study, new formulae are obtained based on the absolute distance to objects from the observer. The formulae given in this work can be used to study the perceived size of the object and the applications introduced from the apparent size relationships. The derived relationships from apparent size formulae are the true diameter expression for the luminous body and the temperature of black-body expression. The temperature of the blac-kbody is expressed only in terms of angular subtense and the apparent intensity of that black-body. The applications derived in this work can play a dominant role in astronomy.

In this work, we are considering a unique view that can range from $0° \; to \; 180°$ by keeping the apparent size and perceived size terms to be

Corresponding Author: G. C. Vishnu Kumar **Email**: gcvkumar@hindustanuniv.ac.in

the same. Consider an isoscele view of visual angle θ towards length **s** of two points A and B.

Let d be the absolute distance from the observer O to the midpoint of the length s. The apparent length of AB decreases with the distance d from the observer due to the decrease in visual angle. At $\theta = 0, \dot{S} = 0$, where, $\dot{S}$ = apparent length and *s* = absolute length.

2. Law of Appearance

The visible length $\dot{S}$ to the observer is directly proportional to the square of the absolute length s of the object and inversely proportional to the square of the absolute distance d from the observer O to the midpoint of the length of the object AB (Fig. 1).

$$\dot{S} \propto \frac{s^2}{d^2}$$

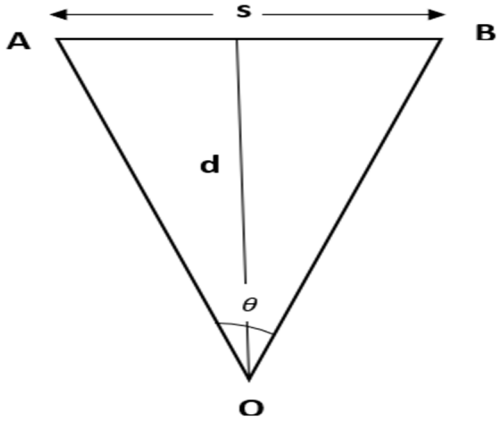

FIG. 1. Isoscele view from O towards length s.

So, by removing the proportionality limit, we get:

$$\dot{S} = \frac{ks^2}{d^2} \quad (1)$$

where, d = distance to the midpoint of the length of an object from the observer (in isoscele view), s = absolute length of the object. Here, the constant k is relative. It depends on the person or instrument like a telescope. We can deduce the law of size constancy from the required appearance law (1).

For the same apparent size of images, $\dot{S}_1 = \dot{S}_2$

$$\frac{s_1}{d_1} = \frac{s_2}{d_2}. \quad (2)$$

This is the law of size constancy in terms of absolute distance. From this result, Emmert's law holds only for the same apparent size of objects.

3. Apparent Size of the Object in Terms of Angular Diameter

Consider the isoscele view of visual angle θ towards length s of two points A and B. Let d be the absolute distance from the observer to the midpoint of the length s. Due to isoscele view, the distance between point A and the observer o and the distance between point B and the observer o are equal. Let us call this distance OA = r. By cosine law, $s^2 = r^2 + r^2 - 2r^2 \cos\theta$, then we obtain $d = \frac{s(1+\cos\theta)}{2\sin\theta}$ and again simplifying this, we will get $d = \frac{s\cot(\frac{\theta}{2})}{2}$. We can use this in (1) to get:

$$\dot{S} = 4k \tan^2\frac{\theta}{2}. \quad (3)$$

This is the relation to the apparent size of the object in terms of angular arc. If we know the angular subtense of the object, we can determine the apparent size of the object without having the true size of the object.

Here, If d = s, then $\dot{S}$ = k. Hence, (3) is based on this condition, $\dot{S}$ = k, then we get $\theta = \pi$ and $\theta = 53.13010235°$. The value of $\theta = \pi$ can be ruled out due to that the apparent size of the object is undetermined at the visual angle *180°*. So, at the value of $\theta = 53.13010235°$, the apparent length is equal to the constant k if and only if $d = s$.

4. Constant for Appearance Formula

The constant k is relative. If we consider the scale of the sun for apparent size, the sun appears as a basketball-size of 24.2 cm in diameter. The distance between the sun and earth $d_s = 149597871\ km$ and the diameter of the sun $s_s = 1.3927 \times 10^6\ km$. We can obtain the value of a constant by using (1); that is:

$$k = 2.79222904678658\ km. \quad (4)$$

5. Apparent Size of Moon

We calculate the apparent size of the moon to support the appearance law (1). So, the distance between earth and moon $d_m = 384{,}400\ km$ and the diameter of the moon $s_m = 3474.2\ km$. By substituting these values in (1), we can get the apparent size of the moon $\dot{S} = 22.80\ cm$. Therefore, the apparent sizes of the sun and moon are having closer values due to closer values of their angular diameters.

6. Apparent Size of the Venus

The closest distance between earth and venus $d_v = 38 \times 10^6\ km$. The diameter of venus $s_v = 12104\ km$. By substituting these values in (1), we can get the apparent size of venus $\dot{S} = 0.2832968\ mm$. Due to more reflection from the surface of venus, we observe that the size of venus is a little more than that.

In the real world, we don't stick only to the isoscele view. Often, we also encounter the scalene view.

7. View in a Scalene Triangle Form

If the line is aligned in the view so that the visual angle is 0°, then the apparent size of the line is zero. So, if we consider a scalene view of length AB (Fig. 1), this can be projected into the half part AC of the isoscele view and the view having 0° visual angle. Let $\angle ABC = \alpha$ and by applying sine rule to ΔOAB, we get $s \times (\sin\alpha) = r_1 \sin\theta_1$. If we use this in (1), we get $\dot{S}' = k \tan^2\theta_1$. This is the apparent size of the projected scalene view into the isoscele view. Also, by dividing the required $\dot{S}'$ with $\sin\alpha$ to get the apparent size $\dot{S}$ of scalene view AB, we get:

$$\dot{S} = \frac{ks\ tan^2\theta_1}{r_1 \sin\theta_1}\ . \qquad (5)$$

If $\theta_1 = \theta$, then (5) tends to isoscele view (Fig. 2). Then,

$$\dot{S} = \frac{kstan^2\ \theta}{\sqrt{\left(\frac{S}{2}\right)^2 + d^2 sin\ \theta}}\ . \qquad (6)$$

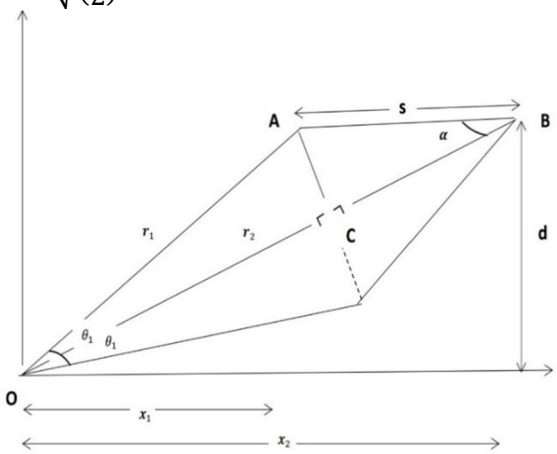

FIG. 2. View in the form of scalene triangle from observer O.

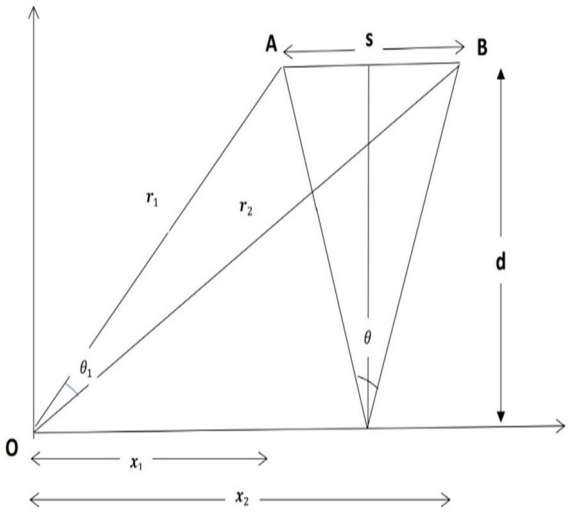

FIG. 3. Scalene view reduced to isoscele view with angular size **θ.**

This is the isoscele view relation obtained from the scalene view in Eq. (5). By arranging Eq. (6) in terms of only angular size, substituting $d = \frac{s\cot(\frac{\theta}{2})}{2}$, we will get:

$$\dot{S} = \frac{ktan^2\ \theta}{\cos(\frac{\theta}{2})}\ . \qquad (7)$$

If we plot the relations of the isoscele view of Eqs. (3) & (7) in the same graph (Graph 1), we will see that both curves are coinciding with each other at smaller angular arcs of the objects.

But, when we zoom Graph 1 vigorously, we will see that the curves do not perfectly coincide with each other (Graph 2).

We can find an error in isoscele view Eq. (7) obtained from scalene relation by subtracting isoscele Eq. (3). So, we can plot the error curve by the difference of Eqs. (7) & (3) using MATLAB.

The scalene relation is a good approximation for only small angular sizes of objects or far away objects. The error in scalene relation increases if the angular size of the object increases.

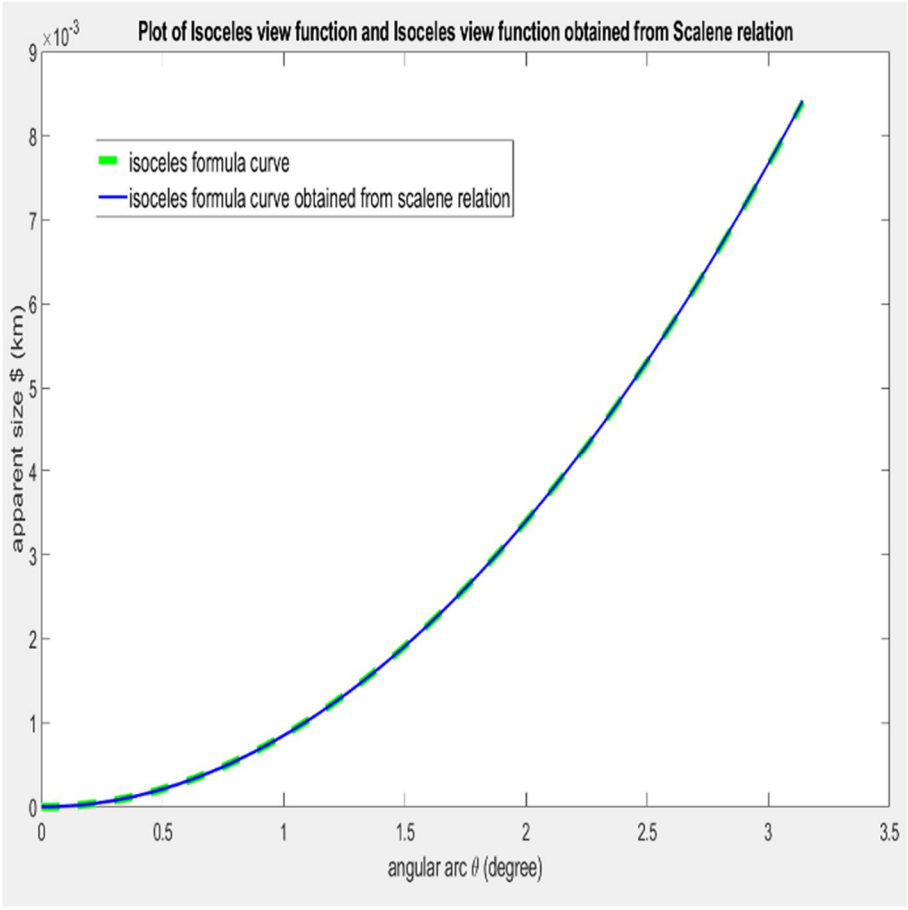

GRAPH 1. Curves of Eqs. (3) & (7).

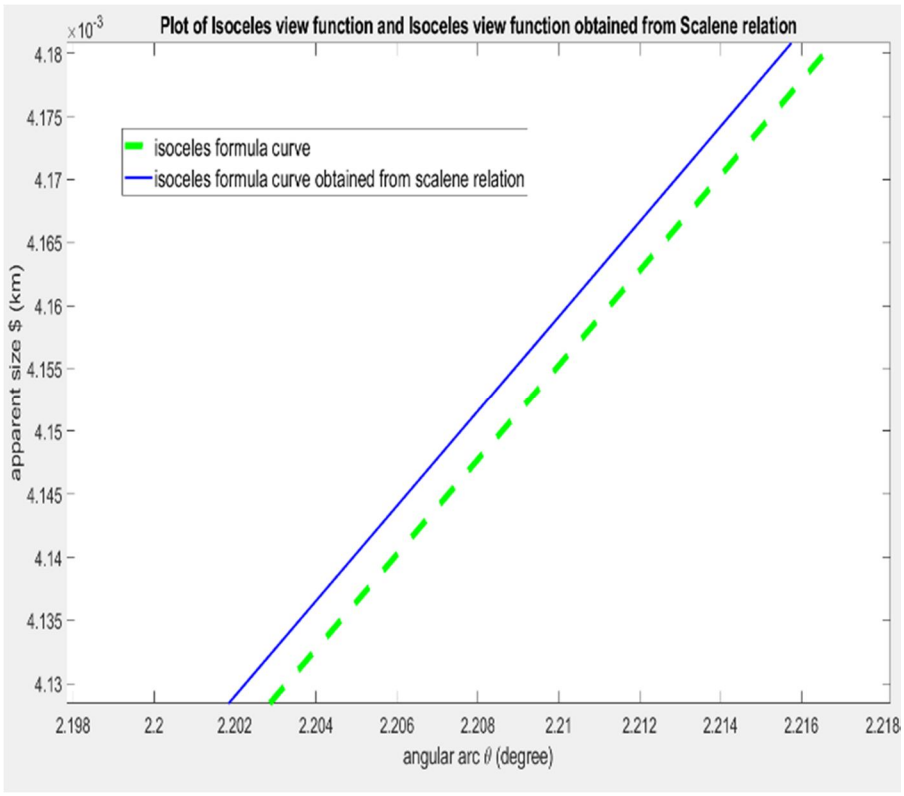

GRAPH 2. Plot of isoscele view function obtained from scalene function.

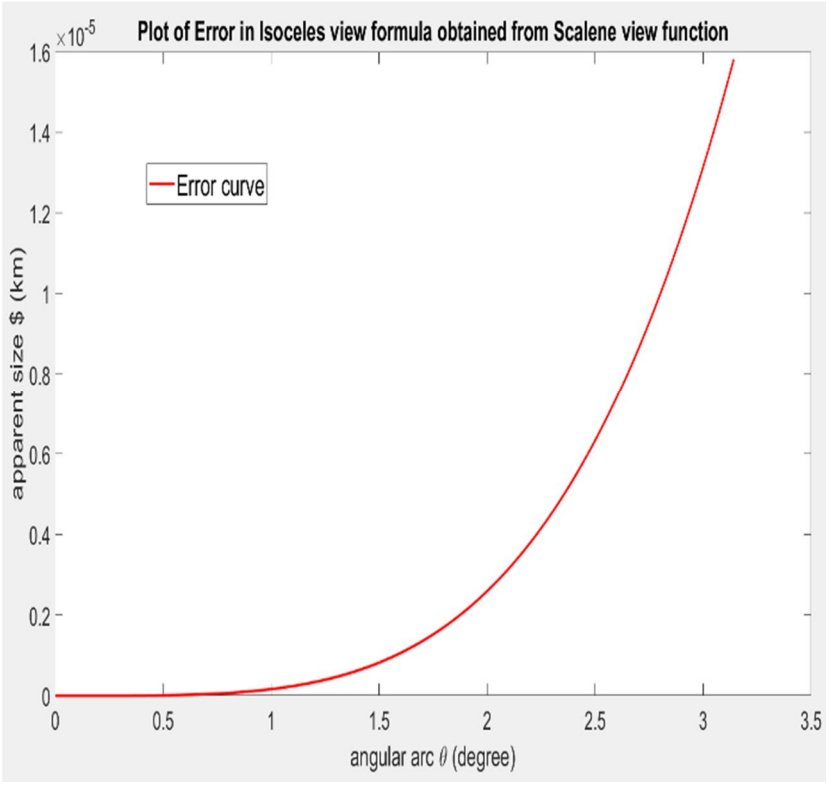

GRAPH 3. Error curve obtained by the difference of the functions from Eqs. (7) and (3).

8. Apparent Size of the Moon by Scalene View Relation

The apparent size of the moon can also be found through the isoscele view obtained from the scalene view relation to support the required Eq. (6). So, the distance between moon and earth $d_m = 384{,}400\ km$, the diameter of the moon $s_m = 3474.2\ km$ and the angular arc of the moon $\theta_m = 0.52°$. If we find the apparent size of the moon by substituting these values in (6), we get the apparent size of the moon, $\dot{S}_m = 22.90\ cm$.

The apparent size of the moon calculated by using the isoscele view Eq. (1) is $22.80\ cm$. It is almost similar to the apparent size calculation of the moon by using scalene view Eq. (6).

9. Diameter of the Luminous Object

We perceive that the intensity of far away luminous bodies is smaller than the absolute intensity. So, the apparent intensity is given as:

$$I = {}^{L}/_{4\pi d^2} \tag{8}$$

where, L = luminosity of the body, d = distance measured from the body to our view. Substituting the value of distance d obtained from apparent intensity Eq. (8) in the appearance formula (1) gives $\dot{S} = {}^{4\pi k s^2 I}/_{L}$. We can use this in the isoscele view relation in terms of angular size (8),

$$s = \sqrt{\frac{L}{\pi I}} \tan\frac{\theta}{2} \tag{9}$$

which is the relation to the diameter of the luminous object. From this, we can derive the temperature of the black body using Stefan-Boltzmann's law.

10. Temperature of the Black Body

The temperature of black bodies will be derived with the help of (9). By Stefan Boltzmann Law for black bodies [5], luminosity is given as

$$L = 4\pi\sigma T^4 R^2 \tag{10}$$

where σ = Stefan Boltzmann constant = 5.67×10^{-8} W/m^2K^4, R = radius of the black body and T = temperature in kelvin. We can substitute the Stefan-Boltzmann law (10) and S = 2R directly in Eq. (9), where, R = radius of the black body and S = diameter of that black body. So, we get:

$$S^2 = \frac{4\Pi\sigma T^4 R^2}{\Pi I} tan^2\frac{\theta}{2} \tag{11}$$

If we simplify Eq. (11) further, we will get:

$$T = \left[\frac{I}{\sigma \tan^2\frac{\theta}{2}}\right]^{\frac{1}{4}} \quad (12)$$

where I represents the apparent intensity of the black body. So, the temperature of black bodies can be found if the angular arc and apparent intensity are known, which can be measured directly.

11. Diameter of the Sun

The diameter of the sun can be easily determined to support Eq. (9) by substituting the required values in that equation. So, the angular arc of the sun, $\theta = 0.5334°$, the apparent intensity of the sun, $I_{sun} = 1360.8\, W/m^2$ and the luminosity of the sun, $L = 3.827 \times 10^{26}\, W$. We can use these values in (9) to obtain the diameter of the sun, s = 1.39×10^6 km

12. Temperature of the Sun

Similarly, the temperature of the sun can be determined by the temperature Eq. (12), because all stars are black bodies. The apparent Intensity of the sun, $I = 1370 W/m^2$ and the angular diameter of the sun, $\theta = 0.5334°$. We got, $T = \left[\frac{I}{\sigma \tan^2\frac{\theta}{2}}\right]^{\frac{1}{4}}$, then using this, we will get the temperature of the sun,$T = 5778.73\, K$.

13. Conclusions

We have derived the relationships for apparent sizes in both isoscele and scalene views. Also, we derived the relative constant to verify the appearance law in calculating the apparent sizes of objects. Applications, such as the expression for the diameter of luminous objects and the expression for the temperature of black bodies, are also developed from the apparent size relationships.

Appendix I

In this appendix, we calculate the diameter of the Sirius star from $s = \sqrt{\frac{L}{\pi I}} \tan\frac{\theta}{2}$ to support the above derivation for the diameter relation. So, the luminosity of Sirius, $L = 25.4\, L\odot$. So, $L = 25.4 \times 3.827 \times 10^{26}\, W$ and the apparent intensity of Sirius, $I = 10^{-7}\frac{W}{m^2}$. The new accurate angular diameter measurement was recently found [6]. So, the angular arc of Sirius, $S = 5.63 \pm 0.08\ arc\, ms = 1.5638888 \times 10^{-6}°$, then we get the diameter of Sirius, $S = 2.4 \times 10^6$ km.

Appendix II

In this appendix, we calculate the temperature to support the derivation of the temperature relation, $T = \left[\frac{I}{\sigma \tan^2\frac{\theta}{2}}\right]^{\frac{1}{4}}$. So, the angular arc of Sirius, $\theta = 1.5638888 \times 10^{-6}°$ and the apparent intensity of Sirius, $I = 10^{-7} W/m^2$. From there, we get the temperature of the Sirius star, T = 9864.56 K. Here, the approximate value of the apparent intensity of Sirius is taken. So, that is why the calculated value is approximately close to the absolute temperature.

References

[1] Boring, E.G., The American Journal of Psychology, 53 (2) (1940) 293.

[2] Kaufman, J., King, T., Bai, S., Kaufman, L., Edlund, S. and Noble, R., Spatial Vision, 19 (5) (2006) 439.

[3] Altaie, M.B., Yousef, Z. and Al-Sharif, A.I; Jordan J. Phys., 9 (2) (2016) 123.

[4] Alobayde, M.A. and Khaleel, S.E., Jordan J. Phys., 6 (1) (2013) 27.

[5] LoPresto, M.C. and Hagoort, N., The Physics Teacher, 49 (2) (2011) 113.

[6] Davis, J. and Tango, W.J., Nature, 323 (1986) 234.

Volume 15, Number 2, 2022. pp. 125-136

Jordan Journal of Physics

ARTICLE

Enhancement of Secondary Gamma Radiation Flux Energies in the Energy Region from 1400 Kev to 1500 Kev during Lunar Eclipse on June 16, 2011 at Udaipur, India

Devendra Pareek and **Pallavi Sengar**

Department of Physics, Bhupal Nobles' University, Udaipur, India.

Doi: **https://doi.org/10.47011/15.2.3**

Received on: 08/10/2020; *Accepted on: 18/01/2021*

Abstract: The lunar eclipse at Udaipur (27^0 43' 12.00" N, 75^0 28' 48.01" E), India was experimentally observed on June 16, 2011 using ground-based NaI (Tl) scintillation detector. Cadences of data were collected at intervals of half an hour. The analyzed data revealed a significant enhancement in the energy region from 1400 keV to 1500 keV of secondary gamma radiation flux (SGRF) on comparison to pre- and after lunar eclipse days**.** On June 16, we observed additional peaks in the energy spectrum of SGR flux in the energy region extending from 1461.010 keV to 1472.536 keV during the progress of lunar eclipse. We interpret such enhancement of SGR flux energies on the basis of combined phenomenon of gravitational lensing effect of Sun and Earth as well as the Sun's magnetic field and the interplanetary magnetic field. Due to such combined effect, primary cosmic and solar radiations bend and may cause strong hitting on the less air surface of the Moon, resulting into emission of secondary particle flux mostly gamma radiation, high energy photo electrons, hard X -radiation, muons, protons and neutrons which may be regarded as back scattering from the Moon surface. Energy of backscattered secondary flux is large enough that it gives such enhancement in the energy region from 1400 keV to 1500 keV during lunar eclipse observation. Also, due to combined gravitational effect, cosmic radiation bent and impinged deep inside the atmosphere of Earth, producing a large shower of secondary radiation particles. These collective effects may give such enhancement of secondary gamma radiation flux energies.

Keywords: Lunar eclipse, Solar magnetic field, Interplanetary magnetic field, Gravitational lensing, Bending of primary cosmic and solar radiations.

1. Introduction

Cosmic radiation - known as galactic cosmic radiation (GCR) - is high-energy charged particles and a composition of cosmic radiation form about 89% of protons, 10% of helium, and about 1% of other heavier elements, such as carbon, oxygen, magnesium, silicon and iron [12]. Charged cosmic particles radiation is almost isotropically distributed and propagates through interplanetary space while arriving on Earth [9]. If these particles have energies of the order of 10 TeV or lower, then they will bend under the influence of solar and interplanetary magnetic fields [8]. Energetic particles that are associated with energetic events on the Sun, known as solar radiation (SR), are accelerated in interplanetary space. It is believed that the bending of cosmic flux becomes significant when the Moon is in the line joining the centers of the Sun and the Earth during the eclipse [1], [6], [20], [2], [3]

It was observed that when the electromagnetic radiation passes near a massive object, then due to gravitational field of the object, it bends. Such phenomenon is called gravitational lensing. The object could be a

Corresponding Author: Devendra Pareek **Email**: deven.pareek69@gmail.com

galaxy, a star or a cluster of galaxies. This was proved by A. S. Eddington and collaborators in a famous experiment during a total solar eclipse in 1919.

Due to the combined effect of gravitational lensing, strong solar and interplanetary magnetic fields, the primary high-energy cosmic radiation and solar radiation bend. These bent radiations strike on the airless surface of the Moon. Therefore, from surface of the moon; mostly gamma radiation, high-energy photo electrons, hard x-rays, muons, protons and neutrons are emitted as secondary emission in the range of several hundred keV to MeV [13], [21], [22].

It is very interesting to collect data of radiation during different celestial events occurring at various times, because it is observed that during such events, GCR and SR are modulated. When high-energy GCR and SR undergo collisions with atoms of the upper atmosphere, they produce a cascade of "secondary" particles known as secondary radiation (SR) and produce a shower of secondary particles. These particles increase rapidly as these move downward in the atmosphere and in each interaction, the particles lose energy. Small fraction of these particles usually comes down to the ground because of the large width of secondary cosmic shower. These particles are detected by appropriate detectors on ground [11], [7].

The secondary radiation can be divided into three components as electromagnetic component, hadronic component and mesonic component. In the electromagnetic component, there is a presence of electrons and gamma radiation. Hadronic component has low-energy protons and neutrons, while mesonic component has pions, muons, neutrinos and kaons. The secondary flux has one component of secondary gamma radiation which is measured by efficient scintillation detectors.

On 15th and 16th June 2011, a Lunar eclipse was witnessed over much of Europe, much of Asia, Australia, Africa, South America, the Pacific, Atlantic, the Indian Ocean and Antarctica [Fig. 1].

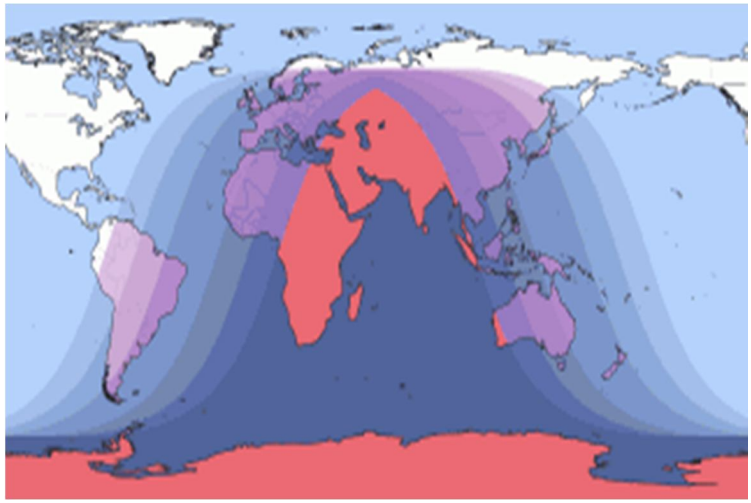

FIG. 1. Lunar eclipse.

2. Celestial Events and Variation of Radiation Flux

Many ground-based experimental studies for observing secondary cosmic and solar radiation flux were conducted during normal days and on days of special celestial events, such as solar eclipse, lunar eclipse, appearance of a comet in the sky, phases of the Moon and closest approach of Venus, with help of scintillation counter.

In lunar-eclipse studies, variation of secondary cosmic and solar gamma radiation flux at some energy had been observed. Such interesting finding can be explained on the basis of bending of primary cosmic radiation and solar radiation by the combined effect of the magnetic field of the Sun and the interplanetary magnetic field, the combined gravitational lensing effect of Sun and Earth and the backscattered secondary flux form the Moon [16]

To observe the variation of secondary radiation, we conducted an experimental study during lunar eclipse on June 16, 2011 at Udaipur, India.

3. Experimental Set-up and Observations

In this experimental study, an efficient scintillation detector of Model 802 was used, made by: Canberra Genie 2000, to detect SCGR (secondary cosmic gamma radiation) produced by the GCR and SR during partial lunar eclipse in the energy range from 2 keV to 2048 keV [Fig. 2]. Diameter of the detector crystal is 50 mm with a thickness of 44.5 mm. NaI (Tl) crystal is optically coupled with photo multiplier tube (PMT) of Model 2007P. To provide high-tension voltage, high-tension voltage supply Model 3102D of 1100 Volts DC was connected with integral line. Using negative polarity of spectroscopic amplifier Model 2022, the negative signal of about 0.5 Volt was amplified to a 5-Volt positive pulse, then the signal was fed to a multi-channel analyzer with 1024 energy channels for acquisition and analysis. The detector system was put into a 2.5-inch lead shield with a small opening pointed towards the partial lunar eclipse. We collected data as a function of time after intervals of half an hour and the data files were stored in computer from 12.00 AM to 3.30 AM on June 15, 16 and 17, 2011. June 15 was a pre-eclipse normal day and June 17 was a post-eclipse day. In India, lunar eclipse began from June 15 at 11.53 PM and ended on June 16 at 3.32 AM. Maximum eclipse was at 1.43 AM. The energy calibration was observed to be 2.0 keV per channel using the standard radioactive source Cs^{137}.

FIG. 2. Scintillation detector.

4. Analysis and Results

As depicted in the panels of Figs. 3, 4 and 5, the energy spectra of SGR flux on pre-eclipse day (15^{th} June), partial eclipse day (16^{th} June) and post-eclipse day (17^{th} June) in the energy range between 800 keV and 2000 keV were taken from 12.00 AM to 3.30 AM with a duration of half an hour integrated data files.

Panels of Figs. 6, 7 and 8 show the existence of specific peaks with the progress of time from 12.00 AM to 3.30 AM. We used Lorentz peak fit concept in order to understand the characteristics and energy variation of SGR flux peaks in the energy range from 1300 keV to 1600 keV.

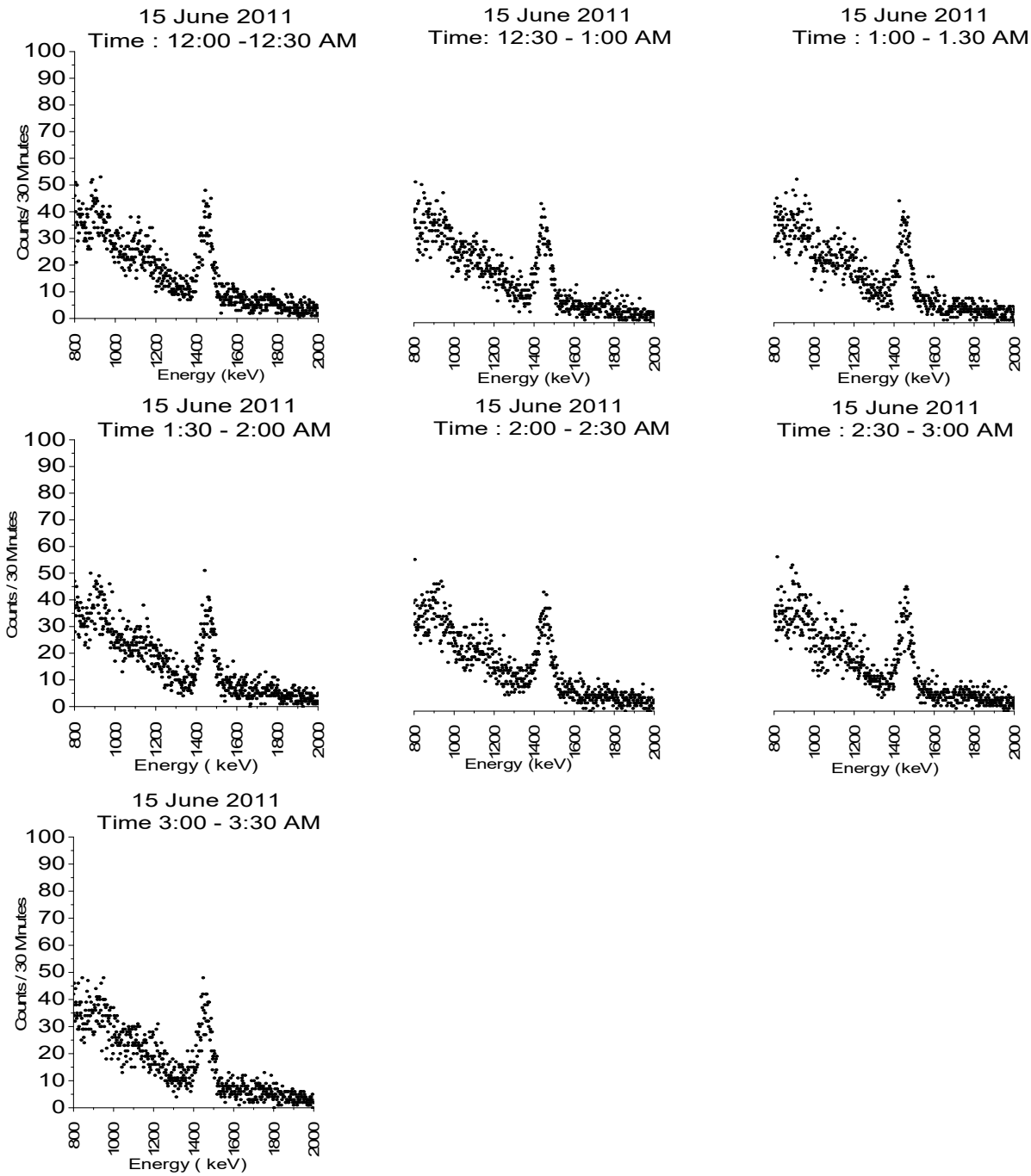

FIG. 3. Panel of energy spectrum of pre-partial lunar-eclipse day.

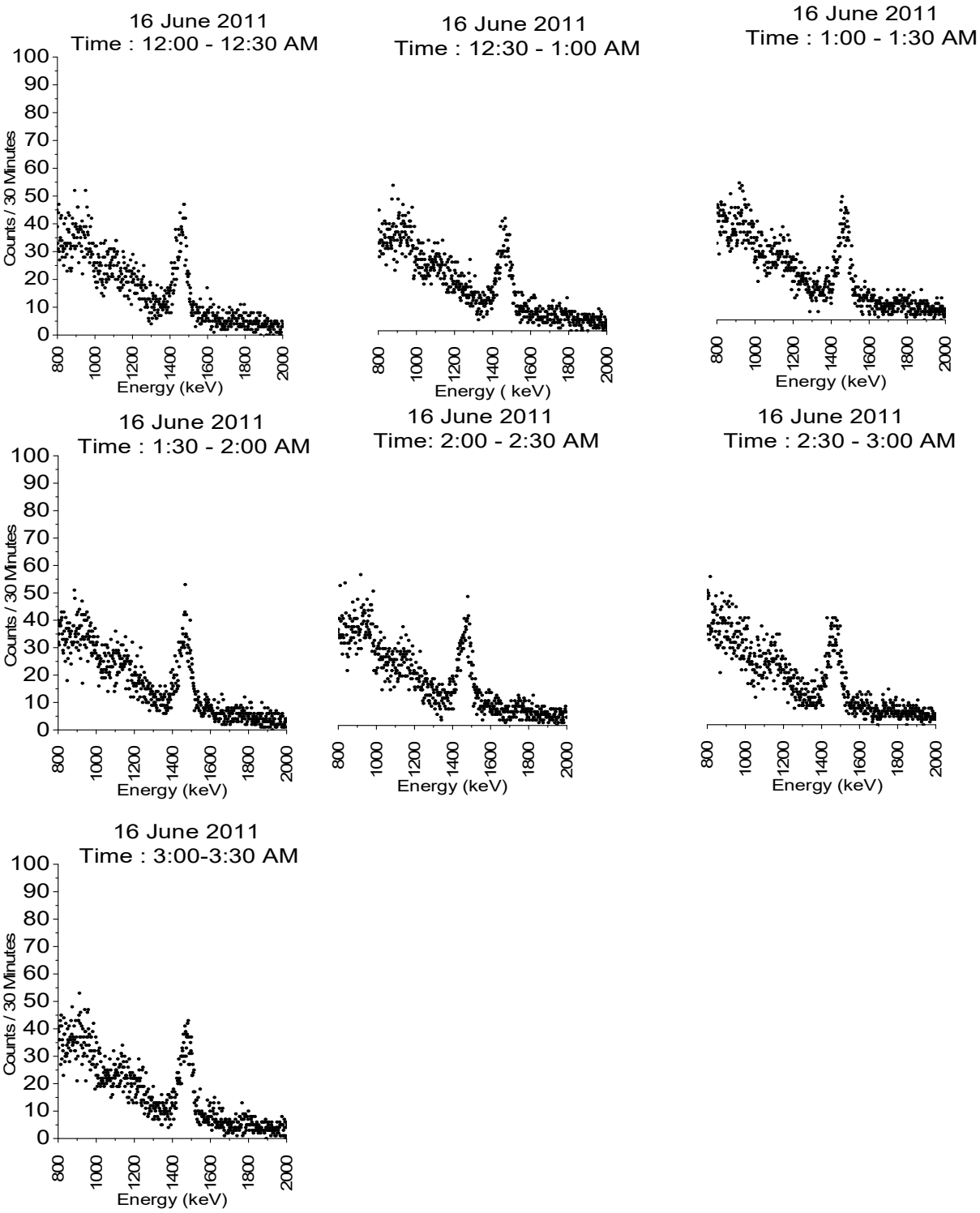

FIG. 4. Panel of energy spectrum of partial lunar-eclipse day.

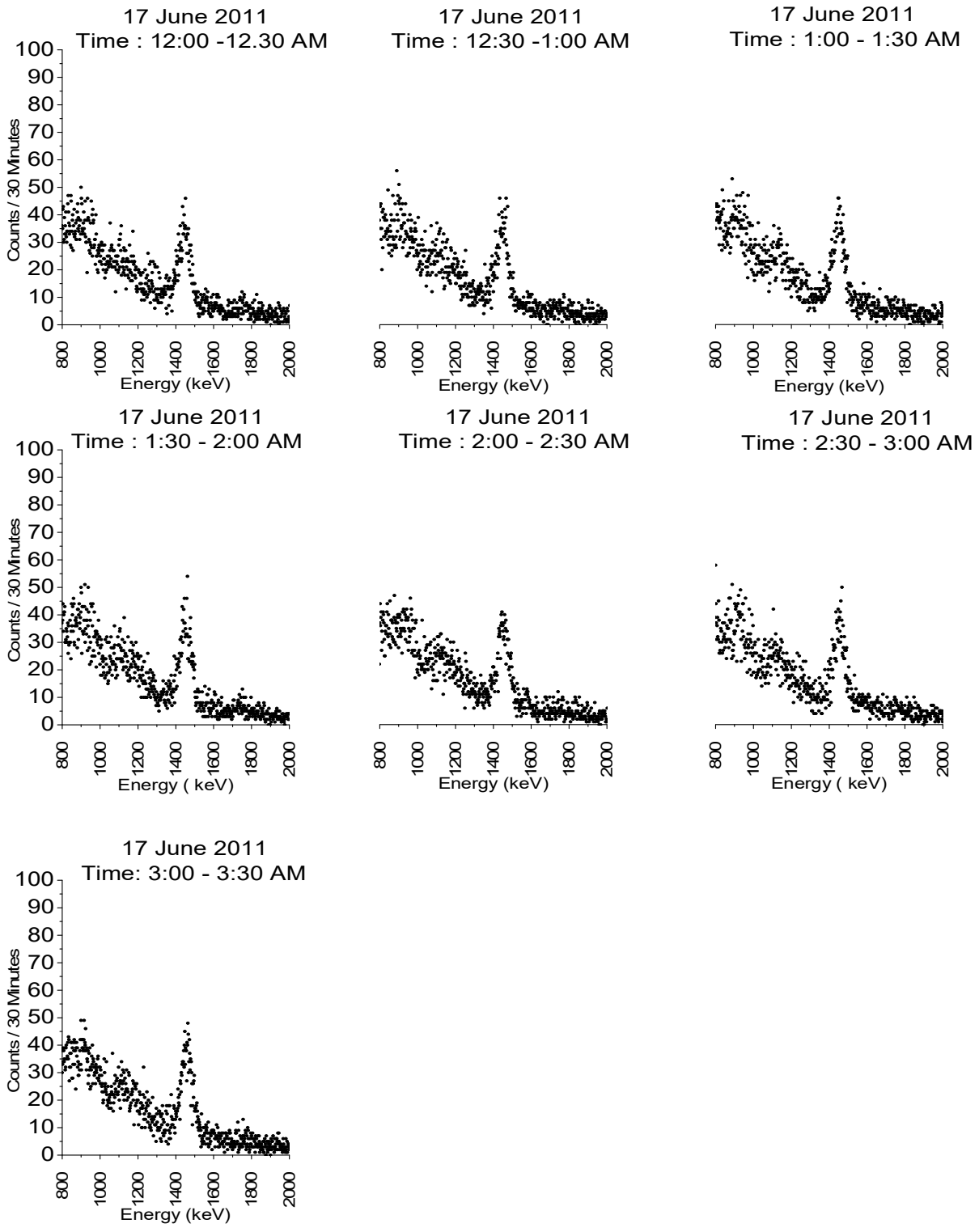

FIG. 5. Panel of energy spectrum of post-partial lunar-eclipse day.

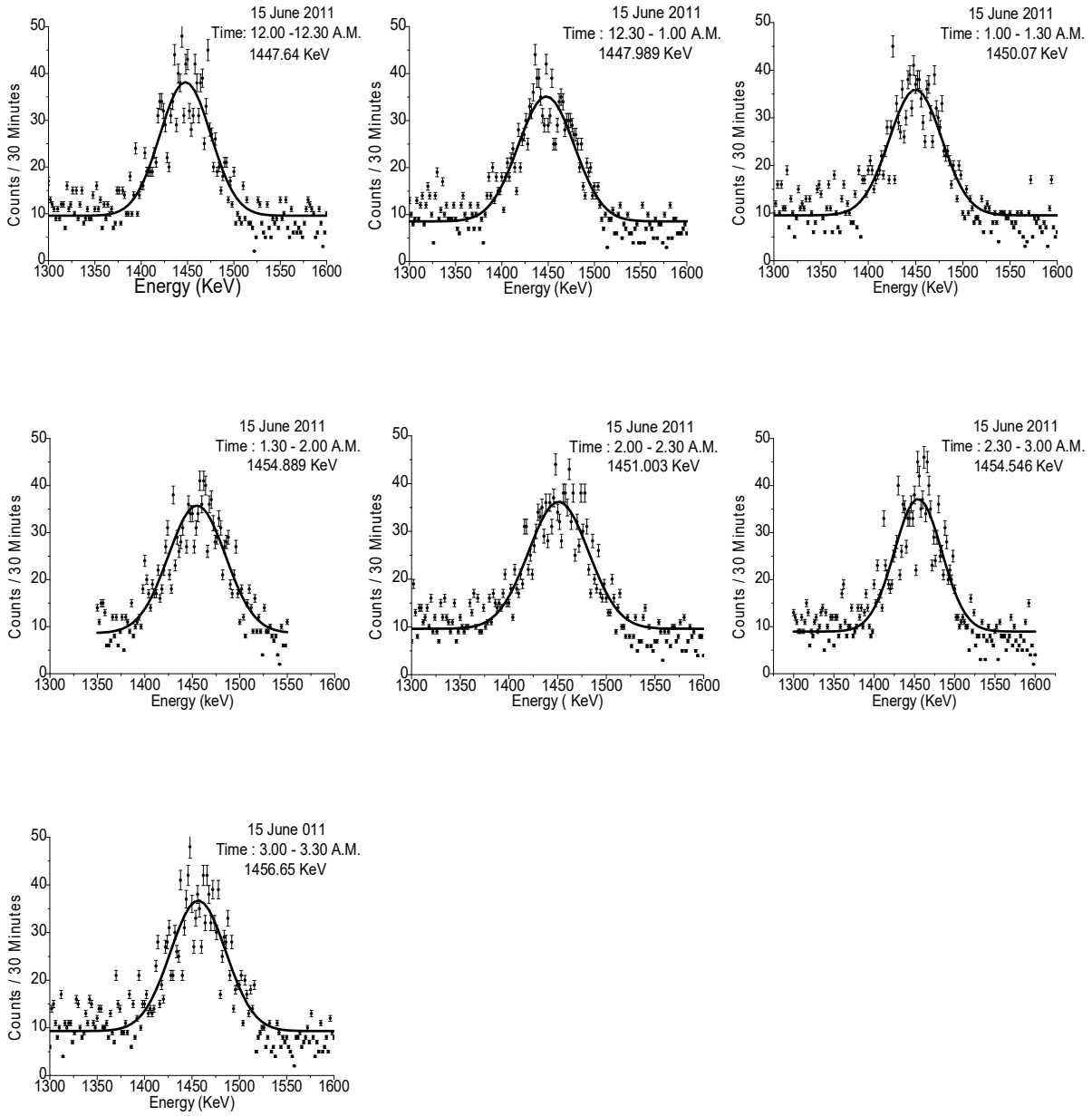

FIG. 6. Lorentz fit for specific peaks in data of SGRF on pre-partial lunar-eclipse day.

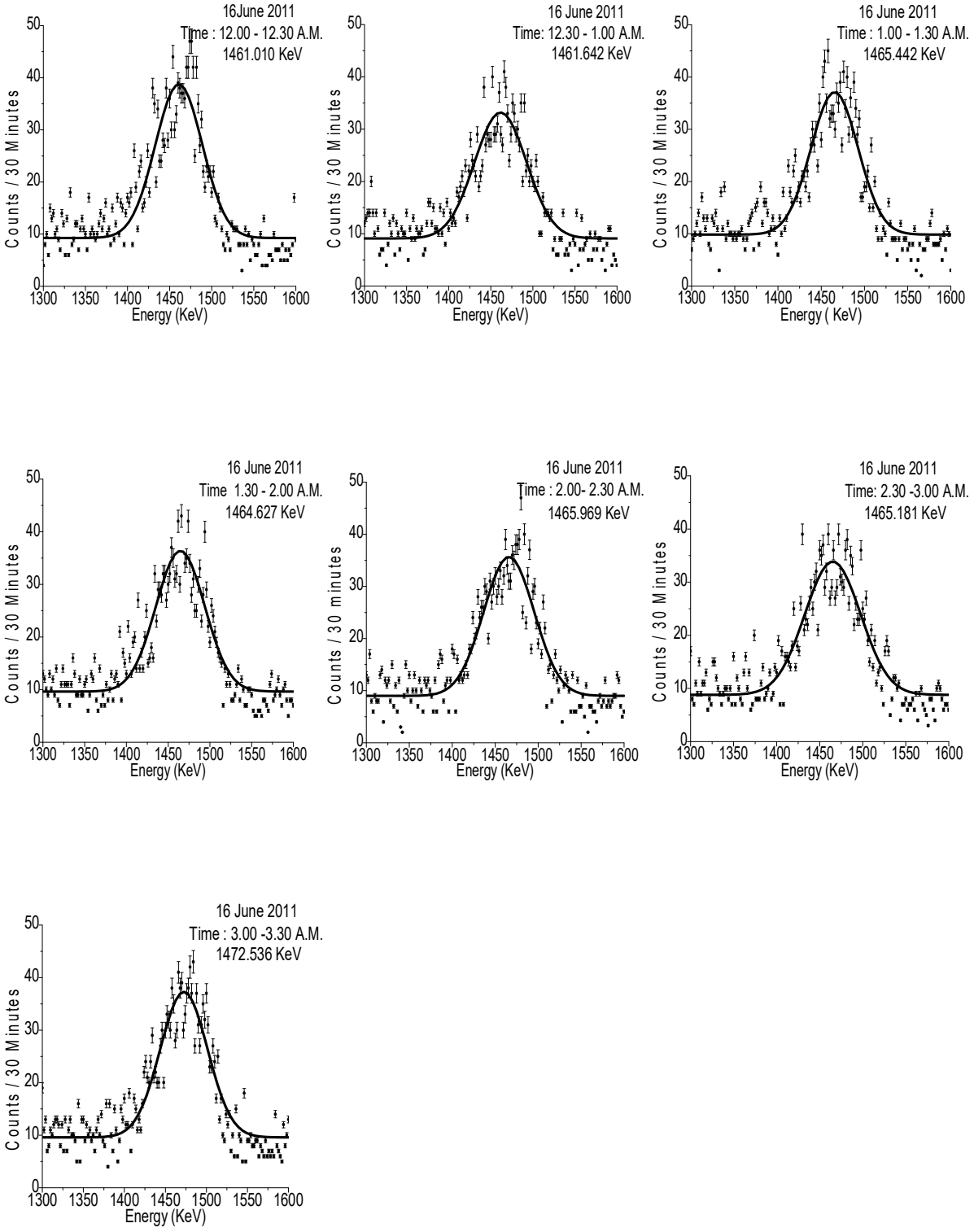

FIG. 7. Lorentz fit for specific peaks in data of SGRF on partial lunar-eclipse day.

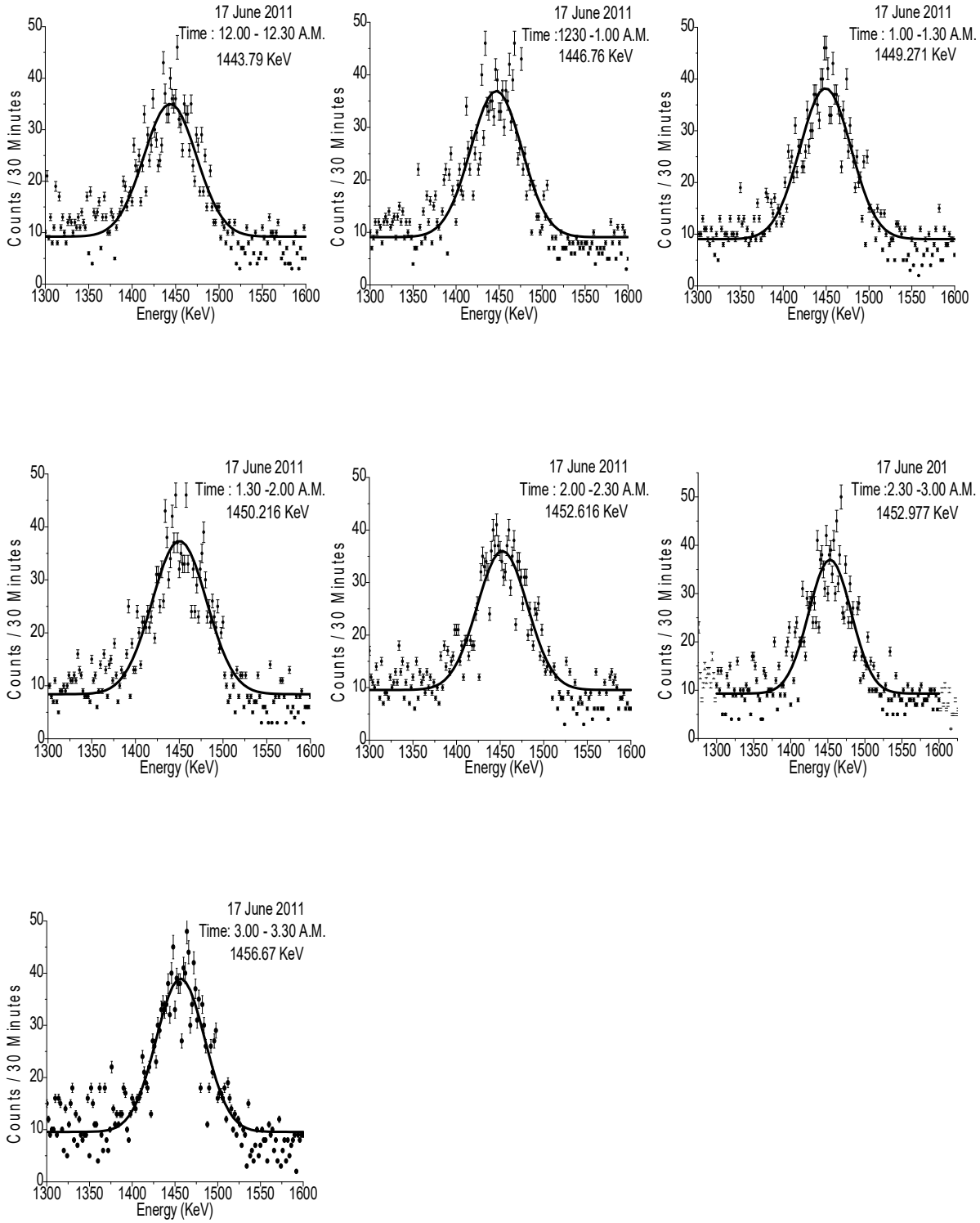

FIG. 8. Lorentz fit for specific peaks in data of SGRF on post-partial lunar-eclipse day.

The time-dependent energy spectrum analysis clearly showed that with the progress of the eclipse, the energy of the observed peak varied consistently from 1461.010 keV to 1472.536 keV on the eclipse day. The figures above show clearly that in comparison to normal days (15 and 17), on the eclipse day, there is an increase of energies of SGRF (secondary gamma radiation flux). The following tables represent the energies of SGRF on pre-lunar eclipse day, lunar eclipse day and post-lunar eclipse day using Figs. 6, 7 and 8, respectively.

SGRF energies on 15 June 2011(Energy Table)			
Sr. No.	Time	Energy (keV)	Mean
1	12.00 – 12.30 A.M.	1447.64	
2	12.30 – 1.00 A.M.	1447.989	
3	1.00 – 1.30 A.M.	1450.07	
4	1.30 – 2.00 A.M.	1454.889	1451.82671 keV
5	2.00 – 2.30 A.M.	1451.003	
6	2.30 – 3.00 A.M.	1454.546	
7	3.00 – 3.30 A.M.	1456.65	

on 16 June 2011 (Energy Table)			
Sr. No.	Time	Energy (keV)	Mean
1	12.00–12.30 A.M.	1461.010	
2	12.30 – 1.00 A.M.	1461.642	
3	1.00 – 1.30 A.M.	1465.442	
4	1.30 – 2.00 A.M.	1464.627	1465.201 keV
5	2.00 – 2.30 A.M.	1465.969	
6	2.30 – 3.00 A.M.	1465.181	
7	3.00 – 3.30 A.M.	1472.536	

on 17 June 2011 (Energy Table)			
Sr. No.	Time	Energy (keV)	Mean
1	12.00– 12.30 A.M.	1443.79	
2	12.30 – 1.00 A.M.	1446.76	
3	1.00 – 1.30 A.M.	1449.271	
4	1.30 – 2.00 A.M.	1450.216	1450.329 keV
5	2.00 – 2.30 A.M.	1452.616	
6	2.30 – 3.00 A.M.	1452.977	
7	3.00 – 3.30 A.M.	1456.67	

Using panels of Figs. 6, 7, 8 and the tables above, Figs. 9 and 10 clearly represent the energy variation of SGRF peaks in the energy range from 1400 keV to 1500 keV on the pre-, post- and lunar eclipse days, showing that there is an increase in energies of SGRF on lunar-eclipse day in comparison to other days, which is noticeable on the lunar-eclipse day.

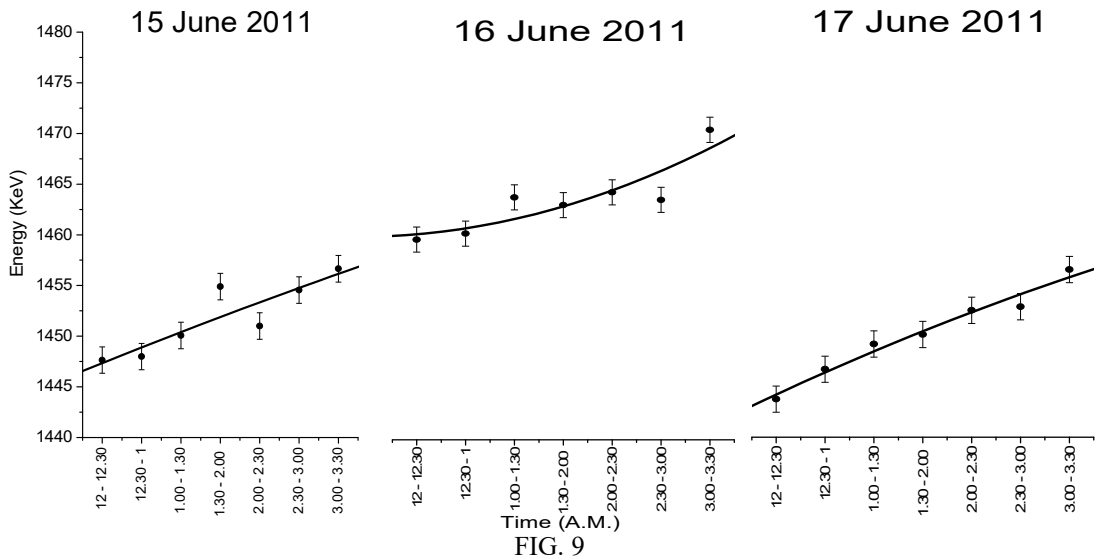

FIG. 9

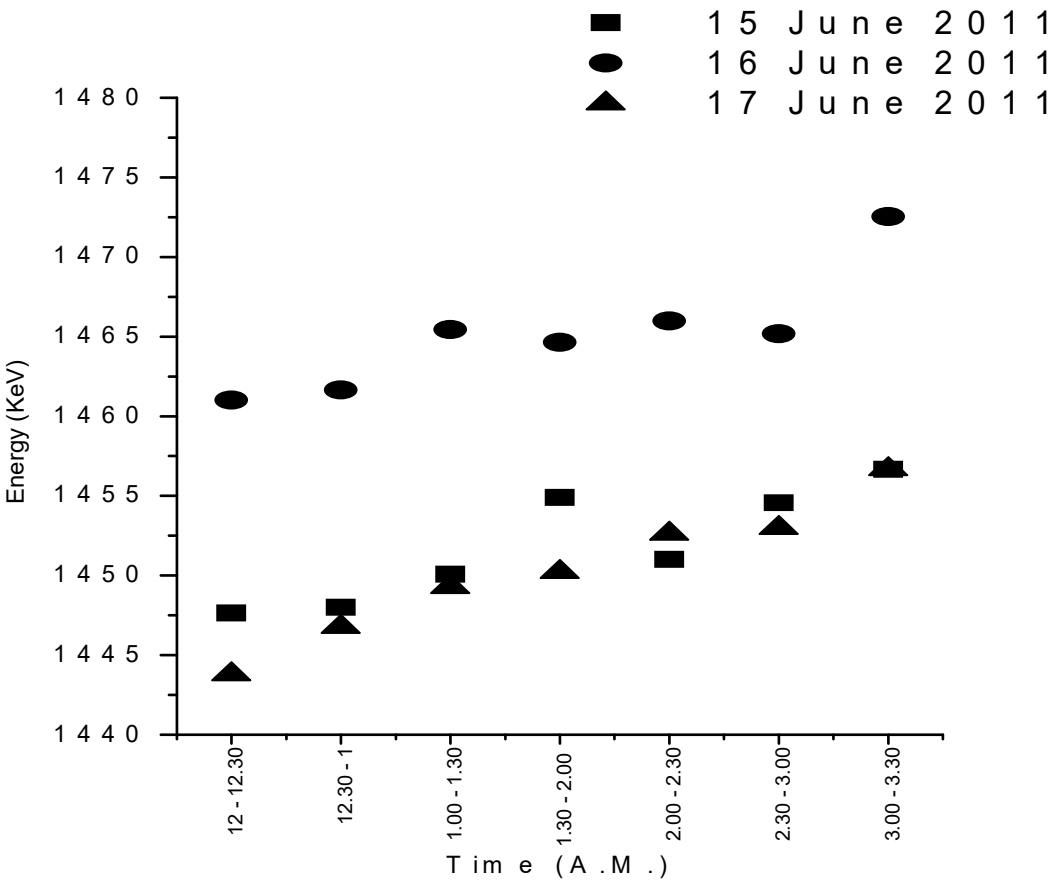

FIG. 10

5. Discussion

The probable reasons in this present study for the enhancement of SGR flux energies in the energy range from 1400 keV to 1500 keV are as follows:

1. Due to the combined effect of gravitational lensing, strong solar and interplanetary magnetic fields, the primary high-energy cosmic radiation and solar radiation bend. These bent radiations strike on the surface of the Moon. From the surface of the Moon, mostly gamma radiation, high-energy photo electrons, hard x-rays, muons, protons and neutrons are emitted as secondary emission in the range of several hundred keV to MeV. These secondary emissions may produce the enhancement of SGR flux energies in the energy range from 1400 keV to 1500 keV which is reported in this present study.
2. Bent primary cosmic radiation and solar radiation penetrate deep inside the atmosphere of the Earth, which produces more showers of secondary radiation particles. This secondary flux reaches the surface of Earth and may produce such enhancement of SGRF energies in the energy range from 1400 keV to 1500 keV

6. Conclusion

From points (1) and (2) above, we can understand that as the eclipse progresses, there is an unusual enhancement of SGRF energies in the energy range between 1400 keV and 1500 keV. This is a new observation reported in the present study for the first time during lunar eclipse and may be examined in detail with more statistics in the next experimental studies.

7. Acknowledgments

The authors wish to thank the anonymous referees for their valuable comments and remarks.

References

[1] Alexandreas, D.E., Physical Review D, 43 (1991) 1735.

[2] Amenomori, M., Astrophys. Journal Letters, 415 (1993) L147.

[3] Amenomori, M., Physical Review D, 47 (1993) 2675.

[4] Bhaskara, A., Purohit, A., Hemalatha, M., Pai, C., Raghav, A., Gurada, C., Radha, S., Yadav, V., Desai, V., Chitnis, A., Sarpotdar, P. and Patankar, A., Astroparticle Physics, 35 (5) (2011) 223.

[5] Bhattacharyya, A., Biswas, S., Chatterjee, B.K., Das, M., Das, P.K., Das, T.K., De, T.K., Engineer, M.H., Mukherjee, R.N., Raha, S., Roy, S.C., Saha, S.K., Sen, A.K., Sinha, B. and Syam, D., Astrophysics and Space Science, 250 (1997) 313.

[6] Borione, A., Catanese, M., Covault, C.E., Cronin, J.W., Fick, B.E., Gibbs, K.G., Green, K.D., Hauptfeld, S., Kieda, D., Krimm, H.A., Mascarenhas, N.C., Matthews, J., McKay, T.A., Müller, D., Newport, B.J., Nitz, D., Ong, R.A., Rosenberg, L.J., Sinclair, D. and van der Velde, J.C., Physical Review D (Particles and Fields), 49 (1994) 1171.

[7] Chilingarian, A., Daryan, A., Arakelyan, K., Hovhannisyan, A., Mailyan, B., Melkumyan, L., Hovsepyan, G., Chilingaryan, S., Reymers, A. and Vanyan, L., Physical Review D, 82 (4) (2010) 043009.

[8] Clark, G.W., Physical Review, 108 (1957) 450.

[9] Fulks, G.J., Journal of Geophysical Research, 80 (1975) 1701.

[10] Kandemir, G. et al., ASP Conference Series, 205 (2000) 202.

[11] Kodama, M., Physical Society of Japan, 52 (1983) 1503.

[12] Longair, M.S., "High-energy Astrophysics 1", second edition, (Pub. Cambridge University Press, 1992).

[13] Morris D.J., Geophysics Res., 89 (10) (1984) 685.

[14] Nayak, P.K. et al., Astroparticle Physics, 32 (2010) 286.

[15] Pareek, D. and Jaaffrey, S.N.A., Internation Journal of Scientific Research, 3 (4) (2014) 411.

[16] Pareek, D. et al., Research Journal of Physical Sciences, 1 (4) (2013) 22.

[17] Pareek, D., Jaaffrey, S.N.A., Daspattnayak, H.T. and Shrimali, M., Global Journal for Research Analysis, 6 (5) (2017) 500 .

[18] Pareek, D. et al., International Journal of Scientific Research, 3 (5) (2014) 6.

[19] Pareek, D., Jaaffrey, S.N.A., Talesra, K.P., Yadav, R. and Ameta, S., Research Journal of Physical Sciences, 1 (5) (2013) 22.

[20] Pomarede, D., Boyle, P.J., Urban, M., Badran, H.M. and Behr, L., Astroparticle Physics, 14 (4) (2001) 287.

[21] Thompson, D.J., Bertsch, D.L., Morris, D.J. and Mukherjee, R., Journal of Geophysical Research, 102 (A7) (1997) 14,735.

[22] Zeilik, M., "Astronomy: The Evolving Universe", (Harper and Row Publishers, New York, 1979) 191-192.

Volume 15, Number 2, 2022. pp. 137-148

Jordan Journal of Physics

ARTICLE

Eigensolution and Expectation Values of the Hulthen and Generalized Inverse Quadratic Yukawa Potential

Peter O. Okoi[a], **Collins O. Edet**[b], **Thomas O. Magu**[c] and **Etido P. Inyang**[d]

[a] *Department of Physics, University of Calabar, Nigeria.*

[b] *Theoretical Physics Group, Department of Physics, University of Port Harcourt, Choba, Nigeria.*

[c] *Department of Pure and Applied Chemistry, University of Calabar, Calabar, Nigeria.*

[d] *Department of Physics ,National Open University of Nigeria,Jabi, Abuja, Nigeria.*

Doi: **https://doi.org/10.47011/15.2.4**

Received on: 12/10/2020; *Accepted on: 24/12/2020*

Abstract: In this study, the Schrödinger equation was solved with a superposition of the Hulthen potential and generalized inverse quadratic Yukawa potential model using the Nikiforov-Uvarov (NU) method. For completeness, we also calculated the wave function. To validate our results, the numerical bound state energy eigenvalues was computed for various principal n and angular momentum ℓ quantum numbers. With the aid of the Hellmann-Feynman theorem, the expressions for the expectation values of the square of inverse of position, r^{-2}, inverse of position, r^{-1}, kinetic energy, $\hat{T}$ and square of momentum, $\hat{p}$ are calculated. By adjusting the potential parameters, special cases of the potential were considered, resulting in Generalized Inverse Quadratic Yukawa potential, Hulthen potential, Coulomb potential, Kratzer potential, Inversely Quadratic Yukawa potential and Coulomb plus inverse square potential, respectively. Their energy eigenvalue expressions and numerical computations agreed with the literature.

Keywords: Schrödinger equation, Hulthen potential (HP), Generalized inverse quadratic Yukawa potential (GIQYP), Nikiforov-Uvarov method.

PACS: 03.65.−w, 03.65.Ca, 03.65.Ge.

1. Introduction

It is well established that the exact solutions of the Schrödinger equation contain all the necessary information for a quantum system. This is attributed to the fact that the eigenfunctions associated with these problems contain very pertinent information regarding the quantum systems under consideration [1-4].

Recently, researchers have showed great interest in the analytical solutions of the Schrödinger equation with some physical potential models by using different methods [5]; the asymptotic iteration method (AIM) [6,7], exact-quantization rules [8-10], the Nikiforov–Uvarov (NU) method [11–20], supersymmetric quantum mechanics (SUSYQM) [21], Wentzel-Kramers-Brillion and Jeffery (WKBJ) approximation method [22-24], the Nikiforov–Uvarov-functional analysis method (NUFA) [25,26],the series expansion method [27-30] and so on.

Hulthen potential is one of the important molecular potentials used in different areas of physics, such as nuclear and particle, atomic and condensed matter physics and chemical physics, to describe the interaction between two atoms [31].

Corresponding Author: C. O. Edet **Email**: collinsokonedet@gmail.com

Several works have been carried out on this potential. For instance, the asymptotic iteration method has been applied to obtain the solution of the Schrödinger equation with Hulthen potential [32-34].

The Klein-Gordon equation has previously been solved with a position-dependent mass [35, 36]. Authors in Ref. [37,38] solved the Schrödinger equation with Hulthen plus ringed-shaped potential and [31] solved the Schrödinger equation for the interaction of Coulomb and Hulthen potentials within the framework of supersymmetric approach and Nikiforov-Uvarov method.

The generalized inverse quadratic Yukawa potential (GIQYP) is a combination of the inverse quadratic Yukawa (IQY) and the Yukawa potentials. It is asymptotic to a finite value as $r \to \infty$ and becomes infinite at $r = 0$ [39].

In the present work, we attempt to investigate the bound-state solutions of the non-relativistic radial Schrödinger equation with the interaction of Hulthen plus Generalized Inverse Quadratic Yukawa potential:

$$V(r) = -\frac{V_0 e^{-2\alpha r}}{1-e^{-2\alpha r}} - V_1 U^2, \qquad (1a)$$

where V_1 is the coupling strength of the potential, α is the screening parameter, V_0 is the strength of the potential, $r(fm)$ is the radial distance to the particle and $U = 1 + \frac{e^{-\alpha r}}{r}$.

Hence, Eq. (1a) can be rewritten as:

$$V(r) = -\frac{V_0 e^{-2\alpha r}}{1-e^{-2\alpha r}} - C - \frac{B e^{-\alpha r}}{r} - \frac{A e^{-2\alpha r}}{r^2}, \qquad (1b)$$

where $A = C = V_1$ and $B = 2V_1$.

In Fig. 1a and Fig. 1b, we show the shape of the potential under study as it varies with r for different values of the adjustable screening parameter and for potentials: HP, GIQYP and HPGIQYP, respectively.

The work is organized as follows. We present a brief review of the Nikiforov-Uvarov method in Section 2, while in Section 3, this method is applied to obtain the bound-state solutions of the Hulthen plus Generalized Inverse Quadratic Yukawa potential (HPGIQYP). In Section 4, we deduce some special cases by adjusting some parameters of the potential and Section 5 presents the results and discussion. We use the Hellman-Feynmann theorem to calculate the expectation values of some physical observables in Section 6 and finally, our concluding remarks are captured in Section 7.

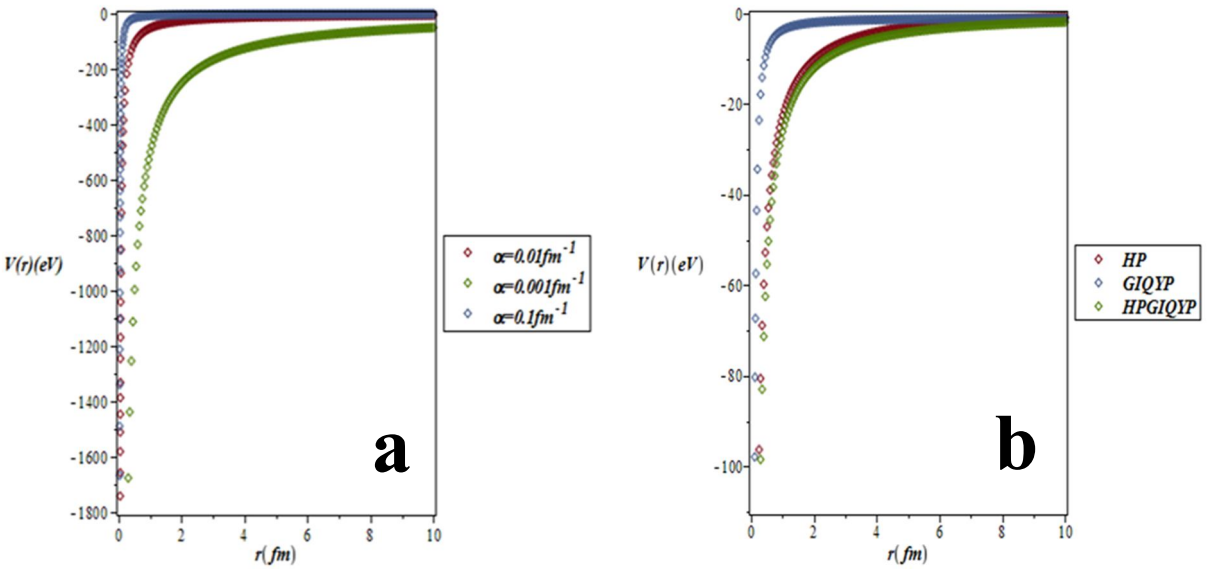

FIG. 1. **(a)** The shape of the Hulthen potential plus generalized inverse quadratic Yukawa potential for $V_0 = A = C = 1.00eV$ and $B = 2eV$ by varying values of α. **(b)** The shape of the Hulthen potential, generalized inverse quadratic Yukawa and Hulthen potential plus generalized inverse quadratic Yukawa potential for $V_0 = 5eV, A = C = 1.00eV, B = 2eV$ and $\alpha = 0.1fm^{-1}$.

2. Review of the Nikiforov-Uvarov Method

The Nikiforov-Uvarov (NU) method is based on solving hypergeometric-type second-order differential equations by means of special orthogonal functions [40]. The main equation which is closely associated with the method is given in the following form [40];

$$\psi''(z) + \frac{\tilde{\tau}(z)}{\sigma(z)}\psi'(z) + \frac{\tilde{\sigma}(z)}{\sigma^2(z)}\psi(z) = 0 \quad (2)$$

where $\sigma(z)$ and $\tilde{\sigma}(z)$ are polynomials at most second-degree, $\tilde{\tau}(z)$ is a first-degree polynomial and $\psi(z)$ is a function of the hypergeometric type.

The exact solution of Eq. (2) can be obtained by using the following transformation:

$$\psi(z) = \phi(z)y(z). \quad (3)$$

This transformation reduces Eq. (2) into a hypergeometric-type equation of the form:

$$\sigma(z)y''(z) + \tau(z)y'(z) + \lambda y(z) = 0. \quad (4)$$

The function $\phi(s)$ can be defined as the logarithm derivative:

$$\frac{\phi'(z)}{\phi(z)} = \frac{\pi(z)}{\sigma(z)} \quad (5)$$

where

$$\pi(z) = \frac{1}{2}[\tau(z) - \tilde{\tau}(z)] \quad (6)$$

with $\pi(z)$ being at most a first-degree polynomial. The second $\psi(z)$ being $y_n(z)$ in Eq. (3) is the hypergeometric function with its polynomial solution given by Rodrigues relation:

$$y^{(n)}(z) = \frac{B_n}{\rho(z)}\frac{d^n}{ds^n}[\sigma^n(z)\rho(z)] \quad (7)$$

Here, B_n is the normalization constant and $\rho(z)$ is the weight function which must satisfy the conditions:

$$(\sigma(z)\rho(z))' = \sigma(z)\tau(z); \quad (8)$$

$$\tau(z) = \tilde{\tau}(z) + 2\pi(z). \quad (9)$$

It should be noted that the derivative of $\tau(s)$ with respect to s should be negative. The eigenfunctions and eigenvalues can be obtained using the definition of the following function $\pi(s)$ and parameter λ, respectively:

$$\pi(z) = \frac{\sigma'(z)-\tilde{\tau}(z)}{2} \pm \sqrt{\left(\frac{\sigma'(z)-\tilde{\tau}(z)}{2}\right)^2 - \tilde{\sigma}(z) + k\sigma(z)} \quad (10)$$

where

$$k = \lambda - \pi'(z). \quad (11)$$

The value of k can be obtained by setting the discriminant of the square root in Eq. (10) equal to zero. As such, the new eigenvalue equation can be given as:

$$\lambda_n = -n\tau'(z) - \frac{n(n-1)}{2}\sigma''(z), n = 0,1,2, \ldots \quad (12)$$

3. Bound-state Solution with Hulthen and Generalized Inverse Quadratic Yukawa Potential

The radial Schrödinger equation can be given as [41]:

$$\frac{d^2R_{nl}}{dr^2} + \frac{2\mu}{\hbar^2}\left[E_{nl} - V(r) - \frac{\hbar^2\ell(\ell+1)}{2\mu r^2}\right]R_{nl} = 0, \quad (13)$$

where μ is the reduced mass, $E_{n\ell}$ is the energy spectrum, $\hbar$ is the reduced Planck's constant and n and l are the radial and orbital angular momentum quantum numbers, respectively (or vibration-rotation quantum number in quantum chemistry). Substituting Eq. (1b) into Eq. (13) gives:

$$\frac{d^2R_{nl}}{dr^2} + \frac{2\mu}{\hbar^2}\left[E_{nl} + \frac{V_0e^{-2\alpha r}}{1-e^{-2\alpha r}} + C + \frac{Be^{-\alpha r}}{r} + \frac{Ae^{-2\alpha r}}{r^2} - \frac{\hbar^2\ell(\ell+1)}{2\mu r^2}\right]R_{nl} = 0. \quad (14)$$

Employing the Greene and Aldrich approximation scheme [42], which is given by:

$$\frac{1}{r^2} = \frac{4\alpha^2e^{-2\alpha r}}{(1-e^{-2\alpha r})^2}. \quad (15)$$

Eq. (14) becomes;

$$\frac{d^2R_{nl}}{dr^2} + \frac{2\mu}{\hbar^2}\left[E_{nl} + \frac{V_0e^{-2\alpha r}}{1-e^{-2\alpha r}} + C + \frac{Be^{-\alpha r}}{r} + \frac{Ae^{-2\alpha r}}{r^2} - \frac{2\hbar^2\ell(\ell+1)\alpha^2e^{-2\alpha r}}{\mu(1-e^{-2\alpha r})^2}\right]R_{nl} = 0. \quad (16)$$

$$\frac{d^2R_{n\ell}(r)}{dr^2} + \frac{2\mu}{\hbar^2(1-e^{-2\alpha r})^2}\left[(E_{nl}+C)(1-e^{-2\alpha r})^2 + V_0e^{-2\alpha r}(1-e^{-2\alpha r}) + 2B\alpha e^{-2\alpha r}(1-e^{-2\alpha r}) + 4A\alpha^2e^{-4\alpha r} - \frac{2\hbar^2\ell(\ell+1)\alpha^2e^{-2\alpha r}}{\mu}\right]R_{n\ell}(r) = 0. \quad (17)$$

Eq. (17) can be simplified and introducing the following dimensionless abbreviations:

$$\left\{\begin{array}{c} -\varepsilon_n = \frac{\mu(E_{nl}+C)}{2\hbar^2\alpha^2} \\ \beta = \frac{\mu V_0}{2\hbar^2\alpha^2} \\ \gamma = \ell(\ell+1) \\ \delta = \frac{\mu B}{\hbar^2\alpha} \\ \eta = \frac{2\mu A}{\hbar^2} \end{array}\right\}, \quad (18)$$

and using the transformation $s = e^{-2\alpha r}$, we obtain:

$$\frac{d^2R_{n\ell}(r)}{dr^2} = 4\alpha^2 s^2 \frac{d^2R_{n\ell}(s)}{ds^2} + 4\alpha^2 s \frac{dR_{n\ell}(s)}{ds}. \quad (19)$$

Substituting Eqs. (18) and (19) into Eq. (17) yields:

$$\frac{d^2R_{n\ell}(s)}{ds^2} + \frac{1-s}{s(1-s)}\frac{dR_{n\ell}(s)}{ds} + \frac{1}{s^2(1-s)^2}[-s^2(\varepsilon_n + \beta + \delta - \eta) + s(2\varepsilon_n + \beta + \delta - \gamma) - \varepsilon_n]R_{n\ell}(s) = 0 \ . \quad (20)$$

By comparing Eqs. (20) and (2), we obtain the following parameters:

$$\left\{\begin{array}{c} \tilde{\tau}(s) = 1 - s \\ \sigma(s) = s(1-s) \\ \tilde{\sigma}(s) = -s^2(\varepsilon_n + \beta + \delta - \eta) \\ +s(2\varepsilon_n + \beta + \delta - \gamma) - \varepsilon_n \end{array}\right\}. \quad (21)$$

Substituting these polynomials into Eq. (21) gives:

$$\pi(s) = -\frac{s}{2} \pm \sqrt{(a-k)s^2 + (b+k)s + c}, \quad (22)$$

where:

$$\left\{\begin{array}{c} a = \frac{1}{4} + \varepsilon_n + \beta + \delta - \eta \\ b = -2\varepsilon_n - \beta - \delta + \gamma \\ c = \varepsilon_n \end{array}\right\}. \quad (23)$$

To find the constant k, the discriminant of the expression under the square root of Eq. (22) must be equal to zero. As such, we have that:

$$k_{\pm} = (\beta + \delta - \gamma) \pm 2\sqrt{\varepsilon_n\left(\frac{1}{4} + \gamma - \eta\right)}. \quad (24)$$

Substituting Eq. (24) into Eq. (22) yields:

$$\pi(s) = -\frac{s}{2} \pm \left[\left(\sqrt{\left(\frac{1}{4} + \gamma - \eta\right)} + \sqrt{\varepsilon_n}\right)s - \sqrt{\varepsilon_n}\right]. \quad (25)$$

From our knowledge of NU method, we choose the expression $\pi(s)$, where the function $\tau(s)$ has a negative derivative. This is given by:

$$k_{-} = (\beta + \delta - \gamma) - 2\sqrt{\varepsilon_n\left(\frac{1}{4} + \gamma - \eta\right)}. \quad (26)$$

From Eq. (9), the parameter $\tau(s)$ becomes:

$$\tau(s) = 1 - 2s - 2\left[\left(\sqrt{\left(\frac{1}{4} + \gamma - \eta\right)} + \sqrt{\varepsilon_n}\right)s - \sqrt{\varepsilon_n}\right]. \quad (27)$$

Referring to Eq. (11), the constant λ is obtained as:

$$\lambda = -\frac{1}{2} - \left(\sqrt{\left(\frac{1}{4} + \gamma - \eta\right)} + \sqrt{\varepsilon_n}\right) + (\beta + \delta - \gamma) - 2\sqrt{\varepsilon_n\left(\frac{1}{4} + \gamma - \eta\right)}. \quad (28)$$

Employing Eq. (12) and taking that:

$$\tau'(s) = -2 - 2\left(\sqrt{\left(\frac{1}{4} + \gamma - \eta\right)} + \sqrt{\varepsilon_n}\right) < 0 \quad (29)$$

and

$$\sigma''(s) = -2, \quad (30)$$

we have:

$$\varepsilon_n = \frac{1}{4}\left[\frac{\beta+\delta-\eta-\left(n+\frac{1}{2}+\sqrt{\frac{1}{4}+\gamma-\eta}\right)^2}{\left(n+\frac{1}{2}+\sqrt{\frac{1}{4}+\gamma-\eta}\right)}\right]^2. \quad (31)$$

Substituting Eq. (23) into Eq. (31) yields the energy eigenvalue equation of the Hulthen plus Generalized Inverse Quadratic Yukawa potential in the form:

$$E_{n\ell} = -C - \frac{\hbar^2\alpha^2}{2\mu}\left[\frac{\frac{\mu V_0}{2\hbar^2\alpha^2} + \frac{\mu B}{\hbar^2\alpha} - \frac{2\mu A}{\hbar^2}}{\left(n+\frac{1}{2}+\sqrt{\frac{1}{4}+\ell(\ell+1)-\frac{2\mu A}{\hbar^2}}\right)} - \left(n + \frac{1}{2} + \sqrt{\frac{1}{4} + \ell(\ell+1) - \frac{2\mu A}{\hbar^2}}\right)\right]^2. \quad (32)$$

The corresponding wave functions can be evaluated by substituting $\pi(s)\ and\ \sigma(s)$ from Eq. (25) and Eq. (21), respectively, into Eq. (5). Solving the first-order differential equation gives:

$$\Phi(s) = s^{\sqrt{\varepsilon_n}}(1-s)^{\frac{1}{2}+\sqrt{\frac{1}{4}+\gamma-\eta}}. \quad (33)$$

The weight function $\rho(s)$ from Eq. (8) can be obtained as:

$$\rho(s) = s^{2\sqrt{\varepsilon_n}}(1-s)^{2\sqrt{\frac{1}{4}+\gamma-\eta}} \quad . \tag{34}$$

From the Rodrigues relation of Eq. (7), we obtain:

$$y_n(s) \equiv N_{n,l} P_n^{\left(2\sqrt{\varepsilon_n}, 2\sqrt{\frac{1}{4}+\gamma-\eta}\right)}(1-2s), \tag{35}$$

where $P_n^{(\theta,\vartheta)}$ is the Jacobi polynomial.

Substituting $\Phi(s)$ *and* $y_n(s)$ from Eq. (33) and Eq. (35), respectively, into Eq. (3), we obtain the radial wave function as:

$$R_n(s) = N_{n,l} s^{\sqrt{\varepsilon_n}}(1-s)^{\frac{1}{2}+\sqrt{\frac{1}{4}+\gamma-\eta}} P_n^{\left(2\sqrt{\varepsilon_n}, 2\sqrt{\frac{1}{4}+\gamma-\eta}\right)}(1-2s). \tag{36}$$

4. Deductions from Eq. (32)

In this section, we take some adjustments of constants in Eq. (1b), noting that $A = C = V_1$ and $B = 2V_1$, to have the following cases:

a. Generalized Inverse Quadratic Yukawa Potential

If $V_0 = 0$, Eq. (1b) reduces to the Generalized Inverse Quadratic Yukawa potential:

$$V(r) = -V_1\left(1 + \frac{e^{-\alpha r}}{r}\right)^2. \tag{37}$$

and then Eq. (32) becomes:

$$E_{n\,\ell} = -V_1 - \frac{2\hbar^2\alpha^2}{\mu}\left[\frac{\frac{2\mu V_1}{\hbar^2}\left(\frac{1}{\alpha}-1\right) - \left(n+\frac{1}{2}(1+\varrho)\right)^2}{2\left(n+\frac{1}{2}(1+\varrho)\right)}\right]^2, \tag{38}$$

where

$$\varrho = \sqrt{(2\ell+1)^2 - \frac{8\mu V_1}{\hbar^2}}. \tag{39}$$

Eq. (38) is in full agreement with the results in Eq. (24) of [39].

b. Hulthen Potential

If $V_1 = 0$ and $V_0 = Ze^2\alpha$, Eq. (1b) reduces to the Hulthen potential:

$$\mathrm{V}(r) = -\frac{Ze^2\alpha\, e^{-2\alpha r}}{1-e^{-2\alpha r}}. \tag{40}$$

and Eq. (32) becomes:

$$E_{n\,\ell} = -\frac{\hbar^2\alpha^2}{2\mu}\left[\frac{\mu Ze^2}{\hbar^2\alpha(n+\ell+1)} - \frac{(n+\ell+1)}{2}\right]^2. \tag{41}$$

Eq. (41) is identical with the energy eigenvalues formula given in Eq. (32) of Ref. [26].

c. Coulomb Potential

If $A = C = V_1 = 0$, $\alpha \to 0$ and $V_0 = 0$, Eq. (1b) reduces to the Coulomb potential and the energy from Eq. (32) becomes:

$$E_{n\,\ell} = -\frac{\mu B^2}{2\hbar^2\left(n+\frac{1}{2}+\sqrt{\frac{1}{4}+\ell(\ell+1)}\right)^2} \tag{42}$$

Eq. (42) is very consistent with the result obtained in Eq. (101) of Ref. [29].

d. Kratzer Potential

If $\alpha \to 0$ and $V_0 = 0$ and if we set $A = -V_1$, $B = 2V_1$ and $C = -V_1$, then Eq. (1b) reduces to

$$V(r) = C - \frac{B}{r} + \frac{A}{r^2}. \tag{43}$$

Eq. (32) becomes:

$$E_{n\,\ell} = \mathrm{C} - \frac{\mu B^2}{2\hbar^2\left(n+\frac{1}{2}+\sqrt{\frac{1}{4}+\ell(\ell+1)+\frac{2\mu A}{\hbar^2}}\right)}. \tag{44}$$

Eq. (44) is very consistent with the result obtained in Eq. (125) of Ref. [29].

e. Inversely Quadratic Yukawa Potential

If $V_0 = 0$, $A = -V_1$, $B = 2V_1$, $C = V_1$ and $C = B = 0$, the potential Eq. (1b) reduces to the Inverse Quadratic Yukawa potential

$$V(r) = -\frac{Ae^{-2\alpha r}}{r^2}. \tag{45}$$

Eq. (32) becomes:

$$E_{n\,\ell} = -\frac{\hbar^2\alpha^2}{2\mu}\left[\frac{\frac{2\mu A}{\hbar^2}+\left(n+\frac{1}{2}+\sqrt{\frac{1}{4}+\ell(\ell+1)-\frac{2\mu A}{\hbar^2}}\right)^2}{\left(n+\frac{1}{2}+\sqrt{\frac{1}{4}+\ell(\ell+1)-\frac{2\mu A}{\hbar^2}}\right)}\right]^2. \tag{46}$$

Eq. (46) is identical to the results in; Eq. (37) of Ref. [33].

f. Coulomb Plus Inverse-Square Potential

If we set $C = 0$, $V_0 = 0$ and $\alpha \to 0$, Eq. (1b) reduces to the Coulomb plus Inverse-Square potentia

$$V(r) = -\frac{B}{r} + \frac{A}{r^2}. \tag{47}$$

Eq. (32) becomes:

$$E_{n\,\ell} = -\frac{\mu B^2}{2\hbar^2\left(n+\frac{1}{2}+\sqrt{\frac{1}{4}+\ell(\ell+1)+\frac{2\mu A}{\hbar^2}}\right)}. \tag{48}$$

5. Results and Discussion

In the present consideration, the energy eigenvalues of the Hulthen potential plus Generalized Inverse Quadratic Yukawa potential were computed using Eq. (32). The explicit values of these energies for different principal and angular quantum numbers are given in Table 2.

For comparison and validation of our results, we have also computed the energy eigenvalues of the Generalized Inverse Quadratic Yukawa potential using the energy equation given in Eq. (38) as a special case. The results in Table 1 show for energy eigenvalue of GIYQP that for a fixed value of the azimuthal quantum number l, the energy spectrum increases slowly with an increase in the principal quantum number n; for small adjustable screening parameter α for weak potential coupling strength V_1 in the range 0.5 – 1.0 fm^{-1}, which is in good agreement with the results in Table 1 of Ref. [39]. In Table 2 (which shows the results of our work), the energy eigenvalues of HPGIYQP are shown. We have observed that, as the state (n, l) increases (i.e., from ground state to first excited state, second excited state … etc.), there is a slow increase in the energy eigenvalues. But when the coupling strengths of the potential increase in a particular potential range, there is a rapid decrease in the energy eigenvalues in any state. More so, it is seen that the energy eigenvalues are very sensitive to the potential range (screening parameter) as they decrease more rapidly as the screening parameter decreases in all states.

However, Figs. 2a-2c give graphical expressions of Table 2, re-affirming the above observations. Fig. 2d shows the dependence of energy on the screening parameter for p-wave which is consistent with the above observations. The relationship between the energy spectrum and the screening parameter is an exponential increasing function. So, for screening parameter $0.02 < \alpha < 1.0eV$, there are exponential increases in the energy spectrum. Finally, Fig. 2e and Fig. 2f present the relationships of dependence of the energy spectrum on the potential strength V_0 and the coupling strength V_1. Both curves establish a decaying exponential relationship. Figs. 2e and 2f show that the highest energy possible for all states is when $V_0 = 0\ eV$, after which as V_0 increases, the energy eigenvalue curves for different states fall towards zero.

6. Hellmann-Feynman Theorem (HFT)

This theorem is so invaluable for obtaining the expectation values of physical observables for any value of the principal and angular momentum quantum numbers n, l. This can however be achieved if the Hamiltonian H of a given quantum system is known. So, the theory states that [43] if the Hamiltonian $H(q)$ of a physical system, the energy eigenvalues $E(q)$ and eigenfunction $\psi(q)$ all depend on the parameter q, then:

$$\frac{\partial E_{nl}(q)}{\partial q} = \langle \psi_{nl}(q) \left| \frac{\partial \hat{H}(q)}{\partial q} \right| \psi_{nl}(q) \rangle, \tag{49}$$

provided that the $\psi_{nl}(q)$ associated normalized eigenfunction is continuous with respect to q. However, the effective Hamiltonian containing the potential which corresponds to the non-relativistic spectrum given by Eq. (32) is:

$$\hat{H} = -\frac{\hbar^2}{2\mu}\frac{d^2}{dr^2} + \frac{\hbar^2}{2\mu r^2} l(l+1) - \frac{V_0 e^{-2\alpha r}}{1-e^{-2\alpha r}} - A - \frac{Be^{-\alpha r}}{r} - \frac{Ce^{-2\alpha r}}{r^2} \tag{50}$$

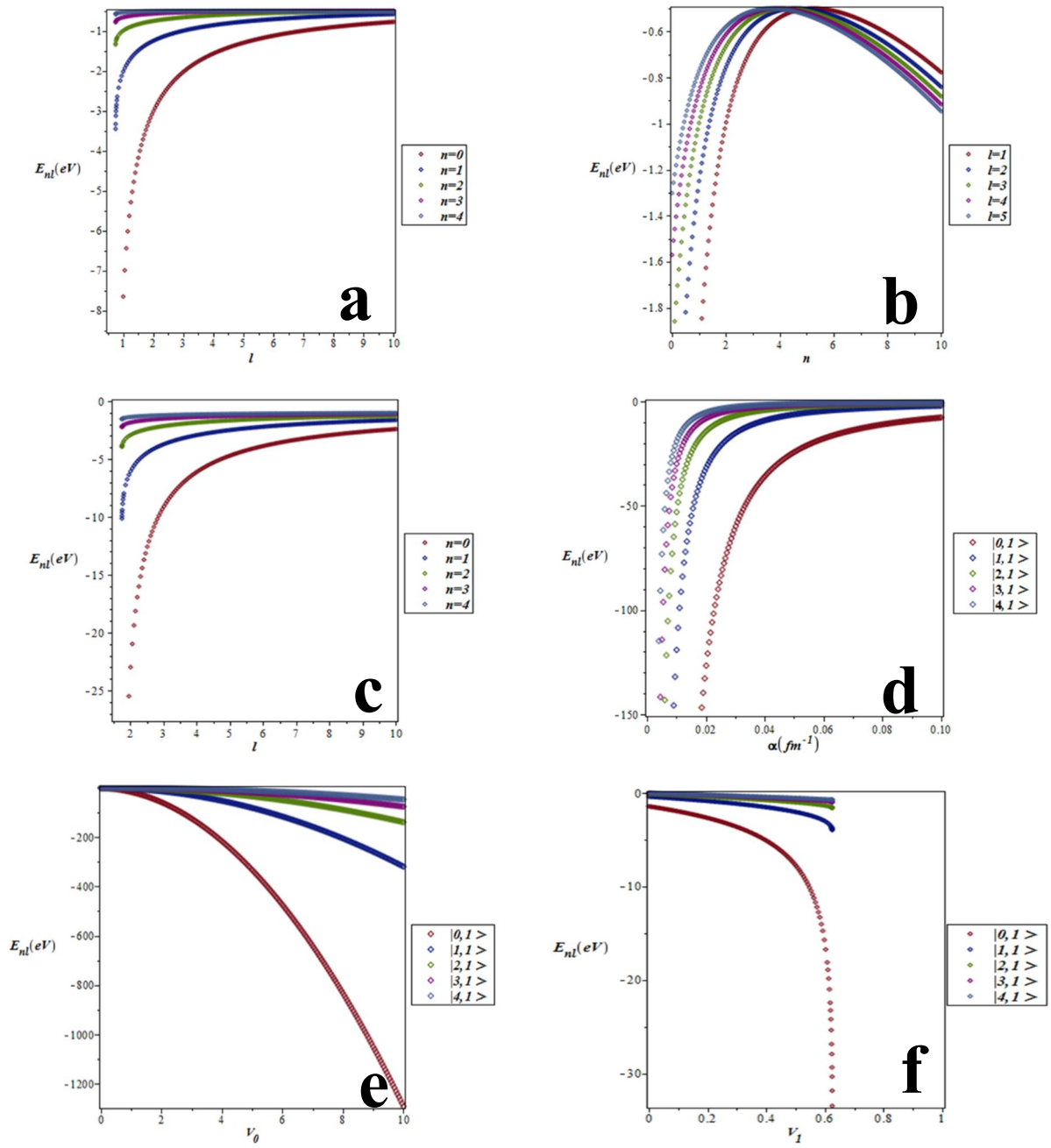

FIG. 2. Energy eigenvalues of the non-relativistic Hulthen potential plus generalized inverse quadratic Yukawa potential against **(a)** ℓ for various values of n. $V_0 = 0.6\text{fm}^{-1}$, $V_1 = 0.5\text{fm}^{-1}$ and $\alpha = 0.1fm^{-1}$, **(b)** against n for various values of ℓ. $V_0 = 0.6\ \text{fm}^{-1}$, $V_1 = 0.5\text{fm}^{-1}$ and $\alpha = 0.1fm^{-1}$, **(c)** against ℓ for various values of n. $V_0 = 1\text{fm}^{-1}$, $V_1 = 1\text{fm}^{-1}$ and $\alpha = 0.1fm^{-1}$, **(d)** against α for various values of "n and ℓ". $V_0 = 0.6\text{fm}^{-1}$, $V_1 = 0.5\text{fm}^{-1}$, **(e)** against V_0 for various values of "n and ℓ".,$V_1 = 0.5\ \text{fm}^{-1}$ and **(f)** against V_1 for various values of "n and ℓ". $V_0 = 0.6\text{fm}^{-1}$.

TABLE 1. The bound-state energy levels (in units of fm^{-1}) of the GIQYP for various values of n, l and for $\hbar = \mu = 1$, noting that $A = C = V_1$ and $B = 2V_1$.

n	l	E_{nl} $V_1 = 0.5, \alpha = 0.001$	PQR[23]	E_{nl} $V_1 = 1, \alpha = 0.001$	PQR[23]	E_{nl} $V_1 = 0.5, \alpha = 0.01$	PQR[23]	E_{nl} $V_1 = 1, \alpha = 0.01$	PQR[23]
0	1	-0.6896035397	−0.6896035396138025	-2.9940045000	−2.994004500000000	-0.6774133456	−0.6774133455125515	-2.9404500000	−2.940450000000000
1	1	-0.5718076188	−0.5718076188414074	-1.4970045000	−1.497004500000000	-0.5619400366	−0.5619400365376546	-1.4704500000	−1.470450000000000
2	1	-0.5371277912	−0.5371277912043335	-1.2197845000	−1.219784500000000	-0.5281909973	−0.5281909972598103	-1.1984500000	−1.198450000000000
3	1	-0.5224100938	−0.5224100938146438	-1.1227601250	−1.122760125000000	-0.5141450483	−0.5141450483150030	-1.1035125000	−1.103512500000000
0	2	-0.5630508544	−0.5630508543825075	-1.3022018720	−1.302201872184403	-0.5533867400	−0.5533867400061118	-1.2792683390	−1.279268338661399
1	2	-0.5337240097	−0.5337240097533026	-1.1553639390	−1.155363939225181	-0.5249118233	−0.5249118232916035	-1.1353673650	−1.135367365171019
2	2	-0.5207493205	−0.5207493205425896	-1.0939382320	−1.093938232041968	-0.5125947737	−0.5125947736790960	-1.0754456090	−1.075445608618366
3	2	-0.5138959793	−0.5138959792881225	-1.0625485320	−1.062548531648839	-0.5063882922	−0.5063882922242523	-1.0451201250	−1.045120125270810
0	3	-0.5326018749	−0.5326018749170197	-1.1436858170	−1.143685816860237	-0.5238335921	−0.5238335921350012	-1.1239490570	−1.123949057454857
1	3	-0.5201906957	−0.5201906956637058	-1.0883107370	−1.088310737089324	-0.5120761646	−0.5120761646075057	-1.0699832630	−1.069983262515873
2	3	-0.5135787736	−0.5135787736130005	-1.0594189440	−1.059418943879603	-0.5061129918	−0.5061129917794308	-1.0421247450	−1.042124745183449
3	3	-0.5096463319	−0.5096463318898519	-1.0424680190	−1.042468019323530	-0.5028802558	−0.5028802557635820	-1.0260919330	−1.026091932802665
0	4	-0.5199025668	−0.5199025668480347	-1.0856649680	−1.085664968464422	-0.5118093031	−0.5118093030597658	-1.0674179890	−1.067417988764047
1	4	-0.5134143289	−0.5134143288870058	-1.0579298620	−1.057929861731356	-0.5059709011	−0.5059709010589428	-1.0407023850	−1.040702385388879
2	4	-0.5095438531	−0.5095438530724833	-1.0415487330	−1.041548732718895	-0.5028023247	−0.5028023247194076	-1.0252361230	−1.025236123010328
3	4	-0.5070530264	−0.5070530264169021	-1.0310763970	−1.031076397206152	-0.5010876689	−0.5010876689076859	-1.0156716870	−1.015671686891542

TABLE 2. The bound-state energy levels (in units of fm^{-1}) of the HPGIQYP for various values of n, l and for $\hbar = \mu = 1$.

n	l	E_{nl} $V_1 = 0.5, V_0 = 0.6,$ $\alpha = 0.1$	E_{nl} $V_1 = 1, V_0 = 1,$ $\alpha = 0.1$	E_{nl} $V_1 = 0.5, V_0 = 0.6,$ $\alpha = 0.01$	E_{nl} $V_1 = 1, V_0 = 1,$ $\alpha = 0.01$
0	1	-3.02794168	-23.4450000	-183.6065088	-1351.440450
1	1	-1.25382506	-6.12000000	-70.24922680	-338.2204500
2	1	-0.75642115	-2.93388889	-36.87401010	-150.5873389
3	1	-0.57323417	-1.84500000	-22.70756380	-84.91601250
0	2	-0.50160252	-2.93388889	-47.30232586	-150.58733890
1	2	-0.50884962	-1.84500000	-27.50904441	-84.91601250
2	2	-0.54151791	-1.36980000	-18.00072816	-54.51985800
3	2	-0.59051577	-1.14222222	-12.71389828	-38.00867222
0	3	-0.56948304	-1.54875057	-22.36746921	-66.28180714
1	3	-0.50775385	-1.22868582	-15.21644814	-44.64029952
2	3	-0.50313291	-1.07529324	-11.04000634	-32.15364428
3	3	-0.53270349	-1.01122095	-8.391149730	-24.30197400
0	4	-0.58486300	-1.14222222	-13.13851287	-38.00867222
1	4	-0.64567506	-1.03683674	-9.744735670	-28.05326632
2	4	-0.71825487	-1.00125000	-7.530023660	-21.59215312
3	4	-0.80186936	-1.01043210	-6.005476110	-17.16277099

a. Expectation Value $< r^{-2} >$

Here, we let $q = l$ in Eq. (49).

$$\frac{\partial E_{nl}(l)}{\partial l} = \langle \psi_{nl}(q) \left| \frac{\partial \hat{H}(l)}{\partial l} \right| \psi_{nl}(l) \rangle \quad (51)$$

Taking the partial derivative of Eq. (32) with respect to l, we have:

$$\frac{\partial E_{nl}(l)}{\partial l} = -\frac{2\hbar^2\alpha^2}{2\mu}(2l+1)\left[\frac{\sigma}{n+\frac{1}{2}+\lambda} - n + \frac{1}{2} + \lambda\right]\left[-\frac{\sigma}{2\lambda\left(n+\frac{1}{2}+\lambda\right)^2} - \frac{1}{2\lambda}\right] \quad (52)$$

where

$$\sigma = \frac{\mu V_0}{2\hbar^2\alpha^2} + \frac{\mu B}{\hbar^2\alpha} - \frac{2\mu C}{\hbar^2}$$
$$\lambda = \sqrt{\frac{1}{4} + l(l+1) - \frac{2\mu C}{\hbar^2}} \quad (53)$$

and

$$\langle \psi_{nl}(q) \left| \frac{\partial \hat{H}(l)}{\partial l} \right| \psi_{nl}(l) \rangle = \frac{\hbar^2}{2\mu}(2l+1)\langle r^{-2} \rangle \quad (54)$$

Then, on equating Eq. (52) and Eq. (54), we find:

$$\langle r^{-2} \rangle = \frac{\alpha^2}{\lambda}\left[\frac{\sigma}{n+\frac{1}{2}+\lambda} - n + \frac{1}{2} + \lambda\right]\left[\frac{\sigma}{\left(n+\frac{1}{2}+\lambda\right)^2} + 1\right]. \quad (55)$$

b. Expectation Value $< r^{-1} >$

Letting $q = B$, in Eq. (49), and taking the partial derivative of Eq. (32) with respect to B,

$$\frac{\partial E_{nl}(B)}{\partial B} = -\frac{2\hbar^2\alpha^2}{2\mu}\frac{\frac{\mu}{\hbar^2\alpha}}{n+\frac{1}{2}+\lambda}\left[\frac{\sigma}{n+\frac{1}{2}+\lambda} - n + \frac{1}{2} + \lambda\right] \quad (56)$$

Similarly,

$$\langle \psi_{nl}(B) \left| \frac{\partial \hat{H}(B)}{\partial B} \right| \psi_{nl}(B) \rangle = -e^{-\alpha r}\langle r^{-1} \rangle. \quad (57)$$

Then, on equating Eq. (56) and Eq. (57), we obtain:

$$\langle r^{-1} \rangle = \frac{2\hbar^2\alpha^2}{2\mu}\frac{\frac{\mu}{\hbar^2\alpha}}{n+\frac{1}{2}+\lambda}e^{\alpha r}\left[\frac{\sigma}{n+\frac{1}{2}+\lambda} - n + \frac{1}{2} + \lambda\right]. \quad (58)$$

c. Expectation Values $< p^2 >$ **and** $< T >$ **or the Viral Theorem**

Here, we take the partial derivative of Eq. (32) with respect to μ to obtain:

$$\frac{\partial E_{nl}(\mu)}{\partial \mu} = -\frac{\hbar^2\alpha^2}{2\mu}\left[\frac{\left(n+\frac{1}{2}+\lambda\right)\left(\frac{V_0}{2\hbar^2\alpha^2} + \frac{B}{\hbar^2\alpha} - \frac{2C}{\hbar^2}\right)}{n+\frac{1}{2}+\lambda} + \sigma\frac{2C}{2\hbar^2\lambda}}{\left(n+\frac{1}{2}+\lambda\right)^2} + \sigma\frac{2C}{2\hbar^2\lambda}\right] + \frac{\hbar^2\alpha^2}{2\mu^2}\left[\frac{\sigma}{n+\frac{1}{2}+\lambda} - n + \frac{1}{2} + \lambda\right] \quad (59)$$

and

$$\langle \psi_{nl}(\mu) \left| \frac{\partial \hat{H}(\mu)}{\partial \mu} \right| \psi_{nl}(\mu) \rangle = -\frac{1}{\mu}\left(\frac{\hbar^2}{2\mu}\frac{d^2}{dr^2} - \frac{\hbar^2}{2\mu r^2}l(l+1)\right) = -\frac{1}{\mu}\left[\hat{H} - V\right] = -\frac{1}{\mu}\langle T \rangle \quad (60)$$

So, on equating Eq. (59) and Eq. (60), we obtain:

$$\langle T \rangle = \frac{\hbar^2\alpha^2}{2}\left[\frac{\frac{\left(n+\frac{1}{2}+\lambda\right)\left(\frac{V_0}{2\hbar^2\alpha^2} + \frac{B}{\hbar^2\alpha} - \frac{2C}{\hbar^2}\right)}{n+\frac{1}{2}+\lambda} + \sigma\frac{2C}{2\hbar^2\lambda}}{\left(n+\frac{1}{2}+\lambda\right)^2} + \sigma\frac{2C}{2\hbar^2\lambda}\right] - \frac{\hbar^2\alpha^2}{2\mu}\left[\frac{\sigma}{n+\frac{1}{2}+\lambda} - n + \frac{1}{2} + \lambda\right]. \quad (61)$$

But,

$$-\frac{1}{\mu}\langle T \rangle = -\frac{1}{2\mu^2}\langle p^2 \rangle. \quad (62)$$

So,

$$\langle p^2 \rangle = \mu\hbar^2\alpha^2\left[\frac{\frac{\left(n+\frac{1}{2}+\lambda\right)\left(\frac{V_0}{2\hbar^2\alpha^2} + \frac{B}{\hbar^2\alpha} - \frac{2C}{\hbar^2}\right)}{n+\frac{1}{2}+\lambda} + \sigma\frac{2C}{2\hbar^2\lambda}}{\left(n+\frac{1}{2}+\lambda\right)^2} + \sigma\frac{2C}{2\hbar^2\lambda}\right] - \hbar^2\alpha^2\left[\frac{\sigma}{n+\frac{1}{2}+\lambda} - n + \frac{1}{2} + \lambda\right]. \quad (63)$$

7. Conclusion

In this study, we have presented the approximate analytical bound-state solutions of the Schrödinger equation for an interaction of the Hulthen potential with the Generalized Inverse Quadratic Yukawa potential obtained within the Nikiforov-Uvarov framework. The corresponding energy eigenvalues and eigenfunctions were computed for different quantum states and the adjustable screening parameter was obtained. Expectation values of some physical observables have also been calculated using the Hellmann-Feynmann Theorem (HFT). Further, special cases of our potential have been discussed and for limiting cases, our results conform to those of available literature.

References

[1] Inyang, E.P., William, E.S. and Obu, J.A., Rev. Mex. Fis., 67 (2021) 193.

[2] Inyang, E.P., Ntibi, J.E., Inyang, E.P., Ayedun, F., Ibanga, E.A., Ibekwe, E.E. and William, E.S., Appl. J. Phys. Sci., 3 (2021) 92.

[3] Akpan, I.O., Inyang, E.P., Inyang, E.P. and William, E.S., Rev. Mex. Fis., 67 (2021) 490.

[4] Inyang, E.P., Ntibi, J.E., Ibanga, E.A., Ayedun, F., Inyang, E.P., Ibekwe, E.E., William, E.S. and Akpan, I.O., Comm. Phys. Sci., 7 (2021) 114.

[5] Ikot, A.N., Okorie, U.S., Ngiangia, A.T., Onate, C.A., Edet, C.O., Akpan, I.O. and Amadi, P.O., Eclet. Quím. J., 45 (2020) 65.

[6] Inyang, E.P., Inyang, E.P., William, E.S. and Ibekwe, E.E., Jordan. J. Phys., 14 (2021) 345.

[7] Edet, C.O., Okorie, U.S., Ngiangia, A.T. and Ikot, A.N., Indian J. Phys., 94 (2019) 425.

[8] Edet, C.O., Okorie, K.O., Louis, H. and Nzeata-Ibe, N.A., Indian J. Phys., 94 (2020) 243.

[9] Louis, H., Ita, B.I., Akakuru, O.U., Nzeata-Ibe, N.A., Ikeuba, A.I., Magu, T.O., Amos, P.I. and Edet, C.O., Oriental J. Phys. Sci., 3 (2018) 1.

[10] Inyang, E.P., Inyang, E.P., William, E.S., Ibekwe, E.E. and Akpan, I.O., (2020). http://arxiv.org/abs/2012.10639.

[11] Okoi, P.O., Edet, C.O. and Magu, T.O., Rev. Mex. Fis., 66 (2020) 1.

[12] Inyang, E.P., William, E.S., Obu, J.O., Ita, B.I., Inyang, E.P. and Akpan, I.O., Mol. Phys., 119 (2021) e1956615. https://doi.org/10.1080/00268976.2021.1956615.

[13] Inyang, E.P., William, E.S., Omugbe, E., Inyang, E.P., Ibanga, E.A., Ayedun, F., Akpan, I.O. and Ntibi, J.E., Rev. Mex. Fis., 68 (2022) 14.

[14] Inyang, E.P., Iwuji, P.C., Ntibi, J.E., Omugbe, E., Ibanga, E.A. and William, E.S., East Eur. J. Phys., 2 (2022) 51.

[15] Edet, C.O., Amadi, P.O., Onyeaju, M.C., Okorie, U.S., Sever, R. and Rampho, G.J., J. Low Temp. Phys., 12 (2020) 23.

[16] Inyang, E.P., Ita, B.I. and Inyang, E.P., Eur. J. Appl. Phys., 3 (2021) 47.

[17] William, E.S., Okon, I.B., Ekerenam, O.O., Akpan, I.O., Ita, B.I., Inyang, E.P., Etim, I.P. and Umoh, I.F., Intl. J. Quan. Chem., (2022) e26925.

[18] William, E.S., Obu, J.A., Akpan, I.O., Thompson, E.A. and Inyang, E.P., Eur. J. Appl. Phys., 2 (2020) 28.

[19] William, E.S., Inyang, E.P., Akpan, I.O., Obu, J.A., Nwachukwu, A.N. and Inyang, E.P., Indian J. Phys., (2022). https://doi.org/10.1007/s12648-0222-02308-0.

[20] Edet, C.O., Okoi, P.O., Yusuf, A.S., Ushie, P.O. and Amadi, P.O., Indian J. Phys., 10 (2020) 45.

[21] William, E.S., Inyang, E.P. and Thompson, E.A., Rev. Mex. Fis., 66 (2020) 730.

[22] Edet, C.O., Okoi, P.O., Yusuf, A.S., Ushie, P.O. and Amadi, P.O., Indian J. Phys., 95 (2021) 471.

[23] Omugbe, E., Osafile, O.E., Okon, I.B., Inyang, E.P., William, E.S. and Jahanshir, A., Few-Body Syst., 63 (2022) 7.

[24] Omugbe, E., Osafile, O.E., Okon, I.B., Eyube, E.S., Inyang, E.P., Okorie, U.S., Jahanshir, A. and Onate, C.A., Eur. Phys. J. D., 76:72 (2022) 11.

[25] Inyang, E.P., Inyang, E.P., Akpan, I.O., Ntibi, J.E. and William, E.S., Can. J. Phys., 99 (2021) 990. https://doi.org/10.1139/cjp-2020-0578.

[26] Inyang, E.P., Inyang, E.P., Ntibi, J. E., Ibekwe, E. E. and William, E. S., Indian J. Phys., 95 (2021) 2739. https://doi.org/10.1007/s12648-020-01933-x

[27] Inyang, E.P., Inyang, E.P., Akpan, I.O., Ntibi, J.E. and William, E.S., Eur. J. Appl. Phys., 2 (2020) 26.

[28] Inyang, E.P., Inyang, E.P., Kamiliyus J., Ntibi, J.E. and William E.S., Eur. J. Appl. Phys., 3 (2021) 55.

[29] Inyang, E.P., Inyang, E.P., Ntibi, J.E. and William, E.S., Bul. Pure and Appl. Sci., 40 (2021) 24.

[30] Ibekwe, E.E., Okorie, U.S., Emah, J.B., Inyang, E.P. and Ekong, S.A., Eur. Phys. J. Plus., 87 (2021) 136.

[31] Ita, B.I., Louis, H., Akakuru, O.U., Nzeata-Ibe, N.A., Ikeuba, A.I., Magu, T.O., Amos, P.I. and Edet, C.O., Bulg. J. Phys., 45 (2018) 323.

[32] Edet, C.O., Amadi, P.O., Onyeaju, M.C., Okorie, U.S., Sever, R., Rampho, G.J., Abdullah, H.Y., Salih, I.H. and Ikot, A.N., Journal of Low Temperature Physics, 202 (2021) 83.

[33] Edet, C.O., Amadi, P.O., Okorie, U.S., Tas, A., Ikot, A.N. and Rampho, G., Rev. Mex. Fıs., 66 (2020) 824.

[34] Okorie, U.S., Edet, C.O., Ikot, A.N., Rampho, G.J. and Sever, R., Indian J. Phys., 95 (2021) 411.

[35] Ikhdair, S.M. and Sever, R., Phys. Scr., 79 (2009) 035002.

[36] Ikhdair, S.M., Eur. Phys. J. A, 39 (2009) 307.

[37] Hassanabadi, H., Zarrinkamar, S. and Rahimov, H., Commun. Theor. Phys., 56 (2011) 423.

[38] Agboola, D., Phys. Scr., 80 (2009) 065304.

[39] Oluwadare, O.J. and Oyewumi, K.J., Chin. Phys. Lett., 34 (2017) 110301.

[40] Nikiforov, S.K. and Uvarov. V.B., "Special Functions of Mathematical Physics", (Birkhauser, Basel, 1988)

[41] Edet, C.O., Ikot, A.N., Onyeaju, M.C., Okorie, U.S., Rampho, G.J., Lekala, M.L. and Kaya, S., Physica E, 131 (2021) 114710.

[42] Greene, R.L. and Aldrich, C., Phys. Rev. A., 14 (1976) 2363.

[43] Okon, I.B., Popoola, O. and Isonguyo, C.N., Advances in High-Energy Physics, 20 (2017) 9671816.

Volume 15, Number 2, 2022. pp. 149-160

Jordan Journal of Physics

ARTICLE

BALQARAD Geant4 Model: Enhancement in γ-ray Spectroscopy and Validation

E. Ababneh[a], **S. Al-Amarat**[a], **S. Okoor**[b] , **M. M. Imran**[a] and **S. Dababneh**[a]

[a] *Department of Physics, Faculty of Science, Al-Balqa Applied University, Salt 19117, Jordan.*

[b] *Physics Department, Yarmouk University, Irbid 21163, Jordan.*

Doi: **https://doi.org/10.47011/15.2.5**

Received on: 12/10/2020; *Accepted on: 12/01/2021*

Abstract: Advances in gamma-ray spectroscopy allow for excellent background suppression and increased efficiency using composite Clover detectors with combinations of active shields. The events from such combinations, registered in list mode and analyzed offline, promote significant sensitivity improvements for gamma detection. This study utilizes the modularity of such composite of high-purity germanium radiation detectors to investigate their applicability in different possible fields. A comprehensive survey is conducted on the appropriate radioactive isotope serving each application. According to its decay scheme, investigation on the proper modes of operation for each isotope is carried out by Monte Carlo simulation applied to the Clover detector geometry. Addback factor measurements were performed using the newly acquired BALQARAD Clover. In an offline analysis through self-developed software, the Clover direct and addback performances are deduced *versus* gamma-ray energy. Measurement results obtained using the Clover detectors agree reasonably well with those obtained by Monte Carlo simulation.

Keywords: Geant4, HPGe, Clover-type detector, Detector modeling and simulation, Modes of operation, Addback factor.

Introduction

While standard gamma-ray spectrometry is commonly used to satisfy various requirements, many significant applications involving highly sensitive detection and gamma-ray measurement are hampered by ambient backgrounds and need enhanced signal-to-background ratios. Therefore, due to crystal size restriction, poor time characteristics and large Doppler broadening of the energy spectrum, standard spectroscopy is not well-suited for such applications. Nowadays, the increasing number of stations around the world for radiation detection equipment, mainly gamma-ray detectors, reflects the public interest in radioactive wastes and other contaminations in the surrounding environment. Recent advances using composite and segmented HPGe Clover detectors as active shields in conjunction with scintillators provide high degrees of versatility for various kinds of ambient, cosmic and sample relevant to background suppression. Besides, attempts to maximize efficiency by measuring at close geometry with standard setups are combined with severe associated effects, like summing, and limiting the measurement's accuracy. Combined with extensive Monte Carlo simulations, the essential corrections due to self-absorption, extended source and true coincidence summing can be reliably obtained, allowing for accurate measurement combined with high efficiency. Therefore, in addition to national security applications, food and water radiological

Corresponding Author: E. Ababneh **Email**: eshraq.ababneh@bau.edu.jo

protection, energy and natural resource applications, many environmental radioactivity measurements are foreseen to benefit from such a sensitive system.

Continued global research dedicated to the detection of low activities and yields by specific gamma signatures is reported in various literature articles [1-5], which revealed steady improvements through the use of arrays of Ge detectors in resolving power, efficiency and high ratio of full-energy to partial-energy events.

Researchers were motivated to investigate further the early encouraging results of using Clover HPGe detectors in several applications and fields. Dababneh *et al.,* (2004) examined the benefits and disadvantages of different modes of operation. An experimental approach for determining the summing correction factor was formulated for the setup of two Clover HPGe detectors of the Karlsruhe Research Center in Germany [6]. Besides, in 2014, Dababneh *et al.,* reported on a setup of Clover HPGe detector in coincidence with specified energy windows in BGO counters covering a large solid angle and combined with large plastic veto counters, which led to a significantly improved sensitivity that allows for clear identification of specific γ-transitions [7]. Different modes of operation have been tested for optimizing the final experimental setup. Sarmiento *et al*. used an experimental setup consisting of composite Ge and strongly segmented Si detectors in 2012 to investigate the nuclear structure of the heaviest elements [8]. A comparison between the simulated detector response of complex decay modes and the experimental data was constructed. A contrast was constructed between the simulated detector response of complex modes of decay and the experimental data [8]. The results provided an excellent testing scenario for new gating and triggering possibilities. Furthermore, a Canberra CryoPulse 5 high-purity germanium (HPGe) semiconductor detector was used to classify and quantify the isotopes that emit gamma in ports and waterways [9]. An experimental setup consisting of 8 segmented Clover HPGe detectors [10] has also investigated collective excitation and single-particle state interaction. For any composite detector, the full detection mode is calculated by simultaneously testing direct and addback modes. The addback mode's advantage arises when the escaped events from one crystal may be recorded in the other crystals. This substantially increases the contribution to the full-energy peak (FEP) efficiency and reduces the Compton continuum [11].

Despite the above research efforts, when complex isotopes are involved in the decay mode or complicated calculation methods, many measurement difficulties can arise. It is worth mentioning here that there is no widely used integrated measurement method with well-defined calculation techniques. This study aims to perform a comprehensive analysis and review of different radioactive elements, analyze the application used and analyze preferable modes of operation based on the isotope decay scheme. This can be carried out with a validated and well-controlled measurement method *via* a newly acquired active shielded Clover detector named BALQARAD Clover, located at Saed Dababneh Laboratory (SDL) for Radiation Measurements at Al-Balqa Applied University in Salt, Jordan. The BALQARAD Clover, to the best of our knowledge, is the first of its kind in the Middle East and in the Arab world. A model was developed by Geant4 code for the Clover and then validated after comparison was performed between experimental and simulated data using various radioactive point sources. Finally, for the BALQARAD Clover, the addition factor as a function of gamma energy was also calculated.

Materials and Methods

Clover Detector Setup

The BALQARAD detection system is a composite detection array consisting of four high-purity germanium crystals of the N-type arranged as Clover-shaped and different scintillator types. Each crystal's size is 60 mm in diameter and 60 mm in length and each crystal has a relative efficiency of 40%. For the BALQARAD Clover, a highly segmented active shield is specifically designed and consists of several BGO ($Bi_4Ge_3O_{12}$) and CsI(TI) scintillators surrounding the Clover (front, side and back scintillators). Large plastic scintillator panels fixed on top, right and left sides of the setup were used to select or reject particular Clover signals according to different criteria, mainly reducing cosmic-ray backgrounds. Each of Ge crystals and active shields provides energy-time information recorded event-by-event in the list file.

Modes of Operation

Different modes of operation are used for counting and analyzing the data. The perfect mode used for sample characterization depends on the decay scheme of the studied nuclide, the energies of gamma being analyzed and other nuclides in the sample that may interfere with the analysis being performed. As a result of the addback mode, events that are registered within a given timing window and then added together are considered. By adding Compton's energies scattered among all the crystals, the full-energy peak is populated by more events and the Compton continuum is reduced. Therefore, less background continuum at low energy will be provided in the spectrum. If two or more photons are emitted simultaneously and detected in separate crystals, the addback mode integrates these energies before binning them into the spectrum. This true coincidence summing is the drawback of using the addback mode. Thus, when studying radionuclides with cascade gammas in the addback mode, careful consideration must be taken. When each of the crystals is treated as a separated detector, then the operation is called direct mode. In this mode, each signal is registered separately and then the number of counts is added together, channel by channel, into the final direct mode spectrum summed up. Due to the solid angle, the direct mode is not oversensitive to true coincidence summing, although Compton's continuum is much higher.

Geant4 Model of the Clover Crystals

Monte Carlo simulation has been conducted to investigate the BALQARAD detection system's characteristics in various operation modes for different isotopes. Therefore, the experimental setup shown in Fig. 1 was modeled using the toolkit Geant4 [12] and extensive simulation runs were performed. The detector's model geometry consisted of the four Ge crystals, the scintillators surrounding them, the front shield of the BGO, the side shield of the BGO and the back catcher of the CsI, as well as the canisters containing these components. The lead shield and the source housings have also been modeled. It is worth mentioning here that the validation of the scintillation detectors output of the BALQARAD system will not be included in the current study.

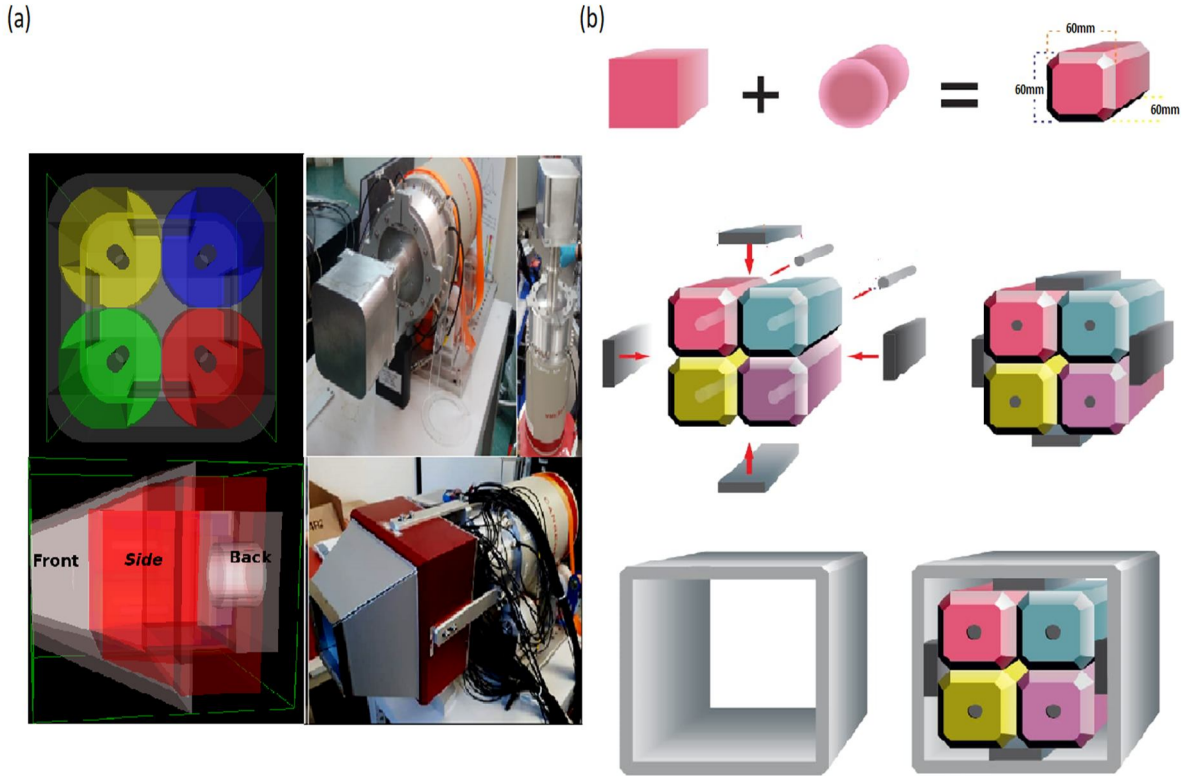

FIG. 1. The BALQARAD active shielded Clover detector at Al-Balqa Applied University in Jordan. (a) Right panel: side pictures of the Clover and the active shield of the system. Left panel: The Monte Carlo model prepared using Geant4 showing the different components of the active shield and the Clover four crystals. (b) Sketch of the Boolean structure of the Clover crystals, which was constructed by detailed Geant4 simulation.

In the design, four germanium crystals were specified; each one was separately identified. Each crystal is a composite of many geometric shapes designed and then fused to obtain the crystal's final shape, as shown in Fig. 1. We first describe the crystal's geometry and construct the physical structure by thorough assignment of its component material, such as density, atomic number and mass number. Finally, the physical and geometrical definitions are linked together and the final crystal coordination is determined in the defined world.

Addback Factor

The addback factor F is defined as the ratio of the FEP detection efficiency of the addback mode to that of the direct mode. Therefore, the addback factor measures the increase in the FEP efficiency for a certain gamma-ray of energy E_γ [11].

Duchene explored the main feature of photopeak detection efficiency in composite detectors such as Clover in 1999 and the findings were contrasted with those obtained by simulation [3]. He found that the fit of the experimental data leads to an expression for the addback factor $F(E_\gamma) = 1 + f(E_\gamma)$, where f is the addition factor that directly depends on the photon energy. The photoelectric effect is dominant at gamma-ray energy below 130 keV. Consequently, the FEP normally does not contribute much to multiple events and both direct and addback modes are the same. The addback factor F is equivalent to 1 ($f = 0$) over an energy range of less than 130 keV. The Compton scattering probability is increased at higher energies (above 130 keV) due to photon scattering in more than one crystal. The addition factor begins to increase with energy, as the addback mode would be more efficient. Therefore, the present work aims to test the BALQARAD device addback factor (F) using several gamma-ray energies obtained from ^{60}Co, ^{137}Cs and ^{22}Na point sources. For this purpose, the Clover's physical model was developed and the additional factor equation was obtained and compared with the simulated one.

Results and Discussion

The geometry was evaluated using a hypothetical Geant4 particle called Geantino (a non-interacting particle), after creating a Monte Carlo code based on comprehensive modeling of the device architecture. To verify the modeled geometry, which was perfectly matched with the real one, the particle-tracking information was used. A special simulation run was also carried out to compare our built code's performance to the experimental measurements.

The Validation of BALQARAD Clover Simulation Model

A comparison was carried out between experimental data and the results obtained from the simulation. In the validation process, several point sources (^{60}Co, ^{137}Cs and ^{22}Na) located at 24 mm from the Clover's front side were used. The source-detector distance used in the validity was settled at 24 cm, typically to avoid high detection dead time. Table 1 shows the full peak net area for the point sources in the addback and direct modes. It is evident that the simulated and measured net areas are in good agreement, with an average error percentage of less than 6%. It is also clear that the addback mode is better than the direct mode for all isotopes due to the high addback efficiency in the full-energy peak on the expense of the corresponding Compton continuum. Measurements of a simple decay scheme, as in ^{137}Cs source with energy 661.65 keV where Compton scattering is the dominant interaction, confirmed the addback gain as illustrated in the gamma-ray spectrum in Fig. 2a. In more complex decay schemes, such as ^{60}Co and ^{22}Na, two full energy peaks appear in coincidence. This will reduce the events recorded at the full-energy peak and cause the summing peak's appearance as shown in ^{60}Co and ^{22}Na gamma-ray spectrum in Fig. 2b and Fig. 2c, respectively. It can be seen that in each spectrum, the addback mode is higher than the direct one. For ^{22}Na, the slight difference between the two modes occurs due to the strong annihilation peak at 511 keV observed in the ^{22}Na isotope. Therefore, the summing peak is considered high in the case of the addback mode, since the full and the annihilation peaks coincide.

TABLE 1. Experimental and simulated full-peak net areas for ^{60}Co, ^{137}Cs and ^{22}Na point sources.

Source		^{137}Cs	^{60}Co		^{22}Na
Energy Peak		661 keV	1173 keV	1332 keV	1274 keV
Direct	Experimental	710057	149040	133963	39020
	Simulation	747316	147298	133168	37360
Percentage error (%)		5%	1%	0.5%	4%
Addback	Experimental	933151	185027	167071	39345
	Simulation	984908	180790	164531	38651
Percentage error (%)		5%	2%	1%	1%

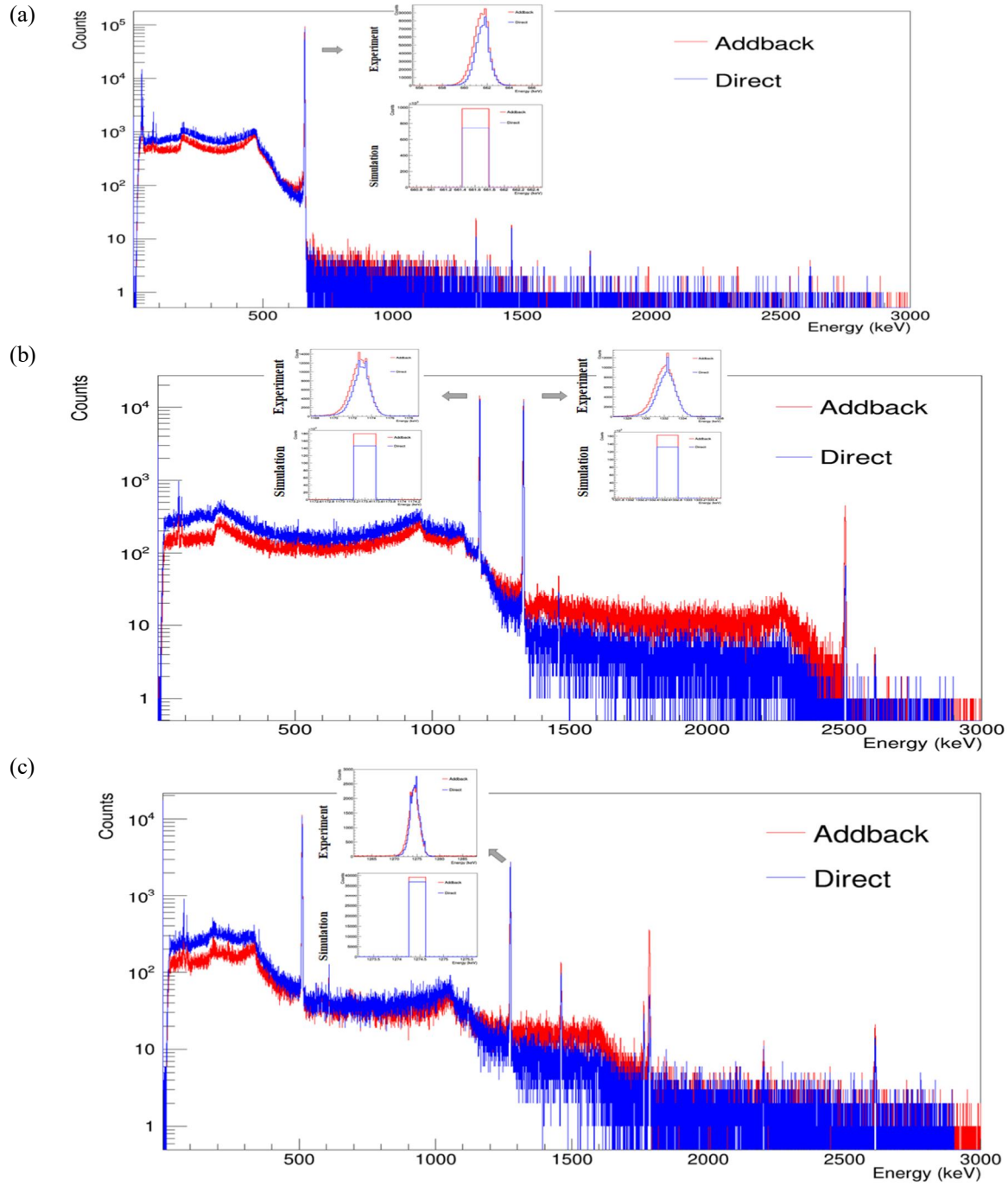

FIG. 2. Gamma-ray spectra in different modes of operation. The observed full peak is compared with the simulated peak; both peaks confirmed the addback gain for (a) ^{137}Cs, (b) ^{60}Co and (c) ^{22}Na; the slight difference between the two modes in ^{22}Na is observed due to the summing peak at 1785 keV as a result of 511 keV and 1274 keV addition.

Simulated Detection Mode for Different Radionuclides

A literature survey shows that, for safety applications, the radiation content of various radiological, environmental, food and water samples has been reviewed. Each application involves measuring a particular radioisotope for a specific sample composition with its decay scheme. All radionuclides of concern in various applications that are part of the pathways leading to internal and external exposure are involved in the summarized survey in Table 2.

The well-validated simulation code was used to run a simulation to determine the radionuclide addback/direct mode in various environmental applications. A separate code written in the ROOT environment [30] is consequently used to finalize the analysis and to evaluate the counts in these two modes. The perfect mode to be used in any sample depends on the decay scheme of the studied nuclide, the energies of gamma that being analyzed and other nuclides in the sample which may interfere with the analysis being performed. One million events at the energies of interest were found to be sufficient to achieve satisfactory statistics. It is well known that photopeak interference occurs in complicated spectra produced from some environmental materials. For example, a typical case is the 186 keV photopeak, generated from the ^{235}U and ^{226}Ra photons of 185.72 keV and 186.25 keV, respectively [31].

TABLE 2. List of radionuclides of interest for different applications.

Application	Radionuclide	References
Water	^{238}U, ^{235}U, ^{226}Ra, ^{232}Th, ^{40}K, ^{137}Cs, ^{228}Ra, ^{222}Rn, ^{210}Po, ^{210}Pb, ^{230}Th, ^{90}Sr, ^{224}Ra, ^{223}Ra	[13-16]
Air	^{3}H, ^{14}C, ^{51}Cr, ^{54}Mn, ^{60}Co, ^{65}Zn, ^{85}Kr, ^{90}Sr, ^{99}Tc, ^{103}Ru, ^{106}Ru, ^{125}Sb, ^{129}I, ^{131}I, ^{137}Cs, ^{144}Ce, ^{154}Eu, ^{155}Eu, ^{234}U, ^{235}U, ^{238}U, ^{238}Pu, ^{239}Pu, ^{240}Pu, ^{241}Am	[17]
Food	^{238}Pu, ^{239}Pu, ^{240}Pu, ^{241}Am, ^{90}Sr, ^{106}Ru, ^{129}I, ^{131}I, ^{235}U, ^{35}S, ^{60}Co, ^{89}Sr, ^{103}Ru, ^{134}Cs, ^{137}Cs, ^{144}Ce, ^{192}Ir, ^{3}H, ^{14}C, ^{99}Tc	[18-20]
Soil	^{60}Co, ^{137}Cs, ^{90}Sr, ^{238}Pu, ^{239}Pu, ^{240}Pu, ^{235}U, ^{232}Th, ^{226}Ra, ^{210}Pb, ^{40}K, ^{228}Ac, ^{214}Bi, ^{222}Rn, ^{131}I, ^{134}Cs, ^{129m}Te, ^{95}Nb	[21-23]
Spices	^{226}Ra, ^{232}Th, ^{40}K	[24]
Brazil nuts	^{222}Ra, ^{224}Ra, ^{226}Ra	[25]
Coal	^{238}U, ^{226}Ra, ^{210}Po, ^{210}Pb, ^{232}Th, ^{228}Ra, ^{40}K	[26]
Oil and gas	^{238}U, ^{226}Ra, ^{210}Po, ^{210}Pb, ^{222}Rn, ^{232}Th, ^{228}Ra, ^{224}Ra	[26]
Phosphate rocks	^{238}U, ^{232}Th, ^{226}Ra, ^{228}Ra, ^{40}K	[26]
Fertilizer production	^{238}U, ^{232}Th, ^{226}Ra	[26]
Building materials	^{226}Ra, ^{232}Th, ^{40}K	[27,28]
Rare metals	^{238}U, ^{232}Th, ^{40}K	[29]

However, the use of the Clover system allows for identifying such events in terms of direct and addback modes with high sensitivity. Table 3 summarizes the isotopes of interest in the environmental applications, the counts in both direct and addback modes for each isotope's full-energy peaks, and finally, the preferred operation mode for each isotope due to the complexity of the decay scheme. For gamma emitters of low-energy range (less than 130 keV) such as ^{129}I, which has a simple decay scheme and emitting gamma-ray of energy ≈ 39.5 keV, the direct mode and addback mode are the same and appear to be in harmony at low-energy region due to the dominance of photoelectric effect. The behavior in the addback mode is better than in the direct mode because of the superiority of the Compton effect for higher energies (above 130 keV), as in the case of ^{40}K with a simple decay scheme characterized by its dominant gamma line at 1460.820 keV with 10.66% relative intensity.

TABLE 3. The simulated peak net area recorded by addback and direct modes for isotopes that may be used in different applications.

Nuclide		Gamma energy (keV)	Intensity (%)	Direct net area	Addback net area	Preferred operation mode
^{238}U	^{234}Th	63.29	3.7	95260	66151	Direct
	^{214}Bi	609.320	45.49	239382	221785	Direct
	^{214}Bi	768.360	4.894	20639	18873	Direct
	^{214}Bi	934.056	3.107	11394	10752	Direct
	^{214}Bi	1120.294	14.92	47450	47290	Both
	^{214}Bi	1238.122	5.834	16889	16832	Both
	^{214}Bi	1377.669	3.988	11384	14364	Addback
	^{214}Bi	1407.988	2.394	5899	5968	Addback
	^{214}Bi	1509.210	2.130	5361	5698	Addback
	^{214}Bi	1729.595	2.878	7616	12851	Addback
	^{214}Bi	1764.491	15.30	35503	42286	Addback
	^{214}Bi	1847.429	2.025	4872	7215	Addback
	^{214}Bi	2204.059	4.924	9354	11432	Addback
^{226}Ra	^{226}Ra	186.211	3.64	50366	38219	Direct
	^{214}Pb	241.9950	7.251	91381	81017	Direct
	^{214}Pb	295.2228	18.42	197532	185453	Direct
	^{214}Pb	351.9321	35.60	327074	314925	Direct
	^{214}Bi	609.320	45.49	244968	239571	Direct
	^{214}Bi	768.360	4.894	20603	20066	Both
	^{214}Bi	934.056	3.107	11593	11574	Both
	^{214}Bi	1120.294	14.92	48827	51226	Addback
	^{214}Bi	1238.122	5.834	17240	18200	Addback
	^{214}Bi	1377.669	3.988	11675	15311	Addback
	^{214}Bi	1407.988	2.394	5890	6240	Addback
	^{214}Bi	1509.210	2.130	5602	6139	Addback
	^{214}Bi	1729.595	2.878	7642	13943	Addback
	^{214}Bi	1764.491	15.30	35631	45263	Addback
	^{214}Bi	1847.429	2.025	5016	7759	Addback
	^{214}Bi	2204.059	4.924	9752	12616	Addback
^{232}Th	^{228}Ac	129.065	2.42	46973	30801	Direct
	^{228}Ac	209.253	3.89	60827	47027	Direct
	^{212}Pb	238.632	43.6	516350	411188	Direct
	^{228}Ac	270.245	3.46	48365	36452	Direct
	^{228}Ac	328.000	2.95	37135	29168	Direct
	^{228}Ac	338.320	11.27	113876	102628	Direct
	^{228}Ac	463.004	4.40	29916	24927	Direct
	^{212}Bi	727.330	6.67	30177	28729	Direct
	^{228}Ac	794.947	4.25	19723	17478	Direct
	^{228}Ac	911.204	25.8	94982	99604	Addback
	^{228}Ac	964.766	4.99	18318	18685	Both
	^{228}Ac	968.971	15.8	54711	57703	Addback
	^{228}Ac	1588.20	3.22	8060	9305	Addback
------	^{40}K	1460.820	10.66	30356	43364	Addback
------	^{137}Cs	661.657	85.10	466011	614233	Addback
------	^{210}Pb	46.539	4.25	83107	83573	Both
------	^{224}Ra	240.986	4.10	50129	44752	Direct
------	^{223}Ra	144.235	3.27	63108	60106	Direct
	^{223}Ra	154.208	5.70	106522	102944	Direct

Nuclide		Gamma energy (keV)	Intensity (%)	Direct net area	Addback net area	Preferred operation mode
	^{223}Ra	269.463	13.9	159912	168859	Addback
	^{223}Ra	323.871	3.99	34906	38125	Addback
	^{223}Ra	338.282	2.84	23974	26526	Addback
------	^{51}Cr	320.0824	9.910	104427	123046	Addback
------	^{54}Mn	834.848	99.9760	453507	614488	Addback
------	^{60}Co	1173.228	99.85	329146	404409	Addback
	^{60}Co	1332.492	99.9826	297208	366926	Addback
------	^{65}Zn	1115.539	50.04	182279	253582	Addback
------	^{85}Kr	513.997	0.434	2889	3741	Addback
------	^{103}Ru	497.085	91.0	640853	810077	Addback
	^{103}Ru	610.333	5.76	33602	44224	Addback
	^{125}Sb	176.314	6.84	110480	106298	Direct
	^{125}Sb	427.874	29.6	237780	291185	Addback
	^{125}Sb	463.365	10.49	79268	101993	Addback
------	^{125}Sb	600.597	17.65	104273	135082	Addback
	^{125}Sb	606.713	4.98	29377	37962	Addback
	^{125}Sb	635.950	11.22	63330	84218	Addback
------	^{129}I	39.578	7.51	143884	145440	Both
	^{131}I	80.185	2.62	58006	48723	Direct
	^{131}I	284.305	6.12	69965	74362	Addback
------	^{131}I	364.489	81.5	757827	918408	Addback
	^{131}I	636.989	7.16	40545	53346	Addback
------	^{144}Ce	133.515	11.09	216271	207295	Direct
	^{154}Eu	123.0706	40.4	790576	687963	Direct
	^{154}Eu	247.9290	6.89	81733	68840	Direct
	^{154}Eu	591.755	4.95	27690	27563	both
	^{154}Eu	723.3014	20.06	95466	104538	Addback
	^{154}Eu	756.8020	4.52	19849	19350	Direct
------	^{154}Eu	873.1834	12.08	50387	54728	Addback
	^{154}Eu	996.29	10.48	43048	56802	Addback
	^{154}Eu	1004.76	18.01	65759	81286	Addback
	^{154}Eu	1274.429	34.8	109927	139796	Addback
------	^{155}Eu	86.5479	30.7	703934	711483	Addback
	^{155}Eu	105.3083	21.1	465286	473785	Addback
------	^{234}U	53.20	0.1230	25146	18045	Direct
------	^{241}Am	59.5409	35.9	1032390	734439	Direct
	^{134}Cs	563.246	8.338	48301	45903	Direct
	^{134}Cs	569.331	15.373	86988	82722	Direct
	^{134}Cs	604.721	97.62	539785	586465	Addback
------	^{134}Cs	795.864	85.46	377127	424450	Addback
	^{134}Cs	801.953	8.688	36859	37773	Addback
	^{134}Cs	1365.185	3.017	10372	19894	Addback
	^{192}Ir	295.9565	28.71	290490	241766	Direct
	^{192}Ir	308.4550	29.70	291476	251717	Direct
	^{192}Ir	316.5061	82.86	813063	769592	Direct
------	^{192}Ir	468.0688	47.84	333895	354465	Addback
	^{192}Ir	588.5810	4.522	24581	23995	Direct
	^{192}Ir	604.411	8.216	52665	81939	Addback
	^{192}Ir	612.426	5.34	37139	67763	Addback
	^{228}Ac	129.065	2.42	46722	30574	Direct
------	^{228}Ac	209.253	3.89	60353	46628	Direct

Nuclide		Gamma energy (keV)	Intensity (%)	Direct net area	Addback net area	Preferred operation mode
	^{228}Ac	270.245	3.46	48997	36966	Direct
	^{228}Ac	328.000	2.95	37440	29227	Direct
	^{228}Ac	338.320	11.2	113617	102526	Direct
	^{228}Ac	463.004	4.40	30008	24968	Direct
	^{228}Ac	794.947	4.25	19237	17154	Direct
	^{228}Ac	911.204	25.8	95052	100085	Addback
	^{228}Ac	964.766	4.99	18510	18724	Both
	^{228}Ac	968.971	15.8	54594	57456	Addback
	^{214}Bi	609.320	45.49	256754	284582	Addback
	^{214}Bi	768.360	4.894	21747	23831	Addback
	^{214}Bi	934.056	3.107	11764	13323	Addback
	^{214}Bi	1120.294	14.92	51117	59571	Addback
	^{214}Bi	1238.122	5.834	18278	21672	Addback
	^{214}Bi	1377.669	3.988	12175	17988	Addback
------	^{214}Bi	1407.988	2.394	6206	7390	Addback
	^{214}Bi	1509.210	2.130	5895	7205	Addback
	^{214}Bi	1729.595	2.878	8037	15795	Addback
	^{214}Bi	1764.491	15.30	37576	53803	Addback
	^{214}Bi	1847.429	2.025	5240	9233	Addback
	^{214}Bi	2204.059	4.924	10140	14795	Addback
------	^{129m}Te	459.60	7.7	57422	69809	Addback
	^{129m}Te	487.39	1.42	10532	14276	Addback
------	^{95}Nb	765.803	99.808	484958	651595	Addback
------	^{228}Ra	13.52	1.60	3097	1663	Direct
------	^{222}Ra	324.31	2.77	28457	33224	Addback

However, for radionuclides with complex decay schemes such as ^{228}Ac and ^{214}Bi (Fig. 3 depicts the simulated complex decay schemes of ^{214}Bi), which are the decay products of natural radioactive decay chains, it is observed from the simulation spectra that the addback mode is poor due to coincidence summing. The secular equilibrium occurs in a radioactive decay chain when the daughter's half-life is much shorter than that of the parent radionuclide. In this situation, the parent's decay rate and the production rate of the daughter are approximately constant.

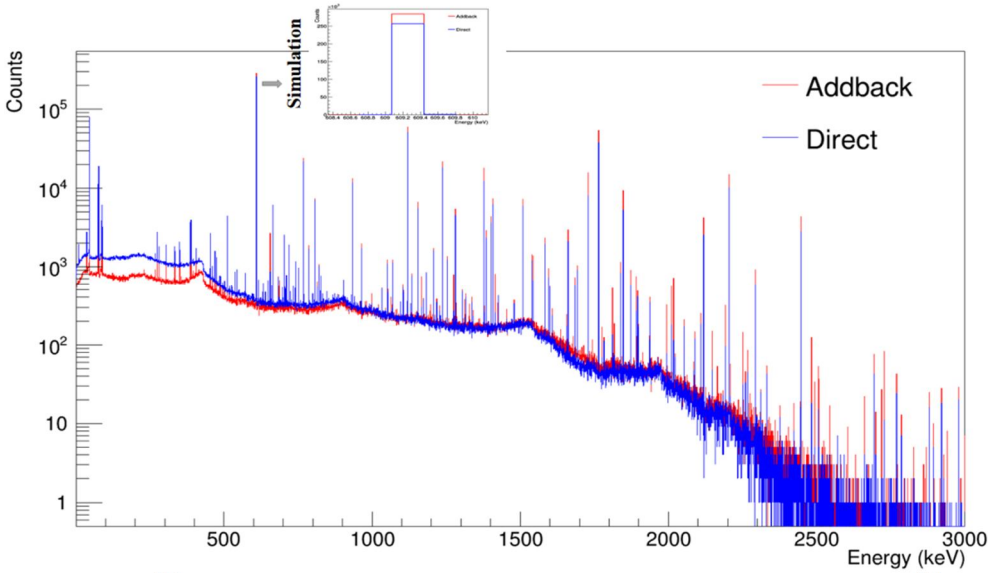

FIG. 3. Simulated ^{214}Bi gamma-ray spectra for both addback and direct modes, where the ^{214}Bi dominant gamma line is at 609.32 keV with 45.49 % relative intensity.

Addback Factor

The addition factor (f) has been performed after measuring the addback factor (F) over different gamma energies obtained from ^{60}Co, ^{137}Cs and ^{133}Ba point sources. The acquired experimental data was fitted to get an equation compared to the simulated one given in Table 4 and Fig. 4a. The ratio is approximately one, because the Compton scattering is very low at lower energies. With the increase in gamma-ray radiation, the addback factor begins to rise, so Compton's scattering becomes more probable. The addback factor becomes almost constant at very high energy, although the likelihood of scattering is still dominant compared with photoelectric absorption in the second crystal.

TABLE 4. The simulated addition factors for several gamma energies compared with those obtained from the experimental results.

Energy (keV)	Addition factor f (Experimental)	Addition factor f (Simulated)
356	0.10773±0.0029	0.12060±0.00318
661	0.2544±0.00355	0.25576±0.00381
1173	0.30734±0.00306	0.30172±0.00305
1332	0.32484±0.00319	0.31388±0.00322

The fitted addition factor equation is expressed, according to Duchene (1999), by the relationship with E_γ in keV [3]:

$$f(E_\gamma) = \begin{cases} P_1 + P_2 \ln E_\gamma, E_\gamma > 130\ keV \\ 0, E_\gamma \leq 130\ keV. \end{cases} \quad (1)$$

The fitting parameters of the experimental results acquired from BALQARAD Clover were P_1 = -0.83052 and P_2 = 0.16172. The experimental values are comparable with the simulated full geometry performance, with P_1= -0.77315 and P_2 = 0.15276 fitting parameters (compare two datasets in Fig. 4a and Fig. 4b). The two datasets exhibit the same behavior as predicted and provide a strong agreement between the established Clover model and the actual experiment with satisfactory evidence. After the validation of the Clover simulation code, it is possible now to adopt the code and run the simulation with isotopes of wide energy range such as; ^{133}Ba (356.01 keV with 62.05%), ^{134}Cs (604.72 keV with 97.62%, 569.33 keV with 15.4% and 795.86 keV with 85.5%), ^{137}Cs (661.66 keV with 85.1%), ^{88}Y (898.04 keV with 93.7% and 1836.06 with 99.2%) and ^{60}Co (1173 keV with 99.85% and 1332.49 keV with 99.98%). The new fitting parameters for simulated addback factor with different isotopes with wide energy range are shown in Fig. 4c.

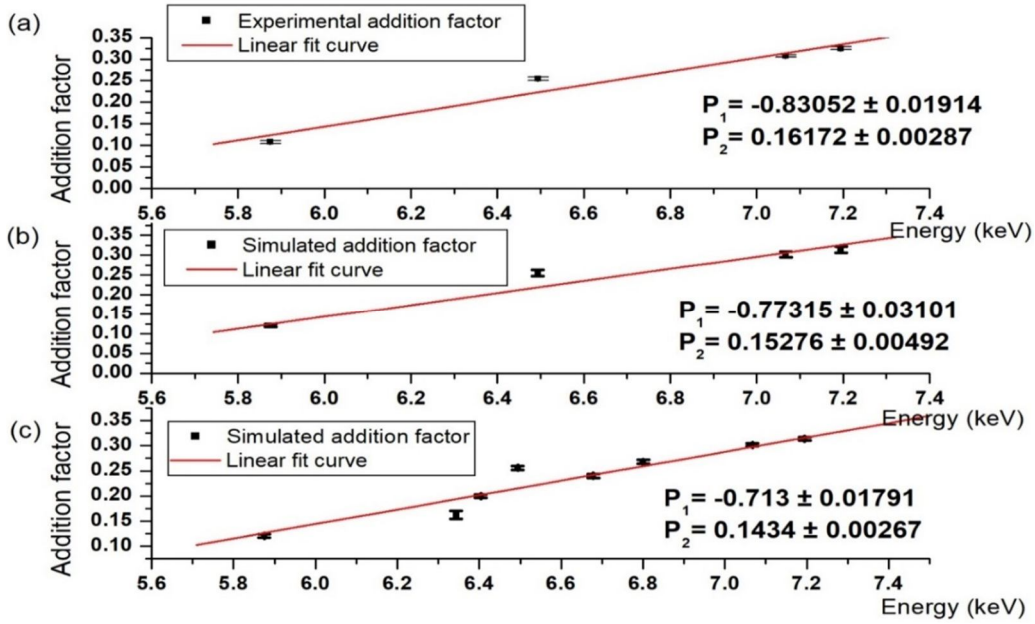

FIG. 4. The linear fit for (a) experimental and (b) simulated addition factors for available radionuclides in the radiation lab. (c) The linear fit for the simulated addition factor for a set of isotopes with a wide range of energy.

Conclusions

To examine possible applications, we have used the modularity of composite HPGe radiation detectors. Comprehensive Monte Carlo simulations based on detailed modeling of the system geometry were performed and compared with the obtained data experimentally. After using the Geant4 model, the results have shown that it is a highly valuable tool for simulating the HPGe system response. The measured addback factor $F(E_\gamma)$ is larger than or equal to one. The measured addition factor has underlined strong agreement between the two sets of data by using experimental and simulated data. For each application, a detailed survey was performed on the appropriate radioactive isotope and the desired operating mode of the Clover detector was determined. Further research into the perception of regional patterns in radionuclides is inspired by the early promising results of using Clover HPGe detectors in many applications and fields.

Acknowledgments

BALQARAD project is supported by the Jordanian Scientific Research Support Fund (SRSF) under grant #Bas/2/4/2014. The authors would like to acknowledge and appreciate the support given by the late BALQARAD founder, Prof. S. Dababneh.

References

[1] Saha Sarkar, M., Datta, P., Ray, I., Deya, C.C., Chattopadhyay, S., Goswami, A., Banerjee, P., Singh, R.P., Joshi, P.K., Paul, S.D., Bhattacharya, S., Bhowmik, R., Chatterjee, J.M., Jain, H.C., Sen, S. and Dasmahapatra, B., Nucl. Instr. and Meth. A, 491 (2002) 113.

[2] Eberth, J. and Simpson, J., Prog. Part. Nucl. Phys., 60 (2008) 283.

[3] Duchêne, G., Beck, F.A., Twin, P.J., De France, G., Curien, D., Han, L., Beausang, W.C., Bentley, A.M., Nolan, J.P. and Simpson, J., Nucl. Instr. and Meth. A, 432 (1999) 90.

[4] Boynton, V.W., Feldman, C.W., Squyres, W.S. *et al.,* Science, 297 (2002) 81.

[5] Horne, M.S., Ph.D. Thesis, The University of Texas at Austin, (2013), USA. http://hdl.handle.net/2152/21557.

[6] Dababneh, S., Patronis, N., Assimakopoulos, A.P., Görres, J., Heil, M., Käppeler, F., Karamanis, D., O'Brien, S. and Reifarth, R., Nucl. Instr. and Meth. A, 517 (2004) 230.

[7] Dababneh, S., Görres, J., Heil, M., Käppeler, F., Reifarth, R. and Wiescher, M., Nucl. Instr. and Meth. A, 737 (2014) 135.

[8] Sarmiento, L.G., Andersson, L.L. and Rudolph, D., Nucl. Instr. and Meth. A, 667 (2012) 26.

[9] Chick, D.M., Master Thesis, Western Kentucky University, (2016), Kentucky. https://digitalcommons.wku.edu/theses/1744.

[10] Belvito, B., Master Thesis, University of Milano, (2015), Italy. http://www.infn.it/thesis/PDF/getfile.php?filename=10181-Belvito-magistrale.pdf.

[11] Rizwan, U.,Garnsworthy, B.A., Andreoiu, C. *et al.,* Nucl. Instr. and Meth. A, 820 (2011) 126.

[12] Geant4. https://geant4.web.cern.ch. Accessed on 20 April 2019.

[13] World Health Organization (WHO), "Guidelines for Drinking-water Quality", Third Edition, (2008). https://www.who.int/water_sanitation_health/publications/gdwq3rev/en/.

[14] Milvy, P. and Cothern, R.C., Environ. Geochem. Health, 11 (1989) 63.

[15] Munter, R., Proc. Estonian Acad. Sci., 62 (2013) 122.

[16] Ahmed, K.N. and Turkish J., Eng. Env. Sci., 28 (2004) 345.

[17] Fritz, G.B. and Patton W.G., Radionuclide Concentrations in Air on the Hanford Site (No. PNNL-13909), A Ten-year Trend Report 1991 through 2000, Pacific Northwest National Lab (PNNL), United States, (2002).

[18] World Health Organization (WHO), Nuclear accidents and radioactive contamination of foods (2011). https://www.who.int/foodsafety/fs_management/radionuclides_and_food_300311.pdf.

[19] Codex Alimentarius Commission (CAC), Fact Sheet on Codex Guideline Levels for Radionuclides in Foods Contaminated Following a Nuclear or Radiological Emergency, (2011). http://www.fao.org/fileadmin/user_upload/agns/pdf/codex_guideline_for_radionuclitide_contaminated_food.pdf.

[20] US Food and Drug Administration (FDA), Supporting document for guidance levels for radionuclides in domestic and imported foods, (2004). https://www.fda.gov/food/chemicals/supporting-document-guidance-levels-radionuclides-domestic-and-imported-foods

[21] Simmons, A.M., Poston, M.T., Fritz, G.B. and Bisping, E.L., Radionuclide Concentrations in Terrestrial Vegetation and Soil Samples on and around the Hanford Site, 1971 through 2008 (PNNL-20577). Pacific Northwest National Lab, United States, (2011).https://www.pnnl.gov/main/publications/external/technical_reports/PNNL-20577.pdf.

[22] Maphoto, P.K., Ph. D. Thesis, University of the Western Cape, (2004). http://hdl.handle.net/11394/1462.

[23] Pallavicini, N., Master Thesis, Swedish University of Agricultural Sciences, Department of Soil and Environment, (2011). https://stud.epsilon.slu.se/3703/2/pallavicini_n_111215.pdf.

[24] Amin, M.R. and Ahmed, F., Pelagia Research Library Advances in Applied Science Research, 4 (2013) 350.

[25] Martins, M., Pacheco, M.A., Lucas, S.C.A., Andrello, C.A., Appoloni, R.C. and Xavier, M.J.J., Acta Amazonica, 42 (2012) 157.

[26] World Nuclear Association, Naturally Occurring Radioactive Materials (NORM). http://www.world-nuclear.org/information-library/safety-and-security/radiation-and-health/naturally-occurring-radioactive-materials-norm.aspxx. Accessed on 01 April 2019.

[27] Quintana, B., Pedrosa, C.M., Vázquez-Canelas, L., Santamaría, R., Sanjuán, A.M. and Puertas, F., Radiat. Isot., 134 (2018) 470.

[28] Ahmed, H.A., Jafir, O.A. and Abdullah, M.H., Jordan J. Phys., 13 (1) (2020) 73.

[29] Shives, K.B.R., British Columbia Geological Survey Paper, 3 (2015) 199.

[30] Brun, R. and Rademakers, F., Nucl. Instr. and Meth. A, 389 (1997) 81.

[31] Anagnostakis, J.M., Radiat. Phys. Chem., 116 (2015) 3.

Volume 15, Number 2, 2022. pp. 161-168

Jordan Journal of Physics

ARTICLE

X-Wave Propagation Characteristics in a Collisional, Inhomogeneous Plasma Slab

Manal M. Al-Ali

Department of Physics, Yarmouk University, Irbid, Jordan.

Doi: **https://doi.org/10.47011/15.2.6**

Received on: 17/10/2020; *Accepted on: 26/01/2021*

Abstract: Normally incident electromagnetic wave on a collisional, inhomogeneous magnetoplasma slab has been treated as a multilayered system of homogeneous sub-cells within the transfer matrix method. For incident wave frequencies much above the ion cyclotron frequency, the extraordinary elliptically polarized wave mode is relevant for wave propagation normal to a dc-magnetic field. For a sinusoidal plasma density profile, the transmittance, reflectance and absorbance are plotted *versus* wave frequency normalized to electron cyclotron frequency ω_0 / ω_{ce} for different ratios of electron cyclotron to electron plasma frequencies. For fixed ω_{ce} and by varying the wave frequency, the curves of the transmittance and reflectance show two pass and two stop bands. When the ratio of cyclotron frequency to plasma frequency $\omega_{ce} / \omega_{pc}$ is increased, all bands shift to the region of low wave frequency, the pass bands become broader and the stop bands become narrower. The absorbance show three absorption bands; namely, two collisional absorption bands of evanescent waves at the X-wave cut-off frequencies and a resonance absorption band at the upper hybrid frequency. It has also been found that a homogeneous plasma slab overestimates the collisional absorption at cut-offs and has a broader absorption band of the upper hybrid resonance.

Keywords: Waves in inhomogeneous magnetoplasma, Upper hybrid resonance, Reflectance, Absorbance, Transmittance.

I. Introduction

Scattering, interaction and propagation of electromagnetic waves in a magnetoplasma have been attracting many researchers [1-10] due to the wide range of applications that includes, but is not limited to, atmospheric and space plasma, stealth plasma, telecommunications, fabricated industrial absorbers and filters, as well as other applications.

Due to their unique electrical and dynamical properties, plasmas support a wide range of plasma oscillations and waves. The importance of waves in plasmas as non-perturbing diagnostic, probing and exciting tools, makes plasma waves one of the active sub--disciplines in plasma physics research [11-15]. Of practical and theoretical interest are the classification, understanding and characterization of linear and/or nonlinear waves in different regimes of plasma.

Owing to its wide range of variables, a plasma slab can be especially engineered and its parameters controlled in a way to tailor the material with the attempted optical properties to serve the intended application. By interacting with the tailored slab, the electromagnetic wave properties are then studied and the effect of the different plasma parameters on the reflection, absorption and transmission of the EM--wave is discussed.

Corresponding Author: Manal M. Al-Ali **Email**: manal.alali@yu.edu.jo

Gurel and Oncu [3] studied the interaction of EM-waves with a strongly collisional plasma slab of partially linear and partially sinusoidal density profile and found that highly collisional and high-density plasma greatly absorbs the electromagnetic wave power along a wide frequency band.

AL-Khateeb et al. [8] used the forward recursion approach to study the characteristics of EM-wave perpendicular propagation in a collisional plasma slab in the GHz range for a set of parameters that may suit reentry blackout. The forward recursion method showed results that are consistent with those shown in the literature using the scattering matrix method qualitatively and qualitatively. Laroussi [16] and Hu [17] used the scattering matrix method to obtain reflectance, absorbance and transmittance of EM-waves in an inhomogeneous plasma slab.

In this work, inhomogeneous magnetoplasma with a sinusoidal plasma density profile is considered. The magnetoplasma will be treated as a multilayered system of homogeneous sub-slabs within the Max-Born transfer matrix technique [10, 18, 19]. The present work is a continuation of the work published recently by Rawwaqa et al. [10], where they studied the characteristics of waves propagating along the ambient magnetic field resulting in right and left circularly polarized waves (R-waves and L-waves). The present study, however, treats the case of wave propagation normal to an externally applied magnetic field with the wave modes supported by the magnetoplasma being of extraordinary nature (X-waves) with elliptical polarization. The X-waves have a completely different nature from that of the R-wave and L-wave in terms of resonance and cut-off behaviors that affect magnitude, morphology and intervals of reflection, absorption and transmission. The paper is organized as follows: In Section II, we present the model equations. Numerical results are presented in Section III. Finally, in section IV, we discuss the main results and conclusions.

II. Model Equations

Fig. 1 shows the geometry of the plasma slab, where we assume that waves are normally incident from the left semi-infinite medium into the bound plasma slab of width a. The dielectric permittivity of left and right semi-infinite regions are ϵ_ℓ and ϵ_r, respectively.

Assume an incident linearly polarized plane wave in the y-direction such that $\vec{E}(\mathrm{z},\mathrm{t}) = \hat{y}E_y(\mathrm{z},\mathrm{t})$ and the incident, reflected and transmitted waves are propagating along the x-axis perpendicular to a background uniform magnetostatic field $\vec{\mathrm{B}} = \hat{z}B_0$, as shown in Fig. 1. As the wave propagates into the magnetoplasma slab, it induces an electric field E_x along $\vec{k}$ and thus becomes partly longitudinal and partly transverse. Wave modes in a magnetoplasma slab with the induced electric field being normal to the dc-magnetic field tend to be elliptically polarized [12-14].

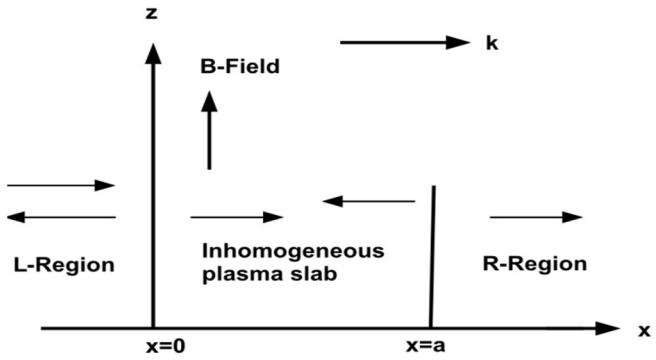

FIG. 1. Bound inhomogeneous plasma slab in a dc-magnetic field.

The inhomogeneous plasma slab is divided into N sufficiently thin homogeneous layers of width $d_{m+1} - d_m$, where $m = 1, 2, 3, \ldots\ldots, N$ [10, 18, 20]. The electromagnetic fields at the inner face of the exit layer $m = N$ are related to the fields at the input interface of incidence by the well-established global transfer matrix M of the whole multilayered structure; namely,

$$M = \prod_{m=1}^{N} M_m = \begin{pmatrix} M_{11} & M_{12} \\ M_{21} & M_{22} \end{pmatrix}, \qquad (1)$$

$$M_m = \begin{pmatrix} \cos\delta_m & \frac{\mathrm{i}}{\gamma_m}\sin\delta_m \\ \mathrm{i}\gamma_m \sin\delta_m & \cos\delta_m \end{pmatrix}, \quad (2)$$

where M_m stands for the m^{th} layer transfer matrix. The parameters γ_m and δ_m for normal incidence are as follows:

$$\gamma_m = \sqrt{\mu_m \epsilon_m} = \sqrt{\mu_0 \epsilon_0}\sqrt{\varepsilon_m}\,,\ \delta_m = \omega d_m \gamma_m\,, \quad (3)$$

where ω is the angular frequency of the incident wave, μ_m, ϵ_m, d_m and ε_m are, respectively, the m^{th} layer permeability, permittivity, width and dielectric function. All necessary information to characterize the propagation of electromagnetic waves across the inhomogeneous plasma slab is contained in Eqs. (1-3). The complex transmission $\tilde{\tau}$ and reflection $\tilde{\rho}$ coefficients in terms of global transfer matrix elements are [18, 20]:

$$\tilde{\tau} = \frac{2\gamma_\ell}{\gamma_\ell M_{11} + \gamma_\ell \gamma_r M_{12} + M_{21} + \gamma_r M_{22}}, \quad (4)$$

$$\tilde{\rho} = \frac{\gamma_\ell M_{11} + \gamma_\ell \gamma_r M_{12} - M_{21} - \gamma_r M_{22}}{\gamma_\ell M_{11} + \gamma_\ell \gamma_r M_{12} + M_{21} + \gamma_r M_{22}}. \quad (5)$$

The corresponding reflectance R and transmittance T are obtained as $R = \tilde{\rho}\tilde{\rho}^*$ and $T = \sqrt{\frac{\varepsilon_r}{\varepsilon_\ell}}\tilde{\tau}\tilde{\tau}^*$. The absorbance (A) is defined as $A = 1 - R - T$.

III. Numerical Results

We assume a sinusoidal plasma density which is appropriate for ionospheric applications such that $n_e(\mathrm{x}) = \mathrm{n}_{0e}\sin\frac{\pi x}{a}$ for $0 \le x \le \frac{a}{2}$ and $n_e(\mathrm{x}) = \mathrm{n}_{0e}[1 - \sin\frac{\pi}{a}(\mathrm{x} - \frac{a}{2})]$ for $\frac{a}{2} \le x \le a$, where n_{0e} is the peak density of plasma electrons. For wave propagation perpendicular to the applied magnetic field, a magnetoplasma of cold electrons and cold immobile ions supports both ordinary (O) and extraordinary (X) transverse electromagnetic wave modes. Since the ordinary wave is unaffected by the magnetic field, only the X-wave will be considered [22-24].

The *X*-wave has two pass bands in the frequency ranges $\omega_L < \omega < \omega_{uh}$ and $\omega > \omega_R$ which are separated by a stop band in the frequency range $\omega_{uh} < \omega < \omega_R$. Here, ω_{pe} is the electron plasma frequency, ω_{uh} is the upper hybrid frequency, ω_L and ω_R are, respectively, the left and right cut-off frequencies of the X-wave [12]-[14]. They are given by the following formulae;

$$\omega_{uh} = \sqrt{\omega_{pe}^2 + \omega_{ce}^2}\,,\ \omega_{pe} = \sqrt{\frac{e^2 n_e}{\epsilon_0 m_e}}\,, \quad (6)$$

$$\omega_L = \frac{1}{2}\sqrt{\omega_{ce}^2 + 4\omega_{pe}^2} - \frac{\omega_{ce}}{2}\,, \quad (7)$$

$$\omega_R = \frac{1}{2}\sqrt{\omega_{ce}^2 + 4\omega_{pe}^2} + \frac{\omega_{ce}}{2}\,. \quad (8)$$

The m^{th} layer dielectric function for the X-wave is given by [21]:

$$\varepsilon_X^{(m)} = \frac{[1 - \frac{\omega_{pe,m}^2}{\omega(\omega - \omega_{ce,m} - j\nu_{e,m})}][1 - \frac{\omega_{pe,m}^2}{\omega(\omega + \omega_{ce,m} - j\nu_{e,m})}]}{1 - \frac{\omega - j\nu_{e,m}}{\omega}\frac{\omega_{pe,m}^2}{(\omega - j\nu_{e,m})^2 - \omega_{ce,m}^2}}, \quad (9)$$

where $\omega_{ce,m}$ and $\nu_{e,m}$ are the electron plasma frequency and the collision frequency with neutrals of the m^{th} sub-slab, respectively.

In all numerical examples presented below, we use normalized quantities and therefore, we initiate the calculations by an arbitrary incident wave frequency $\omega = \omega_0$. In all calculations to follow, we adopt the normalized width of the plasma slab $a/\lambda_0 = 5$. The normalized electron plasma frequency in each plasma slab can take one of the values $\omega_{pe}/\omega_{ce} = 1/\sqrt{2}, 1, \sqrt{2}$. The normalized collision frequency of electrons with neutrals has a fixed ratio of $\nu_e/\omega_{pe} = 0.01$, which accounts for weak, but relevant, collisional damping.

To characterize the X-wave propagation in an inhomogeneous magnetoplasma slab, we use the ratio ω_0/ω_{ce} as an independent variable. Accordingly, the magnetic field increases by moving to the left at fixed wave frequency ω_0 or

the wave frequency increases as we move to the right at a fixed value of the dc-magnetic field.

In Figs. 2-4, we plot the reflectance, transmittance and absorbance *versus* ω_0 / ω_{ce} for three different plasma frequencies. For each fixed value of the cyclotron frequency and by varying the wave frequency ω_0, the curves of Figs. 2 and 3 show two pass and two stop bands. The pass bands are in the frequency ranges $\omega_L < \omega_o < \omega_{uh}$ and $\omega_0 > \omega_R$, and the corresponding stop bands are such that $0 < \omega_o < \omega_L$ and $\omega_{uh} < \omega_o < \omega_R$.

With increasing the ratio $\omega_{ce} / \omega_{pe}$, all bands are shifted to the left. The pass bands of the transmittance become broader (Fig. 2), while the corresponding stop bands of the reflectance become narrower (Fig. 3). We observe the same behavior in the absorbance curves of Fig. 4. The absorbance curves show the appearance of three absorption bands. From left to right, the first and third bands of each curve are due to collisional absorption of evanescent waves at the cut-off frequencies $\omega_0 = \omega_L$ and $\omega_0 = \omega_R$, respectively. The second (middle) absorption band is due to upper hybrid resonance which is localized around ω_{ce}.

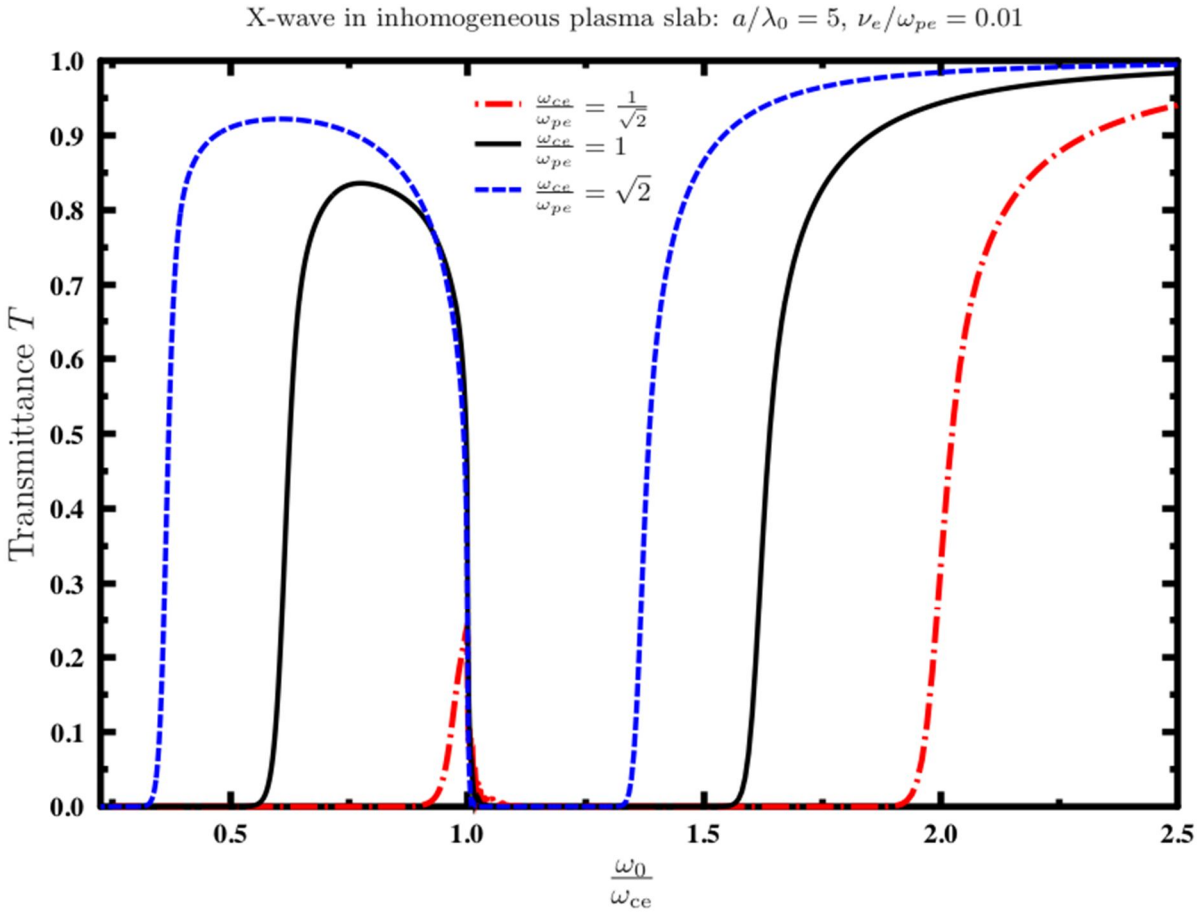

FIG. 2. Transmittance for inhomogeneous magnetoplasma slab.

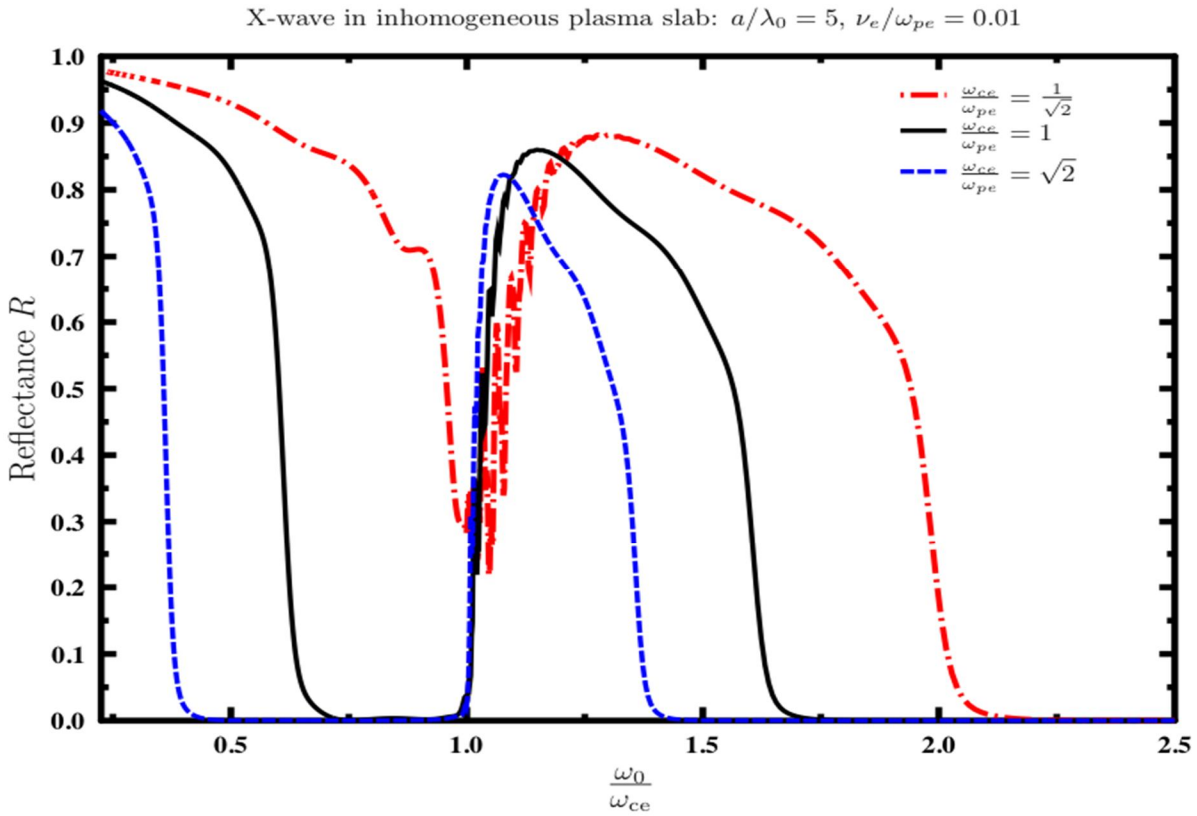

FIG. 3. Reflectance for inhomogeneous magnetoplasma slab.

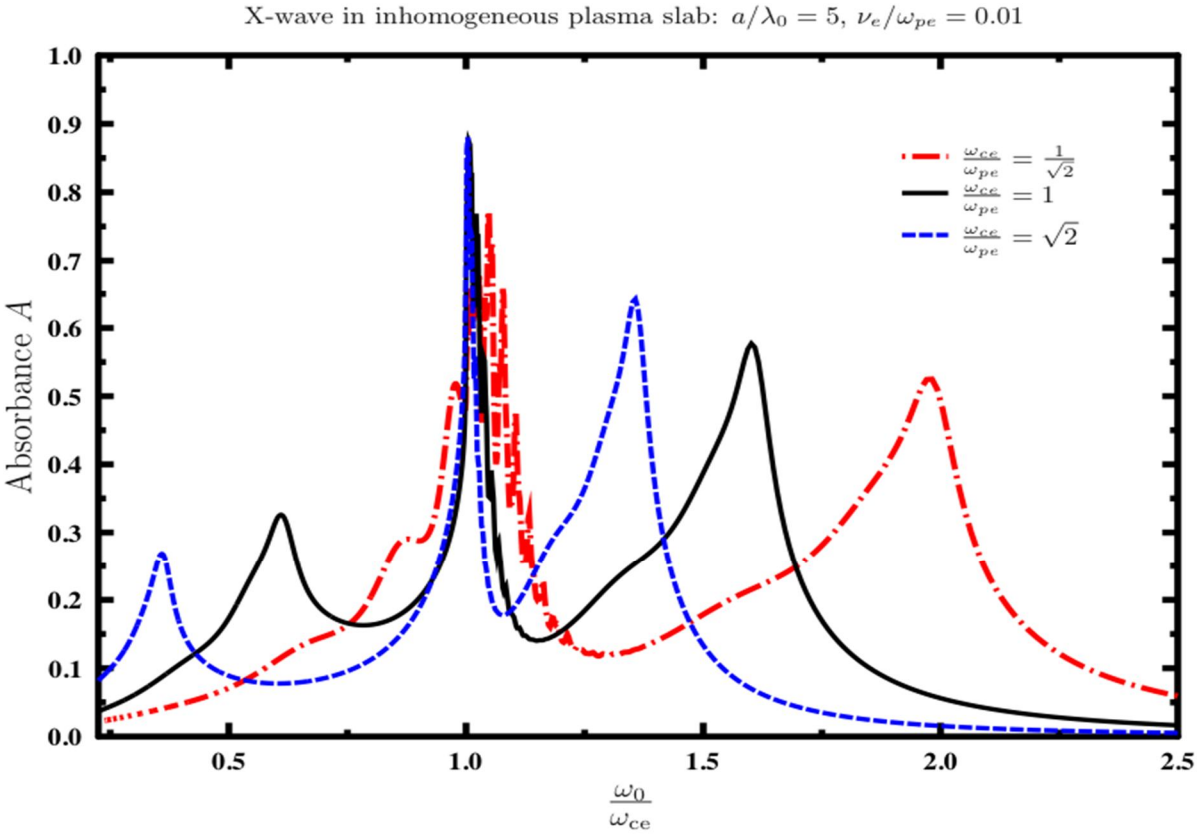

FIG.4: Absorbance for inhomogeneous magnetoplasma slab.

To complete the discussion on the X-wave propagation characteristics in an inhomogeneous magnetoplasma slab of finite thickness, we plot in Figs. 5 and 6 the curves of R and A for homogeneous and inhomogeneous magnetoplasma slabs. We observe from Fig. 5 that the stop band $\omega_{uh} < \omega_o < \omega_R$ is narrower for a homogeneous slab, while the second stop band $0 \le \omega_o < \omega_L$ is broader. The ripples in curves of R for the homogeneous plasma slab are of geometrical nature and are due to the in-plasma interferences. The ripples in R are smeared out for an inhomogeneous plasma slab.

The absorbance curves of Fig. 6 show the appearance of three absorption bands for the homogeneous plasma slab. These absorption bands are due to the collisional absorption of evanescent waves and to the upper hybrid resonance. We observe that the effect of inhomogeneity is to down shift the absorption (and the stop) bands to the left toward lower wave frequencies. From Fig. 6, we see that a homogeneous plasma slab overestimates collisional absorption at cut-offs and broadens the upper hybrid resonance absorption band.

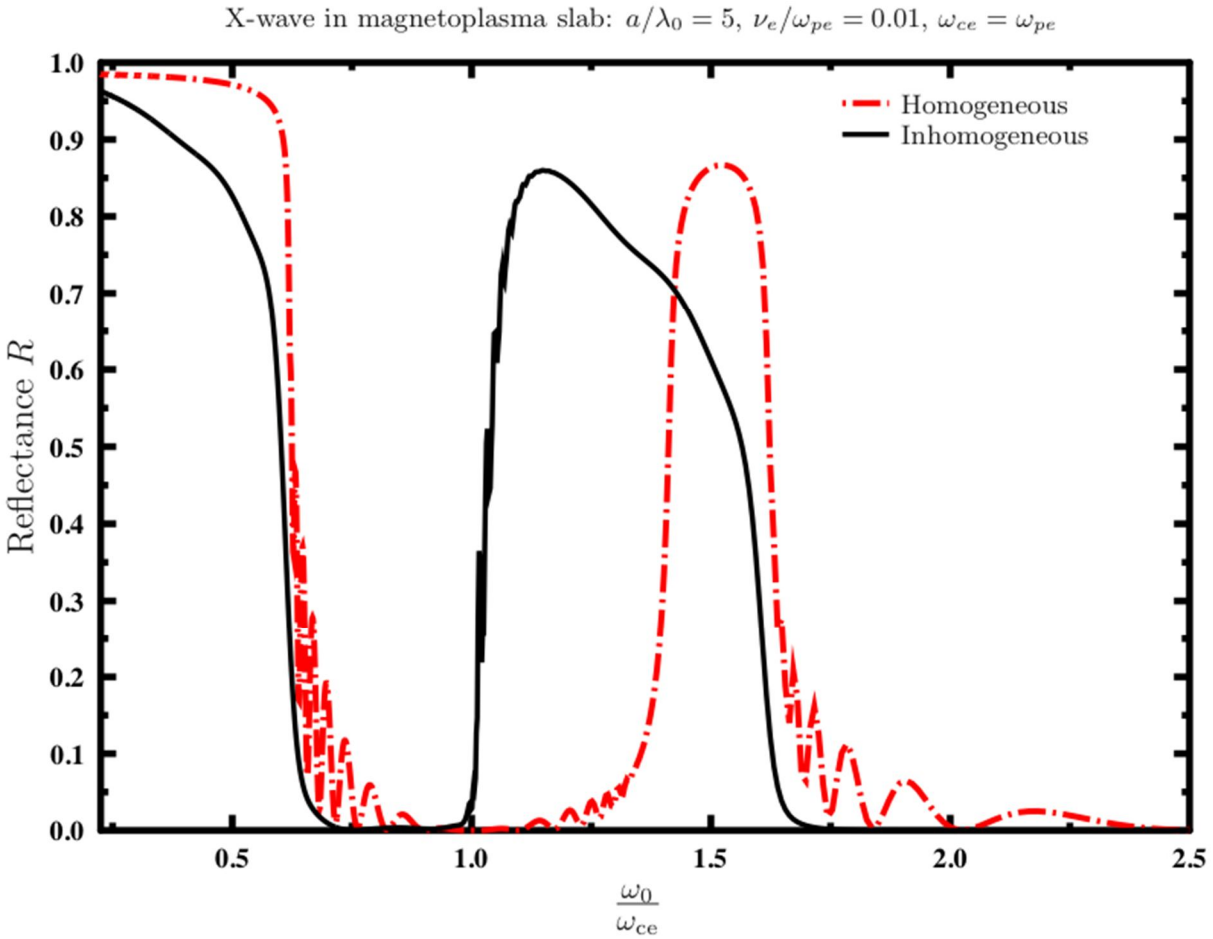

FIG. 5. Reflectance for homogeneous and inhomogeneous magnetoplasma slabs.

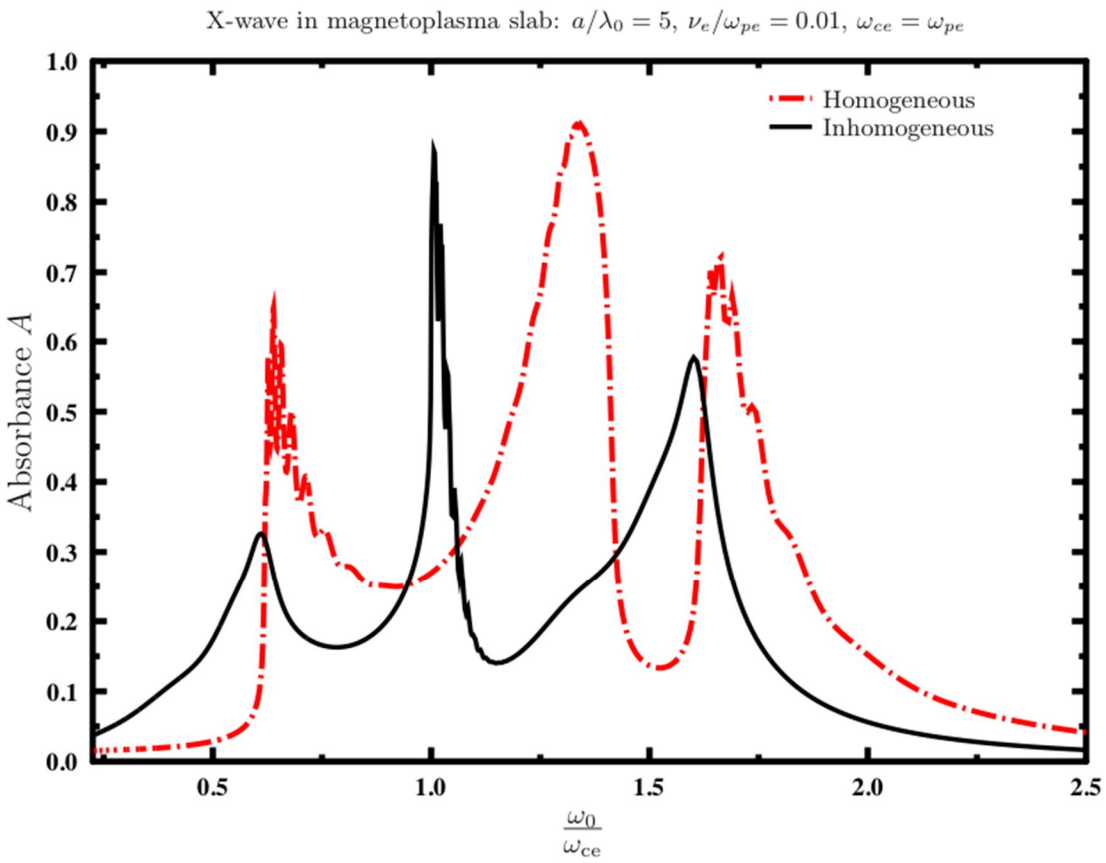

FIG. 6. Absorbance for homogeneous and inhomogeneous magnetoplasma slabs.

IV. Conclusion

In this paper, we investigate the propagation characteristics of a normally incident electromagnetic wave on a cold, weakly collisional and inhomogeneous magnetoplasma slab. Within the transfer matrix technique and for sinusoidal plasma density profile, the inhomogeneous slab is treated as a multilayered system of homogeneous sub-slabs. We only considered electron motion for wave frequencies much above the ion cyclotron frequency. For wave propagation perpendicular to a static magnetic field, only the elliptically polarized extraordinary wave is coupled to the electrons.

In Figures 2-6, the transmittance, reflectance and absorbance are plotted *versus* ω_0 / ω_{ce} for different ratios of cyclotron to plasma frequencies. By varying the wave frequency ω_0 for fixed ω_{ce}, the curves of transmittance and reflectance show two pass and two stop bands. When the ratio $\omega_{ce} / \omega_{pe}$ is increased, the bands shift to the region of low wave frequency, the pass bands become broader and the stop bands become narrower.

Curves of the absorbance show three absorption bands. The first and third bands (from left to right) of each curve are collisional absorption bands of evanescent waves at the cut-off frequencies ω_L and ω_R, respectively. The middle absorption band is due to the upper hybrid resonance.

X-wave propagation characteristics in an inhomogeneous magnetoplasma slab of finite thickness have been compared with those of a homogeneous plasma slab. The stop band $\omega_{uh} < \omega_0 < \omega_R$ for a homogeneous slab is narrower, while the stop band $0 < \omega_0 < \omega_L$ is broader. The ripples in the reflectance curves for the homogeneous slab due to in-plasma interferences are washed out by inhomogeneity. The effect of the inhomogeneity on the absorbance curves of Fig.6 is to down shift the absorption (and the stop) bands to the left toward lower wave frequencies.

A homogeneous plasma slab overestimates a collisional absorption at cut-offs and broadens the upper hybrid resonance absorption band.

References

[1] Sharma, S.R., Canadian Journal of Physics, 44 (1966) 255.

[2] Zhang, J., Fu, H. and Scales, W., IEEE Transactions on Plasma Science, 46 (2018) 2146.

[3] Gurel, C.S. and Oncu, E., Progress in Electromagnetics Research Letters, 12 (2009) 171.

[4] Bawa'aneh, M.S., Al-Khateeb, A.M. and Sawalha, A.S., Canadian Journal of Physics, 90 (2012) 241.

[5] Bawa'aneh, M.S., Al-Khateeb, A.M. and Sawalha, A.S., IEEE Transactions on Plasma Science, 41 (2013) 2496.

[6] Bawa'aneh, M. S., Al-Khateeb, A.M. and Ghim, Y.-C., IEEE Transactions on Antennas and Propagation, 66 (2018) 6525.

[7] Chen, X.-Y., Shen, F.-F., Liu, Y.-M., Ai, W. and Li, X.-P., IEEE Trans. Plasma Sci., 46 (2018) 1755.

[8] Al-Khateeb, A.M., Khasawneh, M.A. and Bawa'aneh, M.S., Advanced Electromagnetics, 8 (2019) 44.

[9] Mori, T., Nishiura, M., Yoshida, Z. and Kenmochi, N., Plasma and Fusion Research, 14 (2019) 3401134.

[10] Rawwaqa, F., Al-Ali, M.M., Al-Khateeb, A.M. and Bawa'aneh, M.S., Advanced Electromagnetics, 9 (2020) 25.

[11] Daqa, W.M., Al-Khateeb, A.M., Al-Sharif, A.I. and Laham, N.M., Jordan J. Phys., 1 (2008) 9.

[12] Chen, F.F., "Introduction to Plasma Physics and Controlled Fusion", 2nd Edn., (Plenum, New York, 1984).

[13] Stix, T.H., "Waves in Plasmas", (AIP, New York, 1992).

[14] Swanson, D.G., "Plasma Waves", 2nd Edn., (IOP Publishing, Ltd, 2003).

[15] Hutchinson, I.H., "Plasma Diagnostics", 2nd Edn., (Cambridge University Press, 2002).

[16] Laroussi, M. and Roth, J.R., IEEE Trans. Plasma Sci., 21 (1993) 366.

[17] Hu, B.J., Wei, G. and Lai, S.L., IEEE Transactions on Plasma Science, 27 (1999) 1131.

[18] Born, M. and Wolf, E., "Principles of Optics: Electromagnetic Theory of Propagation, Interference and Diffraction of Light", 7th Edn., (Cambridge University Press, 2003).

[19] Budden, K.G., "Radio Waves in the Ionosphere", (Cambridge University Press, 1961).

[20] Pedrotti, F.L., Pedrotti, L.M. and Pedrotti, L.S., "Introduction to Optics", 3rd Edn., (Cambridge University Press, 2017).

[21] Lieberman, M.A. and Lichtenberg, A.J., "Principles of Plasma Discharges and Materials Processing", 2nd Edn., (John Wiley & Sons, Inc., Hoboken, New Jersey, 2005).

[22] Bawa'aneh, M.S., Contributions to Plasma Physics, 43 (2003) 447.

[23] Bawa'aneh, M.S., Journal of Plasma Physics, 72 (2006) 687.

[24] Bawa'aneh, M.S. and Boyd, T.J.M., Journal of Plasma Physics, 73 (2007) 159.

Volume 15, Number 2, 2022. pp. 169-177

Jordan Journal of Physics

ARTICLE

Raman Spectroscopy Investigation on Semi-curve Woven Fabric-graphene Synthesized by the Chemical Vapor Deposition Process

Krishna Bahadur Rai and **Ram Phul Yadav**

Department of Physics, Patan Multiple Campus, Tribhuvan University, Kathmandu, Nepal.

Doi: **https://doi.org/10.47011/15.2.7**

Received on: 31/10/2020; *Accepted on: 04/02/2021*

Abstract: Graphene is a single layer of two-dimensional carbon atoms bound in a hexagonal lattice structure with zero band gap semiconductor. Chemical vapor deposition (CVD) is one of the most promising, inexpensive and readily ways for synthesizing monolayer pristine graphene. We have synthesized monolayer graphene shaped in semi-curve woven frabic-graphene (SWF-G) on SiO_2/Si substrate. Using Raman spectroscopy, we studied the central suspended portion (i.e., 1-6) of it exerting compression (stress) to the graphene supported on the substrate. The concentration of hole impurities on either side of the central position of semi-curve woven fabric-graphene (SWF-G) is more than on its central position. The variation of such hole doping concentration results in an upshift of 2D peak position (pos(2D)) which is opposite for high electron doping even if there is no intentional control of doping. The synthesized graphene is a single-layer high-quality new structure graphene.

Keywords: Semi-curve woven fabric-graphene, Raman spectroscopy, Charge impurities, Compression, Doping.

Introduction

Graphene is a two-dimensional single layer of carbon atoms bound in a hexagonal lattice structure with zero band gap semiconductor [1]. Graphene is now further expected to play an important role in future nanoscience and nanotechnology due to its exceptional electrical conductivity, high carrier mobility, high thermal conductivity, high optical transparency and super-hydrophobicity [2]. Chemical vapor deposition (CVD) is one of the most promising, inexpensive and readily ways for fabricating high-quality and large-area graphene. The synthesis of monolayer pristine graphene using CVD method across thin copper (Cu) foil of any size presents interesting possibilities for structural techniques. Graphene is formed based on the principle of decomposition of methane gas over a Cu substrate typically held at 1020 °C and of low solubility of carbon in Cu, such that the growth is self-limited to a single layer of graphene [3]. There are different structures of graphene, like long twisted graphene tube in millimeter length with self-supportive, partially collapsed and vertically suspended graphene [4], graphene microtubings [5], 3-D pillared graphene [6] and plane graphene, that have different chemical, electrical and mechanical properties.

The ionized impurities such as Na^+ on the silica (SiO_2) film and charged impurities introduced during the transfer process of CVD graphene induce charge puddles [7]. The impurities existing in the graphene-covered SiO_2/Si wafer strongly influence the electronic properties of graphene [8, 9, 10]. The silanol (SiOH), a hydrophilic film formed on a SiO_2/Si wafer, easily attracts polar adsorbates such as water molecules and causes carrier doping in the graphene after being transferred onto SiO_2/Si

Corresponding Author: Krishna Bahadur Rai **Email**: krishnarai135@gmail.com

wafer [11, 12, 9]. The chemical functionalization is used to shift the Fermi energy of graphene through charge transfer [7] as well as to introduce the energy band gap in a designed manner. This chemical functionalization rate and yield can be altered by using different supporting substrates [13]. An experiment suggests that when graphene is transferred onto the hydrophobic film such as polydimethylsiloxane (PDMS), the number of impurities and defects created by chemical molecules can be reduced [14]. Charge transfer complexes can be used for room-temperature deintercalation of metal atoms located between graphene and a substrate, so that the electronic properties of graphene are controlled [15]. However, research findings on the existence of doping with charge impurities and charge puddles in the semi-curve woven fabric-graphene (SWF-G or sometimes written as SGWF-G) on SiO_2/Si substrate have not been found. Along with this, it was a big challenge to tailor and assemble graphene into well-defined configuration such as SWF-G due to the lack of scalable assembly method for graphene nanostructure. In this research, we have studied the doping due to charge impurities on the different positions of SWF-G along with its way of new structure.

Experimental Details

CVD is the most useful technique for the synthesis of high-quality and large-area monolayer graphene. In this work, we used a thin foil of Cu with a thickness of 25 micrometers (μm) and a copper wire woven mesh (CWWM) having a diameter of 56 μm (Alfa-Aesar). Then, the CWWM made up using 56-μm diameter was kept over the 25-μm thickness Cu foil, as shown in schematic Fig. 1(a). Fig. 1(b) represents the schematic figure of semi-circular copper wire for the synthesis of CVD graphene. The template shown in Fig. 1(a) was employed into the thermal CVD silica chamber for the subsequent growth of SWF-G. In the initial phase, the chamber pressure was maintained at about 10^{-2} Torr and then Argon (Ar) gas was let into it at the rate of 99 sccm (sccm – standard cubic centimeters per minute) together with heating till the temperature reached 950 °C. The chamber was again adjusted to reach the temperature of 1020 °C and then Hydrogen (H_2) gas was started to pass through it at the temperature of 1003 °C for 1 hour at the rate of 99 sccm. After 1 hour cleaning with the H_2 gas at 1020 °C temperature, methane (CH_4) gas was passed into the hot-silica chamber with a gas flow rate of 21 sccm for 15 minutes at around 9.7 Torr pressure such that the system carried out the growth of SWF-G on the copper wire woven mesh-copper template. Finally, the sample was cooled rapidly at room temperature under Ar ambient atmosphere. The SWF-G/copper wire woven mesh-copper was spin-coated with polymethylmethacrylate (PMMA) followed by copper etching with ferric chloride ($FeCl_3$). Then, this PMMA/SWF-G was rinsed with deionized (DI) water more than five times (for approximately 30 minutes each). PMMA on the top of SWF-G was removed with the help of acetone for about 30 minutes used after the PMMA/SWF-G was transferred onto a bare SiO_2/Si wafer. At last, the sample of SWF-G/SiO_2/Si was cleaned by rinsing it into the DI water for more than five times again.

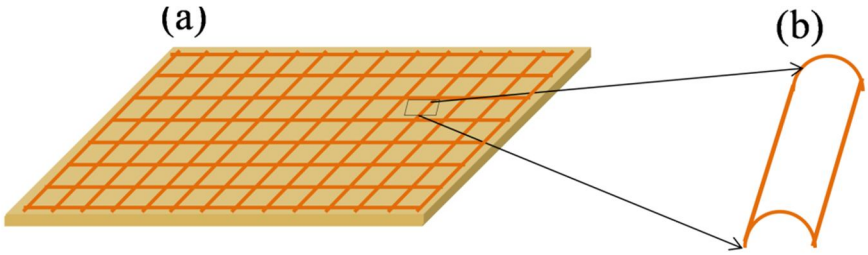

FIG. 1. (a) Schematic figure of copper foil with a thickness of 25 μm and copper wire woven mesh with a diameter of 56 μm placed over a copper foil. (b) Schematic figure of semi-circular copper wire for the synthesis of CVD graphene.

Results and Discussion

Raman spectroscopy is a sensitive tool for distinguishing single layer, bilayer and multi-layer graphene and for detecting the electronic properties of graphene [16]. It is also sensitive to defects [17], carrier doping level [18] and strains [19]. Here, we used Raman system (Inviva) with 1800 lines/mm grating, 532 nm excitation laser with 50X objective lens to confirm graphene

layer and charge impurities. The laser power was kept sufficiently lower than the damage threshold of graphene to avoid any heat-induced effects.

Fig. 2(a) shows the optical images of SWF-G/SiO_2/Si and it contains semi-curve hollow tube-graphene. Here Fig. 2(b) clearly confirms that the synthesized graphene shape is semi-curve hollow tube-graphene on SiO_2/Si substrate. In Fig. 2(c), the semi-curve hollow tube-graphene is assigned with the schematic semi-curve red line having different red spot positions and numbers of about 4.5 µm distance to each other for taking Raman spectrum.

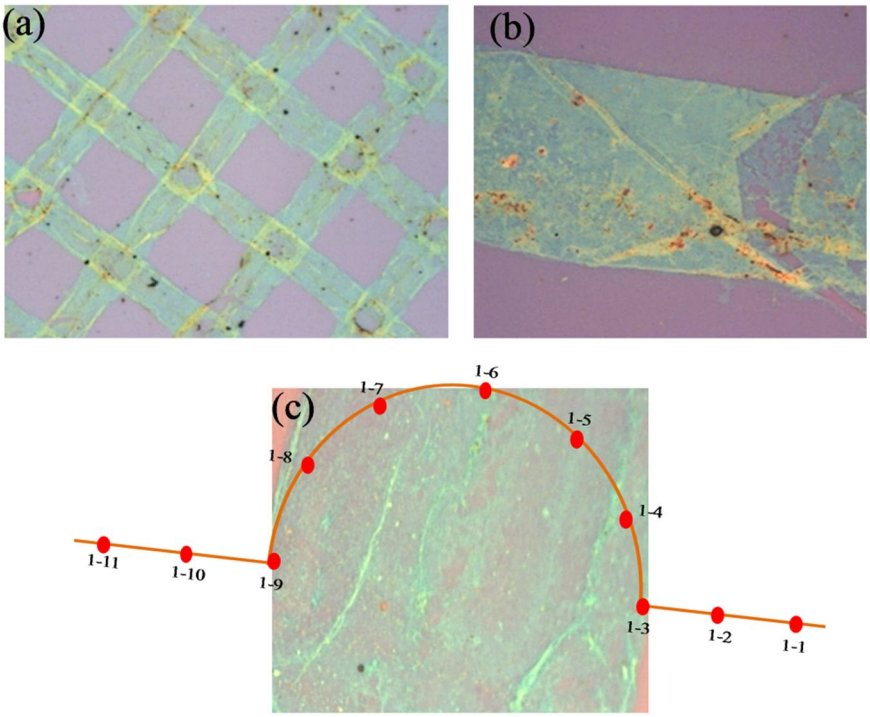

FIG. 2. (a) Woven fabric-graphene (WF-G) on SiO_2/Si. (b) Figure confirming that the synthesized graphene shape is semi-curve hollow tube graphene on SiO_2/Si substrate. (c) 11 different positions of the focused laser scanned across the semi-curve woven fabric-graphene surface on SiO_2/Si with the line mapping (red line with dot – schematic) interval of points at about 4.5 µm distance for taking Raman spectrum.

Fig. 3(a) shows the Raman spectra at 11 different positions of SWF-G with G peak position (pos(G)) and 2D peak position (pos(2D)) at 1594±4 cm^{-1} and 2684±4 cm^{-1}, respectively, from the central position 1-6. Here, the G peak (E_{2g} mode) is related to the C-C in-plane stretching for all sp^2 carbon atoms and the 2D peak (G' mode) is related to the second-order double-resonance process [20]. Raman I_{2D}/I_G intensity ratio of the central semi-curve hollow tube graphene with the value of 1.93 to about 1.41 on either side indicates that the graphene is a monolayer graphene. In the same figure, the D peak position is 1346±3 cm^{-1} on either side of position 1-6 and such D peak is the dominant sp^2 Raman signature of disorder or defects. In Fig. 3(b), pos(G) and pos(2D) peaks of 1-5, 1-4, 1-3, 1-2, 1-1 positions and 1-7, 1-8, 1-9, 1-10, 1-11 positions reveal the blue shift as compared to the pos(G) and pos(2D) peak of central position 1-6. This blue shift on either side of the central laser focused position is attributed to the compression strain [21] of semi-curve hollow tube woven fabric graphene film. The Raman spectra of pos(G) and pos(2D) peaks increase on either side of the central position in a sense that the central portion (i.e., position 1-6) of graphene is making compression stress to the graphene supported on the substrate. Slight upshifts of pos(G) = 7 cm^{-1} and pos(2D) = 7 cm^{-1} indicate a small compression.

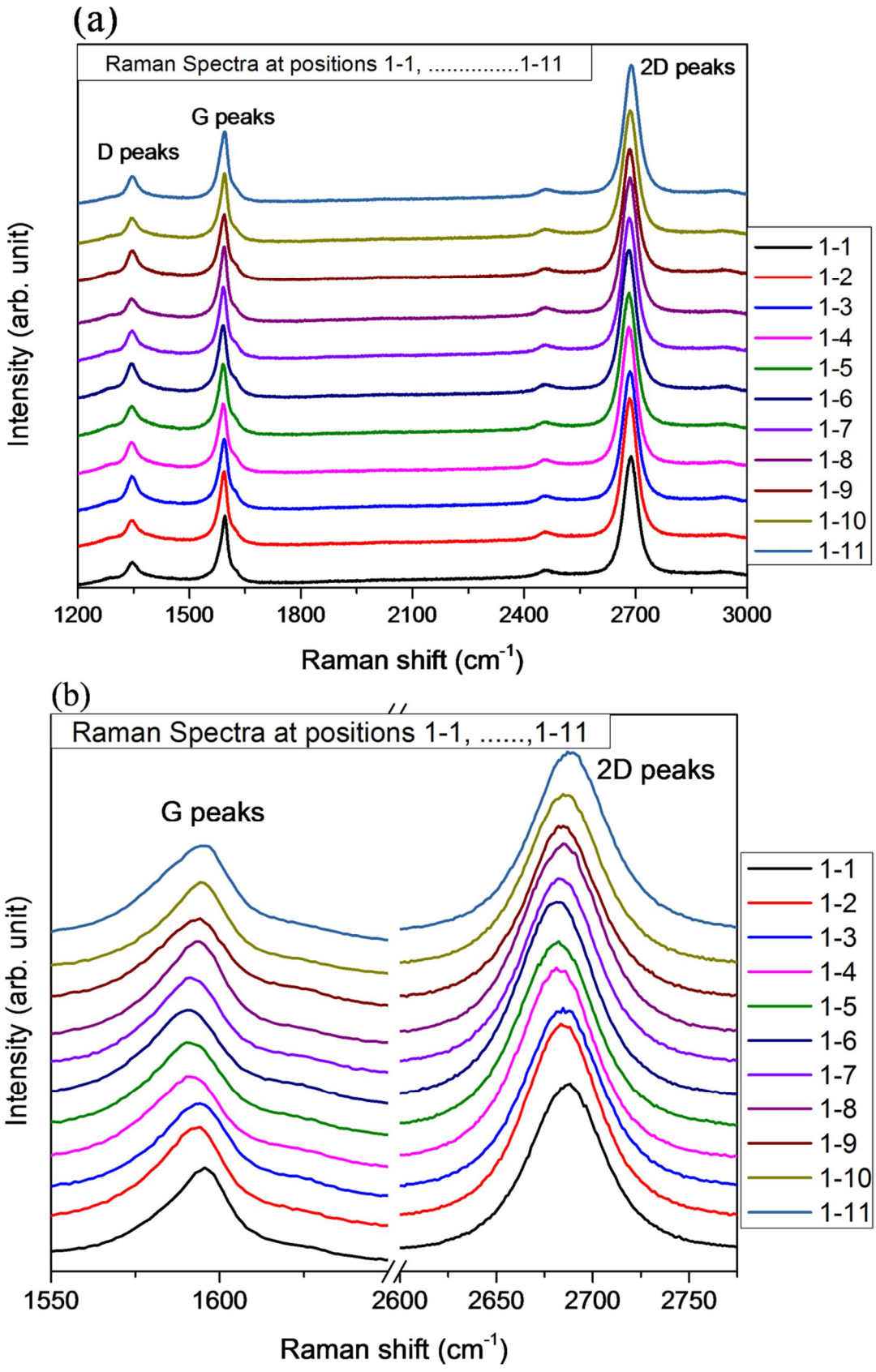
(a)
Raman Spectra at positions 1-1, ...1-11
D peaks
G peaks
2D peaks
Intensity (arb. unit)
1200
1500
1800
2100
2400
2700
3000
Raman shift (cm-1)
1-1
1-2
1-3
1-4
1-5
1-6
1-7
1-8
1-9
1-10
1-11
(b)
Raman Spectra at positions 1-1, ...,1-11
G peaks
2D peaks
Intensity (arb. unit)
1550
1600
2600
2650
2700
2750
Raman shift (cm-1)
1-1
1-2
1-3
1-4
1-5
1-6
1-7
1-8
1-9
1-10
1-11

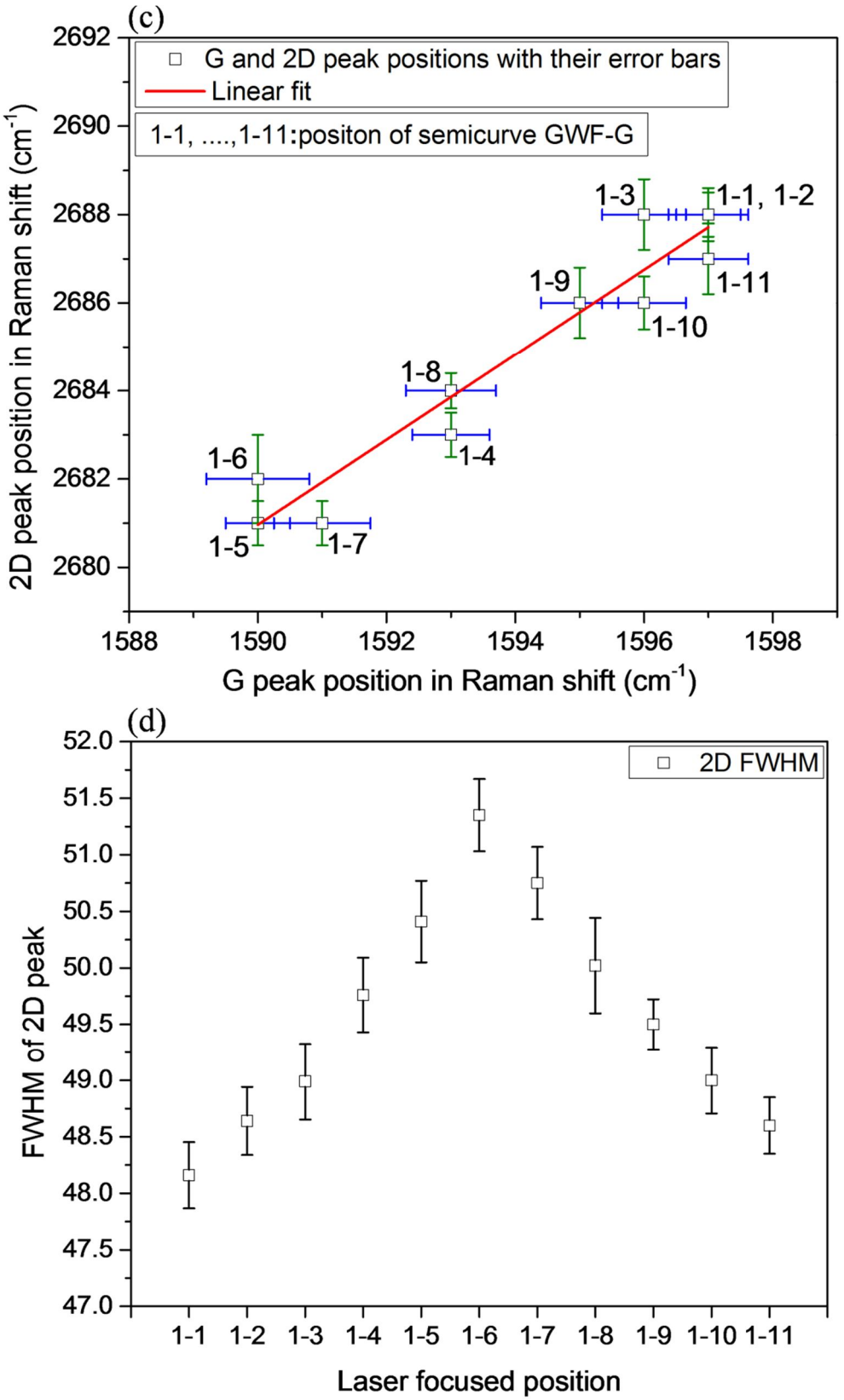

FIG. 3. (a) Raman spectra of SWF-G at 11 different positions. (b) The spectra with the G peak on the left and 2D peak on the right in which pos(G) and pos(2D) upshift from central position (i.e., 1-6) of SWF-G. (c) Linear fit for the pos(G) and pos(2D) with their blue color error bars and green color error bars for G peak position and 2D peak position, respectively. (d) FWHM of pos(2D) with their error bars and laser focused at 11 different positions with a distance of about 4.5 μm to each other on the SWF-G.

The graphene sample checked here is a monolayer graphene, as it is CVD-synthesized. The integrated intensity ratio of the 2D and G peaks (I_{2D}/I_G) is related to the doping with charged impurities in which a larger I_{2D}/I_G refers to a smaller amount of charged impurities and vice versa [14]. The upshift of the G band also reflects the doping with charged impurities [22]. However, this peak shift is less sensitive to doping than the I_{2D}/I_G ratio [18]. In Fig. 3(b), the intensities of 2D peaks at different focused positions are different in which 2D peak intensities gradually decrease on either side of the central position (i.e., at 1-6), but all G peak spectra have nearly the same intensity due to the very weak substrate charged impurities effect on the G-band intensity. Fig. 3(c) has a linear fit that correlates pos(2D) and pos(G) with their respective error bars (blue color) for G peak position and green color error bars for 2D peak position. Like the pos(G) peak, the pos(2D) peak upshifts in the same excitation energy. This allows to distinguish electron - from hole - doping in graphene [23, 24]. Fig. 3(c) also shows that pos(2D) peaks at different focused positions; i.e., at 1-1, 1-11, 1-2, 1-10 and 1-3, 1-9 is sensitive to doping as compared to pos(2D) peaks at 1-4, 1-8, 1-5, 1-7, 1-6 positions. The variation of the pos(2D) peak shift is mainly due to the hole doping resulting in an upshift and which is opposite for high-electron doing [18] even if there is no intentional control of doping. Adsorbents induced chemical doping, substrate and water could explain the p-doping [25] on positions 1-1, 1-11, 1-2, 1-10 and 1-3, 1-9. Fig. 3(d) shows the plot of 11 different laser focused positions and Full Width at Half Maximum (FWHM) of 2D peak with their error bars having values ±0.294 for position 1-1, ±0.301 for position 1-2, ±0.337 for position 1-3, ±0.33 for position 1-4, ±0.361 for position 1-5, ±0.319 for position 1-6, ±0.32 for position 1-7, ±0.422 for position 1-8, ±0.223 for position1-9, ±0.294 for position 1-10 and ±0.25 for position 1-11. From Ref. [25] and Fig. 3(c), Fig. 3(d) indicates that FWHM of 2D peak decrease corresponds to the pos(2D) peak increase on either side of position 1-6. This is quite similar to what we observed in intentionally doped graphene, where the Fermi energy was modulated using a gate [26].

In Fig. 4(a), the Raman 2D band was fitted with Lorentzian-shaped curve at various positions of the SWF-G sample. The symmetric shape and narrow width of the 2D band [27] suggest that the synthesized graphene is in fact of a single layer and the situation background of graphene quality is understood. Since the Raman spectrum of graphene is on the SiO_2 substrate and there is no fluorescence effect, this 2D band Lorentzian has the phonon flat background**.** Raman spectrum in Fig. 4(b) shows Lorentzian line shape fit of the G peak of single-layer graphene. Fig. 4(c) has FWHM of G peak and Ref. [28] studied that the peak pos(G) band in Fig. 3(c) and FWHM of G band have an inverse relation in monolayer-graphene sample. Fig. 4(d) shows the G peak position and the I_{2D}/I_G ratio as a function of position of laser focused points in SWF-G (or SGWF-G). The different I_{2D}/I_G ratios at different positions are: at position 1-1, I_{2D}/I_G = 1.41, at position 1-2, I_{2D}/I_G = 1.42, at position 1-3, I_{2D}/I_G = 1.64, at position 1-4, I_{2D}/I_G = 1.78; at position 1-5, I_{2D}/I_G = 1.9, at position 1-6, I_{2D}/I_G = 1.93, at position 1-7, I_{2D}/I_G = 1.89, at position 1-8, I_{2D}/I_G = 1.79, at position 1-9, I_{2D}/I_G = 1.6, at position 1-10, I_{2D}/I_G = 1.41 and at position 1-11, I_{2D}/I_G = 1.4. This clearly shows a large variation with hole doping: at low doping, the 2D peak intensity is stronger than the G peak intensity such that I_{2D}/I_G ratio is 1.93 (maximum) at that central position 1-6 and this is due to the no-substrate effect on the top of semi-curve hollow graphene. The decreases in maximum I_{2D}/I_G ratio on either side corresponds to the blue shift in the 2D peaks [29] for other laser focused positions. At high doping, the I_{2D}/I_G ratio is low and corresponds to 1.41 at position 1-1, while at position 1-11, I_{2D}/I_G = 1.4. This may indicate that the doping on the graphene is due to the charge transfer from the underlying substrate SiO_2/Si.

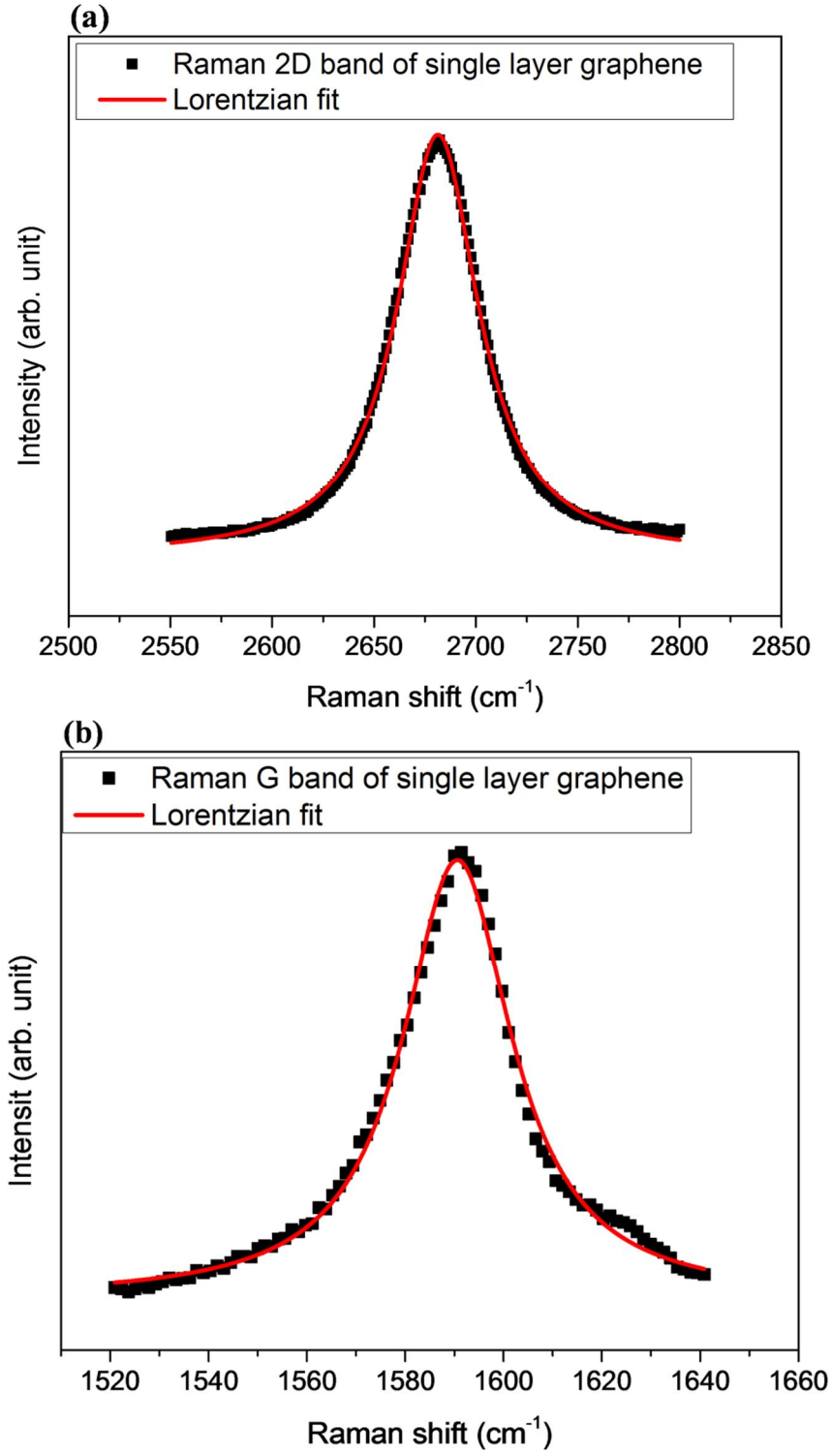
(a)
Raman 2D band of single layer graphene
Lorentzian fit
Intensity (arb. unit)
2500
2550
2600
2650
2700
2750
2800
2850
Raman shift (cm-1)
(b)
Raman G band of single layer graphene
Lorentzian fit
Intensit (arb. unit)
1520
1540
1560
1580
1600
1620
1640
1660
Raman shift (cm-1)

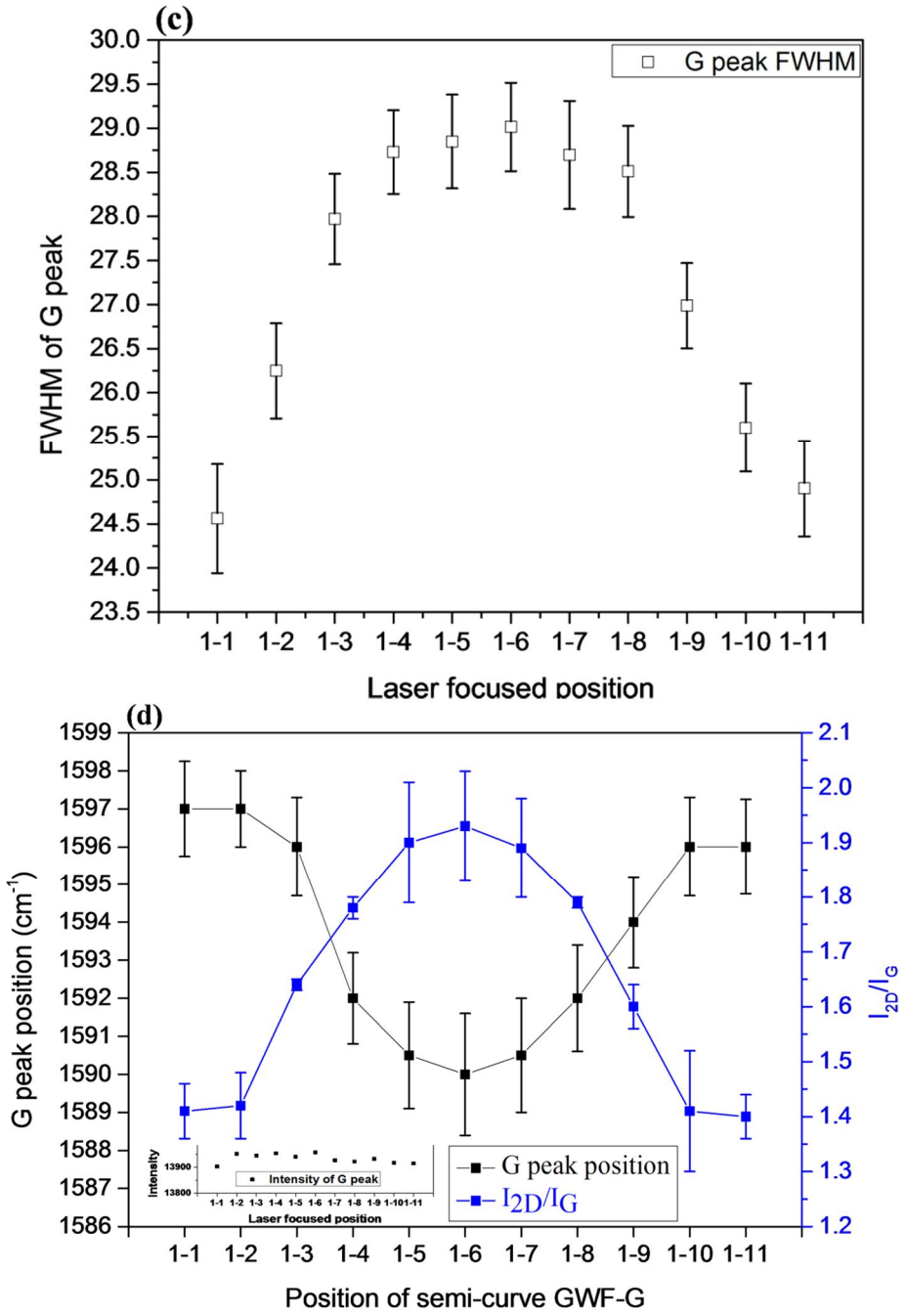

FIG. 4. (a) Raman spectrum (black dot line) of SWF-G fitted by Lorentzian fitting (red line). (b) Lorentzian fit of the G peak. (c) FWHM and its error bars for G peak at 11 different positions. (d) Pos(G) and I_{2D}/I_G ratio as function of 11 different laser focused positions of SWF-G or SGWF-G. An inset in the bottom left of the figure contains nearly the same intensity of the G peak.

Conclusions

We presented a systematic analysis of the Raman spectra of deposited semi-curve woven fabric-graphene on SiO_2/Si substrate. The increasing pos(G) and pos(2D) peak on either side of the central portion (i.e., position 1-6) of graphene is making compression (stress) to the graphene supported on the substrate. The large variation in Raman parameters is assigned to inhomogeneous unintentional hole doping from substrate's charge impurities. In particular, we show how graphene doping levels vary within the same flake depending on the distance between the graphene and substrate. Such structure of graphene (SWF-G) might have future applications on supercapacitor and hydrogen energy storage devices.

References

[1] Novoselov, K.S., Geim, A.K., Morozov, S.V., Jiang, D., Zhang, Y., Dubonos, S.V., Grigorieva, I.V. and Firsov, A.A., Science, 306 (2004) 666.

[2] Zhu, Y., Murali, A., Cai, W., Li, X., Suk, J.W., Potts, J.R. and Ruoff, R.S., Adv. Mater., 22 (2010) 3906.

[3] Polat, E.O., Balci, O., Kakenov, N., Uzlu, H.B., Kocabas, C. and Dahiya, R., Sci. Rep., 5 (2015) 16744.

[4] Rai, K.B., Int. J. Adv. Eng., 2(2) (2019) 31.

[5] Hu, C., Zhao, Y., Cheng, H., Wang, Y., Dong. Z., Jiang, C., Zhai, X., Jiang, L. and Qu, L., Nano Lett., 12(11) (2012) 5879.

[6] Gosh, K., Yue, C.Y., Moniruzzaman, S.K. and Jena, R.K., Appl. Mater. and Interfaces, 9(18) (2017) 15350.

[7] Fan, X., Nouchi, R., Tanigaki, K., J. Phys. Chem. C, 115 (2011) 12960.

[8] Jimenez-Villacorta, F., Climent-Pascual, E., Ramirez-Jimenez, R., Sanchez-Marcos, J., Prieto, C. and Andres, A.D., Carbon, 101 (2016) 305.

[9] Lafkioti, M., Krauss, B., Lohmann, T., Zschieschang, U., Klauk. H., Klitzing, K.V. and Hosono, H., Nano Lett., 10 (2010) 1149.

[10] Kreil, D., Haslhofer, M. and Bohm, H.M., Lithuanian Journal of Physics, 59(1) (2019) 35.

[11] Lee, D.E., Ahn, G. and Ryu, S., J. Am. Chem. Soc., 136 (18) (2014) 6634.

[12] Brandenburg, J.G., Zen, A., Fitzner, M., Ramberger, B., Kresse, G., Tsatsoulis, T., Gruneis, A., Michaelides, A. and Alfe, D., J. Phys. Chem. Lett., 10 (2019) 358.

[13] Wang, Q.H., Jin, Z., Kim, K.K., Hilmer, A.J., Paulus, G.L. C., Shih, C.J., Ham, M.H., Sanchez-Yamaghishi, J.D., Watanabe, K., Taniguchi, T., Kong, J., Jarrilo-Herero, P. and Strano, M.S., Nat. Chem., 4 (2012) 724.

[14] Rai, K.B., Khadka, I.B., Kim, E.H., Ahn, S.J., Kim, H.W. and Ahn, J.R., J. Korean Phys. Soc., 72 (1) (2018) 107.

[15] Shin, H.C., Ahn, S.J., Kim, H.W., Moon, Y., Rai, K.B., Woo, S.H. and Ahn, J.R., Appl. Phys. Lett., 109 (2016) 081603.

[16] Bayle, M., Reckinger, N., Huntzinger, J.R., Felten, A., Bakaraki, A., Landois, P., Colomer, J.F., Henrard, L., Zahab, A.A., Sauvajol, J.L. and Paillet, M., Phys. Status Solidi B, 252 (11) (2015) 2375.

[17] Ferrari, A.C. and Basko, D.M., Nat. Nanotechnol., 8 (2013) 235.

[18] Kim, S.J., Park, S.J., Kim, H.Y., Jang, G.S., Park, D.J., Park, J.Y., Lee, S. and Ahn, Y.H., Appl. Phys. Lett., 108 (2016) 203111.

[19] Mueller, N.S., Heeg, S., Alvarez, P.M., Kusch, P., Wasserroth, S., Clark, N., Schedin, F., Parthenios, J., Papagelis, K., Galiotis, C., Kalbac, M., Vijayaraghavan, A., Huebner, U., Gorbacheb, R., Frank, O. and Reich, S., 2D Mater., 5 (2017) 015016.

[20] Jorio, A., Dresselhaus, M.S., Saito, R. and Dresselhaus, G., "Raman Spectroscopy in Graphene-related System", 1st Edn., (Weinheim Wiley, 2011).

[21] Ding, J., Fisher, F.T. and Yang, F.H., J. Vac. Sci. Technol. B, 34 (2016) 051205.

[22] Ni, Z.H., Yu, T., Luo, Z.Q., Wang, Y.Y., Liu, L., Wong, C.P., Miao, J., Huang, W. and Shen, Z.X., ACS Nano, 3 (3) (2009) 569.

[23] Bruna, M., Otta, A.K., LJas, M.I., Yoon, D., Sassi, Y. and Ferrai, A.C., ACS Nano, 8 (7) (2014) 7432.

[24] Mazeikiena, R., Niaura, G., Eicher-Lorka, O. and Malinauskas, A., Chemija, 30 (2) (2019) 78.

[25] Schedin, F., Geim, A.K., Morozov, S.V., Hill, E.H., Blake, P., Katsnelson, M.I. and Novoselov, K.S., Nat. Mater., 6 (2007) 652.

[26] Pisana, S., Lazzeri, M., Casiraghi, C., Novoselov, K.S., Geim, A.K., Ferrai, A.C. and Mauri, F., Nat. Mater., 6 (2007) 198.

[27] Woehrl, N., Ochedowski, O., Gottlieb, S., Shibasaki, K. and Schulz, S., AIP Adv., 4 (2014) 047128.

[28] Casiraghi, C., Pisana, S., Novoselov, K.S., Geim, A.K. and Ferrai, A.C., Appl. Phys. Lett., 91 (2007) 233108.

[29] Oh, T., Trans. on Electrical and Electronic Mater., 14 (5) (2013) 246.

Volume 15, Number 2, 2022. pp. 179-193

Jordan Journal of Physics

ARTICLE

Solutions of the Non-relativistic Equation Interacting with the Varshni-Hellmann Potential Model with Some Selected Diatomic Molecules

Eddy S. William[a], **Etido P. Inyang**[a,b], **Joseph E. Ntibi**[b], **Joseph A. Obu**[b] and **Ephraim P. Inyang**[b]

[a] *Department of Physics, National Open University of Nigeria, Jabi, Abuja, Nigeria*
[b] *Theoretical Physics Group, Department of Physics, University of Calabar, PMB 1115, Calabar, Nigeria.*

Doi: **https://doi.org/10.47011/15.2.8**
Received on: 13/11/2020; *Accepted on: 01/02/2021*

Abstract: The approximate solutions of Schrödinger equation for the newly proposed Varshni-Hellmann potential (VHP) are obtained within the framework of the Nikiforov-Uvarov method by employing the Greene-Aldrich approximation scheme to deal with the centrifugal term. The numerical results of the ro-vibrational energies and normalized wavefunction in closed form are obtained in terms of Jacobi polynomials for various quantum states of the diatomic molecules of LiH, TiH, CrH and ScN, respectively. Four special cases of the potential are also studied and their numerical energy eigenvalues evaluated are in agreement with those reported in the existing literature. Also, the behavior of the energy spectra for the ground state of the selected diatomic molecules is illustrated graphically.

Keywords: Schrödinger equation; Varshni-Hellmann potential, Nikiforov-Uvarov method, Diatomic molecules.

1. Introduction

The exact and approximate solutions of quantum wave equations like Schrödinger, Lippmann-Schwinger, Klein-Gordon and Dirac equations, have been a striking research area under discussion in physics, chemistry and applied mathematics [1-4]. The Schrödinger equation is a second-order differential equation used in solving quantum mechanical problems [5]. The eigenvalues and wave functions contain considerable information about quantum systems, such as atomic structure, quantum electrodynamics and vibrations in molecules [6-9]. The wave functions and their equivalent eigenvalues give considerable information on describing different quantum systems, such as the atomic structure theory, quantum-chemical theory, quantum electrodynamics theory and theory of molecular vibrations [6-9]. With the experimental proof of the Schrödinger wave equation, researchers have dedicated much attention to solving the radial Schrödinger equation with different analytical methods to obtain approximate bound-state solutions for some physical potential models, such as Yukawa potential [10], Wood-Saxon potential [11], Eckart potential [12], generalized Morse potential [13], Makorov potential [14], Hulthen potential [15], Hellmann potential [16], … etc., by using certain approximation schemes. The most widely used approximation was introduced by Pekeris [17] and another form was suggested by Greene and Aldrich [18].

Efforts have been made by many researchers to solve the Schrödinger and Klein-Gordon equations by the superposition of different potentials, which can be used for a wider range of applications [19, 20]. For example, William et al. studied Hulthen potential together with

Corresponding Author: Etido P. Inyang **Email**: etidophysics@gmail.com

Hellmann potential [21], Ahmadov et al. solved the Klein-Gordon equation by Manning-Rosen plus a class of Yukawa potentials [22], Manning-Rosen potential plus a ring-shaped like potential [23], Aspoukeh and Hamad studied the Klein-Gordon equation for vector and scalar Hellmann plus modified Kratzer potentials [24] and Hans Hellmann investigated the Schrödinger equation with a linear combination of Coulomb and Yukawa potential, which is called Hellmann potential [25]. The Hellmann potential has been applied to several branches in physics, such as atomic physics, plasma physics, solid-state physics, … etc. [26–30], as well as in the study of electron-core [31], electron-ion [32] and inner-shell ionization problems and alkali hydride molecules [33]. The bound-state energy eigenvalues have been obtained by other researchers in Refs. [34-41]. The Hellmann potential is of the form [25, 42-46]:

$$V(r) = -\frac{c}{r} + \frac{de^{-\beta r}}{r} \tag{1}$$

where r is the inter-nuclear distance, c, and d are the strengths of Coulomb and Yukawa potentials and β is the screening parameter. The Varshni potential is of the form [47]:

$$V(r) = a\left[1 - \frac{b}{r}e^{-\beta r}\right] \tag{2}$$

where a and b are the strengths of the Varshni potential, respectively and β is the screening parameter which controls the shape of the potential energy curve. Varshni potential is a short-range repulsive potential energy function which has been investigated within the formalism of the Schrödinger equation and plays a fundamental role in chemical and molecular physics. Many authors have worked on this potential, such as in Refs. [48, 49].

In this study, we attempt to study the radial Schrödinger equation with a newly proposed potential obtained by the superposition of Varshni and Hellmann potential (VHP). The potential is of the form:

$$V(r) = a - \frac{abe^{-\beta r}}{r} - \frac{c}{r} + \frac{de^{-\beta r}}{r}. \tag{3}$$

The shape of this potential as a function of inter-nuclear distance of LiH, TiH, CrH and ScN diatomic molecules is presented in Fig. 1.

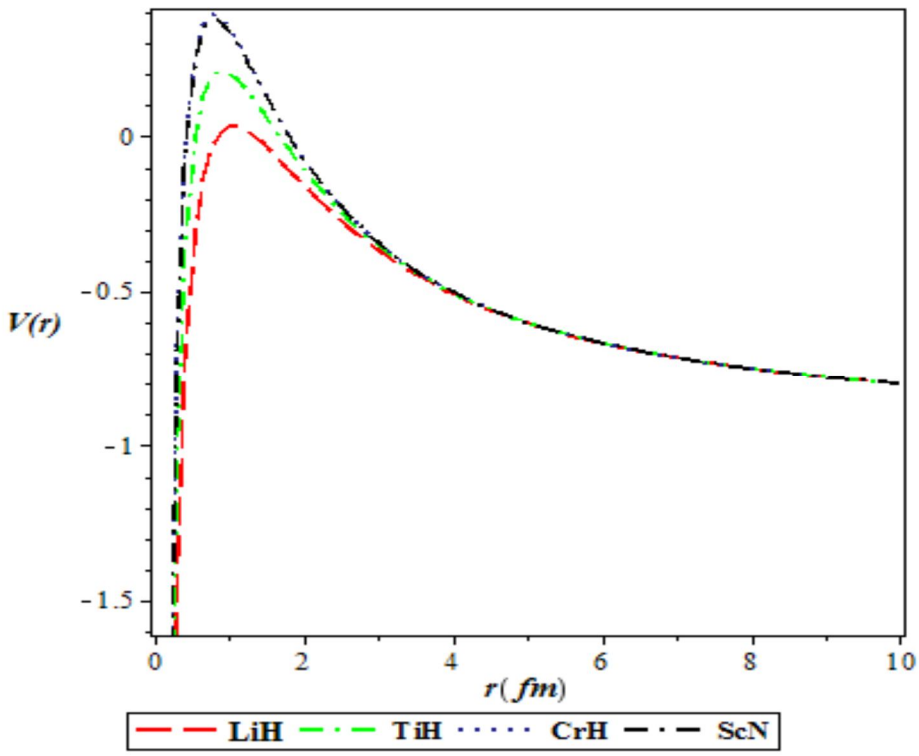

FIG. 1. Variation of Varshni plus Hellmann potential as a function of r for the selected diatomic molecules.

2. Bound-state Solutions of the Schrödinger Equation with VHP

The radial part of the Schrödinger equation is given by [50, 51]:

$$\frac{d^2R_{nl}(r)}{dr^2}+\left[\frac{2\mu}{\hbar^2}(E_{nl}-V(r))-\frac{l(l+1)}{r^2}\right]R_{nl}(r)=0 \quad (4)$$

where μ is the reduced mass, E_{nl} is the energy spectrum to be determined, $\hbar$ is the reduced Planck's constant, r is the inter-particle distance, $V(r)$ is the interacting potential, $\frac{\ell(\ell+1)}{r^2}$ is the centrifugal term and n and l are the radial and orbital angular momentum quantum numbers, respectively. In solving Eq.(4) analytically, we introduce the Greene-Aldrich approximation scheme [18,52] to deal with the centrifugal barrier. This approximation scheme is a good approximation to the centrifugal barrier which is valid for $\beta << 1$ and is given as:

$$\frac{1}{r^2}\approx\frac{\beta^2}{\left(1-e^{-\beta r}\right)^2}. \quad (5)$$

Substituting Eq. (3) and Eq. (5) into Eq. (4), we have:

$$\frac{d^2R_{nl}(r)}{dr^2}+\left[\frac{2\mu}{\hbar^2}\left(E_{nl}-a+\frac{ab\beta e^{-\beta r}}{(1-e^{-\beta r})}+\frac{c\beta}{(1-e^{-\beta r})}-\frac{d\beta e^{-\beta r}}{(1-e^{-\beta r})}\right)-\frac{\beta^2 l(l+1)}{(1-e^{-\beta r})^2}\right]R_{nl}(r)=0. \quad (6)$$

By using coordinate transformation:

$$x=e^{-\beta r}. \quad (7)$$

we obtain the differential equation of the form:

$$\frac{d^2R(x)}{dx^2}+\frac{1-x}{x(1-x)}\frac{dR(x)}{dx}+\frac{1}{x^2(1-x)^2}[-(\varepsilon+\varsigma_0)x^2+(2\varepsilon+\varsigma_0-\varsigma_1)x-(\varepsilon-\varsigma_1+\gamma)]R(x)=0 \quad (8)$$

where

$$-\varepsilon=\frac{2\mu E_{nl}}{\hbar^2\beta^2}-\frac{2a\mu}{\hbar^2\beta^2},\varsigma_0=\frac{2ab\mu}{\hbar^2\beta}-\frac{2d\mu}{\hbar^2\beta},\varsigma_1=\frac{2c\mu}{\hbar^2\beta},\gamma=l(l+1). \quad (9)$$

Comparing Eqs. (8) and (A1),we have the following parameters:

$$\tilde{\sigma}(x)=-(\varepsilon+\varsigma_0)x^2+(2\varepsilon+\varsigma_0-\varsigma_1)x-(\varepsilon-\varsigma_1+\gamma),\sigma(x)=x(1-x),\tilde{\tau}(x)=1-x\}. \quad (10)$$

Substituting Eq. (10) into Eq. (A9), we obtain:

$$\pi(x)=-\frac{x}{2}\pm\sqrt{(A-k)x^2+(k+B)x+C} \quad (11)$$

where

$$A=\frac{1}{4}+\varepsilon+\varsigma_0,B=-(2\varepsilon+\varsigma_0-\varsigma_1),C=\varepsilon-\varsigma_1+\gamma\Big\}. \quad (12)$$

To find the constant k, the discriminant of the expression under the square root of Eq. (11) must be equal to zero. As such, we have:

$$k=\varsigma_0+\varsigma_1-2\gamma\pm2\sqrt{\varepsilon-\varsigma_1+\gamma}\sqrt{\gamma+\frac{1}{4}}. \quad (13)$$

Substituting Eq. (13) into Eq. (11), we obtain:

$$\pi(x)=-\frac{x}{2}\pm\left(\sqrt{\varepsilon-\varsigma_1+\gamma}+\sqrt{\gamma+\tfrac{1}{4}}\right)x-\sqrt{\varepsilon-\varsigma_1+\gamma}, \quad (14)$$

with $\tau(x)$ being obtained as:

$$\tau(x)=1-2x-2\sqrt{\varepsilon-\varsigma_1+\gamma}x-2\sqrt{\gamma+\tfrac{1}{4}}x+2\sqrt{\varepsilon-\varsigma_1+\gamma}. \quad (15)$$

Taking the derivative of Eq. (15) with respect to x, we have:

$$\tau'(x)=-2-2\left(\sqrt{\varepsilon-\varsigma_1+\gamma}+\sqrt{\gamma+\frac{1}{4}}\right). \quad (16)$$

Referring to Eq. (A10), we define the constant λ as:

$$\lambda=-\frac{1}{2}-\sqrt{\varepsilon-\varsigma_1+\gamma}-\sqrt{\gamma+\tfrac{1}{4}}+\varsigma_0+\varsigma_1-2\gamma-2\sqrt{\varepsilon-\varsigma_1+\gamma}\sqrt{\gamma+\tfrac{1}{4}}. \quad (17)$$

Also, taking the derivative of σ(x) with respect to x from Eq. (10), we have:

$$\sigma''(x)=-2. \quad (18)$$

Substituting Eqs. (15) and (18) into Eq. (A11), we obtain:

$$\lambda_n = n^2 + n + 2n\left(\sqrt{\varepsilon - \varsigma_1 + \gamma} + \sqrt{\gamma + \frac{1}{4}}\right). \quad (19)$$

Equating Eqs. (17) and (19) and substituting Eq.(9) yield the energy eigenvalues equation of the Varshni plus Hellmann potential in the form:

$$E_{nl} = a + \frac{\beta^2\hbar^2 l(l+1)}{2\mu} - \beta c - \frac{\beta^2\hbar^2}{8\mu}\left[\frac{(n+l+1)^2 + \frac{2ab\mu}{\hbar^2\beta} + \frac{2d\mu}{\hbar^2\beta} - \frac{2c\mu}{\hbar^2\beta} + l(l+1)}{(n+l+1)}\right]^2. \quad (20)$$

To obtain the corresponding wave function, we consider Eq. (A4) and upon substituting Eqs. (10) and (14) and integrating, we get:

$$\phi(x) = x^{\sqrt{\varepsilon - \varsigma_1 + \gamma}}\left(1-x\right)^{\frac{1}{2} + \sqrt{\frac{1}{4} + \gamma}}. \quad (21)$$

To get the hypergeometric function, we first determine the weight function of Eq. (A6); upon differentiating the left hand side we obtain:

$$\frac{\rho'(x)}{\rho} = \frac{\tau(x) - \sigma'(x)}{\sigma(x)}. \quad (22)$$

Substituting Eqs. (14) and (10) into Eq. (22) and integrating, we simplify obtain:

$$\rho(x) = x^{2\sqrt{\varepsilon - \varsigma_1 + \gamma}}\left(1-x\right)^{2\sqrt{\frac{1}{4} + \gamma}}. \quad (23)$$

By substituting Eqs. (10) and (23) into Eq. (A5), we obtain the Rodrigues equation as:

$$y(x) = N_{nl}x^{-2\sqrt{\varepsilon - \varsigma_1 + \gamma}}(1 - x)^{-2\sqrt{\frac{1}{4} + \gamma}}\frac{d^n}{dx^n}\left[x^{n+2\sqrt{\varepsilon - \varsigma_1 + \gamma}}(1-x)^{n+2\sqrt{\frac{1}{4} + \gamma}}\right] \quad (24)$$

where N_{nl} is the normalization constant. Equation (24) is a equivalent to:

$$P_n^{\left(2\sqrt{\varepsilon - \varsigma_1 + \gamma}, 2\sqrt{\frac{1}{4} + \gamma}\right)}(1 - 2x) \quad (25)$$

where $p_n^{(\alpha,\beta)}$ is the Jacobi Polynomial. The wave function is given as:

$$\psi_{nl}(x) = N_{nl}x^{\sqrt{\varepsilon - \varsigma_1 + \gamma}}(1 - x)^{\frac{1}{2} + \sqrt{\frac{1}{4} + \gamma}}P_n^{\left(2\sqrt{\varepsilon - \varsigma_1 + \gamma}, 2\sqrt{\frac{1}{4} + \gamma}\right)}(1 - 2x). \quad (26)$$

Using the normalization condition, we obtain the normalization constant as follows:

$$\int_0^\infty |\psi_{nl}(r)|^2\, dr = 1. \quad (27)$$

From our coordinate transformation of Eq. (7), we have:

$$-\frac{1}{\beta x}\int_1^0 |\psi_{nl}(x)|^2\, dx = 1. \quad (28)$$

By letting $y = 1 - 2x$, we have:

$$\frac{N_{nl}^2}{\beta}\int_{-1}^{1}\left(\frac{1-y}{2}\right)^{2\sqrt{\varepsilon+\gamma}}\left(\frac{1+y}{2}\right)^{1+2\sqrt{\frac{1}{4}+\gamma}}\left[P_n^{\left(2\sqrt{\varepsilon+\gamma}, 2\sqrt{\frac{1}{4}+\gamma}\right)}y\right]^2 dy = 1. \quad (29)$$

Let

$$\upsilon = 1 + 2\sqrt{\frac{1}{4} + \gamma}, \upsilon - 1 = 2\sqrt{\frac{1}{4} + \gamma}, \; u = 2\sqrt{\varepsilon + \gamma}\Big\}. \quad (30)$$

By substituting Eq. (30) into Eq. (29), we have:

$$\frac{N_{nl}^2}{\beta}\int_{-1}^{1}\left(\frac{1-y}{2}\right)^{u}\left(\frac{1+y}{2}\right)^{\upsilon}\left[P_n^{(2u,\upsilon-1)}y\right]^2 dy = 1. \quad (31)$$

According to Onate and Ojonubah [53], the integral of the form in Eq. (31) can be expressed as:

$$\int_{-1}^{1}\left(\frac{1-p}{2}\right)^{x}\left(\frac{1+p}{2}\right)^{y}\left[P_n^{(2x,2y-1)}p\right]^2 dp = \frac{2\Gamma(x+n+1)\Gamma(y+n+1)}{n!x\Gamma(x+y+n+1)}. \quad (32)$$

Hence, by comparing Eq. (31) with the standard integral of Eq. (32), we obtain the normalization constant as:

$$N_{nl} = \sqrt{\frac{n!u\beta\ \Gamma(\mathrm{u}+\upsilon+\mathrm{n}+1)}{2\Gamma(u+n+1)\Gamma(\upsilon+n+1)}}. \quad (33)$$

3. Results and Discussion

In this section, we present the numerical results of the energy eigenvalues in atomic mass units $(\hbar = 2\mu = 1)$ of VHP as a function of the screening parameter for 1S, 2S, 2P, 3S, 3P, 3d, 4S and 4P states with three different values of the potential range: $a = -1, \mathrm{b} = 1, c = 1, d = -1$; $a = -2, b = 2, c = 2, d = -2$ and $a = 1,\ b = -1,\ c = 4,\ d = -4$, respectively, as presented

in Table 1. It is observed that as the potential range increases, the energy of the system decreases. It is also observed that as the orbital angular momentum quantum number increases, the energy of the system increases. We then apply the spectroscopic data obtained from Ref. [54], as presented in Table 2, to compute the ro-vibrational energies of VHP for the diatomic molecules of LiH, TiH, CrH and ScN with the help of Eq. (20) and the numerical computation is presented in Table 3. Here, we have implemented the conversions: 1 amu = 931.494028 MeV/c^2 and $\hbar c =$ 1973.29 eVÅ [55]. It is observed that for each vibrational quantum number, the ro-vibrational energy increases with the increase in the rotational quantum number, for each selected diatomic molecule.

TABLE 1. Energy eigenvalues (eV) of the VHP in atomic mass units $(\hbar = 2\mu = 1)$.

State	α	$a=-1, b=1,$ $c=1, d=-1$	$a=-2, b=2,$ $c=2, d=-2$	$a=1, b=-1,$ $c=4, d=-4$
1s	0.025	−3.237656250	−17.95015625	−19.23765625
	0.050	−3.225625000	−17.90062500	−19.22562500
	0.075	−3.213906249	−17.85140626	−19.21390625
	0.100	−3.202500000	−17.80250000	−19.20250000
	0.150	−3.180625000	−17.70562499	−19.18062500
2s	0.025	−1.550625000	−5.950625000	−4.050625000
	0.050	−1.540000000	−5.902500000	−4.040000000
	0.075	−1.530625000	−5.855625002	−4.030625000
	0.100	−1.522500000	−5.810000000	−4.022500000
	0.150	−1.510000000	−5.722499998	−4.010000000
2p	0.025	−1.540351562	−5.924726562	−4.021601562
	0.050	−1.517656250	−5.848906250	−3.980156250
	0.075	−1.494414062	−5.772539065	−3.938164062
	0.100	−1.470625000	−5.695625000	−3.895625000
	0.150	−1.421406250	−5.540156250	−3.808906250
3s	0.025	−1.238906250	−3.729184028	−1.238906250
	0.050	−1.230625000	−3.683402778	−1.230625000
	0.075	−1.225156250	−3.640434028	−1.225156250
	0.100	−1.222500000	−3.600277778	−1.222500000
	0.150	−1.225625000	−3.528402777	−1.225625000
3p	0.025	−1.233819444	−3.717152778	−1.225486111
	0.050	−1.218611111	−3.657500000	−1.201944445
	0.075	−1.204375000	−3.598819444	−1.179375000
	0.100	−1.191111111	−3.541111111	−1.157777778
	0.150	−1.167500000	−3.428611110	−1.117500000
3d	0.025	−1.227517361	−3.703906250	−1.210850695
	0.050	−1.227517361	−3.626736111	−1.168402778
	0.075	−1.172656250	−3.546267361	−1.122656250
	0.100	−1.140277778	−3.462500000	−1.073611111
	0.150	−1.065625000	−3.285069444	−0.9656250000
4s	0.025	−1.130625000	−2.952500000	−0.2556250000
	0.050	−1.125625000	−2.910000000	−0.2506250000
	0.075	−1.125625000	−2.872500000	−0.2506250000
	0.100	−1.130625000	−2.840000000	−0.2556250000
	0.150	−1.155625000	−2.790000000	−0.2806249998
4p	0.025	−1.127353516	−2.945322266	−0.2476660160
	0.050	−1.117226562	−2.893789062	−0.2328515620
	0.075	−1.110244141	−2.845400390	−0.2211816405
	0.100	−1.106406250	−2.800156250	−0.2126562500
	0.150	−1.108164062	−2.719101562	−0.2050390622

TABLE 2. Model parameters for some selected diatomic molecules in this study [57].

Molecule	$\mu(amu)$	$\alpha\left(\overset{0}{\mathrm{A}}^{-1}\right)$
LiH	0.880122100	1.12800
TiH	0.987371000	1.32408
CrH	0.988976000	1.52179
ScN	10.68277100	1.50680

TABLE 3. Energy spectra (in eV) of Varshni plus Hellmann potential for various n and l quantum numbers of LiH, TiH, CrH and ScN diatomic molecules.

n	l	LiH	TiH	CrH	ScN
0	0	−3.256755417	−3.649087811	−4.044803588	−4.013711055
1	0	−3.259021670	−3.651871246	−4.048474354	−4.014044221
1	1	−3.258350187	−3.651046525	−4.047386719	−4.013945505
2	0	−3.262798757	−3.656510305	−4.054592298	−4.014599497
2	1	−3.263601388	−3.657496105	−4.055892360	−4.014717493
2	2	−3.259897954	−3.652947508	−4.049893716	−4.014173045
3	0	−3.268086680	−3.663004987	−4.063157419	−4.015376884
3	1	−3.270383149	−3.665825534	−4.066877128	−4.015714492
3	2	−3.268170615	−3.663108077	−4.063293372	−4.015389223
3	3	−3.261426672	−3.654825096	−4.052369861	−4.014397784
4	0	−3.274885437	−3.671355293	−4.074169717	−4.016376381
4	1	−3.278683508	−3.676020123	−4.080321649	−4.016934742
4	2	−3.277968774	−3.675142279	−4.079163956	−4.016829668
4	3	−3.272725415	−3.668702331	−4.070671018	−4.016058832
4	4	−3.248634679	−3.656693577	−4.054833994	−4.014621434
5	0	−3.283195030	−3.681561221	−4.087629193	−4.017597989
5	1	−3.288498369	−3.688074838	−4.096219285	−4.018377642
5	2	−3.289285583	−3.689041704	−4.097494377	−4.018493372
5	3	−3.285545217	−3.684447747	−4.091435914	−4.017943494
5	4	−3.277272556	−3.674287178	−4.078036258	−4.016727315
5	5	−3.264465670	−3.658557625	−4.057292283	−4.014844553

We have presented the plot of energy spectra of VHP as a function of vibrational quantum number in the ground state in Figs. 2-5. It is observed that there is a decrease in energy in the ground state as the vibrational and rotational quantum numbers increase. In Figs. 6 and 7, we plotted the energy spectra of VHP *versus* the potential strengths a, c. Here, the energy decreases as the potential strengths increase.

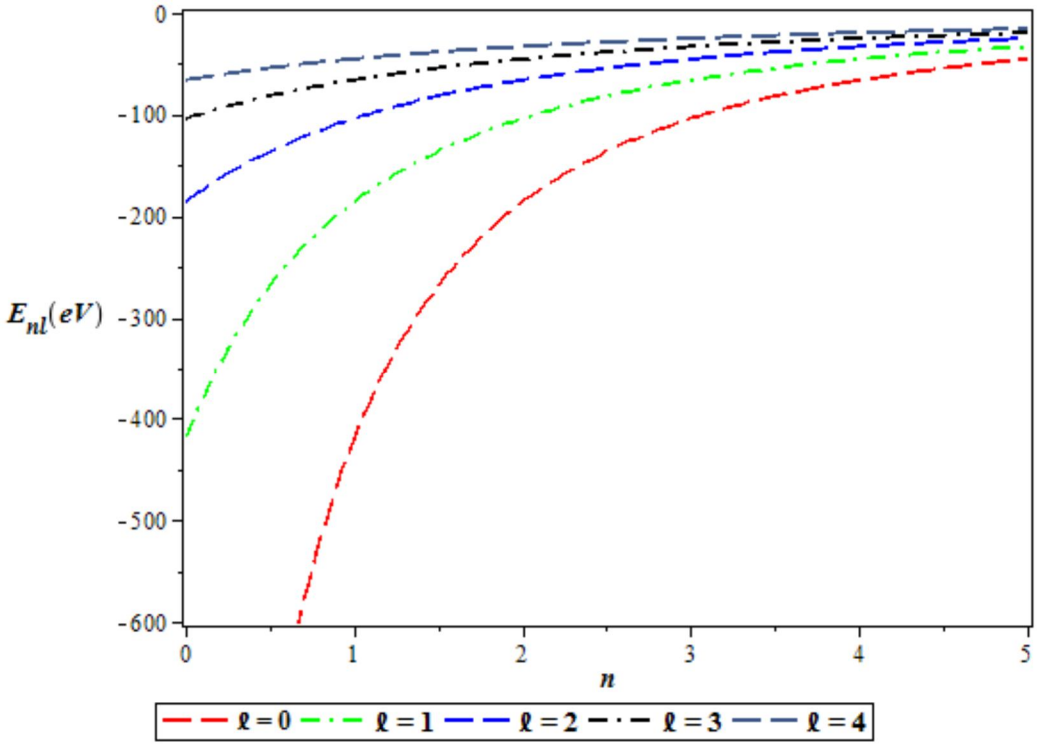

FIG. 2. Variation of the ground-state energy spectra of LiH molecule for various l as a function of n. We choose $a = 1, b = -1, c = 2$ *and* $d = -1$·

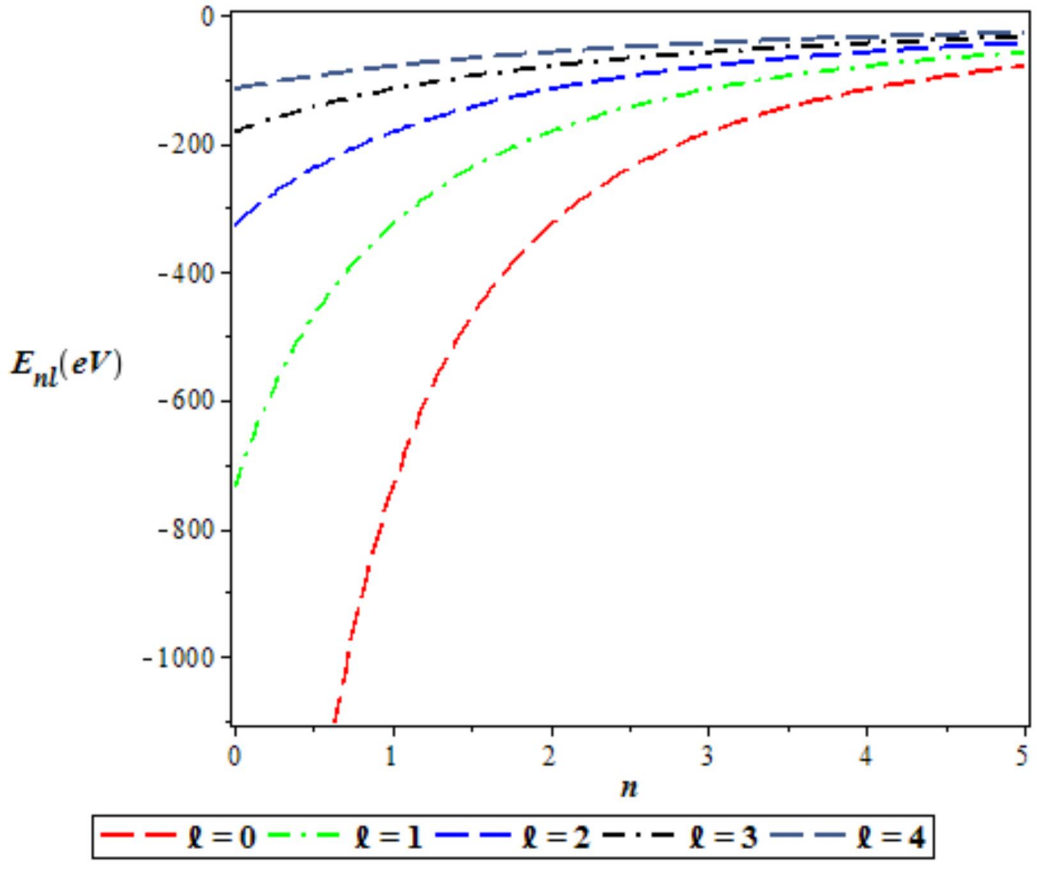

FIG. 3. Variation of the ground-state energy spectra of TiH molecule for various l as a function of n .We choose $a = 1, b = -1, c = 2$ *and* $d = -1$·

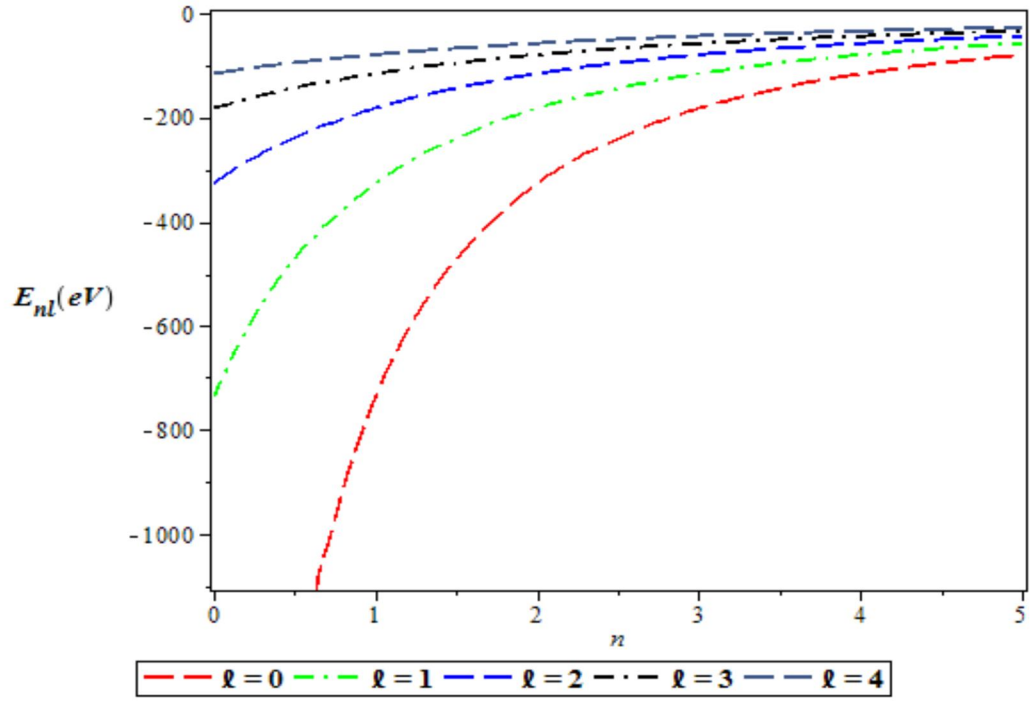

FIG. 4. Variation of the ground-state energy spectra of CrH molecule for various l as a function of n .We choose $a = 1, b = -1, c = 2 \; and \; d = -1$·

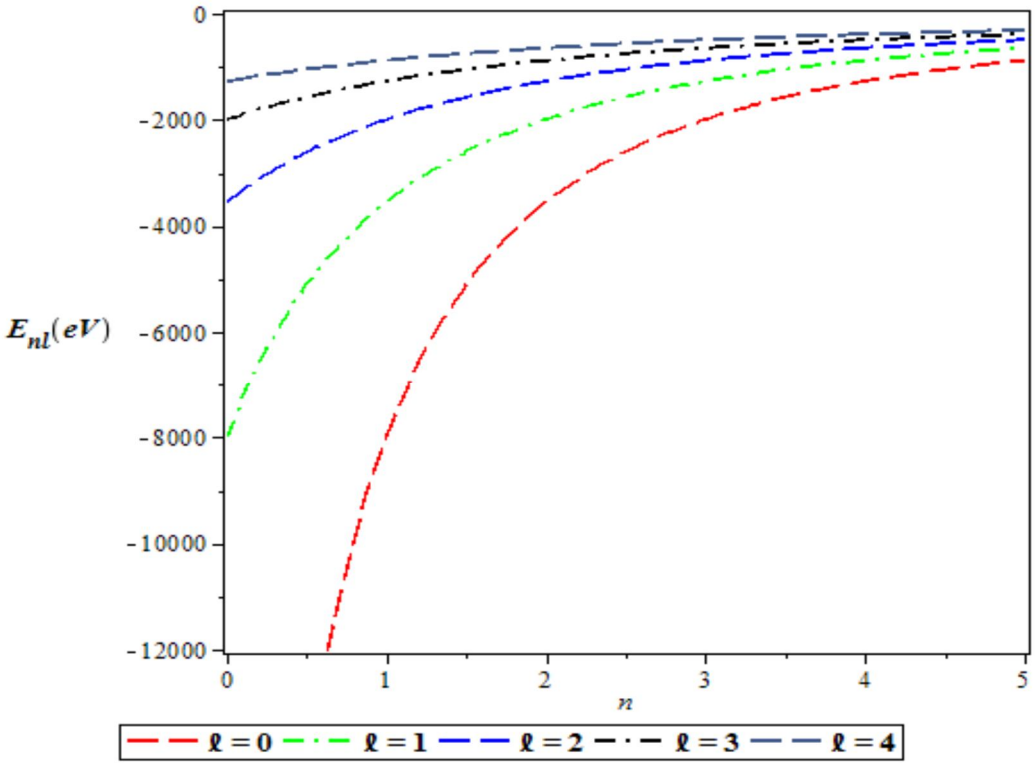

FIG. 5. Variation of the ground-state energy spectra of ScN molecule for various l as a function of n .We choose $a = 1, b = -1, c = 2 \; and \; d = -1$·

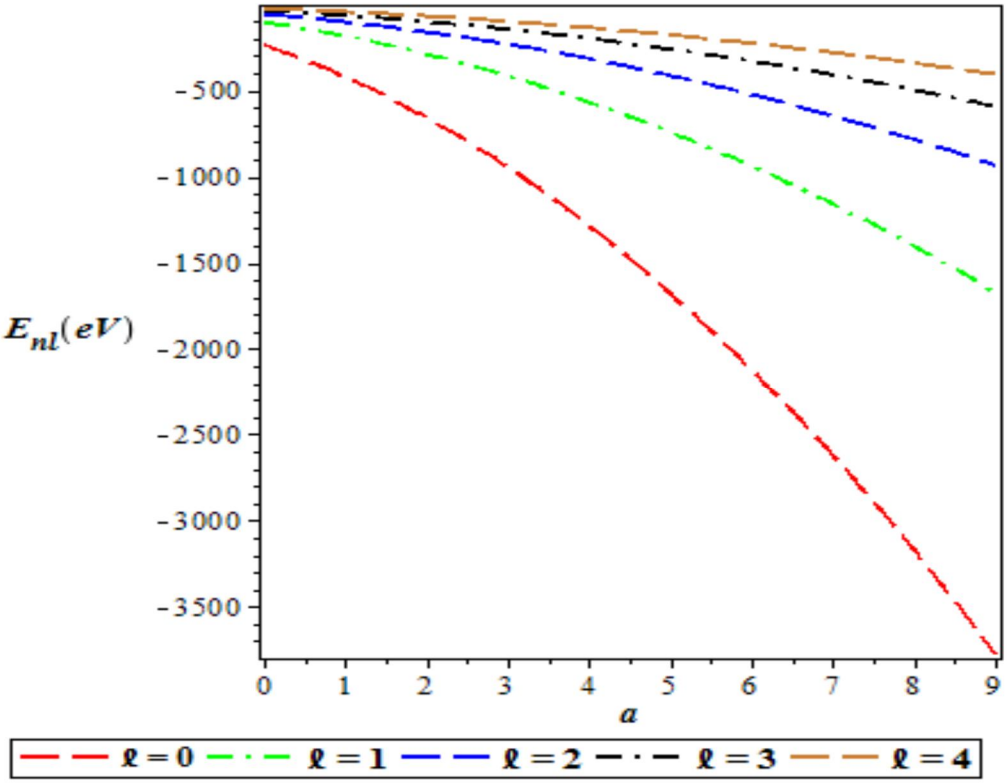

FIG. 6. Variation of the ground-state energy spectra of LiH molecule for various l as a function of a .We choose $a = 1, b = -1, c = 2$ *and* $d = -1$·

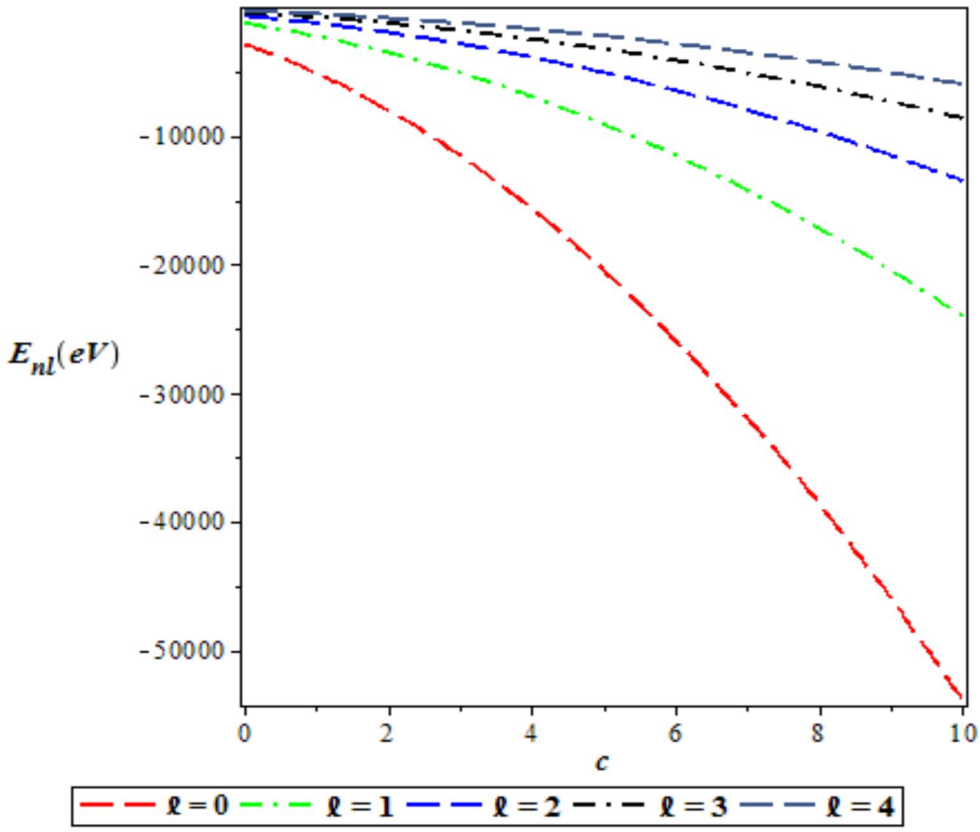

FIG. 7. Variation of the ground-state energy spectra of ScN molecule for various l as a function of c .We choose $a = 1, b = -1, c = 2$ *and* $d = -1$·

Special Cases

In this sub-section, we present the energy eigenvalues for adjusted VHP as special cases in order to test for the accuracy of our results.

1) By setting the Varshni potential strength to zero in Eq. (20); i.e., $a = b = 0$, we obtain the energy eigenvalue equation for Hellmann potential as:

$$E_{nl} = \frac{\beta^2\hbar^2 l(l+1)}{2\mu} - \beta c - \frac{\beta^2\hbar^2}{8\mu}\left[\frac{(n+l+1)^2+\frac{2\mu}{\hbar^2\beta}(d-c)+l(l+1)}{(n+l+1)}\right]^2. \quad (34)$$

Eq. (34) is in agreement with Eq. (38) of Ref. [21]. The numerical energy eigenvalues are presented in Table 4 for $c = 2$ and $d = -1$. The results are in good agreement with the earlier results of [21] with NU and AP, as well as the PT method of [56].

TABLE 4. Energy eigenvalues (eV) in atomic mass units $(\hbar = 2\mu = 1)$ of Hellmann potential as a function of the screening parameter α for $a = b = 0, c = 2$ and $d = -1$.

State	α	Present method	(NU) [52]	(AP) [52]	(PT) [53]
1S	0.001	−2.250500250	-2.250 500	- 2.248 981	- 2.249 000
	0.005	−2.252506250	-2.252 506	- 2.244 993	- 2.245 010
	0.01	−2.255025000	-2.255 025	- 2.240 030	- 2.240 050
2S	0.001	−0.5630010000	- 0.563 001	- 0.561 502	- 0.561 502
	0.005	−0.5650250000	- 0.565 025	- 0.557 549	- 0.557 550
	0.01	−0.5676000000	- 0.567 600	- 0.552 697	- 0.552 697
2P	0.001	−0.5622502500	- 0.563 000	- 0.561 502	- 0.561 502
	0.005	−0.5612562500	- 0.565 000	- 0.557 541	- 0.557 541
	0.01	−0.5600250000	- 0.567 500	- 0.552 664	-0.552 664
3S	0.001	−0.2505022500	- 0.250 502	- 0.249 004	- 0.249 004
	0.005	−0.2525562500	- 0.252 556	-0245 110	- 0.245 111
	0.01	−0.2552250000	- 0.255 225	-0.240 435	- 0.240 435
3p	0.001	−0.2501680278	-0.250 501	- 0.249 004	- 0.249 004
	0.005	−0.2508673611	-0.252 531	-0.245 102	-0.245 103
	0.01	−0.2518027778	-0.255 125	-0.240 404	-0.240 404
3d	0.001	−0.2495002500	-0.250 833	-0.249 003	-0.249 003
	0.005	−0.2475062500	-0.254 151	-0.245 086	-0.245 086
	0.01	−0.2450250000	-0.258 269	-0.240 341	-0.240 341
4S	0.001	−0.1411290000	-0.141 129	-0.139 633	-0.139 633
	0.005	−0.1432250000	-0.143 225	-0.135 819	-0.135 819
	0.01	−0.1460250000	-0.146 025	-0.131 380	-0.131 381
4p	0.001	−0.1409405625	-0.141 128	-0.139 632	0.139 633
	0.005	−0.1422640625	-0.143 200	-0.135 811	0.135 811
	0.01	−0.1440562500	-0.145 925	-0.131 350	-0.131 351
4d	0.001	−0.1405640625	-0.141 314	-0.139 632	-0.139 632
	0.005	−0.1403515625	-0.144 089	-0.135 795	-0.135 796
	0.01	−0.1401562500	-0.147 606	-0.131 290	-0.131 290
4f	0.001	−0.1400002500	-0.141 686	-0.139 631	-0.139 631
	0.005	−0.1375062500	-0.145 902	-0.135 772	-0.135 772
	0.01	−0.1344000000	-0.151 106	-0.131 200	-0.131 200

2) If we set the Hellmann potential strength to zero in Eq. (20); i.e., $c = d = 0$, we obtain the energy eigenvalue equation for Varshni potential as:

$$E_{nl} = a + \frac{\beta^2\hbar^2 l(l+1)}{2\mu} - \frac{\beta^2\hbar^2}{8\mu}\left[\frac{(n+l+1)^2+\frac{2ab\mu}{\hbar^2\beta}+l(l+1)}{(n+l+1)}\right]^2. \quad (35)$$

The numerical energy eigenvalues are presented in Table 5 for three ranges of Varshni potential strength. It is observed that as the screening parameter increases, the energy of the system decreases. Similarly, by interchanging Varshni potential strength, the energy increases in the same proportion as the screening parameter increases. In order to test the accuracy of our results, we compared the result of Varshni potential with the result of Ebomwonyi et al. [49] who used the formula method. As can be seen from Table 5, our result is in agreement with previous results.

3) If we set $a = b = c = 0$ in Eq. (20), we obtain the energy eigenvalues for Yukawa potential as:

$$E_{nl} = \frac{\beta^2\hbar^2 l(l+1)}{2\mu} - \frac{\beta^2\hbar^2}{8\mu}\left[\frac{(n+l+1)^2+\frac{2d\mu}{\hbar^2\beta}+l(l+1)}{(n+l+1)}\right]^2. \tag{36}$$

It is observed that as the screening parameter increases, the energy eigenvalue increases. The results are in good agreement with the earlier results of [57] with AIM and [58] of the numerical method.

TABLE 5. Energy eigenvalues (eV) in atomic mass units $(\hbar = 2\mu = 1)$ of Varshni potential as a function of the screening parameter α .

State	α	Present method $a=b=-1$	(FM) [48] $a=b=-1$	Present method $a=-1,b=-2$	Present method $a=-2,b=-1$
1S	0.001	−1.063124562	-	−2.001000250	−3.001000250
	0.050	−1.092656250	-	−2.050625000	−3.050625000
	0.100	−1.120625000	-	−2.102500000	−3.102500000
2S	0.001	−1.063001000	-	−1.251001000	−2.251001000
	0.050	−1.090000000	-	−1.302500000	−2.302500000
	0.100	−1.122500000	-	−1.360000000	−2.360000000
2P	0.001	−1.063124562	-1.0617502	−1.251249562	−2.251249562
	0.050	−1.092656250	-1.0256250	−1.311406250	−2.311406250
	0.100	−1.120625000	-0.9900000	−1.370625000	−2.370625000
3S	0.001	−1.028280028	-	−1.112113361	−2.112113361
	0.050	−1.058402778	-	−1.166736111	−2.166736111
	0.100	−1.100277778	-	−1.233611111	−2.233611111
3p	0.001	−1.028334111	-	−1.112223000	−2.112223000
	0.050	−1.057500000	-	−1.168611111	−2.168611111
	0.100	−1.091111111	-	−1.230000000	−2.230000000
3d	0.001	−1.028386250	- 1.0269447	−1.112330694	−2.112330694
	0.050	−1.051736111	- 0.9867361	−1.165625000	−2.165625000
	0.100	−1.062500000	- 0.9469444	−1.206944444	−2.206944444
4S	0.001	−1.016129000	-	−1.063504000	−2.063504000
	0.050	−1.050625000	-	−1.122500000	−2.122500000
	0.100	−1.105625000	-	−1.202500000	−2.202500000
4p	0.001	−1.016158766	- 1.0150656	−1.063565016	−2.063565016
	0.050	−1.048476562	- 0.9951563	−1.121914062	−2.121914062
	0.100	−1.093906250	- 0.9900000	−1.193906250	−2.193906250
4d	0.001	−1.028386250	- 1.0149391	−1.063624062	−2.063624062
	0.050	−1.051736111	- 0.9851563	−1.116406250	−2.116406250
	0.100	−1.062500000	- 0.9625000	−1.063624062	−2.165625000
4f	0.001	−1.016212391	- 1.0147502	−1.063681141	−2.063681141
	0.050	−1.029414062	- 0.9725000	−1.105976562	−2.105976562
	0.100	−1.011406250	- 0.9306250	−1.117656250	−2.117656250

4) If we set $a = b = d = \beta = 0$ in Eq. (20), we obtain the energy eigenvalues for Coulomb potential as:

$$E_{nl} = -\frac{\mu c^2}{2\hbar^2(n+l+1)^2}. \tag{37}$$

The result of Eq. (37) is consistent with the result obtained by Eq. (36) in Ref. [47].

TABLE 6. Energy eigenvalues (eV) in atomic mass units $(\hbar = \mu = 1)$ of Yukawa potential as a function of the screening parameter α with $d = \sqrt{2}$.

State	α	Present method	AIM[54]	Numerical[55]	SUSY[56]
1S	0.002	- 0.9954605000	−0.99600	−0.99600	−0.99601
	0.005	- 0.9835031250	−0.99003	−0.99004	−0.99000
	0.010	−0.980100000	−0.98014	−0.98015	−0.98010
	0.020	−0.960400000	−0.96059	−0.96059	−0.96060
	0.025	−0.950620000	−0.95092	−0.95092	−0.95090
	0.050	−0.90250000	−0.90363	−0.90363	−0.90360
2S	0.002	−0.24601000	−0.24602	−0.24602	−0.24600
	0.005	−0.24010000	−0.24014	−0.24015	−0.24010
	0.010	−0.23040000	−0.23058	−0.23059	−0.20360
	0.020	−0.21160000	−0.21229	−0.21230	−0.21230
	0.025	−0.20250000	−0.20355	−0.20355	−0.23060
	0.050	−0.16000000	−0.16354	−0.16351	−0.16350
2P	0.002	−0.24601000	−0.24601	−0.24602	−0.24600
	0.005	−0.24010000	−0.24012	−0.24012	−0.24010
	0.010	−0.23040000	−0.23049	−0.23049	−0.23050
	0.020	−0.21160000	−0.21192	−0.21192	−0.21190
	0.025	−0.20250000	−0.20298	−0.20299	−0.20300
	0.050	−0.16000000	−0.16148	−0.16144	−0.16150
3p	0.002	−0.10714000	−0.10716	−0.10716	−0.10720
	0.005	−0.10133000	−0.10141	−0.10142	−0.10140
	0.010	−0.09201000	−0.09230	−0.09231	−0.09231
	0.020	−0.07471000	−0.07570	−0.07570	−0.07570
	0.025	−0.06673000	−0.06815	−0.06814	−0.06816
	0.050	−0.03361000	−0.03711	−0.03739	−0.03712
3d	0.002	−0.10714000	−0.10715	−0.10715	−0.10720
	0.005	−0.10133000	−0.10136	−0.10140	−0.10140
	0.010	−0.09201000	−0.09212	−0.09212	−0.09212
	0.020	−0.07471000	−0.07503	−0.07502	−0.07503
	0.025	−0.06673000	−0.06714	−0.06713	−0.06715
	0.050	−0.03361000	−0.03383	−0.03388	−0.03383

4. Conclusion

In this study, the radial Schrödinger equation for the newly proposed Varshni-Hellmann potential (VHP) is obtained within the framework of the Nikiforov-Uvarov method by employing the Greene-Aldrich approximation scheme to the centrifugal term. The numerical results obtained of the ro-vibrational energies for LiH, TiH, CrH and ScN diatomic molecules are observed to increase with an increase in the quantum state considered. It is noticed that the selected molecular diatomic molecules studied in this work have similar behaviors. By adjusting the potential strength, we deduced four special cases with their numerical energy eigenvalues. The results obtained are in agreement with those of the works of other researchers using different methods. Also, we have discussed the results of the ground-state energy spectra obtained graphically.

Appendix: Review of Nikiforov-Uvarov (NU) Method

The NU method according to Nikiforov and Uvarov is used to transform Schrödinger-like equations into a second-order differential equation through a coordinate transformation $x = x(r)$ of the form [57, 58]:

$$\psi''(x) + \frac{\tilde{\tau}(x)}{\sigma(x)}\psi'(x) + \frac{\tilde{\sigma}(x)}{\sigma^2(x)}\psi(x) = 0 \quad \text{(A1)}$$

where $\tilde{\sigma}(x)$ and $\sigma(x)$ are polynomials, at most second-degree, while $\tilde{\tau}(x)$ is a first-degree polynomial.

The exact solution of Eq. (A1) can be obtained by using the transformation:

$$\psi(x)=\phi(x)y(x). \quad \text{(A2)}$$

This transformation reduces Eq.(A1) into a hypergeometric-type equation of the form:

$$\sigma(x)y''(x)+\tau(x)y'(x)+\lambda y(x)=0\ . \quad \text{(A3)}$$

The function $\phi(x)$ can be defined as the logarithm derivative:

$$\frac{\phi'(x)}{\phi(x)}=\frac{\pi(x)}{\sigma(x)}, \quad \text{(A4)}$$

with $\pi(x)$ being at most a first-degree polynomial. The second part of the wave function in Eq. (A2) is a hypergeometric-type function obtained by Rodrigues relation:

$$y(x)=\frac{N_{nl}}{\rho(x)}\frac{d^n}{dx^n}\left[\sigma^n(x)\rho(x)\right] \quad \text{(A5)}$$

where N_{nl} is the normalization constant and $\rho(x)$ the weight function which satisfies the condition below;

$$\left(\sigma(x)\rho(x)\right)'=\tau(x)\rho(x) \quad \text{(A6)}$$

where also

$$\tau(x)=\tilde{\tau}(x)+2\pi(x). \quad \text{(A7)}$$

For bound solutions, it is required that:

$$\frac{d\tau(x)}{dx}<0\ . \quad \text{(A8)}$$

The eigenfunctions and eigenvalues can be obtained using the definition of the following function $\pi(x)$ and parameter λ, respectively:

$$\pi(x)=\frac{\sigma'(x)-\tilde{\tau}(x)}{2}\pm\sqrt{\left(\frac{\sigma'(x)-\tilde{\tau}(x)}{2}\right)^2-\tilde{\sigma}(x)+k\sigma(x)} \quad \text{(A9)}$$

and

$$\lambda=k_{-}+\pi'_{-}(x). \quad \text{(A10)}$$

The value of k can be obtained by setting the discriminant in the square root in Eq. (A9) equal to zero. As such, the new eigenvalue equation can be given as

$$\lambda_n+n\tau'(x)+\frac{n(n-1)}{2}\sigma''(x)=0,(n=0,1,2,\dots). \quad \text{(A11)}$$

References

[1] Inyang, E.P., William, E.S. and Obu, J.A., Rev. Mex. Fis., 67 (2021) 193.

[2] Inyang, E.P., Inyang, E.P., Ntibi, J.E. and William, E.S., Bulletin of Pure & Applied Sciences- Physics, 40d (2021) 14.

[3] Alsadi, K.S., J. Taibah Uni. Sci., 14 (2020) 1163.

[4] Inyang,E.P.,William,E.S., Obu,J.O., Ita,B.I., Inyang,E.P.,and Akpan,1.O., Mol. Phys., 119 (2021) e1956615. https://doi.org/ 10.1080/00268976.2021.1956615

[5] Inyang,E.P., Inyang, E.P., Akpan, I.O., Ntibi, J.E. and William, E.S., Can. J. Phys., 99 (2021) 990.https://doi.org/10.1139/cjp-2020-0578.

[6] Ibekwe, E.E., Okorie, U.S., Emah, J.B., Inyang, E.P. and Ekong, S.A., Eur. Phys. J. Plus, 87 (2021) 136.

[7] Inyang, E.P., Inyang, E.P., William, E.S. and Ibekwe, E.E., Jordan J. Phys., 14 (4) (2021) 337.

[8] Inyang, E.P., William, E.S., Omugbe, E., Inyang, E.P., Ibanga, E.A., Ayedun, F., Akpan, I.O. and Ntibi, J.E., Rev. Mex. Fis., 68 (2022) 14.

[9] Inyang, E.P., Ntibi, J.E., Inyang, E.P., William, E.S. and Ekechukwu, C.C., Intl. Innov. Sci. Engr. Tech., **7** (2020)

[10] Inyang, E.P., Inyang, E.P., Ntibi, J.E., Ibekwe. E.E. and William, E.S., Ind. J. Phys., 95 (2021) 2733.

[11] Romaniega, C., Gadella, M., Betan, R.M. *et al.,* Eur. Phys. J. Plus, 135 (2020) 372.

[12] Zhang, M.C., Chin. Phys. Lett., 30 (2013) 11030.

[13] Zhang, L.H., Li, X.P. and Jia, C.S., Intl. J. Quan. Chem., 111 (2011) 870.

[14] Makarov, A.A., Smorodinsky, J.A., Valiev, K.H. and Winternitz, P., Nuov. Cim. A, 52 (1967) 1061.

[15] Ahmadov, H.I., Jafarzade, S.I. and Qocayeva, M.V., Int. J. Mod. Phys. A, 30 (2015) 1550193.

[16] Inyang, E.P., Iwuji, P.C., Ntibi, J.E., William, E.S. and Ibanga, E.A. East Eur. J. Phys.1(2022)11.https://doi.org/10.26565/2312-4334-2022-2-02

[17] Pekeris, C.L., Phys. Rev., 45 (1934) 98.

[18] Greene, R.L. and Aldrich, C., Phys. Rev. A, 14 (1976) 2363.

[19] Inyang, E.P., William, E.S. and Obu, J.A., Revista Mexicana de Física, 67 (2) (2021) 193.

[20] Omugbe, E., Osafile, O.E., Okon,,I. B., Eyube ,E.S., Inyang, E.P., Okorie U.S., Jahanshir, A. and Onate,C.A., Eur. Phys. J. D.,76:72 (2022)11.

[21] William, E.S., Inyang, E.P. and Thompson, E.A., Rev. Mex. Fis., 66 (2020) 730.

[22] Ahmadov, A., Demirci, M., Aslanova, S. and Mustamin, M., Phys. Lett. A, 384 (2020) 126372.

[23] Ahmadov, A., Aydin, C. and Uzun, O., Int. J. Mod. Phys. A, 29 (2014) 1450002.

[24] Aspoukeh, P. and Hamad, S.M., Chin. J. Phys., 68 (2020) 235.

[25] Hellmann, H., J. Chem. Phys., 3 (1935) 61.

[26] Callaway, J. and Laghos, P., Phys. Rev., 187 (1969) 192.

[27] William, E.S., Obu, J.A., Akpan, I.O., Thompson, E.A. and Inyang, E.P., European Journal of Applied Physics, 2 (6) (2020) 28.

[28] Kleinman, L. and Phillips, J.C., Phys. Rev., 116 (1959) 880.

[29] Hughes, A.J. and Callaway, J., Phys. Rev., 136 (1964) A1390.

[30] Akpan, I.O., Inyang, E.P., Inyang, E.P. and William, E.S., Revista Mexicana de Física, 67 (3) (2020) 482.

[31] McGinn, G., J. Chem. Phys., 53 (1970) 3635.

[32] Gryaznov, V.K., Zhernokletov, M.V., Zubarev, V.N., Losilevskii, I.L. and Tortov, V.E., J. Exp. Theo. Phys., 78 (1980) 573.

[32] William, E.S., Inyang, E.P., Akpan, I.O., Obu, J.A., Nwachukwu, A.N. and Inyang, E.P., Indian J. Phys., (2022). https://doi.org/10.1007/s12648-0222-02308-0.

[33] Dutt, R., Mukherji, U. and Varshni, Y.P., Phys. Rev. A, 34 (1986) 777.

[34] Ikhdair, S.M. and Sever, R., Intl. J. Mod. Phys. A, 21 (2006) 6465.

[35] Ntibi, J.E., Inyang, E.P., Inyang, E.P. and William, E.S., Intl. J. Innov. Sci. Engr. Tech., **7** (11) (2020) 28.

[36] Varshni, Y.P. and Shukla, R.C., Rev. Mod. Phys., 35 (1963) 130.

[37] Inyang, E.P., Inyang, E.P., Akpan, I.O., Ntibi, J.E. and William, E.S., European Journal of Applied Physics, 2 (6) (2020) 26

[38] Okoi,P.O., Edet, C.O., Magu, T.O., and Inyang,E.P., Jordan J. Phys. 15(2022)148.

[39] Inyang, E.P., William , E.S., Ntibi, J.E., Obu, J.A., Iwuji, P.C. and Inyang, E.P. Can. J. Phys. (2022). https://doi.org/10.1139/cjp-2022-0030

[40] Omugbe, E., Osafile, O.E., Okon, I.B., Inyang, E.P., William, E.S. and Jahanshir, A., Few-Body Syst., 63 (2022) 7**.**

[41] Hamzavi, M., Thylwe, K.E. and Rajabi, A.A., Commun. Theo. Phys., 60 (2013) 602.

[42] Roy, A.K., Jalbout, A.F. and Proynow, E.I., arXiv:1307.2983v (2013) [quant-ph].

[43] Onate, C.A., Ojonubah, J.O., Adeoti, A., Eweh, E.J. and Ugboja, M., Afri. Rev. Phys., 9 (2014) 0062.

[44] Arda, A. and Sever, R., Phy. Scripta., 89 (2014) 105204.

[45] Oluwadare, O.J. and Oyewumi, K.J., Adv. High Ener. Phys., 2018 (2018) 5214041.

[46] Edet, C.O., Okorie, U.S., Ngiangia, A.T. and Ikot, A.N., Ind. J. Phys., 37 (2019) 288.

[47] Inyang, E.P., Ntibi, J.E., Ibanga, E.A., Ayedun, F., Inyang, E.P., Ibekwe, E.E., William, E.S. and Akpan, I.O., Comm. Phys. Sci., 7 (2021) 114.

[48] Ebomwonyi, O., Onate, C.A. and Odeyemi, O.E., J. Appl. Sci. Env. Mangt., 23 (2019) 19.

[49] Inyang, E.P., Inyang, E.P., William, E.S., Ibekwe, E.E. and Akpan, I.O., (2020) http://arxiv.org/abs/2012.10639.

[50] William, E.S., Okon, I.B., Ekerenam, O.O., Akpan, I.O., Ita, B.I., Inyang, E.P., Etim, I.P. and Umoh, I.F., Intl. J. Quan. Chem., (2022) e26925.

[51] Hamzavi, M., Thylwe, K.E. and Rajabi, A.A., Commun.Theo. Phys., 60 (2013) 8.

[52] Oluwadere, O.J. and Oyewumi, K.J., Eur. Phys. J. Plus, 133 (2018) 422.

[53] Okon, I.B., Antia, A.D., Akpabio, L.E. and Archibong, B.U., J. Appl. Phys. Sci Intl., 10 (2018) 268.

[54] Ikhdair, S.M and Sever, R., J. Mol. Struct.: THEOCHEM, 809 (2007) 113.

[55] Karakoc, M. and Boztosun, I., Intl. J. Mod. Phys. E, 15 (6) (2006) 1253.

[56] Gonul, B., Koksal, K. and Bakir, E., Phy. Scripta., 98 (2018) 453.

[57] Nikiforov, A.F. and Uvarov, V.B., "Special Functions of Mathematical Physics", (Birkhauser, Basel, 1988) pp. 456-459.

[58] Inyang, E.P., Iwuji, P.C., Ntibi, J.E., Omugbe, E., Ibanga, E.A. and William, E.S., East Eur. J. Phys., 2 (2022) 51.

Volume 15, Number 2, 2022. pp. 195-199

Jordan Journal of Physics

ARTICLE

Transit of the Sun across Constellations Libra, Virgo and Variation of Secondary Gamma Radiation Flux in the Months of November 2018 and September 2019, Respectively at Udaipur, India

Devendra Pareek and **Pallavi Sengar**

Department of Physics, Bhupal Nobles' University, Udaipur 313001, India.

Doi: **https://doi.org/10.47011/15.2.9**

Received on: 19/12/2020; *Accepted on: 18/01/2021*

Abstract: We reported a significant variation of secondary gamma radiation flux (SGR) in month November 2018 and month September 2019 at Udaipur during transit of Sun across constellations. The data was collected as a function of time using a ground-based NaI (Tl) scintillation detector. We interpret such variation of SGR flux on the basis of combined gravitational pulling along with gravitational lensing effect on background radiation by the Sun, constellations and radiation from constellations.

Keywords: Cosmic radiation, Sun, Solar radiation, Secondary gamma radiation, Libra constellation, Virgo constellation, Planets, Gravitational pulling, Gravitational lensing.

Introduction

High-energy charged particles named cosmic radiation travel at nearly the speed of light. Composition of cosmic radiation is about 89% protons, 10% helium and about 1% other heavier elements [8]. Such radiation is isotropically distributed and propagates through space while arriving on the Earth [5]. When cosmic radiation (CR) and solar radiation (SR) collide with atoms of the atmosphere of the Earth, they produce "secondary" radiation. Such radiation contains pions, muons, neutrinos, gamma radiation, electrons and positrons. Presence of gamma radiation in secondary radiation is known as secondary gamma radiation (SGR), which can be detected using an appropriate detector on ground [3, 7].

It was observed that when the electromagnetic radiation passes near a massive object, then due to gravitational field of the object, it bends. This phenomenon is called gravitational lensing. This object may be a galaxy, a star or a cluster of galaxies [4, 9, 10]. This phenomenon was proved by A. S. Eddington and collaborators in a famous experiment during a total solar eclipse in 1919.

Due to gravitational force of the celestial object, it provides gravitational pull-on background radiation.

Many scientist groups, such as Bhattcharya et al. [2], Kandemir et al. [6], Nayak et al. [11], Bhaskar et al. [1] and Pareek et al. [12], observed the variation of secondary radiation flux during solar eclipse.

During lunar eclipse, Pareek et al. [13] observed a variation in secondary gamma radiation flux. Such interesting finding during lunar eclipse can be explained on the basis of bending of primary cosmic radiation and solar radiation combined with gravitational lensing effect of Sun and Earth and back-scattered secondary radiation from the Moon.

Pareek at al. [14] conducted an experimental study using a scintillation counter for phases of the Moon in the month of September 2000. This experimental study had been planned to observe

Corresponding Author: Devendra Pareek **Email**: deven.pareek69@gmail.com

gravitational lensing effect. During observation, the Moon passes background of Capricornus constellation on September 9 and 10, 2000. On these dates, we observed an abrupt change in the energy spectra of secondary gamma radiation due to gravitational lensing effect.

With the fact that during different celestial events happening in the sky, the flux of cosmic and solar radiation is modulated, we attempted to see the combined gravitational lensing and gravitational pulling effect of celestial objects on radiations from constellations. We conducted a ground-based experimental study using a scintillation detector at Udaipur, India during transit of the Sun across constellations.

Experimental Setup and Observations

In the experimental studies for months of November 2018 and September 2019, we used a scintillation detector (GR611M) to collect the secondary gamma radiation flux. NaI (Tl) crystal was 50 mm in thickness and 44.5 mm in diameter and optically coupled with a photo multiplier tube and connected to a high-tension voltage supply of 2000 Volts DC (HV 502). Using the negative polarity of a linear amplifier (LA 520), a negative signal of about 0.5 Volt was amplified to a 5-Volts positive pulse. This signal was fed to an analog digital counter circuit (SC 530). This digital circuit has a counter circuit (CT 541A) to count the secondary cosmic radiation particles. The scintillation counter was kept open to collect the counts every date for three hours and with the same LLD. This scintillation counter was shielded with lead. This setup [Fig. 1] was placed in the Astronomy Laboratory of the Department of Physics. Data was collected in the month of November 2018 from 2:00 PM to 5:00 PM and in the month of September 2019 from 12:00PM to 3:00 PM at Udaipur, India.

FIG. 1. Experimental setup.

Analysis and Results

Depicted in Table 1 are the integrated counts of secondary gamma radiation flux for the month of November 2018.

Using Table 1, we made Fig. 2 to show the relationship between the dates of the month of November and the integrated counts of secondary gamma radiation flux:

TABLE 1. Integrated counts of secondary gamma radiation flux for November 2018.

Sr. No.	Date	Integrated Counts
1	13	2159
2	14	2120
3	16	1395
4	17	971
5	19	990
6	20	958
7	26	1120
8	27	997
9	28	326
10	30	422

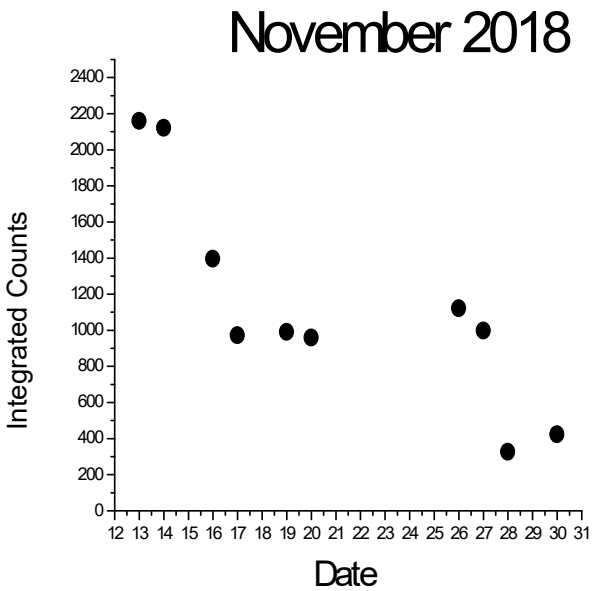

FIG. 2. Relationship between the dates of November 2018 and integrated counts of secondary gamma radiation.

The dates of observation were 13, 14, 16, 17, 19, 20, 26, 27, 28 and 30 November 2018. The secondary gamma radiation flux decreased from 2159 to 958 counts from 13 November to 20 November. On 26 November, the counts were 1120 and then decreased on 30 November.

For the month of September 2019, we started observation from 4 September. The dates of observation were 4, 5, 11, 19, 20, 21, 23 and 28 September 2019. The secondary gamma radiation flux increased from 1916 to 2200 counts. From 4 September onwards, the Sun was approaching Virgo constellation and on 28 September, we observed highest counts because the Sun, planet Venus and planet Mercury were in constellation Virgo. All these events produced combined gravitational lensing effect and gravitational pulling effect on background radiation. For the month September 2019, the integrated counts of secondary gamma radiation are given in Table 2.

TABLE 2. Integrated counts of secondary gamma radiation flux for September 2019.

Sr. No.	Date	Integrated Counts
1	4	1916
2	5	1987
3	11	1960
4	19	2055
5	20	2093
6	21	2048
7	23	2156
8	28	2200

Using Table 2, we made Fig. 3 to show the relationship between the dates of the month of September and the integrated counts of secondary gamma radiation flux:

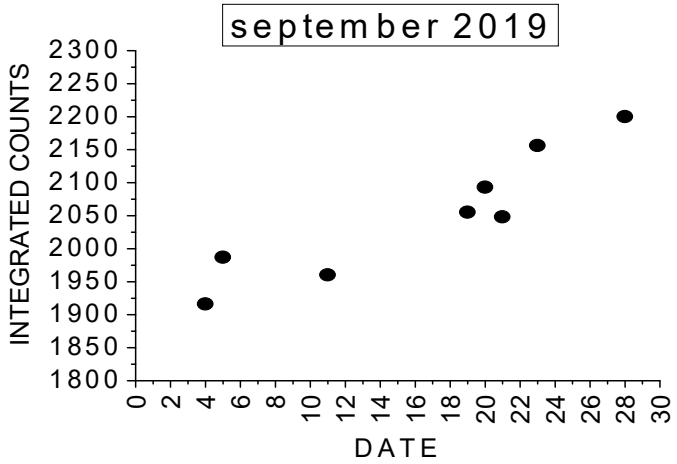

FIG. 3. Relationship between the dates of September 2019 and integrated counts of secondary gamma radiation.

Discussion

For the Month of November 2018

1. On 13 November, the Sun was in the Libra constellation and on other dates, the Sun was shifted away from this constellation; so there was a decrease in counts. This clearly represents the combined gravitational lensing effect and gravitational pulling effect on the background radiation due to constellation Libra and the Sun.
2. On 13 November, radiation coming from constellation Libra exposed the Sun to gravitational lensing effect. Therefore, more radiation was bent, which may produce a stronger shower of secondary gamma radiation particles in the atmosphere of the Earth.
3. On 26 November, again there was an increase in the integrated counts. On this date, the Sun was close to planets Jupiter and Mercury. Therefore, due to combined gravitational lensing and gravitational pulling by the Sun and planets Jupiter and Mercury, there was an increase in the counts of secondary gamma radiation flux.

Therefore, on 13 and 26 November, more radiation came and bent. This bent radiation impringed deep inside the atmosphere of the Earth, which produced more secondary gamma radiation particles that give such variation in November.

For the Month of September 2019

1. From Table 2 and Fig. 3, we concluded that from 4 September onwards, integrated counts increased and on 28 September, the highest counts were observed. From 4 September onwards, the sun was approaching Virgo constellation and on 28 September, the Sun, planet Venus and planet Mercury were in constellation Virgo. All these events produced combined gravitational pulling effect and gravitational lensing effect on background radiation.
2. From 4 September onwards, the Sun was approaching Virgo constellation and radiation coming from constellation Virgo exposed the Sun gravitational lensing effect. Therefore, more radiation was bent, which may have produced a stronger shower of secondary gamma radiation particles in the atmosphere of the Earth.

As mentioned in points 1 and 2, background radiation and radiation from constellations bent. This more bent radiation penetrated deep inside the atmosphere of the Earth, hence producing secondary gamma radiation that gave such variation in the integrated counts of secondary gamma radiation in the month of September.

These experimental studies are unique and for the first time, such variation of secondary gamma radiation flux during transit of the Sun across constellations was reported.

Conclusion

These experimental studies gave the conclusion that due to combined gravitational pulling and gravitational lensing effects of the celestial objects and radiation from constellations on the surface of the Earth, the secondary gamma radiation flux varies during transit of the Sun across constellations.

Acknowledgements

The authors are thankful to the students Robin Choudhary, Digvijay Singh Chouhan, Chirag Ameta, Ayush Patidar, Himani Gour, Vishal Chipa, Gourav Purohit, Bharti Ameta, Deepika Choubisa, Kavita Sharma, Madan Lakara, Mahaveer Singh Shekhawat, Nidhi Jain, Pooja Menaria, Nisha Tanwar, Shalini Vaishnav, Shrinka Rathore, Shriya Sen and Tarun Sikligar for their he;p in conducting the experimental study in November 2018. Thanks are also due to the students Dinesh Suthar, Aditi Ameta, Bharat Gehlot, Hitesh Chouhan, Parag Vaishnav, Rakesh Parihar, Rahul Panusa, Ranjita Janwa, Chinkal Suthar, Diptika Chundawat, Nisha Kunwar Charan, Robin Choudhary, Digvijay Singh Chouhan, Chirag Ameta, Divyansh Chouhan, Om parkash Choudhary, Darshan Kotiya and Mohsib Pathan, who were involved in the experimental study conducted in September 2019.

References

[1] Bhaskara, A., Purohit, A., Hemalatha, M., Pai, C., Raghav, A., Gurada, C., Radha, S., Yadav, V., Desai, V., Chitnis, A., Sarpotdar, P. and Patankar, A., Astroparticle Physics, 35 (5) (2011) 223.

[2] Bhattacharyya, A., Biswas, S., Chatterjee, B.K., Das, M., Das, P.K., Das, T.K., De, T.K., Engineer, M.H., Mukherjee, R.N., Raha, S., Roy, S.C., Saha, S.K., Sen, A.K., Sinha, B. and Syam, D., Astrophysics and Space Science, 250 (1997) 313.

[3] Chilingarian, A., Daryan, A., Arakelyan, K., Hovhannisyan, A., Mailyan, B., Melkumyan, L., Hovsepyan, G., Chilingaryan, S., Reymers, A. and Vanyan, L., Physical Review D, 82 (4) (2010) 043009.

[4] Walsh, D. et al., Nature, 279 (5712) (1979) 381-4.

[5] Fulks, G.J., Journal of Geophysical Research, 80 (1975) 1701.

[6] Kandemir, G. et al., ASP Conference Series, 205 (2000) 202.

[7] Kodama, M., Physical Society of Japan, 52 (1983) 1503.

[8] Longair, M.S., "High-energy Astrophysics 1", 2nd Edn., (Pub.Cambridge University Press, 1992).

[9] Mellier, Y., Annual Review of Astronomy and Astrophysics, 37 (1999) 127.

[10] Narayan, R. and Bartelmann, M., "Lectures on gravitational lensing", (1996), https://arxiv.org/abs/astro-ph/9606001.

[11] Nayak, P.K. et al., Astroparticle Physics, 32 (2010) 286.

[12] Pareek, D., Jaaffrey, S.N.A., Talesra, K.P., Yadav, R. and Ameta, S., Research Journal of Physical Sciences, 1 (5) (2013) 22.

[13] Pareek, D. et al., Research Journal of Physical Sciences, 1 (4) (2013) 22.

[14] Pareek, D. et al., International Journal of Scientific Research, Ahmedabad, 3 (5) (2014) 6.

Volume 15, Number 2, 2022. pp. 201-206

Jordan Journal of Physics

ARTICLE

Decrement of Secondary Gamma Radiation Flux during Solar Eclipses on January 4, 2011 and December 26, 2019 at Udaipur, India

Devendra Pareek and **Pallavi Sengar**

Department of Physics, Bhupal Nobles' University, Udaipur, India.

Doi: **https://doi.org/10.47011/15.2.10**

Received on: 19/12/2020; *Accepted on: 18/01/2021*

The solar eclipses at Udaipur (27^0 43' 12.00"N, 75^0 28' 48.01"E), India were experimentally observed on January 4, 2011 and December 26, 2019 using a ground-based NaI (Tl) scintillation detector. For the solar eclipse on January 4, 2011, the data files were stored in a computer for a thirty-minute duration from 14.30 IST to 15.00 IST on pre-eclipse normal days as well as on post-eclipse normal days and also on partial eclipse day (January 4, 2011). For solar eclipse on December 26, 2019, cadences of data were collected for three hours from 8 AM to 11 AM on pre-eclipse normal days as well as on post-eclipse normal days and also on eclipse day (December 26, 2019). The analyzed data revealed significant decrement of secondary gamma radiation flux (SGR) on solar eclipse day (January 4, 2011) of about 10 % and on solar eclipse day (December 26, 2019) of about 17 % in the counts of SGR flux on comparison to average counts of normal days. We interpret such decrement of SGR flux on the basis of obstruction effect produced by the Moon during solar eclipses.

Keywords: Solar eclipse, Cosmic radiation, Solar radiation, Secondary gamma radiation, Obstruction effect by the Moon.

Introduction

High-energy charged particles represent about 89% of nuclei of protons, 10% of nuclei of helium and about 1% of nuclei of others heavier elements, such as carbon, oxygen, magnesium, silicon and iron, known as cosmic radiation [9]. The cosmic radiation (CR) is almost isotropically distributed and propagates through space while arriving on the Earth [6]. Radiation coming from the Sun is known as solar radiation (SR) and has energetic particles that are associated with energetic events on the Sun.

It was observed by many scientist groups that during different celestial events, cosmic radiation and solar radiation are modulated. Modulated radiation strikes the atmosphere of the Earth, causing the formation of secondary radiation flux. Such secondary radiation flux contains an electromagnetic component known as secondary gamma radiation and detected by appropriate detectors on ground [8, 4]. On January 4, 2011, a partial solar eclipse was witnessed over Europe, the Arabian Peninsula, North Africa, eastern, north-western and southern Asia including northern and western parts of India, as shown in Fig. 1.

On January 4, 2011 in India at Udaipur, Rajasthan, where the first contact P1 began at 11:40:11.3 IST, the fourth contact P4 ended at 16:00:53 IST and the maximum partial eclipse occurred at 14:20:00 IST. The eclipse magnitude recorded at above geometric coordinates was 0.8576 with gamma=1.0627, Saros series =151, member = 14 of 72. The geometric coordinates

Corresponding Author: Devendra Pareek **Email**: deven.pareek69@gmail.com

of the Sun and the Moon at maximum eclipse were R.A. = 18h59m14.9s, Dec. = - 220 44'21.1", S.D. = 00016'15.9", H.P. = 00000'8.9" and R.A. = 18h58m23.85 Dec. = -21046'01.2", S.D = 00015'18.1", H.P. = 00056'09.6" res.

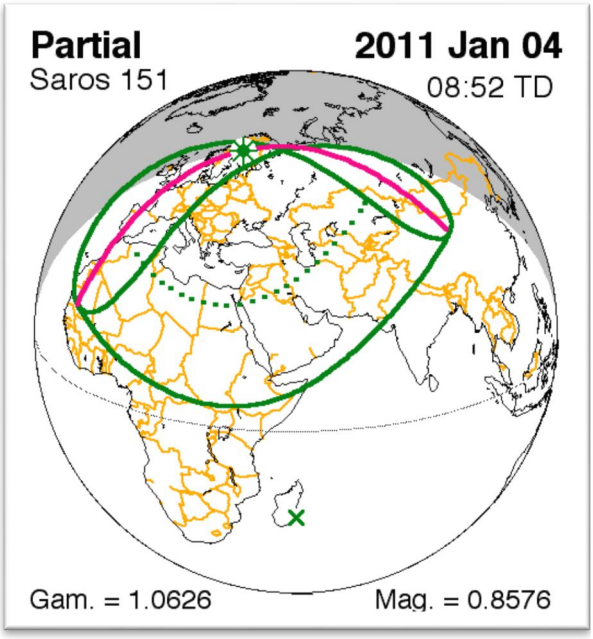

FIG. 1. Partial solar eclipse witnessed on Jan. 4, 2011.

On December 26, 2019, a solar eclipse was witnessed over Eastern Europe, much of Asia, north and west Australia, east Africa and the Pacific and Indian Oceans as shown in Fig. 2.

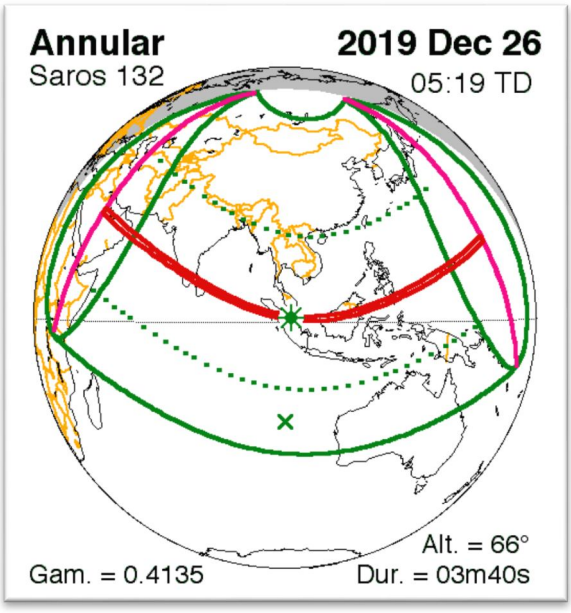

FIG. 2. Solar eclipse witnessed on Dec. 26, 2019.

On December 26, 2019, there was an annular solar eclipse at Udaipur, India from 8.00 AM to 11.00 AM with gamma = 0.4135, magnitude = 0.9701, Saros series =132 and member = 46 of 71.

Solar Eclipse and Variation of Radiation Flux

Many scientist groups, such as Ananda Rao, J.N. [1], Bhaskar et al. [2], Bhattcharya et al. [3], Chintalapudi, S.N. et al. [5], Kandemir, G. et al. [7] and Nayak et al. [10], observed the variation of secondary radiation flux during solar eclipse.

To observe the decrement in secondary gamma radiation flux caused by ground-based solar eclipses: (January 4, 2011), (26 December 2019), studies at Udaipur, India were conducted using a scintillation counter system.

Local Temperature and Whether at Udaipur

TABLE 1. The conditions of temperature and whether on pre-, post- and eclipse days for solar eclipse on January 4, 2011.

Date	Whether	Temperature (o_c)	
		Max.	Min.
2.1.2011	Sunny	18	7
3.1.2011	Sunny	17	6
4.1.2011	Sunny	17	6
5.1.2011	Sunny	18	5
6.1.2011	Sunny	19	6

TABLE 2. The conditions of temperature for solar eclipse on December 26, 2019.

Date	Temperature (o_c)	
	Max.	Min.
23.12.2019	25	19
25.12.2019	24	18
26.12.2019	21	15
27.12.2019	23	14
28.12.2019	22	13

Experimental Set-up and Observations

For the experimental study of solar eclipse on January 4, 2011, the scintillation detector used was of Model 802 (make: Canberra Genie 2000) to detect SGR flux produced during partial solar eclipse [Fig. 3]. Secondary radiation flux was incident on an NaI (Tl) crystal, 50 mm in thickness and 44.5 mm in diameter. This detector was coupled with a photo multiplier tube (PMT) of Model 2007P. This counter system has a high-tension voltage supply of Model 3102D with 1100 Volts DC. Using negative polarity of a

spectroscopic amplifier of Model 2022, a negative signal of about 0.5 Volt was amplified to a 5-Volt positive pulse. The signal was fed to a multi-channel analyzer with a multi-channel buffer of 1024 energy channels. The detector was put into a lead shield. The data files were stored in a computer for half an hour duration from 14.30 IST to 15.00 IST on pre-eclipse normal days 2,3 January as well as on post-eclipse days 5, 6 January 2011 and also on partial-eclipse day January 4, 2011.

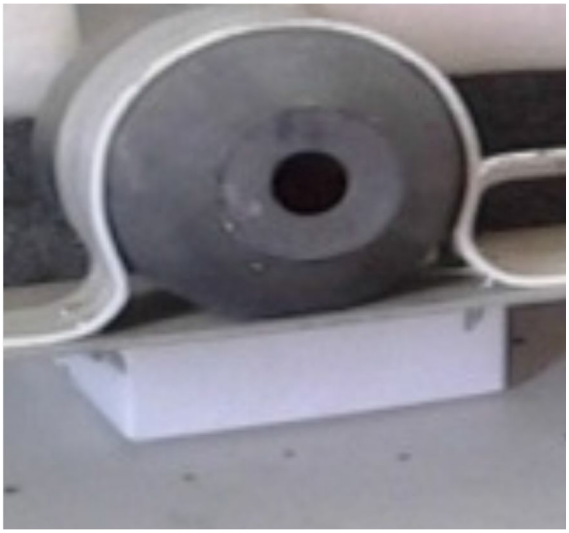

FIG. 3. Scintillation detector.

For the experimental study of solar eclipse on December 26, 2019, a scintillation detector [Fig. 4] of Model (GR611M) was used to detect the secondary gamma radiation flux. The radiations were allowed to enter the NaI (Tl) crystal of 14" width x 10" height x 11.5" depth optically coupled with a photo multiplier tube. This integral line was connected to a high-tension voltage supply of 2000 Volts DC (HV 502). A negative signal of about 0.5 Volt was amplified to a 5-Volt positive pulse using the negative polarity of the linear amplifier (LA 520). This signal was fed to an analog - to - digital counter circuit (SC 530). This digital circuit has a counter circuit (CT 541A) to count the secondary gamma radiation particles.

Scintillation counter was kept open to collect the counts as a function of time. This scintillation counter was shielded with lead. Data was collected from 8:00 AM to 11:00 AM on 23, 25, 26, 27 and 28 December 2019. The pre-eclipse days were 23, 25 and the post-eclipse days were 27, 28. On 26 December 2019, there was an annular solar eclipse at Udaipur, India from 8.00 AM to 11.00 AM.

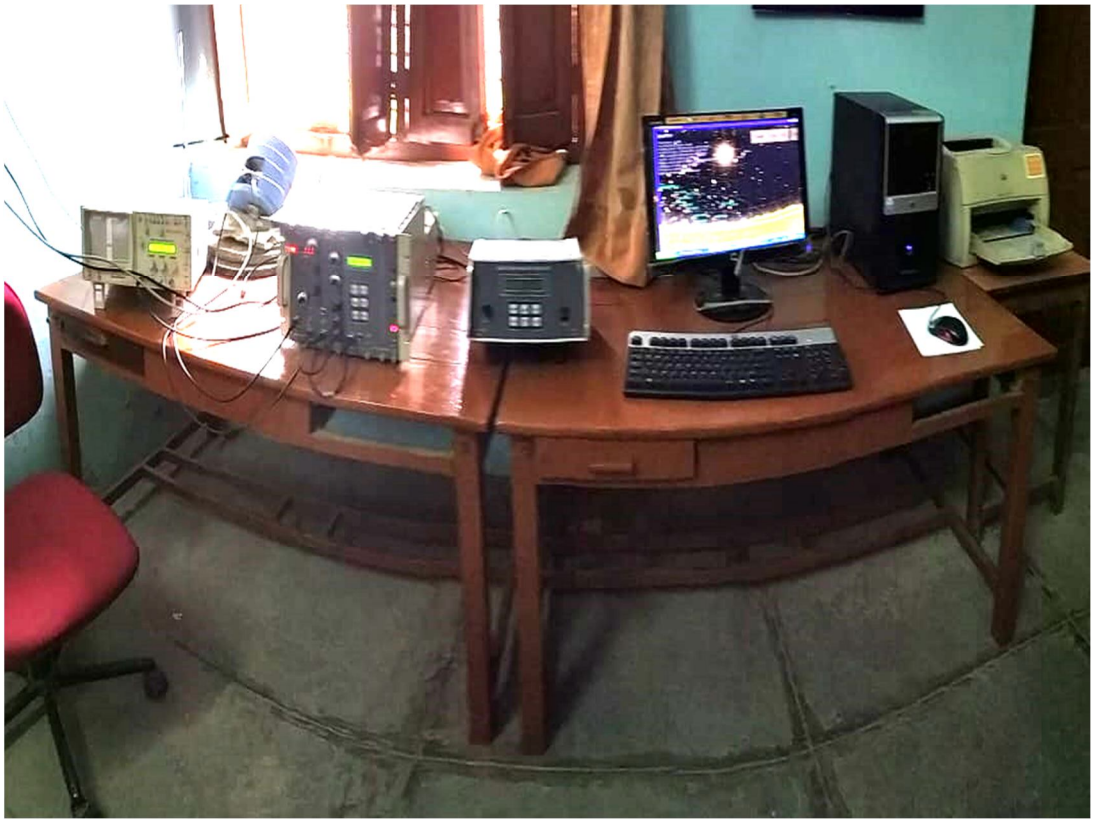

FIG. 4. Scintillation counter system.

Analysis and Results

TABLE 3. Integrated counts on the pre-, post- and solar eclipse days of secondary gamma radiation for solar eclipse on January 4, 2011.

Sr. No.	Date	Integrated Counts
1	2 (Pre-eclipse Day)	56553
2	3 (Pre-eclipse Day)	56672
3	4 (Solar Eclipse Day)	52524
4	5 (Post-eclipse Day)	60343
5	6 (Post-eclipse Day)	60990

By using Table 3, we made Fig. 5 to show the integrated counts *versus* date on pre-eclipse days 2, 3, post-eclipse days 5, 6 and solar eclipse day January 4, 2011.

Table 3 and Fig. 5 clearly show that on the pre-eclipse days 2 and 3, the integrated counts were 56553 and 56672, respectively. On the solar eclipse date of January 4, the counts were 52524. On the post-eclipse dates 5 and 6, the integrated counts were 60343 and 60990, respectively. When the average of integrated counts of all normal days 2, 3, 5 and 6 was taken, then the integrated counts were 58639. Therefore, in comparison, the average counts on solar eclipse day were decreased by 6115. To see the variation in secondary gamma radiation on the eclipse day, we used the following formula:

$$\% \text{ of variation} = \frac{\text{Average counts of normal days} - \text{counts on eclipse day}}{\text{Average counts of normal days}} \times 100.$$

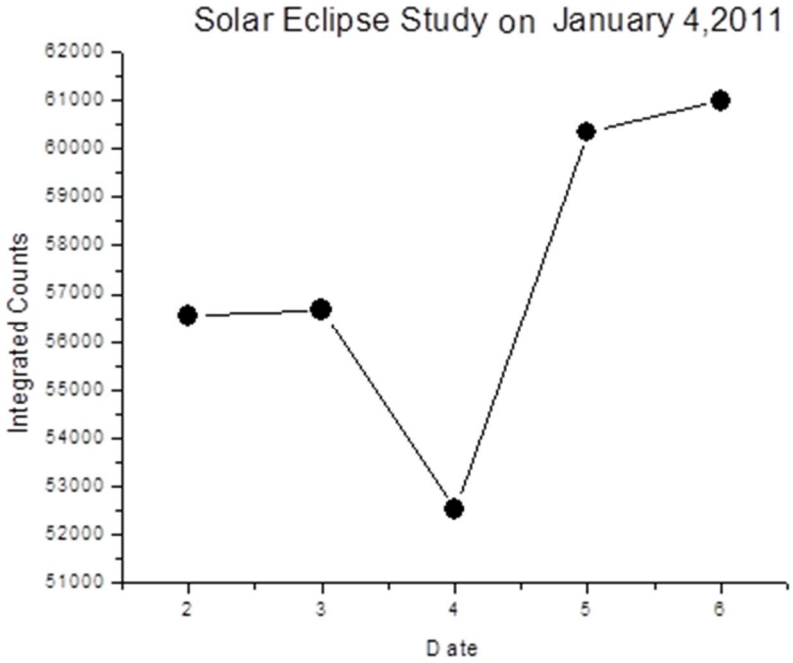

FIG. 5. Integrated counts of secondary gamma radiation *versus* date for solar eclipse on 4 Jan. 2011.

Using this formula, on the eclipse day, there is about 10 % decrement in the counts of SGR flux in comparison to the average counts on normal days.

TABLE 4. Integrated counts of secondary gamma radiation flux on the pre-, post- and solar eclipse days for solar eclipse on December 26, 2019.

Sr. No.	Date	Integrated Counts
1	23 (Pre-eclipse Day)	4892
2	25 (Pre-eclipse Day)	5378
3	26 (Solar Eclipse Day)	4183
4	27 (Post-eclipse Day)	4895
5	28 (Post-eclipse Day)	5183

By using Table 4, we made Fig. 6 to show the integrated gamma radiation counts *versus* date on pre-eclipse days, post-eclipse days and solar eclipse day.

Table 4 and Fig. 6 clearly show that on the pre-eclipse days 23 and 25, the integrated counts were 4892 and 5378, respectively. On the solar eclipse day 26, the counts were 4183. On the post-eclipse days 27 and 28, the integrated counts were 4895 and 5183, respectively. The average of integrated counts of all normal days 23, 25, 27 and 28 was 5087. Therefore, in comparison, on the solar eclipse day, the integrated counts were decreased by 904.

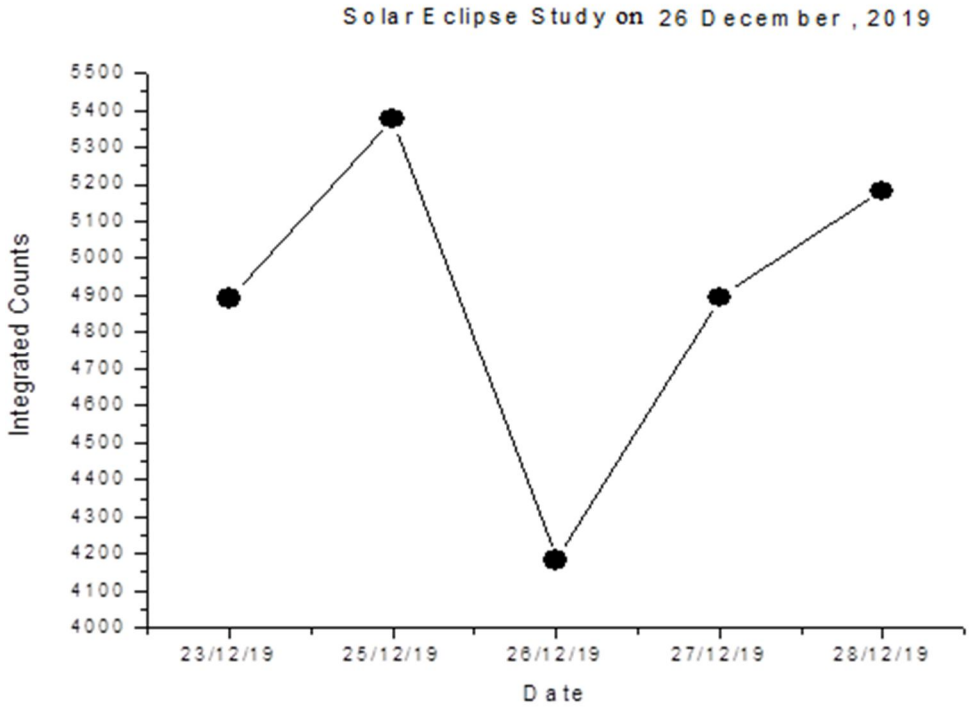

FIG. 6. Integrated counts of secondary gamma radiation *versus* date for solar eclipse on 26 Dec. 2019.

To see the variation in secondary gamma radiation on the eclipse day, we used the following formula:

$$\% \text{ of variation} = \frac{\text{Average counts of normal days} - \text{counts on eclipse day}}{\text{Average counts of normal days}} \times 100.$$

Using this formula, on the solar eclipse day, there is about 17 % reduction in the counts of SGR flux in comparison to the average counts on normal days.

Discussion

The probable reason in these present experimental studies for the decrement in SGR flux is as follows:

- During solar eclipse, the Moon comes between Sun and Earth. Therefore, the Moon acts as a big umbrella and cuts solar and cosmic radiations which are coming towards the atmosphere of the Earth. Hence, the production of secondary gamma radiation is less. Therefore, we observed a decrement of secondary gamma radiation by about 10 % on the solar eclipse day (January 4,2011) and 17 % on the solar eclipse day (December 26, 2019) in comparison to pre- and post-eclipse days.

Conclusion

From the results, we understand that the decrement of secondary gamma radiation flux was due to the obstruction effect produced by the Moon on radiations (CR and SR) during solar eclipse day.

Acknowledgments

The authors wish to thank the anonymous referees for their valuable comments.

References

[1] Ananda Rao, J.N., Phys. Lett. A, 25 (1967) 74.

[2] Bhaskara, A., Purohit, A., Hemalatha, M., Pai, C., Raghav, A., Gurada, C., Radha, S., Yadav, V., Desai, V., Chitnis, A., Sarpotdar, P. and Patankar, A., Astroparticle Physics, 35 (5) (2011) 223.

[3] Bhattacharyya, A., Biswas, S., Chatterjee, B.K., Das, M., Das, P.K., Das, T.K., De, T.K., Engineer, M.H., Mukherjee, R.N., Raha, S., Roy, S.C., Saha, S.K., Sen, A.K., Sinha, B. and Syam, D., Astrophysics and Space Science, 250 (1997) 313.

[4] Chilingarian, A., Daryan, A., Arakelyan, K., Hovhannisyan, A., Mailyan, B., Melkumyan, L., Hovsepyan, G., Chilingaryan, S., Reymers, A. and Vanyan, L., Physical Review D, 82 (4) (2010) 043009.

[5] Chintalapudi, S.N. et al., Kodaikanal Obs. Bull., 13 (1997) 225.

[6] Fulks, G.J., Journal of Geophysical Research, 80 (1975) 1701.

[7] Kandemir, G. et al., ASP Conference Series: The Last Total Solar Eclipse of the Millennium in Turkey, 205 (2000) 202.

[8] Kodama, M., Journal of the Physical Society of Japan, 52 (1983) 1503.

[9] Longair, M.S., "High-energy Astrophysics 1", 2nd Edn. Pub. (Cambridge University Press, 1992).

[10] Nayak, P.K. et al., Astroparticle Physics, 32 (2010) 286.

Volume 15, Number 2, 2022. pp. 207-214

Jordan Journal of Physics

ARTICLE

DNA Reduction of Waterborne *E.coli* by Underwater Capillary Discharge

Muhammad Waqar Ahmed[a], **Irfan Qasim**[a], **Saiqa Riaz**[a], **Najeeb ur-Rehman**[b] and **Habib Bukhari**[c]*

[a] *Department of Physics, Riphah International University, 38000 Islamabad, Pakistan.*
[b] *Department of Physics, COMSATS University, Islamabad, 45550, Pakistan.*
[c] **Department of Biosciences, Kohsar University, Murree, 47200, Pakistan.*

Doi: **https://doi.org/10.47011/15.2.11**
Received on: 20/03/2021; *Accepted on: 08/06/2021*

Abstract: *Escherichia coli* (*E. coli),* (190CRC) is one of the most common waterborne pathogens. It exists in drinking water and most of the water diseases are associated with it. The permanent inactivation of *E.coli* from water requires its DNA distortion, that makes it ineffective for regeneration. The underwater plasma discharge in capillary tube induces reactive oxidant species {$OH^{\cdot}$ radicals, Ozone (O_3), hydrogen peroxide (H_2O_2) and reactive oxygen (O)}. Ultraviolet (UV) radiations are most important shock waves that play a vital role for complete degradation of *E.coli* from water. In the current study, the effects of plasma for different oxygen injection rates and applied voltages on DNA distortion of *E.coli* have been reported. The bactericidal tests including DNA and protein leakage of plasma-treated water showed complete distortion of *E.coli* DNA structure and sterilization of water from bacteria.
Keywords: Capillary discharge, *E.coli*, DNA, Protein leakage, Sterilization.

1. Introduction

Plasma discharge in aqueous systems has attracted the attention of researchers around the globe due to its novel applications in water purification, waste treatment, industrial, agricultural, nanotechnology, semiconductors, material processing and antibacterial activities [1-5]. The required chemical reactions for such applications can be enhanced by plasma-induced ultraviolet (UV) radiations, shock waves, reactive oxidant species (ROSs) as well as charged particles [6]. In recent years, many studies on plasma types, like corona, arc and spark discharges within water and on the surface of water, have been conducted. Different (AC, DC and RF) power sources and electrode assemblies; i.e., pin-pin, pin-plate and plate-plate configurations, have been tested for performance judgement [7-11]. Capillary discharge has proven to be an advantageous technique as compared with the previous approaches in perspective of power consumption for large-volume flowing-water treatment, device portability, system cost and discharge controllability [12-15]. The capillary-produced plasma is supposed to be uniform with average electron density rising to $1x10^{19}cm^{-3}$ and average electron temperature around 2eV [16]. Such uniform plasmas are of great interest for advanced medical, biological and agricultural applications. In this study, we have implemented underwater capillary discharge technique and reported the results for *E.coli* DNA distortion for various values of applied voltages and oxygen injection rates.

Corresponding Authors: Muhammad W. Ahmed **Email**: mwaqar.ahmed@riphah.edu.pk
Habib Bukhari **Email**: vckohsaruniversity@gmail.com

2. Materials and Methods

2.1 Experimental Details

Plasma discharge was initiated in a quartzd capillary tube (outer diameter =4mm, inner Diameter = 2mm, inner, thickness= 1mm). Alternating voltage was applied across two tungsten electrodes (diameter =0.5mm), through a high-frequency (758 kHz) plasma generator CTP-2000S. Fig. 1(a) shows an illustration of the experimental setup, while Fig. 1(b) shows a visual view of capillary discharge. The separation between two electrodes where discharge occurred was kept at 5mm. The water flow was kept at 0.1 L/min, while the flow of oxygen was controlled by a mass-flow controller TELEDYNE-500P and injected by a medical syringe to initiate water bubbles and gas channels inside the capillary. This drastically reduced the required power to initiate the discharge and induced a high concentration of reactive oxidant species useful for disinfection. Emission spectrum was recorded by an Avantes multichannel spectrometer (having an optical resolution of 0.06nm-1.3nm), to determine the concentration of reactive oxidant species ($OH^{\cdot}$ radicals, O_3, H and O). The treated water was tested by the micro-well dilution method, readily after plasma treatment. Later, it was periodically examined after every 12 hours up to 48 hours to detect whether there is a regeneration of *E. coli* in water with the passage of time and an impact of plasma treatment on the geometry of bacterial colonies.

(a)

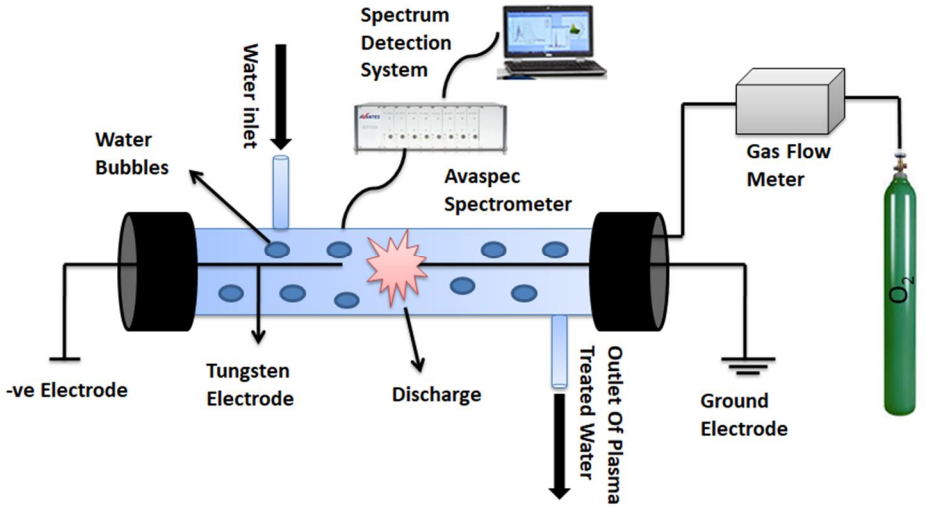

(b)

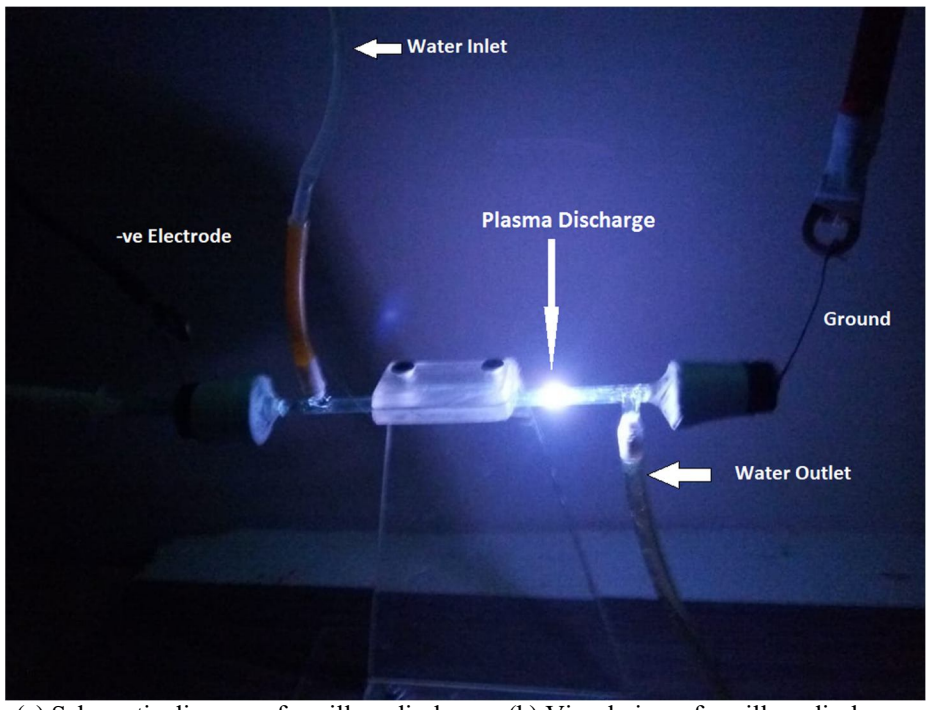

FIG. 1. (a) Schematic diagram of capillary discharge. (b) Visual view of capillary discharge.

2.2 Bacterial Strains Used and Growth Conditions

Multidrug-resistant strains isolated from clinical *Escherichia coli* (190 CRC) samples (resistant to ampicillin, erythromycin, ciprofloxacin, nalidixic acid, streptomycin, sulfamethoxazole –trimethoprim, gentamycin) were collected from Microbiology and Public Health Lab, COMSATS University, Pakistan. *Escherichia coli* was revived on Luria-Bertani (LB) broth (Sigma-Aldrich, Ireland, Ltd.) agar plates. For each set of experiments overnight (16 to 18 hrs), bacterial cultures were grown in Lauria broth at 37°C and used for investigations.

2.3 Bacterial Cell Survival Assay

Overnight, culture of each bacterial strain (~10^7 CFU) was used to inoculate autoclaved distilled water to make water suspensions. These suspensions were then used to prepare different groups of experimental design (with and without treatment) and were then exposed to plasma for different treatment times. Each sample was then serially diluted, spot-plated onto LB agar and the plates were incubated at 37°C for 24 hrs. The number of colonies on each plate was counted and the colony-forming units per ml (CFU/ml) were calculated using the following formula:

$$\text{Colony} - \text{forming units(CFU/ml)} = \frac{\text{No.of colonies X Dilution factor}}{\text{Volume of culture plated}}. \quad (1)$$

The killing % overall inactivation efficiency of plasma was calculated using the following formula:

$$\text{Killing \%} = \left(1 - \frac{\text{No.ofCFU/mlin treated samples}}{\text{No.ofCFU/mlin untreated control samples}}\right) * 100. \quad (2)$$

Untreated water suspension and un-inoculated water were used as positive and negative controls.

2.4 DNA and Protein Leakage Assay

Nightlong grown bacteria cultures were exposed to plasma. The samples were centrifuged at 14000 RPM and the supernatant was moved through a 0.22 µm (TS). By using Nano-drops, the DNA measurement was performed and Bradford assay was used for the perception of protein in the supernatant (Sampathkumar et al., 2003). Leakage index was calculated by using the following formulae:

$$\text{DNA Leakage Index} = (TS_{\text{O.D 260}} - UTS_{\text{O.D 260}})/TTS_{\text{O.D 260}} \quad (3)$$

$$\text{Protein Leakage Index} = (TCS_{\text{O.D 595}} - UTS_{\text{O.D 595}})/TTS_{\text{O.D 595}} \quad (4)$$

Untreated samples (UTS) and Triton X-100 (TTS)-treated cells were used as negative and positive controls. All experiments were performed in triplicate and repeated thrice.

3. Results and Discussion

Visual, biological and statistical methods were used to investigate and report the DNA distortion efficiency of capillary discharge.

3.1 Plasma Emission Spectrum

Due to intrusive nature, optical emission spectroscopy (OES) is a fundamental diagnostic tool, used for determining the plasma composition and concentration of highly reactive oxidant species, which play a vital role in the plasma sterilization process.

Typical emission spectrum of underwater capillary discharge is presented in Fig. 2. The spectrum reveals the existence of highly reactive oxidant species ($OH^{\cdot}$ =309nm, UV radiations = 240-400nm, Reactive oxygen = 777 and 844nm and Ozone =883nm).

After discharge occurrence, the dissociation of O_2 atomic oxygen was formed, while due to collision of electrons and water molecules, reactive hydrogen (H_α = 656 nm, H_β = 444nm) was formed as mentioned in the following reactions [17]:

$$O_2 + e \rightarrow O^+ + O + 2e \quad (5)$$

$$O_2 + e \rightarrow O^- + O \quad (6)$$

$$H_2O + e \rightarrow H + OH + e \quad (7)$$

Ozone (O_3) having a redox potential of 2.07 V was generated when diatomic oxygen gets converted into atomic ions (O^+) by plasma electrons and oxygen radicals and later, these radicals undergo three –body reaction to generate Ozone given as [17, 18, 19]:

$$O + O_2 + M \rightarrow O_3 + M \quad (8)$$

Ozone-produced $OH^{\cdot}$ radicals react with (OH^-) and H_2O_2 as given in the following reactions :

$$O_3 + 2OH^- \rightarrow OH^{\cdot} + HO^*{}_2 + O_2^{\cdot -} \quad (9)$$

$$O_3 + H_2O_2 \rightarrow OH^{\cdot} + HO^*{}_2 + O^{\cdot}{}_2 \quad (10)$$

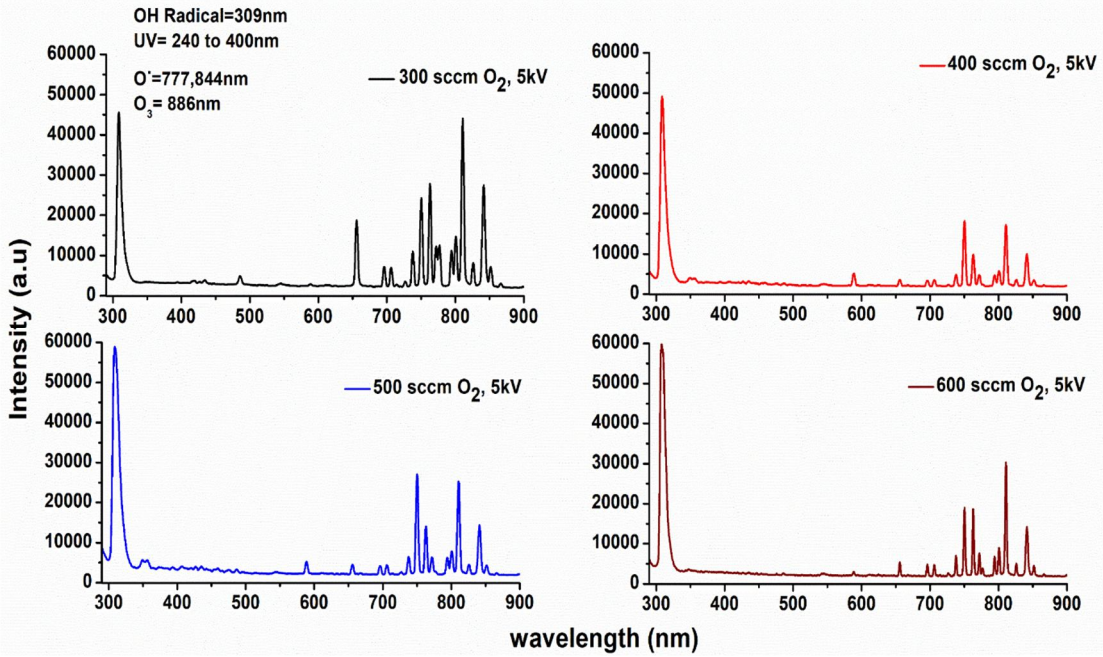

FIG. 2. Typical plasma emission spectrum.

After generating plasma, the transitions (excitations to the ground states) of atomic and molecular species cause emission of UV radiations, observed from the emission spectrum. The emission spectrum represents variation in UV radiation and $OH^{\cdot}$ radical densities as a function of applied voltage for different flow rates. Due to increasing applied voltage and oxygen rate, the power of discharge pulses increased prominently. The production of $OH^{\cdot}$ Radicals and UV radiation also increased and a much brighter discharge spectrum was observed. Since $OH^{\cdot}$ radicals have a short half-life (10^{-8}s), the decay of $OH^{\cdot}$ radicals further triggers the production of other reactive species, such as O_3. The electron temperature rises with the increase in applied voltage, which ultimately enhances the production rates of $OH^{\cdot}$ radicals and UV radiation. Similarly, with the increase in gas-flow rate, electrons will effectively participate in collisional processes, resulting in the creation of more reactive species like $OH^{\cdot}$ radicals and increasing UV radiation intensity.

3.2 *E.coli* Inactivation by Plasma Discharge

E.coli colonies after plasma treatment under different experimental conditions are shown in Fig. 3 in the form of typical images of LB agar plates, while the graphical illustration of all *E.coli* CFUs is presented in Fig. 4. After plasma treatment, at 3Kv, the CFU was reduced from 88 to 2 at 300sccm (standard cubic centimeter per minute) and 600sccm; at 4Kv, the CFU was reduced from 185 to 1 at 300sccm and 600sccm; at 5Kv, the CFU was reduced from 290 to 5 at 300sccm and 600sccm; at 6Kv, the CFU was reduced from 61 to 10 at 300sccm and 600sccm; at 7Kv, the CFU was reduced from 278 to 66 at 300sccm and 600sccm.

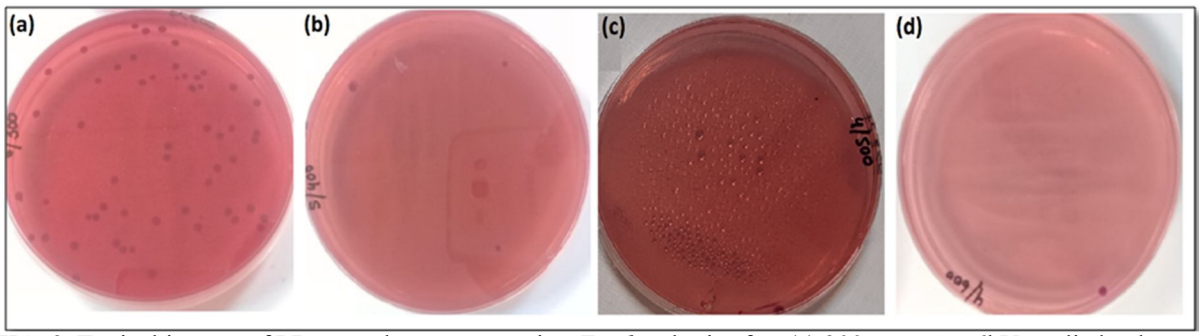

FIG. 3. Typical images of LB agar plates representing *E.coli* colonies for: (a) 300 sccm O_2, 6kV applied voltage. (b) 400 sccm O_2 5kV applied voltage. (c) 500 sccm O_2, 4kV applied voltage. (d) 600 sccm O_2, 4kV applied voltage.

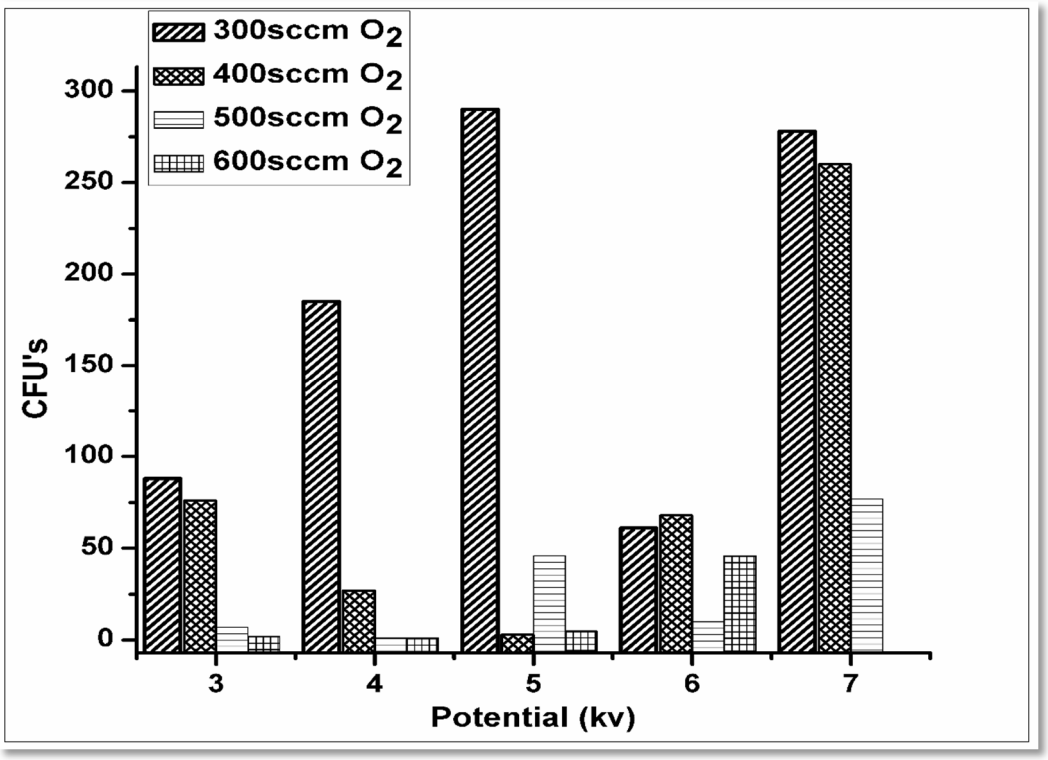

FIG. 4. CFUs of *E.coli* under different oxygen injection rates at various applied voltages.

Oxygen shows a remarkable influence on the inactivation of *E.coli* due to its potential resistance for the growth of bacterial cells. Increased oxygen injection rates encourage greater leakage of ROS from respiratory chain, which affects the DNA and metalloenzymes. This in turn leads towards mutagenesis and impaired growth. The $OH\cdot$ radical, UV radiations and shock waves have participated mainly in the inactivation of *E.coli*. They interact directly with bacteria in water, destroy the DNA structure and disable mutation. Shock waves also to increase the exposure of micro-organisms inactivation by scattering the colonies in liquid.

3.3 Deoxyribonucleic Acid (DNA) Analysis and Protein Leakage Tests

Proteins are important bio-molecules which play an important role in balancing bacterial cell physiological activity. The plasma treatment-induced DNA leakage and protein leakage through membrane of *E. coli* cell are represented in Fig. 5 and Fig. 6, respectively. The DNA damage of isolated nuclei is dependent on the concentration of oxygen. Protein concentrations were found to decrease with the increase in oxygen flow rate, which in turn damages the DNA of *E. coli*. The protein and DNA of gross untreated *E.coli* sample decreased to 0.413µg/mL and 0.011, respectively after 600 sccm at 4kV. DNA and protein leakage leads to bacteria killing by inhibiting antioxidant machinery that damages the membrane protein as well as a cascade of DNA repair. Being the heredity material, DNA is a very important component of the cell and is comprised of a double helix structure. By increasing the oxygen injection rate, the concentration of reactive species also increases, which in turn elevates the rate of DNA and protein leakage. Underwater plasma discharge multiple reactive species ($OH\cdot$, O_2, RO, RH and UV) were involved in DNA distortion. Most of the DNA damage was caused by ionizing radiations mediated by hydroxyl radical ($OH\cdot$) and quintessential reactive oxygen species. Such distortion involves strand splits, caused by the hydroxyl radical by abstracting a deoxyribose hydrogen atom. The presence of UV radiation and other genotoxic chemicals resulted in single and double breaks of the DNA strands. DNA double strand breaks (DSBs) are the most deleterious among various forms of distortion, because they involve both DNA strands and may result in the loss of genetic material. At large concentrations, oxygen-free radicals or more commonly reactive oxygen species (ROSs) may inflict harm to the composition of cells, lipids, proteins and DNA, resulting in oxidative stress that has been implicated in a variety of diseases.

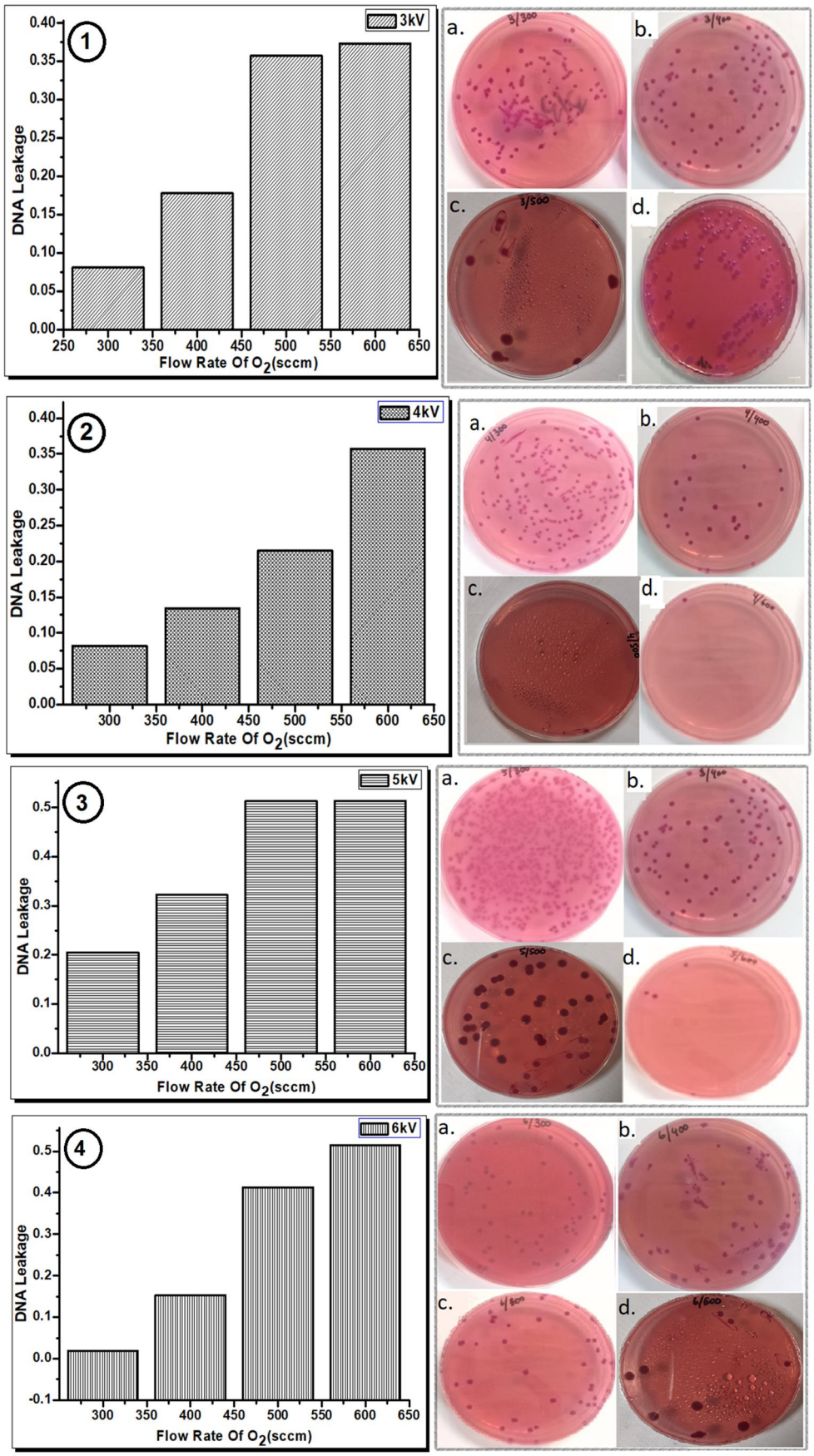
1
3kV
DNA Leakage
Flow Rate Of O_2(sccm)
a.
b.
c.
d.
2
4kV
DNA Leakage
Flow Rate Of O_2(sccm)
a.
b.
c.
d.
3
5kV
DNA Leakage
Flow Rate Of O_2(sccm)
a.
b.
c.
d.
4
6kV
DNA Leakage
Flow Rate Of O_2(sccm)
a.
b.
c.
d.

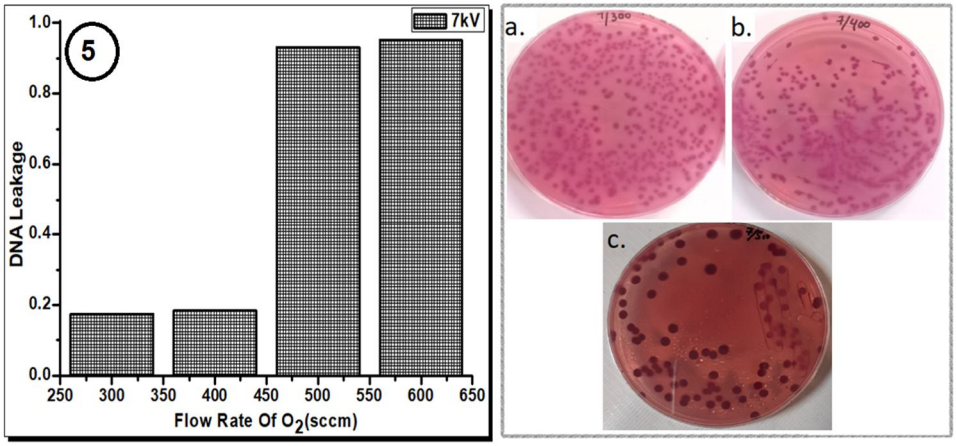

FIG. 5. Graphical visual representation of *E.coli* DNA distortion under different oxygen injection rates and applied potentials. (1). 3 kV applied potential (a) 300sccm (b) 400 sccm (c) 500sccm (d) 600 sccm. (2). 4 kV applied potential (a) 300sccm (b) 400 sccm (c) 500sccm (d) 600 sccm. (3). 5 kV applied potential (a) 300sccm (b) 400 sccm (c) 500sccm (d) 600 sccm. (4). 6 kV applied potential (a) 300sccm (b) 400 sccm (c) 500sccm (d) 600 sccm. (5). 7 kV applied potential (a) 300sccm (b) 400 sccm (c) 500sccm.

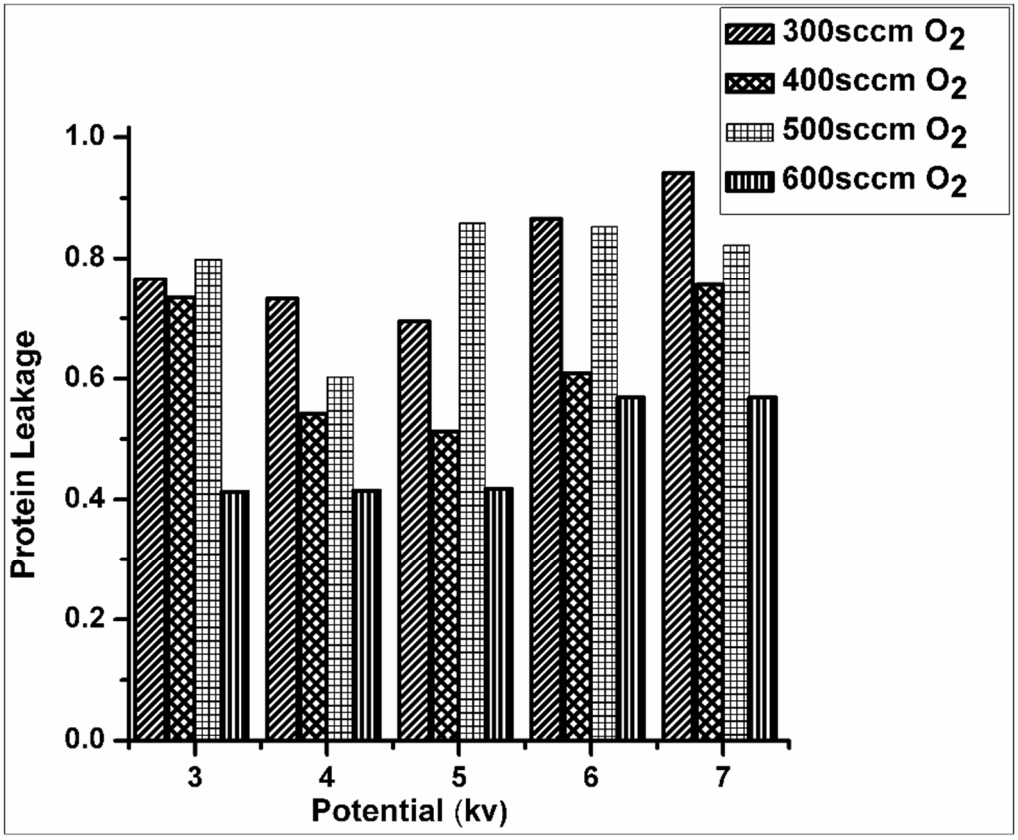

FIG. 6. Protein leakage test of *E.coli* under different oxygen injection rates and applied potentials.

4. Conclusions

Underwater plasma discharge is a novel technique for inactivation of micro-organisms. The inactivation of *E.coli* due to interaction of reactive oxidant species with DNA of gram negative *E.coli* has been studied, which reports that the injection rate of oxygen (300 to 600 sccm) and potential (3kV to 7kV) enhance the concentrations of $OH^{\cdot}$ radicals, O_3, reactive oxygen and UV radiations. At high oxygen injection rate and high potential, an increase in inactivation efficiency of *E.coli* is observed. The presence of ROSs resulted in DNA and protein leakage leads to the permanent inactivation of *E.coli*. Underwater plasma discharge is an effective and non-toxic approach for sterilization of water.

Acknowledgements

This research work was supported by the Physics Department of Riphah International University Islamabad. The researchers are highly thankful to the Department of Physics of COMSATS University, Islamabad and the Microbiology and Public Health Lab of COMSATS University, Islamabad, for providing collaborative research facilities.

References

[1] Qu, X., Brame, J., Li, Q. and Alvarez, P.J.J., Acc. Chem. Res., 46 (3) (2013) 834.

[2] Ostrikov, K., Cvelbar, U. and Murphy, A.B., J. Phys. D: Appl. Phys., 44 (2011) 174001.

[3] Jablonowski, H., Bussiahn, R., Hammer, M.U., Weltmann, K.-D., Von Woedtke, Th. and Reuter, S., Phys. Plasmas, 22 (2015) 122008.

[4] Wani, S., Maker, J.K., Thompson, J.R., Barnes, J. and Singleton, I., Agriculture, 5 (155) (2015) 155.

[5] Schuch, A.P., Galhardo, R.S., Bessa, K.M.de L., Schuch, N.J. and Menck, C.F.M., Photochem. Photobiol. Sci., 8 (111) (2007) 252.

[6] Sharma, P., Bhushan Jha, A., Dubey, R.S. and Pessarakli, M., J. Bot., 2012 (2012) 1.

[7] Yasuoka, K. and Sato, K., Int. J. Plasma Environ. Sci. Technol., 3 (1) (2009) 22.

[8] Hosseini, S.H.R., Iwasaki, S., Sakugawa, T. and Akiyama, H., J. Korean Phys. Soc., 59 (2009) 3526.

[9] Ahmed, M.W., Yang, J.K., Mok, Y.S. and Lee, H.J., J. Korean Phys. Soc., 65 (2014) 1404.

[10] Awe, O.W., Liu, R. and Zaho, Y., JWS, 6 (2) (2016) 63.

[11] Eliasson, B., Egli, W. and Kogelschatz, U., J. Phys. D, 20 (142) (1997) C4-47-66.

[12] Capodaglio, A.G. and Olsson, G., 12 (266) (2019) 2.

[13] Hong, Y.C., Park, H.J., Lee, B.J., Kang, W.S. and Uhm, H.S., Phys. Plasmas, 17 (2010) 053502.

[14] Sunka, P., Phys. Plasmas, 8 (2001) 2587.

[15] Galkin, A.L., Kalashnikov, M.P., Klinkov, V.K., Korobkin, V.V., Romanovsky, M.Y. and Shiryaev, O.B., Phys. Plasmas, 17 (2010) 053105.

[16] Ahmed, M.W., Rahman, M.S., Choi, S., Shaislamov, U., Yang, J.K., Suresh, R. and Lee, H.J., Appl. Sci. Converg. Technol., 26 (5) (2017) 118.

[17] Locke, B.R. and Thagard, S.M., Plasma. Chem. Plasma. Process., 32 (2012) 875.

[18] Schröter, S., Bredin, J., Gibson, A.R., West, A., Dedrick, J.P., Wagenaars, E., Niemi, K., Gans, T. and O'Connell, D., Plasma Sources Sci. Technol., 29 (2020) 105001.

[19] Cuerda-Correa, E.M., Alexandre-Franco, M.F. and Fernández-González, C., Water, 12 (2020) 102.

المراجع: يجب طباعة المراجع بأسطر مزدوجة ومرقمة حسب تسلسلها في النص. وتكتب المراجع في النص بين قوسين مربعين. ويتم اعتماد اختصارات الدوريات حسب نظام Wordlist of Scientific Reviewers.

الجداول: تعطى الجداول أرقاما متسلسلة يشار إليها في النص. ويجب طباعة كل جدول على صفحة منفصلة مع عنوان فوق الجدول. أما الحواشي التفسيرية، التي يشار إليها بحرف فوقي، فتكتب أسفل الجدول.

الرسوم التوضيحية: يتم ترقيم الأشكال والرسومات والرسومات البيانية (المخططات) والصور، بصورة متسلسلة كما وردت في النص.

تقبل الرسوم التوضيحية المستخرجة من الحاسوب والصور الرقمية ذات النوعية الجيدة بالأبيض والأسود، على ان تكون أصيلة وليست نسخة عنها، وكل منها على ورقة منفصلة ومعرفة برقمها بالمقابل. ويجب تزويد المجلة بالرسومات بحجمها الأصلي بحيث لا تحتاج إلى معالجة لاحقة، وألا تقل الحروف عن الحجم 8 من نوع Times New Roman، وألا تقل سماكة الخطوط عن 0.5 وبكثافة متجانسة. ويجب إزالة جميع الألوان من الرسومات ما عدا تلك التي ستنشر ملونة. وفي حالة إرسال الرسومات بصورة رقمية، يجب أن تتوافق مع متطلبات الحد الأدنى من التمايز (1200 dpi Resolution) لرسومات الأبيض والأسود الخطية، و 600 dpi للرسومات باللون الرمادي، و300 dpi للرسومات الملونة. ويجب تخزين جميع ملفات الرسومات على شكل (jpg)، وأن ترسل الرسوم التوضيحية بالحجم الفعلي الذي سيظهر في المجلة. وسواء أرسل المخطوط بالبريد أو عن طريق الشبكة (Online)، يجب أرسال نسخة ورقية أصلية ذات نوعية جيدة للرسومات التوضيحية.

مواد إضافية: تشجع المجلة الباحثين على إرفاق جميع المواد الإضافية التي يمكن أن تسهل عملية التحكيم. وتشمل المواد الإضافية أي اشتقاقات رياضية مفصلة لا تظهر في المخطوط.

المخطوط المنقح (المعدّل) والأقراص المدمجة: بعد قبول البحث للنشر وإجراء جميع التعديلات المطلوبة، فعلى الباحثين تقديم نسخة أصلية ونسخة أخرى مطابقة للأصلية مطبوعة بأسطر مزدوجة، وكذلك تقديم نسخة إلكترونية تحتوي على المخطوط كاملا مكتوبا على Microsoft Word for Windows 2000 أو ما هو استجد منه. ويجب إرفاق الأشكال الأصلية مع المخطوط النهائي المعدل حتى لو تم تقديم الأشكال إلكترونيا. وتخزن جميع ملفات الرسومات على شكل (jpg)، وتقدم جميع الرسومات التوضيحية بالحجم الحقيقي الذي ستظهر به في المجلة. ويجب إرفاق قائمة ببرامج الحاسوب التي استعملت في كتابة النص، وأسماء الملفات على قرص مدمج، حيث يعلَم القرص بالاسم الأخير للباحث، وبالرقم المرجعي للمخطوط للمراسلة، وعنوان المقالة، والتاريخ. ويحفظ في مغلف واقٍ.

حقوق الطبع

يُشكِّل تقديم مخطوط البحث للمجلة اعترافاً صريحاً من الباحثين بأنّ مخطوط البحث لم يُنْشَر ولم يُقَدَّم للنشر لدى أي جهَة أخرى كانت وبأي صيغة ورقية أو إلكترونية أو غيرها. ويُشترط على الباحثين ملء أنموذج يَنُصُّ على نقْل حقوق الطبع لتُصبح ملكاً لجامعة اليرموك قبل الموافقة على نشر المخطوط. ويقوم رئيس التحرير بتزويد الباحثين بإنموذج نقل حقوق الطبع مع النسخة المُرْسَلَة للتنقيح. كما ويُمنع إعادة إنتاج أيِّ جزء من الأعمال المنشورة في المجلّة من دون إذن خَطِّيٍّ مُسبَق من رئيس التحرير.

إخلاء المسؤولية

إن ما ورد في هذه المجلة يعبر عن آراء المؤلفين، ولا يعكس بالضرورة آراء هيئة التحرير أو الجامعة أو سياسة اللجنة العليا للبحث العلمي أو وزارة التعليم العالي والبحث العلمي. ولا يتحمل ناشر المجلة أي تبعات مادية أو معنوية أو مسؤوليات عن استعمال المعلومات المنشورة في المجلة أو سوء استعمالها.

الفهرسة: المجلة مفهرسة في:

Scopus	ULRICHSWEB GLOBAL SERIALS DIRECTORY

معلومات عامة

المجلة الأردنية للفيزياء هي مجلة بحوث علميّة عالمية متخصصة مُحكمة تصدر بدعم من صندوق دعم البحث العلمي والابتكار، وزارة التعليم العالي والبحث العلمي، عمان، الأردن. وتقوم بنشر المجلة عمادة البحث العلمي والدراسات العليا في جامعة اليرموك، إربد، الأردن. وتنشر البحوث العلمية الأصيلة، إضافة إلى المراسلات القصيرة Short Communications، والملاحظات الفنية Technical Notes، والمقالات الخاصّة Feature Articles، ومقالات المراجعة Review Articles، في مجالات الفيزياء النظرية والتجريبية، باللغتين العربية والإنجليزية.

تقديم مخطوط البحث

تقدم البحوث عن طريق إرسالها إلى البريد الإلكتروني : jjp@yu.edu.jo

تقديم المخطوطات إلكترونيًا: اتبع التعليمات في موقع المجلة على الشبكة العنكبوتية.

ويجري تحكيمُ البحوثِ الأصيلة والمراسلات القصيرة والملاحظات الفنية من جانب مُحكّمين اثنين في الأقل من ذوي الاختصاص والخبرة. وتُشَجّع المجلة الباحثين على اقتراح أسماء المحكمين. أما نشر المقالات الخاصّة في المجالات الفيزيائية النَشِطَة، فيتم بدعوة من هيئة التحرير، ويُشار إليها كذلك عند النشر. ويُطْلَب من كاتب المقال الخاص تقديم تقرير واضح يتّسم بالدقة والإيجاز عن مجال البحث تمهيداً للمقال. وتنشر المجلةُ أيضاً مقالات المراجعة في الحقول الفيزيائية النشطة سريعة التغيُّر، وتُشَجّع كاتبي مقالات المراجعة أو مُستَكتبيها على إرسال مقترحٍ من صفحتين إلى رئيس التحرير. ويُرْفَق مع البحث المكتوب باللغة العربية ملخص (Abstract) وكلمات دالة (Keywords) باللغة الإنجليزية.

ترتيب مخطوط البحث

يجب أن تتم طباعة مخطوط البحث ببنط 12 نوعه Times New Roman، وبسطر مزدوج، على وجه واحد من ورق A4 (21.6 × 27.9 سم) مع حواشي 3.71 سم ، باستخدام معالج كلمات ميكروسوفت وورد 2000 أو ما استَجَد منه. ويجري تنظيم أجزاء المخطوط وفق الترتيب التالي: صفحة العنوان، الملخص، رموز التصنيف (PACS)، المقدّمة، طرق البحث، النتائج، المناقشة، الخلاصة، الشكر والعرفان، المراجع، الجداول، قائمة بدليل الأشكال والصور والإيضاحات، ثَمَّ الأشكال والصور والإيضاحات. وتُكْتَب العناوين الرئيسة بخطٍ **غامق**، بينما تُكْتَب العناوين الفرعية بخطٍ *مائل*.

صفحة العنوان: وتشمل عنوان المقالة، أسماء الباحثين الكاملة وعناوين العمل كاملة. ويكتب الباحث المسؤول عن المراسلات اسمه مشارا إليه بنجمة، والبريد الإلكتروني الخاص به. ويجب أن يكون عنوان المقالة موجزا وواضحا ومعبرا عن فحوى (محتوى) المخطوط، وذلك لأهمية هذا العنوان لأغراض استرجاع المعلومات.

الملخص: المطلوب كتابة فقرة واحدة لا تزيد على مائتي كلمة، موضحة هدف البحث، والمنهج المتبع فيه والنتائج وأهم ما توصل إليه الباحثون.

الكلمات الدالة: يجب أن يلي الملخص قائمة من 4-6 كلمات دالة تعبر عن المحتوى الدقيق للمخطوط لأغراض الفهرسة.

PACS: يجب إرفاق الرموز التصنيفية، وهي متوافرة في الموقع http://www.aip.org/pacs/pacs06/pacs06-toc.html.

المقدمة: يجب أن توضّح الهدف من الدراسة وعلاقتها بالأعمال السابقة في المجال، لا أن تكون مراجعة مكثفة لما نشر (لا تزيد المقدمة عن صفحة ونصف الصفحة مطبوعة).

طرائق البحث (التجريبية / النظرية): يجب أن تكون هذه الطرائق موضحة بتفصيل كاف لإتاحة إعادة إجرائها بكفاءة، ولكن باختصار مناسب، حتى لا تكون تكرارا للطرائق المنشورة سابقا.

النتائج: يستحسن عرض النتائج على صورة جداول وأشكال حيثما أمكن، مع شرح قليل في النص ومن دون مناقشة تفصيلية.

المناقشة: يجب أن تكون موجزة وتركز على تفسير النتائج.

الاستنتاج: يجب أن يكون وصفا موجزا لأهم ما توصلت إليه الدراسة ولا يزيد عن صفحة مطبوعة واحدة.

الشكر والعرفان: الشكر والإشارة إلى مصدر المنح والدعم المالي يكتبان في فقرة واحدة تسبق المراجع مباشرة.

Subscription Form

Jordan Journal of PHYSICS

An International Peer-Reviewed Research Journal issued by the Support of the Scientific Research and Innovation Support Fund

Published by the Deanship of Research & Graduate Studies, Yarmouk University, Irbid, Jordan

Name: ..... الأسم:

Specialty:..... التخصص:

Address: ..... العنوان:

P.O. Box:..... صندوق البريد:

City & Postal Code: ..... المدينة/الرمز البريدي:

Country: ..... الدولة:

Phone: ..... رقم الهاتف:

Fax No:..... رقم الفاكس:

E-mail:..... البريد الإلكتروني:

No. of Subscription: ..... عدد الإشتراكات:

Method of Payment:..... طريقة الدفع:

Amount Enclosed:..... المبلغ المرفق:

Signature: ..... التوقيع:

Cheques should be paid to Deanship of Research and Graduate Studies - Yarmouk University.

I would like to subscribe to the Journal
For

- One Year
- Two Years
- Three Years

One Year Subscription Rates

	Inside Jordan	Outside Jordan
Individuals	JD 8	€ 40
Students	JD 4	€ 20
Institutions	JD 12	€ 60

Correspondence

Subscriptions and Sales:

Prof. Mahdi Salem Lataifeh
Deanship of Research and Graduate Studies
Yarmouk University
Irbid – Jordan
Telephone: 00 962 2 711111 Ext. 2075
Fax No.: 00 962 2 7211121

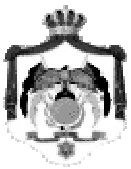

المملكة الأردنية الهاشمية

جامعة اليرموك

المجلة الأردنية
للفيزياء

مجلة بحوث علمية عالمية متخصصة محكّمة

تصدر بدعم من صندوق دعم البحث العلمي والابتكار

المجلد (15)، العدد (2)، حزيران 2022م / ذو القعدة 1443هـ

المجلة الأردنية

للفيزياء

مجلة بحوث علمية عالمية محكّمة

المجلد (15)، العدد (2)، حزيران 2022م / ذو القعدة 1443هـ

المجلة الأردنية للفيزياء: مجلة علمية عالمية متخصصة محكّمة تصدر بدعم من صندوق دعم البحث العلمي والإبتكار، عمان، الأردن، وتصدر عن عمادة البحث العلمي والدراسات العليا، جامعة اليرموك، إربد، الأردن.

رئيس التحرير:

مهدي سالم لطايفة

قسم الفيزياء، جامعة اليرموك، إربد، الأردن.

mahdi.q@yu.edu.jo

هيئة التحرير:

نبيل يوسف أيوب

قسم العلوم الأساسية، الجامعة الألمانية الأردنية، عمان، الأردن.

nabil.ayoub@gju.edu.jo

طارق فتحي حسين

قسم الفيزياء، الجامعة الأردنية، عمان، الأردن.

t.hussein@ju.edu.jo

مروان سليمان الموسى

قسم الفيزياء، جامعة مؤتة، الكرك، الأردن.

mmousa@mutah.edu.jo

محمد خالد الصغير

قسم الفيزياء، الجامعة الهاشمية ، الزرقاء، الأردن.

msugh@hu.edu.jo

محمد العمري

قسم الفيزياء، جامعة العلوم والتكنولوجيا، إربد، الأردن.

alakmoh@just.edu.jo

إبراهيم البصول

قسم الفيزياء، جامعة آل البيت، المفرق، الأردن.

Ibrahimbsoul@yahoo.com

المدقق اللغوي: حيدر المومني

سكرتير التحرير: مجدي الشناق

ترسل البحوث إلى العنوان التالي:

الأستاذ الدكتور مهدي سالم لطايفة

رئيس تحرير المجلة الأردنية للفيزياء

عمادة البحث العلمي والدراسات العليا، جامعة اليرموك

إربد ، الأردن

هاتف 7211111 2 962 00 **فرعي** 2075

E-mail: *jjp@yu.edu.jo* **Website**: *http://Journals.yu.edu.jo/jjp*